
THE UNIVERSITY *of* EDINBURGH

# Application of high-order hydrodynamic models to floating offshore wind TLP: numerical and experimental analysis

Elie Rongé



Doctor of Engineering

IDCORE - The University of Edinburgh

2023

*I'd like to dedicate this thesis to all the friends I made during this journey, from Edinburgh to Paris and beyond, to all those who made this adventure less lonely and enriching*

# Abstract

With the large-scale development in the last decades of fixed offshore wind across Europe and the ever-more-present threat of climate change dominating national and global agenda, the exploitation of wind power in deep-water using floating wind turbines is gathering a significant amount of interest. Compared to other types of floating wind platforms, Tension-leg-platforms (TLPs) are less compliant systems resisting dynamic forces through their pre-tensioned tendons. Whilst this reduces the weight of the platform hull, understanding extreme loading cycles in the mooring system becomes an important design issue.

Recent research has revealed the importance of considering sum-frequency second-order and third-order loads to capture extreme events, such as slack-line events and ringing events. These events occur when high-frequency wave loads excite the resonant vertical modes of large and stiff floating systems. For the offshore wind industry, it is essential to ascertain whether such events can be stochastically predicted across numerous random sea-states, addressing both ultimate limit state and fatigue design scenarios.

This thesis presents a comprehensive review of existing numerical methods available to engineers for calculating second and third-order forces in aero-hydro-servo-elastic time domain solvers, commonly used in the offshore wind industry for assessing multiple design load cases. These models encompass potential (semi-analytical and BEM) and strip-theory approaches (Rainey and FNV). Subsequently, these approaches are applied to a complete academic floating offshore wind TLP platform, considering both fixed and fully dynamic conditions. The nonlinear hydrodynamic loading on the platform in the fixed condition is compared against high-fidelity simulations obtained using a Navier-Stokes CFD numerical wave tank. Furthermore, an experimental campaign is designed to investigate the application of these numerical models to dynamic conditions, encompassing wave and coupled wind-wave excitation.

Both the CFD and experimental results indicate that, while previous literature has primarily focused on inertial loads, viscous effects, particularly vertical drag, exert a more significant influence on the third-order response of the studied TLP system. This finding emphasises the necessity for further research into modelling viscous drag on complex floating structures. Additionally, the experimental campaign underscores the importance of characterizing both structural and viscous damping as significant parameters that strongly affect the resonant response of the floating offshore wind TLP system.

Finally, a time-frequency analysis of the response is undertaken which serves to identify the ringing events. This analysis shows that whilst numerical models fail to capture ringing events adequately, they can still predict their occurrence, albeit with lower amplitudes. This thesis thus presents a comparative review of the numerical wave loading approach available for the stochastic treatment of ringing and slack-line events in floating wind TLP systems, providing valuable insights for the industry.


**Figure 1:** The dance of TLPs. Source: Elie Ronge

# Lay Summary

As the threat of climate change looms large, countries are racing against time to decarbonise their energy sector. Offshore wind power has emerged as a significant contributor to the transition to renewable energy, especially in the UK, Northwestern Europe, and other parts of the world. Until recently, offshore wind turbines were mounted on tower structures that were fixed to the seabed. However, these structures were only viable for relatively shallow water depths due to economic reasons. The cost of these foundations becomes prohibitively expensive in waters deeper than 60m, making the electricity generated uncompetitive. For this reason, offshore wind has been limited to areas close to the shore or in shallow water regions like the North Sea. However, a new foundation concept has emerged in the last decades which consists of installing offshore wind turbines on floating platforms anchored to the seabed with cables. With this technology, wind turbines are much less restricted to water depth which opens many new regions of the world with a suitable wind climate for the development of offshore wind. This small revolution finds its roots in the oil & gas sector which developed over the years various concepts of floating foundations for deep sea exploration and extraction.

Among these concepts comes the tension-leg platform usually abbreviated TLP. This floating foundation is based on the Archimedes principle that if a body is immersed further in water than the point of floating equilibrium, the body will be pushed upwards by the water pressure until equilibrium is found. For TLPs, the body is restrained below its equilibrium point through the use of fully tensioned mooring lines attached to the body, also called tendons, which connect it to the anchors on the sea bed. As the TLP is pushed upwards by the water pressure, the lines become tense, creating a rigid system that limits the motion of the floating wind turbine under the action of waves and wind. However, the issue with such a system is that it is completely reliant on these tendons to achieve stability and it would topple over without them. Therefore, engineers are looking for ways to predict the forces that these lines will undergo during their lifetime, including the probability of extreme forces. It can be likened to having a wind turbine placed on a spring mat, which makes the system rigid and prone to fast vibrations that can be amplified by wave forces. These fast vibrations can affect the tendons over time and being able to predict them is crucial for determining the anchoring system longevity.

This thesis investigated various engineering numerical approaches used in the industry to model wave loads on offshore structures. The aim was to assess the capacity of these approaches to simulate the behaviour of a floating wind turbine on TLP foundations, with a particular focus on predicting strong vibration behaviours and their impact on extreme tensions in the tendons. The thesis used a combination of highly accurate numerical simulations and an experimental campaign using a scaled-down model of a floating wind turbine to assess the accuracy of the predictions given by simpler approaches. The results showed that the existing methods used by the industry are relatively successful in predicting the general behaviour of the floating wind TLP system and can capture a portion of the strong vibration behaviour. However, the study also identified some wave effects that were not adequately scrutinised by the industry, but which are important to predict the vibration behaviour. This work demonstrated their significance numerically and experimentally. Therefore, the results of this work inform engineers on the current capacity of the standards approaches to model floating wind turbine TLP behaviour under severe waves and some of the research gaps affecting our ability to design them.

# Acknowledgements

This research was funded by EPSRC and NERC Industrial CDT in Offshore Renewable Energy (IDCORE), grant number EP/S023933/1. IDCORE is a partnership CDT of the Universities of Edinburgh, Stathclyde and Exeter and Scottish Association for Marine Science (SAMS). The authors wish to thank the collaborating academic institutions of this program and the hosting industrial partner EDF R&D which proposed the project hosted me at their laboratory and without which this thesis would not have been possible. I would like to thank Christophe Peyrard (EDF R&D LNHE) for being an amazingly knowledgeable, patient industrial supervisor who has guided me through these three years. I also cannot forget my main academic supervisor Prof. Vengatesan Venugopal (The University of Edinburgh) for his thorough supervision and constant encouragement which helped greatly in boosting my confidence as a researcher. Furthermore, I would like to acknowledge the valued discussion and support I received from my co-supervisors Prof. Lars Johanning (University of Exeter) and Prof. Qing Xiao (University of Strathclyde) as well as a special thanks to Prof. Michel Benoit (EDF R&D LNHE) who voluntarily supervised part of my work and provided valued contributions.

I also have to thank Maxime Duchet (EDF R&D LNHE) and Clément Buvat (EDF R&D LNHE), the designers of the EDF-TLP and its physical model, for helping me through the ups and downs of experimental work. The tank testing campaign would also not have been possible without the dedication of the lab technicians of the LNHE, especially Nicolas Gueguen (EDF R&D LNHE) who has assisted me throughout the experimental phase. Special thanks go to Šime Malenica (Bureau Veritas, Paris, France) and Bernard Molin (Ecole Centrale Méditerranée, Marseille, France) for providing the third-order semi-analytical diffraction solver and to Fabien Robaux (EDF R&D LNHE, Chatou France) and William Benguigui (EDF R&D MFEE, Chatou, France) for their help in setting up the CFD Numerical Wave Tank and providing valuable insights.

I want to express my gratitude to my colleagues from the 2019 IDCORE cohort and the lively LNHE-LHSV lab. They have provided immense social support during my three-year research journey. Our casual discussions, experience sharing over online chats, and coffee breaks helped me overcome the inevitable doubts and issues that arose, especially with the onset of the Covid-19 pandemic. Last but not least, I would also like to acknowledge the IDCORE programme for its unwavering support. Dr. Katrina Tait and Prof. David Ingram from the University of Edinburgh deserve a special mention for their assistance in resolving administrative hurdles, obtaining software licenses, and organizing social activities and summer schools, which significantly enhanced our research experience.

# Declaration

I declare that this thesis was composed by myself, that the work contained herein is my own except where explicitly stated otherwise in the text, and that this work has not been submitted for any other degree or professional qualification except as specified. Parts of this work have been published in:

- Rongé, E., Peyrard, C., Venugopal, V., Xiao, Q., & Johanning, L. (2022, June). The application of semi-analytical diffraction formulas to predict the second-order dynamic response of a TLP floating wind turbine in monochromatic waves. In Proceedings of the ASME 2022 41st international conference on offshore mechanics and arctic engineering - OMAE (Vol. Ocean Renewable Energy). Hamburg: ASME. doi: 10.1115/OMAE2022-78673
- Rongé, E., Peyrard, C., Benoit, M., Robaux, F., & Venugopal, V. (2022, November). A comparison of engineering third-order wave load models for bottom seated and truncated vertical cylinders. In 18eme journée de l'hydrodynamique (Vol. All days). Poitier. doi: https://jh2022.sciencesconf.org/420817
- Rongé, E. , Peyrard, C., Venugopal, V., Johanning, L., & Xiao, Q. (2023, 06). On the Evaluation of Nonlinear Response of Floating Wind TLPs Hydrodynamics: Numerical and Experimental Modelling. In Proceedings of the 33rd international ocean and polar engineering conference (Vol. All Days, p. ISOPE-I-23-054).
- Rongé, E., Peyrard, C., Venugopal, V., Xiao, Q., Johanning, L., & Benoit, M. (2023). Evaluation of second and third-order numerical wave-loading models for floating offshore wind TLPs. Ocean Engineering, 288, 116064. doi:10.1016/j.oceaneng.2023.116064

# Nomenclature

| | |
|---|---|
| $(p)$ | Frequency domain order |
| $\vec{n}$ | Hull normal vector |
| $\vec{u}$ | Velocity vector |
| $a$ | Cylinder radius |
| $b$ | Hull draft |
| $d$ | Underwater keel clearance |
| $f$ | Wave frequency |
| $f_p$ | Peak wave frequency |
| $f_{xx}$ | Natural roll frequency |
| $f_x$ | Natural surge frequency |
| $f_{yy.c}$ | Coupled natural pitch-tower first bending mode frequency |
| $f_{yy.r}$ | Natural pitch frequency (rigid body) |
| $f_z$ | Natural heave frequency |
| $g$ | Gravity acceleration |
| $h$ | Water depth |
| $i$ | Imaginary number |
| $k$ | Wave number |
| $k_2$ | Wave number of second-order free harmonic |
| $k_m$ | Wave number of evanescent modes |
| $m$ | Order of eigenmode |
| $n$ | Order of Fourier mode about polar angle |
| $q_n$ | Free surface forcing Fourier term |
| $r$ | Radial distance |
| $t$ | Time |
| $u, v, w$ | Wave particle velocity in $x, y, z$ direction |
| $wl$ | Instantaneous waterline surface |
| $x, y, z$ | Cartesian coordinates |
| $A$ | Wave amplitude |
| $A_D$ | Rotor swept area |
| $A_n$ | Velocity potential coefficient of the inner domain |
| $A_{line}$ | Cross sectional area of line |
| $B$ | Radiation damping |
| $B_n$ | Velocity potential coefficient of the outer domain due to inner domain |
| $C_{A.ax}$ | Axial added mass coefficient |
| $C_{A.t}$ | Transverse added mass coefficient |

| | |
|---|---|
| $C_{D.ax}$ | Axial drag coefficient |
| $C_{D.t}$ | Transverse drag coefficient |
| $C_T$ | Turbine thrust coefficient |
| $E$ | Young's modulus |
| $E_n$ | Velocity potential of outer domain |
| $F$ | Force |
| $G$ | Green's function |
| $H$ | Wave height |
| $H_n$ | Hankel function of order n |
| $H_s$ | Significant wave height |
| $I_n$ | Modified Bessel functions of the first kind of order n |
| $J_n$ | Bessel functions of the first kind of order n |
| $K_n$ | Modified Bessel functions of the second kind of order n |
| $M_a$ | Added mass |
| $P$ | Pressure |
| $Q$ | Free surface forcing |
| $S_0$ | Mean wetted hull surface |
| $T$ | Wave period |
| $T_p$ | Peak wave period |
| $V_w$ | Hull displacement |
| $Y_n$ | Bessel functions of the second kind of order n |
| $Z_m$ | vertical eigenfunctions |
| $\vec{M}_{p\to k}$ | Momentum transfer |
| $\mathbf{B_R}$ | Radiation damping matrix |
| $\mathbf{K_K}$ | Hydrostatic stiffness matrix |
| $\mathbf{K_M}$ | Mooring stiffness matrix |
| $\mathbf{M_I}$ | Mass inertia matrix |
| $\mathbf{M_a}$ | Added mass matrix |
| $\mathbf{R}$ | Rotation matrix |
| $\mathbf{X}$ | Cartesian coordinate matrix |
| $\vec{X}$ | Body displacement vector |
| $\Omega$ | Fluid domain |
| $\Phi$ | Phase |
| $\alpha$ | Volume fraction (CFD), JONSWAP spectral coefficient, Rayleigh damping mass coefficient |
| $\alpha_{moor}$ | Angle of tendon mooring lines |
| $\bar{\bar{\tau}}$ | Reynolds-stress tensor |
| $\beta$ | FNV nonlinear potential coefficient, Rayleigh damping stiffness coefficient |
| $\varepsilon_n$ | Fourier series coefficient |

| | |
|---|---|
| $\eta$ | Free surface elevation |
| $\gamma$ | JONSWAP peak enhancement coefficient |
| $\lambda$ | Wave length, Froude scaling factor |
| $\omega$ | Wave angular frequency |
| $\omega_p$ | Peak wave angular frequency |
| $\phi$ | Velocity potential |
| $\phi_D$ | Diffracted velocity potential |
| $\phi_I$ | Incident velocity potential |
| $\phi_R$ | Radiated velocity potential |
| $\phi_S$ | Scattered velocity potential |
| $\rho$ | Water density |
| $\sigma$ | JONSWAP spectral coefficient |
| $\tau$ | Line tension |
| $\tau_0$ | Line pre-tension |
| $\theta$ | Polar angle |
| $\xi$ | Green's function radial distance |
| $\zeta$ | Damping coefficient |
| BEM | Boundary Element Method |
| BEMT | Blade Element Momentum Theory |
| CFD | Computational Fluid Dynamic |
| CoB | Centre of Buoyancy |
| CoG | Centre of Gravity |
| FFT | Fast Fourier Transform |
| FOWT | Floating offshore Wind Turbine |
| HOS | High Order Spectral (method) |
| $K_C$ | Keulegan-Carpenter number |
| NWT | Numerical Wave Tank |
| OWT | Offshore Wind Turbine |
| PF | Potential flow |
| PSD | Power Spectral Density |
| QTF | Quadratic Transfer Function |
| RAO | Response Amplitude Operator |
| RNA | Rotor Nacelle Assembly |
| SIL | Software-in-the-loop |
| SLC | Secondary Loading Cycle |
| TLP | Tension-Leg-Platform |

# Contents

# Figures and Tables

## Figures

# Tables

# Chapter 1

# Introduction

## 1.1 Prospect of floating offshore wind

As the world is recognising the threat of the climate emergency and recent geopolitical tensions highlight a need for more energy independence, renewable energy development is becoming a strategic sector for many countries. This is evident from the various pledges of renewable generation such as the European Union's RepowerEU binding target of 42.5% renewable generation by 2030 (European Commission, 2022) or the UK's pledge of a carbon-free grid by 2035 (Department for Business, Energy & Industrial Strategy, 2021). The rapid deployment of offshore wind in the last decades and the ever-increasing industry interest in floating offshore wind turbines suggest that this technology is likely to play a major role in the future energy landscape. This interest in floating technology is best illustrated by the rapid growth in installed and planned deployment of floating offshore wind turbine (FOWT) prototypes, demonstration projects and commercial wind farm arrays, as shown in Figure 1.1, taken from a review study by Edwards et al. (2023). The market forecast which is based on aggregated data by GWEC (2022) predicts a tenfold increase of deployed floating turbine capacity in the next three years, from around 300 MW in 2023 to 3GW installed by 2026. In Scotland alone, the latest Scotwind auction leasing round led to the announcement of an additional 30GW of new offshore wind capacity with floating wind representing around 60% of the scheduled new developments (Crown Estate Scotland, 2022). As for France, the government is in the process of launching or awarding an auction leasing round for an expected 750MW of capacity for floating wind farm arrays which could represent 10% of the country's offshore wind capacity by 2030 (CEREMA & Minsitere de la Transition Energetique, n.d.).

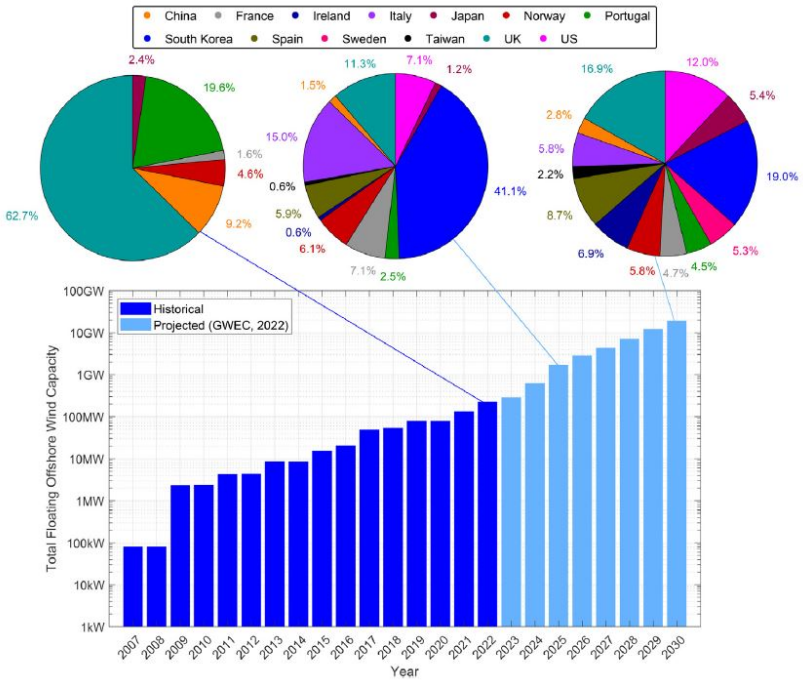


**Figure 1.1:** Historic and projected global capacity of installed floating wind turbines from Edwards et al. (2023) including details of share of new capacity installed per country

The reason for this surge in interest results from the fact that floating foundations are set to open large maritime areas to the exploitation of offshore wind resources at deeper water depths than those currently managed by standard fixed foundations (See Figure 1.2). Areas made accessible by floating foundations are assessed to represent 80% of the world offshore wind resource (GWEC, 2022). Therefore, significant efforts and innovations have been undertaken in the last decade to develop competitive floating wind systems with currently more than 20 platform concepts being tested at sea, from small kW scale devices to large scale demonstrator arrays with multi-MW wind turbines (Edwards et al., 2023). Among the various concept families of floating wind platforms partly inherited from O&G and shown in Figure 1.2, the most popular concept has been the semi-submersible followed by the very similar barge concepts and then the spar type platform. Most current multi-MW at-sea FOWT prototypes are based on semi-submersible (WindFloat 1, Kincardine, Fuyao etc.), barge (IDEOL, SAITEC) or spar foundations (Hywind, TetraSpar etc.) as listed in Edwards et al. (2023). Hence these technologies are the most advanced designs in the short term for commercial auction rounds. On the other hand, the Tension-Leg-Platform (TLP) is a less studied concept. This is illustrated by the fact that whilst other multi-MW FOWT concepts have been in the water for 2-5 years, the first-ever full-scale FOWT-TLPs were just being installed

at the time of writing this thesis at the Provence Grand Large demonstrator wind farm. Part of the delay in the introduction of FOWT-TLPs can be explained by the more complex installation process required. However, their unique hydrodynamic characteristics, which are still being researched, are also likely to play a role in the slow adoption of this technology.

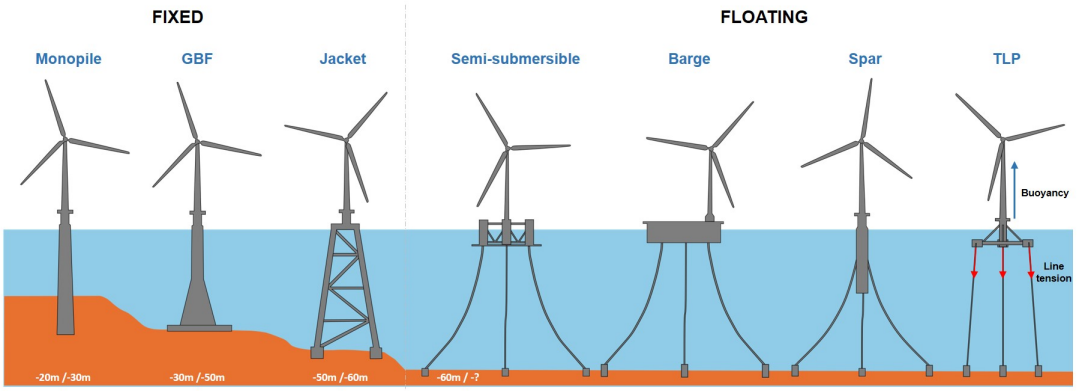


**Figure 1.2:** Offshore wind foundation types

As seen in Figure 1.2, the TLP has the particularity of being restrained by pre-tensioned lines into a position of positive buoyancy. This configuration confers to the mooring system an increasing role in resisting aero-hydrodynamic loads compared to other concepts which enables a reduction of the size of the platform hull. As an order of magnitude, the mass of a TLP floater hull can be around two to four times lighter than that of a semi-submersible for the same turbine class. For example, the reported floater mass of the SBM-TLP carrying a 5MW reference turbine is 1,755 tonnes (Caillé, Bozonnet, Perdrizet, Poirette, & Melis, 2017) whereas, for the same turbine, the DeepCWind semi-submersible floater reports a mass (without ballast) of 3,800 tonnes (A. N. Robertson et al., 2017) and the IDEOL barge one of 8,220 tonnes (Choisnet, Favré, Lyubimova, & Rogier, 2014). Such difference has obviously a cost and environmental implication both in terms of raw material usage but also ease of construction which includes time-frame as well as space required for the assembly of the structure. Furthermore, TLP system results in shorter lines with a lesser footprint on the seabed compared to catenary configurations. Therefore, based on these principles, TLP floaters should theoretically be more sustainable solutions than both semi-submersible and spar floaters. However, part of the issue with the technology lies in the understanding of the hydrodynamics of such a platform. Specifically, a thorough understanding of the extreme loading cycle in the mooring lines is required since they provide stability and thus are key to the structural integrity of the system which would collapse if one of them were to break. This component therefore needs de-risking for the technology to advance.

## 1.2 Hydrodynamics of a Tension-leg-Platform

As mentioned above, pre-tensioned mooring lines restrain the TLP system and constrain vertical motion and inclination. In that, a TLP acts much like a pendulum with the heave motion of the moored floater being strongly coupled to its displacement in the horizontal plane where the system is the most compliant. Therefore, since such a system is very stiff in the vertical degrees of freedom, its natural modes of resonance are located in what is typically referred to as the high-frequency bandwidth. High-frequency aero or hydrodynamic loads can thus generate a resonant response of the system in these degrees of freedom. In the standard DNV-GL (2019b), these responses are typically separated between a "springing" response generated by the steady resonance of the system to the high-frequency components of the wave loads and "ringing" which is a strong transient resonance due to steep nonlinear waves. Another issue is the risk of slacking, referring to an event where one or more lines are de-tensioned which is generally followed by a sudden reloading resulting in extreme tensions with a potential risk of tendon disconnection.

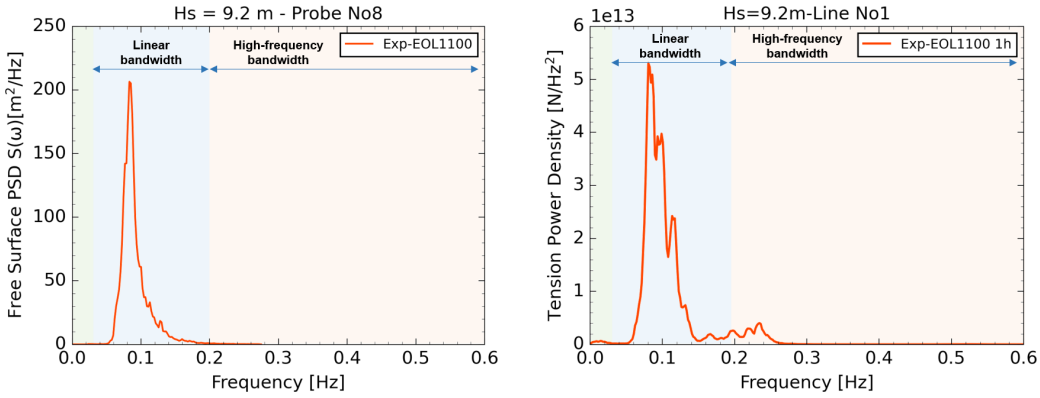


**(a)** **(b)**

**Figure 1.3:** Power Spectral Density plot of (a) Free Surface Elevation; (b) Line Tension obtained experimentally in this thesis. Data scaled up to at-sea prototype units

To understand the meaning of high-frequency wave loads, it is important to recall how we model waves numerically. As seen in Figure 1.3a which shows an experimental reproduction of a typical ocean wave spectrum, most of the ocean energy is concentrated in waves with a fundamental frequency comprised between around 5 s (0.2Hz) to 30 s (0.033 Hz). Often, in offshore engineering, a sea-state is modelled as an infinite sum of independent sine waves which are linearly superposed. This linearisation into independent sine waves derives from the linearisation of the potential flow problem in the frequency domain which allows to consider that each sea-state component interacts independently on an offshore structure at the frequency of its carrier sine wave. However, when considering higher-order

effects, these independent components and their resulting effects on the structure are found to interact. At second-order, waves interact in pairs, producing quadratic hydrodynamic effects that occur at the sum and difference of the frequency pair of the interacting components. At third-order, waves interact in triplets, leading to more complex interactions. Specifically, the sum-frequency effects generate hydrodynamic loads above the typical bandwidth of the linear carrier wave and for that reason, these forces are referred to as high-frequency forces. This is best illustrated by comparing the spectral energy density of a sea-state generated experimentally (Figure 1.3a) and the resulting line-tension response of a TLP floater (Figure 1.3b). Thus, research has shown that including high-frequency wave loads increased the probability of obtaining ringing and slacking response (Bachynski, 2014). Finally, the strong coupling between the tower bending mode and the pitch motion of the platform (Bachynski, 2014; Koo, Goupee, Lambrakos, & Lim, 2013; Molin, Remy, & Facon, 2004) means that the springing and ringing effects have also a strong impact on the fatigue of the floater-tower connection (Bachynski, 2014). Therefore it appears essential for the design of such a system to account for these effects. This is recognised by certification bodies which list high-frequency loads as an important factor to account for in the design of TLP system (DNV-GL, 2019b; IEC, 2019).

Predicting high-frequency loads through high-fidelity time-domain approaches such as fully non-linear Boundary Element Method (BEM) or Navier-Stokes CFD is an expensive endeavour and hardly suitable for a stochastic design process involving many simulations with multiple combinations of sea-state and wind condition. Therefore, access to lower-fidelity engineering numerical models that can predict high-frequency wave loads with a sufficient degree of accuracy is important for the deployment of TLP technologies. The use of frequency domain potential flow solvers is popular in the industry as they resolve the diffraction-radiation problem on arbitrary hull geometries via the Boundary Element Method (BEM). However, these can only be used to calculate hydrodynamic effects up to the second-order which is generally considered sufficient for assessing the "springing" response (DNV-GL, 2010). On the other hand, ringing conditions are thought to be generated by third-order high-frequency wave loads, although the subject has remained a research field since the ’90s. In the potential flow domain, a third-order semi-analytical solution that resolves the diffraction due to a monochromatic wave for a vertical cylinder was derived by Malenica and Molin (1995). However, this method has been developed for regular waves and has never been extended to irregular sea-states. The industry has relied instead on an approximate solution of the potential flow problem on cylinders through the slender-body theory. This approach assumes that the wavelengths are infinitely longer than cylinders and allows the expression of the wave loads in the time domain as a function of the instantaneous wave kinematics. These methods, although doing so through an approximation of the diffraction problem, do take into account the double and triple interaction between waves. Among these approaches, both the FNV (Faltinsen, Newman, &

Vinje, 1995; Kristiansen & Faltinsen, 2017; Newman, 1996a) and Rainey's approach (Manners & Rainey, 1992; Rainey, 1989, 1995) have been used to estimate the second and third-order loads on FOWT-TLP structures (Bachynski, 2014; Jagdale, Ma, & Yan, 2021; Milano et al., 2019). The geometries of TLP floaters tend to work well with such approximation since many designs consist of a vertical truncated cylinder connected to horizontal submerged elements with bracings as can be seen In Figure 1.4. However, these approaches have not been the subject of full comparative analysis that discusses their applicability on complex floater structures, nor have they been validated against experimental measurement which leads to the definition of this project.

**Figure 1.4:** Concepts of TLP floater showing a main surface piercing element in the shape of a truncated cylinder. Photo credits: (a) Stiesdal, (b) Glosten, (c) Bluewater Energy Services

## 1.3 Scope of work

The main objective of this project is to compare low to medium-fidelity "engineering" wave load model predictions in the case of floating offshore wind turbine foundations, with a specific focus on FOWT-TLP. The aim is to apply the following "engineering" approaches :

- Potential flow approaches (inertial) by using:
  - BEM solver: First and second-order diffraction-radiation
  - Semi-analytical method on vertical cylinders: First, second and third-order diffraction solution (Huang & Eatock Taylor, 1996; Malenica & Molin, 1995)
- Strip theory (inertial) and investigate:
  - Rainey approach on cylinders (Manners & Rainey, 1992; Rainey, 1989, 1995)
  - FNV approach on vertical cylinders (Faltinsen et al., 1995; Kristiansen & Faltinsen, 2017; Newman, 1996a)
- Strip-theory (viscous) using:

– Morison drag term (Morison, Johnson, & Schaaf, 1950)

These approaches are to be validated against high-fidelity numerical simulation using CFD Navier Stoke's solver for the high-frequency loads on the structure, and tank testing experimental campaign for the validation of the simulated high-frequency response, including the prediction of "springing" and "ringing".

As pointed out above, the "engineering" hydrodynamic numerical approaches in this thesis refer to those that are applicable to the offshore wind industry multi-physic aero-hydro-servo-elastic time domain solvers for which the basis has been laid by Jonkman (2007). Specifically, this thesis is concerned with the implementation of these approaches in EDF R&D FOWT multi-physic code DIEGO. These solvers rely either on inputs from frequency-domain potential flow diffraction-radiation solution in the form of transfer functions or on instantaneously calculating the hydrodynamic loads using the slender-body approximation in the form of the Morison equation or higher-order strip-theory derivation.

**(a)** **(b)**

**Figure 1.5:** View of the 10MW EDF-TLP academic prototype (a) Physical model; (b) Numerical model

The FOWT-TLP floater used in this thesis as a case study is the EDF-TLP academic prototype. It was designed at EDF R&D LNHE department by Duchet (2019) for carrying the NREL 10MW reference turbine. It consists of a central mast and side buoys connected by an assembly of bracings. A question that this thesis tries to answer is **how can high-frequency loads be taken into account on such a structure using the approaches listed above**. One central assumption that is to be verified is if the application of third-order inertial models solely on the central mast is sufficient or if other elements of the platform can be expected to contribute significantly to the high-frequency loads.

Based on this scope the thesis was separated into two main axes:

- A first axis is focused on assessing the high-frequency loading on fixed structures. This is because most non-viscous engineering hydrodynamic models (referred to as inertial in this thesis) for third-order loads have been derived assuming fixed conditions. The objective of that axis is to qualify the validity of the engineering approaches listed above for modelling third-order loads on a complex FOWT-TLP structure. Most of these methods have been derived for simple geometries, generally circular vertical cylinders. For that reason, the listed approaches are compared on such geometries before being applied to the more complex hull of the EDF-TLP. One of the questions that this axis is meant to answer is if third-order models designed for vertical cylinders are applicable to the central mast of a more complex hull. Secondly, the question is to understand the contribution to high-frequency loads of other elements and the applicability of the engineering models on the full hull. As mentioned above, the validation of numerical approaches is provided by a high-fidelity Navier Stoke's CFD solver and the comparative analysis is carried out using monochromatic waves so as to isolate the high-frequency harmonics and compare the high-order force transfer functions.
- A second axis is focused on analysing the accuracy of the engineering hydrodynamic approaches in predicting the dynamic response of the system. In this case, the numerical wave-loading models applied on the EDF-TLP in anchored conditions are compared against results from a new experimental campaign. Since this experimental campaign consists of EDF's first FOWT tank tests, a significant amount of work is involved in its preparation which is included in this thesis. The tests in dynamic conditions are separated into two parts. First, monochromatic wave cases are tested so as to extract the high-frequency harmonics and analyse the prediction of the steady resonant response which is typically referred to as "springing". The analysis of the response transfer functions serves to qualify the accuracy of engineering approaches for individual frequencies in a manner similar to the numerical work of Jagdale et al. (2021). The response is then analysed in irregular waves assuming storm conditions so as to qualify the accuracy of these engineering models in predicting extreme responses and

springing and ringing conditions. This is to conduct an experimental validation of these approaches following various works on the ringing of FOWT-TLP by several authors (Bachynski, 2014; Milano et al., 2019; Shen, Hu, & Liu, 2016) which were limited to numerical analysis.

## 1.4 Original contribution

A summary of the original work that this thesis has contributed to is summarised below:

- Analysis of the distribution of high-frequency forces generated by monochromatic waves on a complex FOWT-TLP hull using a Navier Stokes' CFD solver and comparison against results predicted using engineering approaches. The results of this work are summarised in a journal article: "*Evaluation of second and third-order numerical wave-loading models for floating offshore wind TLPs*" (Rongé, Peyrard, Venugopal, Xiao, et al., 2023)
- Test of a hybrid numerical model mixing potential flow semi-analytical second-order equations and a strip theory approach to model high-order inertial load on a complex FOWT-TLP system and its springing response. The first results of this work were presented at the 41st International Conference on Ocean, Offshore & Arctic Engineering (OMAE22) with a paper published in the proceedings: "*The application of semi-analytical diffraction formulas to predict the second-order dynamic response of a TLP floating wind turbine in monochromatic waves*" (Rongé, Peyrard, Venugopal, Xiao, & Johanning, 2022)
- Generation of a new experimental data-set and validation of the high-frequency springing response of a FOWT-TLP under monochromatic waves predicted with an aero-hydro-elastic time domain solver using various engineering numerical approaches. The first results of this work were presented at the 33rd International Ocean and Polar Engineering Conference (ISOPE 2023) with a paper published in the proceedings: "*On the Evaluation of Nonlinear Response of Floating Wind TLPs Hydrodynamics: Numerical and Experimental Modelling*" (Rongé, Peyrard, Venugopal, Johanning, & Xiao, 2023)
- Generation of a new experimental data-set and validation of the nonlinear response of a FOWT-TLP under extreme irregular waves predicted with an aero-hydro-elastic time domain solver. This includes a comparative analysis of the probability of exceedance of the extreme response as well as a time-frequency analysis of springing and ringing response using scalograms. Results of such comparison with experimental results have not been published so far for FOWT-TLPs to the knowledge of the author.

## 1.5 Organisation of the document

This document is separated into three parts. Part I is dedicated to the introduction of the literature background on the subject (Chapter 2) and to presenting the theoretical background (Chapter 3) that is necessary to understand the following work. Part II is dedicated to a comparative analysis of the listed "engineering" numerical approaches when applied to fixed structure since most of the third-order methods have been derived assuming such conditions. High-fidelity validation is then provided through the use of a Navier Stoke's CFD solver. Chapter 4 focuses on the simple geometry case of the vertical cylinder starting with a fixed offshore wind monopile case from a study by Kristiansen and Faltinsen (2017) and then moving further offshore by analysing a truncated cylinder case. Chapter 5 then focuses on extending the application of these approaches to a complex academic FOWT-TLP floater with the purpose of assessing the accuracy of these approaches in a realistic industrial case. Finally, Part III presents an analysis of the various approaches applied to dynamic conditions and compares them against a new experimental data-set. This study starts with Chapter 6 which presents the set-up of the experimental campaign and the parallel calibration of the physical and numerical models. It is then followed by Chapter 7 which provides the results of the numerical and experimental dynamic simulation. This chapter includes the result of the monochromatic wave tests which inform on the transfer functions of the TLP response whereas irregular wave cases allow for a comparative analysis of power spectra, the probability of exceedance of extreme responses and time-frequency analysis of the springing and ringing phenomenons.

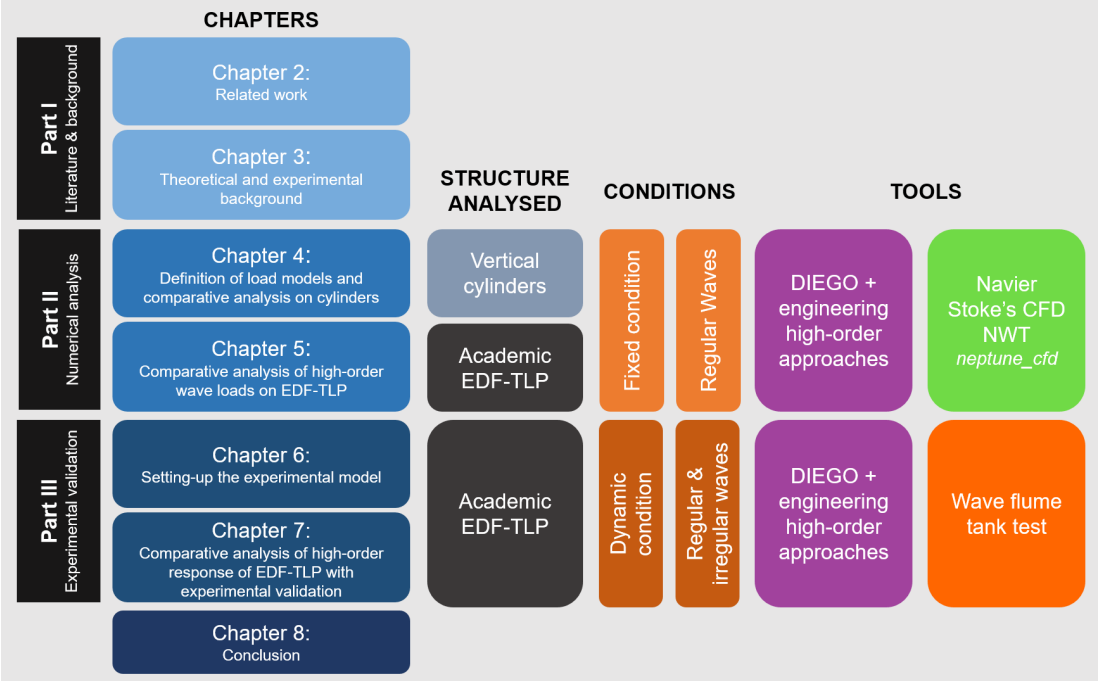


**Figure 1.6:** Graphical summary of the thesis structure

# PART I

# Background and Theory

# Chapter 2

# Related work

## 2.1 Background on wave-structure interaction

### 2.1.1 Development of numerical models

#### Development of "engineering" load models

The basis of the potential flow (PF) method used today to calculate loads on a cylindrical structure was presented by MacCamy and Fuchs (1954) who provided the analytical solution to the linear diffraction problem around a bottom-seated circular cylinder. This was published not long after Morison et al. (1950) proposed a semi-empirical model based on the assumption of slender elements with regard to the wavelength. Lighthill (1979) proposed an indirect method to compute the second-order hydrodynamic loading for deep water waves using Green's identity. The method was adopted by various authors (Abul-Azm & Williams, 1988; Molin, 1979) to propose approaches to solve the second-order diffraction-radiation problem.

Rainey (1989) on the other hand, based on Lighthill's (1979) work, derived a method, following Morison long-wave approximation, to derive the second-order hydrodynamic Froude-Krylov and diffraction loads on slender elements. This method used an energy conservation argument to derive inertial terms assuming nonlinear wave kinematics and convective acceleration and axial divergence terms. In Manners and Rainey (1992), an additional term related to the pressure distribution around a cylinder end was also added as a point load.

Kim and Yue (1989, 1990) derived the basis for a second-order frequency-domain potential flow BEM approach on axisymmetric bodies by using Molin (1979) weak radiation condition and calculated the second-order diffraction forces by direct integration of the free surface integral with a combination of numerical integration near-field and applying an asymptotic behaviour to the first-order potential far-field. Industrial BEM solvers calculating the so-called "full second-order QTFs" are based on their methodology and further improvement (Chen, 2007; Lee, 1995). Their papers also included a semi-analytical solution for the second-order diffraction forces on a vertical cylinder in mono and bi-chromatic waves. A similar

method was proposed by Chau and Eatock Taylor (1992). It was extended later by Huang and Eatock Taylor (1996) to take into consideration the truncated cylinder case with semi-analytical equations published for the monochromatic case. An example of its use in the bi-chromatic case was then later published by Chatjigeorgiou and Mavrakos (2007). Since then, various semi-analytical solutions have also been derived for simple geometries such as an array of bottom-mounted cylinders (Malenica, Eatock Taylor, & Huang, 1999) or single compound cylinders (Chatjigeorgiou & Mavrakos, 2006).

Based on the derivation of the second-order potential, Malenica then undertook the task of deriving the semi-analytical solution for the third-order diffraction on a vertical cylinder in finite depth and monochromatic waves (Malenica, 1994; Malenica & Molin, 1995). This publication coincided with the long-wave approximation of the third-order load derived by Faltinsen et al. (1995), commonly referred to as the FNV approach. The work of Malenica and Molin (1995) compared the semi-analytical results of the force and moments on the structure against the approximation formulae and suggested that the FNV formulation was valid for low $ka$ below a value of approximately $ka = 0.12$ at second-order, and $ka = 0.05$ at the third-order based on an analysis of the complex amplitudes of the horizontal loads. Kinoshita and Bao (2000) extended Malenica and Molin (1995) method to truncated vertical cylinders and validated the original results. Teng and Kato (2002) followed by simplifying the third-order free surface forcing term and also extending the analytical solution to truncated vertical cylinders. Both papers' results show that the difference in the third-order force is negligible for drafts deeper than four times the radius which suggests it is largely localised at the free surface.

Newman (1996a) extended the FNV approach to unidirectional irregular waves and Kristiansen and Faltinsen (2017) generalised it to finite water depth. Rainey (1995) extended his theory to third-order by including a surface intersection term which generates a third-order point load. In the same publication, Rainey argues that theories based on perturbation expansion (FNV or potential flow approach) cannot accurately capture third-order force in severe wave conditions as the series expansion diverges with high wave amplitudes relative to the wavelength or structure diameter. On the other hand, his theory being based on an energy conservation argument, the approach would not suffer from these issues and as such could be applied using realistic fully nonlinear wave kinematics. However, these are points which remain under discussion. It is important to state that several authors (Peyrard, 2018; Rainey, 1995; Tromans, Swan, & Masterton, 2006) have noted that both FNV and Rainey's approaches generate the same load terms in second-order Stokes' waves. Finally, Johannessen (2011) suggested applying a frequency bandwidth parameter to limit frequency interaction in weakly nonlinear mode-coupling approaches. This approach removes the long-short wave interaction challenge in broad-banded spectra, which is known to make a perturbation expansion diverge without using a cut-off frequency that would remove the spectrum tail.

The validity of the approach is reinforced based on nonlinear wave tank observation showing that in a near-breaking wave group, the terms that contribute the most to the amplitudes are close in frequency. On the other hand, in a mode-coupling approach, the interaction between waves with large differences in frequencies accounts for the long-short wave modulation which can be neglected in weakly nonlinear problems. Johanessen applied his method to the extended FNV (Newman, 1996a). From his results showing agreement in the force maximum amplitude, Johanessen suggests somewhat qualitatively that his bandwidth limited approach is applicable to irregular wave spectrum.

**Fully nonlinear numerical methods**

Progress in computing power has also led to the development of more complex potential flow Boundary Element Method (BEM) models taking into account weakly and nonlinear seas as well as their interaction with marine structures. It is worth noting here that the jargon used in the industry can be confusing in that high-order BEM (HOBEM) methods refer to approaches which are based on a panel method more complex than a linear averaging of the potential on each mesh panel. This is therefore not related to the non-linearity of the problem which will depend on the boundary conditions applied. Fully nonlinear potential flow requires time domain solvers since the frequency domain requires the use of perturbations series and relies on the hypothesis of frequency superposition.

Ferrant (1997) developed a Numerical Wave Tank solver using a fully nonlinear potential flow boundary conditions and used it to confirm Malenica and Molin (1995) inline force results for a steepness case of $kA = 0.06, H/\lambda = 2\%$. Furthermore, Ferrant (1999) also showed with the same model that in regular waves, the normalised amplitude of the inline third-order force reduces with increasing wave steepness in agreement with experiments of Huseby and Grue (2000) discussed further below. Shao (2010) proposed a quadratic and high-order BEM (HOBEM) method in the time domain based on a body-fixed coordinate system and applied it to weakly non-linear problems such as the diffraction on a vertical cylinder. The results also showed good agreement with the results of (Malenica & Molin, 1995; Teng & Kato, 2002) although with higher discrepancies on the force term due to the third-order potential. Duan, Chen, and Zhao (2015) proposed a new time domain method which accounts for the first and second derivatives of the velocity potential at the centroid.

CFD methods have been utilised to calculate high-order forces on cylinders and investigate non-linear flow in more detail (Mohseni & Guedes Soares, 2022; Paulsen, Bredmose, Bingham, & Jacobsen, 2014) such as the issue of the secondary load cycle which is described further below. All the last aforementioned methods based in the time domain are computationally expensive. While this captures accurately transient effects, they are hardly applicable to multiple long series of wave realisation and hence their application to the stochastic design of offshore structures is limited.

### 2.1.2 Experimental validation

Following the first important analytical contributions to the development of third-order load models, Chaplin, Rainey, and Yemm (1997) carried out an experimental campaign of focused waves on vertical cylinders in shallow water depth. They observed a secondary load cycle which the authors attributed to the run-up at the rear of the cylinder after the passage of the crest. Furthermore, the peak moments generated by a set of focused waves of varying steepness calculated using Rainey's equation with unsteady particle velocities calculated through a crest-fitting method (Baldock & Swan, 1994), and using regular wave kinematics were compared against the experimental results. These showed that Rainey's long-wave approximation load model leads to realistic results for this particular case when realistic particle velocities are used. Huseby and Grue (2000) carried out an experimental campaign on a vertical cylinder to qualify the influence of wave steepness on the horizontal forces in the case of monochromatic waves. By comparing their experimental results against first, second and third-order semi-analytical potential flow solutions, they concluded that these theoretical models tend to overestimate the high-order wave forces as the steepness increases. However, the experimental results of the third-order inline force show good agreement with the analytical solution of Malenica and Molin (1995) in phase up to a steepness value of $kA = 0.20$ at frequency $ka = 0.245$. In terms of amplitude, the semi-analytical solution appears to constantly overestimate the third-order force by around 20-30% over steepness of $kA = 0.05$.

In a report to the Health & Safety Executive UK, Tromans et al. (2006) undertook a study of the high-order wave loading on a truncated cylinder and a gravity-based-foundation (GBF) by comparing various models and experimental results measured at the Imperial College wave basin. The report compared the measured monochromatic wave-induced forces against results from the third-order extension of models presented above such as third-order extension by Rainey (Manners & Rainey, 1992; Rainey, 1995), the FNV model (Faltinsen et al., 1995; Newman, 1996a). Three wave cases were considered and only the first case details the results of the different models and experimental measurements. The study found that for a case with $ka = 0.21$, $kA = 0.273$ and $h/a \approx 26$, most models overestimated the third-order force amplitude by around 25-30%. Only the Rainey model without Rainey's third-order Stokes'

correction term (See Chaplin et al. (1997)) seemed to match the amplitude. All models are at a leading phase shift of $\approx 45\,\mathrm{deg}$ compared to the experimental measurements. Johannessen (2011) also compared his approach of bandwidth-limited FNV applied on slender cylinders in continuous spectra against tank test experiments by Stansberg (1997). The test conditions were generated by a JONSWAP spectrum with a peak period of 2.40s for fixed cylinders of 0.2m and 0.325m diameter, representing a relative wave number of $ka \approx 0.1$ and $0.08$ respectively. The results consisting of several series of a single irregular wave event show that while the bandwidth-limited approach manages to capture the general shape of the force including non-linear terms, the secondary-loading-cycle is not captured by the FNV method. However, the high-pass filtered time-series showed that the approach still manages to capture the maximum third-order force relatively well.

Kristiansen and Faltinsen (2017) included tank testing experiments on top of their extension of the FNV method to finite water depth irregular waves. The experiments consisted of several regular wave runs with periods from $ka \approx 0.10 - 0.40$ and increasing wave steepness from $H/\lambda \approx 1/140 - 1/16$ on a cylinder of $a = 0.144$m in water depth of $h/a = 5.51$ and $h/a = 7.83$. The regular waves were generated with a wave-maker based on linear potential flow and therefore a second-order free harmonic was added to correct for the parasitic free harmonics. The results of the experiments were compared against numerical results using the FNV approach with fifth-order Stokes' wave kinematics. First, a time-series example of the force on the cylinder is presented for the case $ka = 0.105$, $h/a = 7.83$ and $H/\lambda = 1/25$. The FNV results appear to be very satisfying with the amplitudes and phase of the first and second harmonic of the force in good agreement with the measurements. The third harmonic of the FNV force is reported to be fully in phase with the experimental results although the amplitudes were overestimated by a factor which appears to be around $1.5 - 2$. Then the full results of the experimental campaign are presented for wave steepness of $H/\lambda = 1/25$ & $1/40$. The FNV method appears to capture well the second-harmonic for both wave steepness up to $ka \approx 0.15 - 0.17$, therefore slightly higher than the limit mentioned by Malenica and Molin (1995). Interestingly, the amplitude of the third harmonic of the surge force is very well captured at all frequencies for a wave steepness of $1/40$. However, for the steeper wave event, only short waves appear to be well captured, with $ka > 0.18$. This appears in contradiction with the FNV long-wave approximation. However, the observation could be partly imputed to the normalising in $\rho g A^2 a$ visually reducing differences in the high frequencies instead of the transfer functions normalisation in $\rho g A^3$ used in Malenica and Molin (1995). Furthermore, additional results show that the FNV approach over-predicts the third harmonic surge force for wave steepness over $H/\lambda \approx 0.03$ at $ka = 0.105$ and $H/\lambda \approx 0.04$ at $ka = 0.167$. This confirms the experimental findings of Huseby and Grue (2000) indicating that free surface effects in long and steep waves have negative effects on the applicability of the FNV. A similar study by Dadmarzi, Thys, and Bachynski (2019) using the same laboratory set-up

but using two different monopile diameters compared experimental measurements of the wave force in monochromatic waves against numerical models. The study incorporates two Morison models, a standard Morison model and a modified Morison model which essentially adds Rainey's spatial velocity gradients terms. The paper also incorporates two instances of the Kristiansen and Faltinsen (2017) model with and without drag. All models are applied using fifth-order Stokes' waves kinematics as per the previous study. The results show that all models overestimate the second-order surge force compared to the experimental results beyond frequencies above $ka \approx 0.2$. As expected, the addition of drag does not have an influence on these results confirming that the horizontal drag force is concentrated in the crest and impacts mostly the third-order component. On the other hand, the models appear to model well the third-order surge force for the high frequencies over $ka = 0.25$ as per the findings of Kristiansen and Faltinsen (2017). However, for lower frequencies, the force appears underestimated by 100 to 300 % which is a much higher discrepancy than found in Kristiansen and Faltinsen (2017). Again these results are counter-intuitive when considering Malenica and Molin (1995). This effect therefore might be imputed to drag although the addition of drag in the numerical models leads to higher overestimation. Various wave steepnesses did not appear to have a major impact on the difference in second and third-order load amplitudes between numerical models and experiments.

In a recent publication, Suja-Thauvin et al. (2020) conducted a similar assessment of nonlinear hydrodynamic load models on a monopile, including comparisons with tank test experiments carried out at the DHI lab. The study notably compares the application of Morison's, Rainey's equations and the FNV approach in severe irregular sea-states. The study concludes that both Rainey and FNV give similar predictions which match well the experimental measurements. The difference between the two models is found to be mostly in the third-order surface point term, difference which is shown to decrease with increasing wave heights. Finally, Xiong, Yang, and Tian (2020) investigated forces on a vertical truncated cylinder in varying submergence depths subjected to regular waves of varying steepness and scattering ratio. The wave conditions selected are representative of deep-water conditions. The results confirm the aforementioned results that the amplitude of the wave force transfer functions decreases with increasing wave steepness and as expected with decreasing submergence depth. On top of the above analysis, the authors also investigated the secondary load cycle effect which is discussed below. A summary table of the aforementioned studies and their parameters is provided to the reader to facilitate future referencing on high-order forces on cylinders.

| Study | Cylinder type | Scale | $ka$ range | $kA$ range | $h/a$ range | Harmonics | Numerical | ME-In | ME-Dr | RE | FNV | PF1 | PF2 | PF3 |
|---|---|---|---|---|---|---|---|---|---|---|---|---|---|---|
| (Huseby & Grue, 2000) | Bottom-seated | 0.3-0.4 m | 0.166-0.378 | 0.19 | 1.5-2.0 | 1 to 3 | ✓ | × | × | ✓ | ✓ | ✓ | ✓ | ✓ |
| (Teng & Kato, 2002) | Truncated | 0.25 m | 0.15-1.5 | 0.04-0.25 | 12.64 | 1 to 3 | ✓ | × | × | × | × | ✓ | ✓ | ✓ |
| (Kristiansen & Faltinsen, 2017) | Bottom-seated | 0.144 m | 0.10-0.40 | 0.02-0.20 | 5.51-7.83 | 1 to 3 | ✓ | × | × | ✓ | ✓ | × | × | × |
| (Dadmarzi et al., 2019) | Bottom-seated | 0.18-0.22 m | 0.10-0.62 | 0.08-0.16 | 2.45-3.6 | 1 to 4 | ✓ | ✓ | ✓ | × | ✓ | × | × | × |
| (Xiong et al., 2020) | Truncated | 0.10 m | 0.20-1.26 | 0.1-0.36 | 18.0 | 1 | ✓ | × | × | × | × | ✓ | × | × |

**Table 2.1:** Summary of cited studies with an experimental comparison of high-frequency hydrodynamic forces due to monochromatic waves on vertical circular cylinders against low to medium-fidelity hydrodynamic models. **Hydrodynamic models**: Me-In: Morison inertial, ME-Dr: Morison drag, RE: Rainey equations, FNV: FNV equations, PF1: Potential flow linear excitation force, PF2: Potential flow second-order high-frequency forces, PF3: Potential flow third-order high-frequency forces

### 2.1.3 Secondary load cycle

The question of the secondary load cycle visible in steep regular waves reported in Grue, Bjørshol, Strand, and Ohkusu (1994), Chaplin et al. (1997) and Huseby and Grue (2000) was found to be closely linked to ringing loads on cylinders. This effect was investigated by several authors through the use of fully nonlinear Numerical Wave Tanks (NWTs) based on Navier-Stokes CFD solvers. Paulsen et al. (2014) undertook a numerical study of regular wave interactions with a bottom-mounted cylinder using the CFD solver OpenFOAM with a volume of fluid method. Their results show that the secondary load cycle is a strongly nonlinear effect that involves force components higher than the fifth and sixth harmonics. Kristiansen and Faltinsen (2017) studied the viscous effect with semi-2-D order CFD and observed a similar local run-up at the rear of the cylinder after the passage of the crest similar to the observation of Chaplin et al. (1997) and Tromans et al. (2006). This phenomenon referred to as "Type-2" waves, visible in the tank testing pictures, is identified by the authors as a possible source for the secondary-load cycle which reduces the amplitude of the third harmonic force.

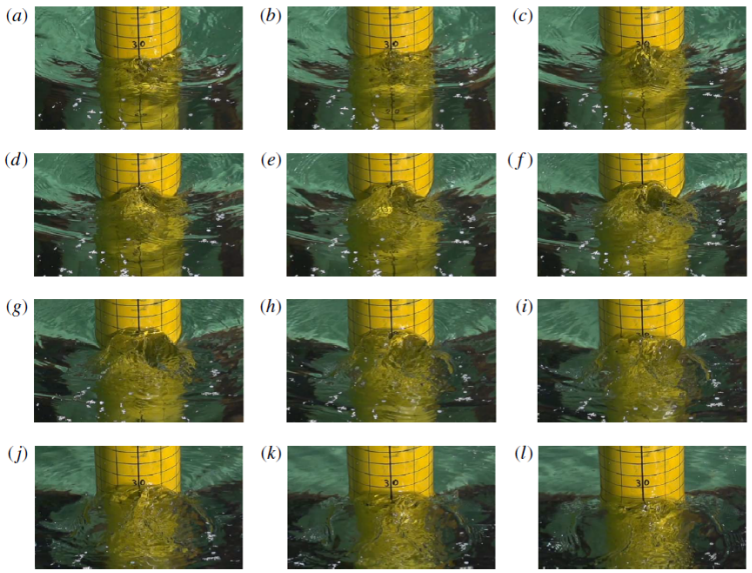


**Figure 2.1:** Rear view of Kristiansen and Faltinsen (2017) cylinder during tank test in regular waves showing the local run-up at the rear. The time instants are approximately T/40 apart.

Xiong et al. (2020) analysed their experimental measurements of the secondary load cycle on a vertical cylinder with band-pass filtering. They showed that the secondary load cycle is a strongly nonlinear effect that mobilises frequencies higher than the sixth harmonic confirming Paulsen et al. (2014). This question is also investigated in a recent paper by Mohseni and Guedes Soares (2022) which analysed the high-order inline forces generated by a monochromatic wave field of wave steepness $H/\lambda = 1/16$ on truncated cylinders and the coincident free surface effect using a CFD Navier-Stokes solver. The investigation concludes that for short and steep waves, the Type 1 scattering consists of a front run-up followed by a circular

diffraction as the waves travel along the cylinder. This involves mostly the incident fundamental harmonic at the front and only generates higher harmonics (up to the 5th) at the back of the cylinder. However, for long and steep waves which follow a Type-2 wave scattering, the edge waves travel along the cylinder, meeting up at the rear and then continuing upstream to create a secondary crest at the front. This secondary crest coincides with the secondary load cycle. This effect involves higher harmonics (up to the 6th) than Type-1 scattering both at the front and back of the cylinder. Although this is not mentioned in the paper, the difference in phase between the 3rd harmonics force generated at the front and back of the cylinder could explain the reduction in the overall high-frequency inline force. Another conjuncture could be that the higher-order terms involved in the Type-2 scattering could have a backward effect on lower-order terms.

## 2.2 Application to floating offshore wind

### 2.2.1 Standard design approaches

In the framework of the offshore wind industry, "engineering" load models have been used widely in research and development as well as design. Figure 2.2 shows the design process for Offshore Wind Turbines (OWT) in IEC (2020) which follows a design philosophy similar to the one found in Eurocodes based on limit states. In the case of floating offshore wind turbines, the main limit states as set in the DNV-GL (2016, 2019b) standard consist of the following.

- Ultimate limit state (ULS) assesses the maximum transient load capacity for structural integrity and stability of the system due to a set of coupled environmental loads and operating conditions which are expected during the design life
- Fatigue limit state (FLS) assesses the accumulated structural damages in the component due to cyclic loading of the system during its design life and the incurring risk to structural integrity
- Accidental limit state (ALS) assesses the survivability of the system due to a set of abnormal or accidental environmental and operating conditions (eg. nacelle alignment, blade pitch or grid failure, line breaking, freak waves etc.)

As set out in the current industry standards, ULS and FLS analysis require partial or full dynamic simulation of FOW systems under a wide range of environmental conditions. This is to assess the maximum load or overall fatigue damage. Engineering hydrodynamic models were incorporated into international standards and certification agency guidance for

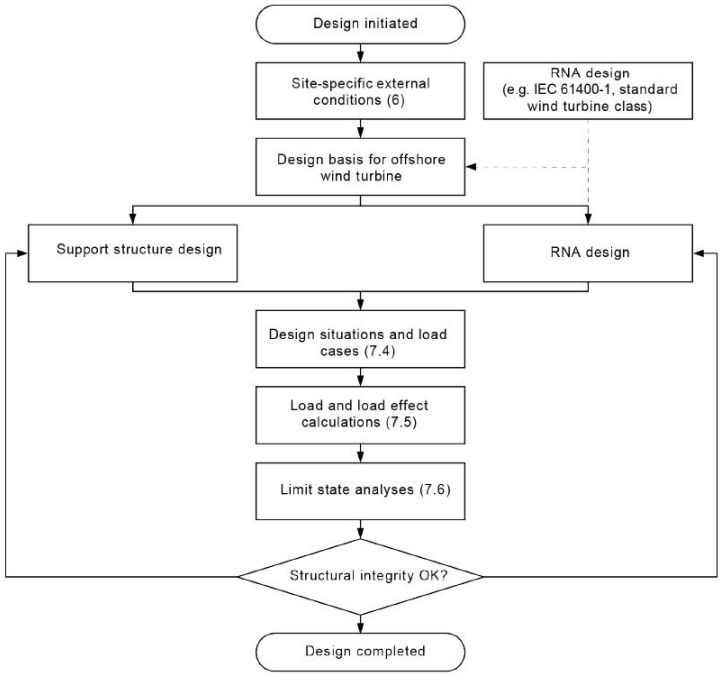


**Figure 2.2:** Design process for offshore wind turbines from IEC 61400-3-1

that purpose. For example the recommended practice document DNV-GL (2010) and the international standard IEC (2020) both provide reference on the use of frequency domain potential flow or slender-element (strip theory) approaches in order to assess hydrodynamic loads.

In offshore wind research, this has led to the development of multi-physics dynamic simulation codes. These are usually referred to as aero-hydro-servo-elastic time domain solvers as they resolve simultaneously the aerodynamic problem on the wind turbine including electro-mechanical control, the hydrodynamic problem on the foundation and the structural problems in various elements of the system (ie. tower, mooring lines etc.). Among the first to be developed is OpenFAST/FAST developed by the NREL which was used very early by Jonkman (2007) to showcase a method for undertaking the concept design of a floating offshore wind design following IEC-64100-3-1 guidance. Following the development of numerous software, efforts have been made to compare the performance of the different codes used by the industry against experimental, full-scale measurements or data obtained from higher-fidelity methods in a format called the Offshore Code Comparison (OC3, OC4, OC5 and OC6) managed by the IEA. This collaborative research project's output related to floating offshore wind turbines focused on several elements. The first task looked at comparing the dynamic simulations of a FOWT spar buoy Jonkman et al. (2010), since spar buoy were the floating foundation used in Hywind, the first completed large-scale floating offshore wind prototype.

The following research in OC4 (A. Robertson et al., 2014), OC5 (A. N. Robertson et al., 2017), and OC6 (A. N. Robertson et al., 2020) focused on comparing models on a semi-submersible prototype (DeepCWind) starting with a code-to-code comparison of standard design load cases (DLCs), followed by comparison with experimental data and then investigation of the low-frequency nonlinear dynamics. Much research has been carried out outside of the IEA projects whether in industrial or academic settings. Some of the most up-to-date research can be found in the following review papers (Gueydon, Bayati, & de Ridder, 2020; Lamei & Hayatdavoodi, 2020; Otter, Murphy, Pakrashi, Robertson, & Desmond, 2022).

Over the recent years, research has mostly been focused on semi-submersible concepts due to their success in driving the development of prototype and pilot projects. In a recent review of current at-sea FOWT prototypes compiled by Edwards et al. (2023), the TLP is the only technology which did not list a single multi-MW full-scale model. The industrial and research outputs have indeed not been as advanced for FOWT-TLPs. The most in-depth research on the design consideration of such a system is summarised in a PhD thesis by Bachynski (2014). Current industry standards also provide specific provisions for TLPs due to their specific low-compliance design. Notably, DNV-GL (2019b) and IEC (2020) mention the importance of taking high-frequency load effects in the design of mooring line tendons. Furthermore, the standard on floating wind turbine by DNV-GL (2019b) highlights the effect of springing and ringing loads on the fatigue damage of the moorings and mentions the possible interaction between the tower's 1st-bending mode and the pitch motion of the platform. It is therefore understood that high-frequency load models become relatively important for simulating ULS and FLS load cases on FOWT-TLPs. The recommended practice on environmental conditions (DNV-GL, 2019a) also notes that the high-frequency loads that are likely to generate springing and ringing responses on TLPs are mostly due to inviscid forces.

### 2.2.2 Experimental analysis of FOWT-TLPs

The state-of-the-art in FOWT tank testing set-up is described in a review paper produced by Gueydon et al. (2020). Whilst the floater is scaled according to the Froude scaling law, the wind load can either be simulated using the so-called full or hybrid method.

The full method consists of scaling the turbine and blade geometry according to Reynolds' scaling law and using a wind tunnel to generate a suitable wind field. This is especially challenging for several reasons. First, this requires specialist facilities that accommodate a wind generation system that is not too turbulent over a wave tank. Secondly, the geometry and

the mass properties of the physical model have to be scaled according to the Froude number in order to be hydrodynamically similar to a full-scale prototype. Conciliating aerodynamic and hydrodynamic scaling gets harder as the model is scaled down and therefore the facilities required also need to accommodate relatively large models.

The Hybrid method is easier to implement for less advanced tank testing facilities without wind tunnels and consists of using real-time measurement to feed in a software-in-the-loop (SIL) algorithm:

- During tank testing, to calculate the wind load virtually based on instantaneous measurements of the platform displacement and apply the resulting thrust force on the nacelle using actuators (ie. winches, fans). This typically models the thrust force with recent efforts aiming at introducing ways to model gyroscopic and aerodynamic moments.
- During wind tunnel tests to calculate the motion of the platform virtually based on the instantaneous measurement of aerodynamic thrust and moments fed to a numerical hydro-elastic simulation actuating the physical model of the wind turbine accordingly (ie. hexapod).

Numerous tank testing experimental studies have been carried out on various floater concepts using both the Full and the Hybrid wind modelling approach. A summary of the published experimental studies on FOWT-TLP is provided in Table 2.2. Considering the depth of the literature on this subject, this section will focus on relevant experimental studies related to TLP testing. A somewhat recent account is provided in Gueydon et al. (2020) for other types of floaters.

In all papers cited in Table 2.2 most studies incorporate:

- Decay tests (DT) where the natural period and damping of the system are measured to characterise the basic dynamic properties and when required, calibrate the numerical models accordingly (drag and structural damping)
- RAOs measurement using a discrete approach with regular waves and/or a spectral approach using irregular waves usually described by a rectangular spectrum also referred to as white noise (WN). These tests usually characterise the linear frequency response of the system in terms of displacement and mooring line tensions.
- Sea-state response measurement in wave only sea-state (WSS), combined wind-wave sea-state (WWSS) or even in some cases combined wind-wave-current sea-states (WWCSS) which will typically aim at understanding the dynamic response statistics of the TLP system and the probability of occurrence of the response peak

| Study | Prototype | Scale | Wind-generation | Case modelled | Numerical validation |
|---|---|---|---|---|---|
| Wehmeyer, Ferri, Frigaard, and Skourup (2013) | Academic AAU-TLP | 1/80 | × | RW/BW/WSS | × |
| Koo et al. (2013) | DeepCWindTLP | 1/50 | Full | DT/WN/SW/WSS/WWSS | MULTISIM+FAST |
| Adam, Myland, Dahlhaus, and Großmann (2014) | GICON® | 1/37 | Full | DT/WWSS | × |
| Laugesen and Hansen (2015) & Pegalajar-Jurado et al. (2016) | Academic DTU-TLP | 1/60 | Full | DT/ RW /WSS/ WWSS | × |
| Vita et al. (2015) | Pelastar | 1/50 | Full | DT/WN/RW/WSS/WWSS | SIMA/OrcaFlex/HAWC2/BLADED |
| Mazarakos and Mavrakos (2017) | MIT/NREL-TLP | 1/40 | Hybrid | RWW | HYDRAEROFLOAT |
| Caillé et al. (2017) | SBM-TLP | 1/40 | Full | DT/WN/RW/WWSS | OrcaFlex/DeepLinesWind |
| Oguz et al. (2018) | TLPWIND | 1/36.67 | Hybrid | DT/DTW/RW/RWW/WWSS | FAST |
| Gueydon, Lindeboom, van Kampen, and de Ridder (2018) | BlueWater/Cable JIP | 1/50 | Both | DT/WN/WWCSS | × |
| Ren, Ma, Shan, Ning, and Ou (2020) | TWWC | 1/50 | Full | DT/SW/RW/RWW/WWSS | AQWA |
| Madsen et al. (2020) | KIER-TLP | 1/60 | Full | DT/WSS/WWSS | × |
| Vittori et al. (2020) | CENTEC-TLP | 1/60 | Hybrid | DT/DTW/SW/WWSS | × |
| Vardaroglu et al. (2022) based on Armenio (2014) | MIT/NREL-TLP | 1/40 | Hybrid | DT/RW/WSS | FAST |

**Table 2.2:** Summary of experimental studies on FOWT-TLP. Abbreviations BW: Bi-chromatic waves, DT: Decay tests, DTW: Decay tests+wind, RW: Regular waves, RWW: Regular waves+wind, SW: Steady wind, WN: White noise, WSS: Wave-only sea-state, WWSS: Wave+wind sea-state, WWCSS: Wave+wind+current sea-sate

Several studies (Gueydon et al., 2018; Madsen et al., 2020; Vittori et al., 2020) have focused on studying various aerodynamic modelling approaches for tank testing. Gueydon et al. (2018) compared the difference between full and hybrid wind modelling on the tension response of a TLP, showing that the full approach could account for some resonant effects induced by the turbine rotor rotational speed which could not be captured with the hybrid SIL approach. Madsen et al. (2020) investigated the turbine control effects on the aero-hydro coupling showing the importance of tuning specific floating offshore wind turbine controllers in order to avoid extreme tension responses. Finally, Vittori et al. (2020) investigated the impact of adding gyroscopic and rotor aerodynamic moments in a SIL approach which could respond to some of the issues pointed out by Gueydon et al. (2018). The results show that the effect of adding the said moments was not significant on the surge response although a higher level of damping was identified. However, a strong increase in the yaw response was observed with the addition of the gyroscopic effect. The study was however limited and did not investigate if the improved SIL approach could capture the resonant response due to the excitation of the tower bending, mooring line bending or pitch modes by the rotor aerodynamic moments.

As seen in Table 2.2, slightly more than half of the experimental studies include a comparison with numerical results with the objective of validating numerical approaches. The first one to be carried out was by Koo et al. (2013) which showed that the nonlinear response of a TLP in wind-wave conditions could be captured relatively well by numerical simulation taking into account linear and second-order loads modelled through the potential flow theory (LIN+QTFs). A strong coupling between the turbine tower-bending mode and TLP response was observed experimentally which was captured numerically. A study by DNV GL and Glosten (Vita et al., 2015) is notable as it proposes a comparison of several numerical models against experimental results of the Pelastar TLP platform in regular and irregular wave cases combined with winds. The effect of the various numerical modelling approaches which are simulated using the tank testing recorded time series will be discussed in more detail in the section below. However, the study concludes that there is a strong coupling between the natural frequencies of the TLP system pitch mode and the turbine's first mode of bending confirming the findings of Koo et al. (2013). Oguz et al. (2018) carried out a validation of a numerical simulation of a TLP response in combined wind-wave conditions using a FAST and a linear hydrodynamic model. The analysis looked at validating regular wave linear RAOs showing that neglecting viscous drag damping in numerical models results in an overestimation of the surge response around the natural frequency in regular waves. This phenomenon is not as marked in irregular waves due to a smaller effect of the viscous damping effect as the structure undergoes random motion instead of large steady sinusoidal oscillations. This provides a good argument for the use of white-noise spectra in tank testing to produce RAOs. The analysis is followed by a comparison of the motion and tension response in irregular combined wind-wave sea-states. The authors noted that the second-order drift loads

measured during tank testing were much smaller than loads generated by the aerodynamic effects. However, it is noted that the latter validation focused mostly on comparing the mean value of the wind-induced trim, surge displacement and mooring line pre-tension without comparing the low-frequency response spectra or extreme motion responses. Furthermore, high-frequency loads and their impact on the vertical motions were not included or discussed in the paper. The most recent study by Vardaroglu et al. (2022) also provides a detailed validation of the numerical simulation of a TLP using FAST against the experimental results of Armenio (2014) this time adding the second-order drift loads via Newman's approximation. However, the effects of second-order difference-frequency loads are thought to be negligible for TLPs (Bachynski, 2014; Molin, 2023) and the study follows a similar investigation to Oguz et al. (2018) without including an analysis of extreme responses.

Wehmeyer et al. (2013) carried out an experimental study on an academic TLP floater and compared laboratory wave generation based on the first and second-order theory. Their study concluded that there was a significant difference in floater response between the runs with first and second-order wave generation. The study highlights the importance of including sum and difference frequency components in laboratory wave generation as this results in an increase in ringing response as well as slacking events.

However, based on this up-to-date literature on the subject of FOWT-TLP experimental testing and to the best knowledge of the author of this thesis, it appears that experimental validation of high-frequency hydrodynamic load models on such a system is still very limited. The author notes second-order sum frequency load models being used in one validation study Koo et al. (2013) This is despite the significant resonant response for these platforms referred to as "springing" and ringing" responses requiring sum-frequency nonlinear wave loads to be modelled accurately as will be explained in detail in the section below.

### 2.2.3 Springing and ringing response of FOWT-TLPs

A non-exhaustive list of conference and journal papers which carried-out numerical analysis of FOWT-TLP using aero-hydro-servo-elastic time domain code is provided in Table 2.3. Most of the studies cited, have looked at validating the system viscous damping and linear response of TLPs. Therefore, the majority of papers do not include fully consistent nonlinear hydrodynamic models. This section will therefore focus on research papers which investigate the non-linear hydrodynamic forces and effects on springing and ringing responses.

As explained in the above sections, the sum-frequency interactions generate forces above the wave spectrum fundamental frequency bandwidth which in the case of FOWT-TLP can lead to structural resonant responses. This is because the TLP stiff pre-tensioned mooring lines restrict the vertical modes of motion and therefore lead to high resonant frequencies. These resonant responses due to high-order wave forces are referred to as springing when they are stationary and ringing when they are transient (DNV-GL, 2010). The DNV-GL (2010) states that high-frequency effects are "mainly governed by inviscid effects".

Following the extensive research on vertical cylinders, simulations of high-order forces' effect on fixed offshore wind structures were carried out such as in the framework of the WAS-XL project (Dadmarzi et al., 2019; Peyrard, 2018) for monopiles and gravity-based-foundations (GBF) structures using the FNV approach. The issue of ringing was investigated for the case of a FOWT-TLP by Bachynski (2014) in a PhD thesis. The numerical approach consisted of a hybrid model coupling potential flow QTFs with third-order FNV forces as set out in Krokstad, Stansberg, Nestegard, and Marthinsen (1998). Analysis of several single-column TLP designs with sum-frequency QTFs and a bandwidth-limited FNV method proposed by Johannessen (2011) was conducted. Based on the numerical work, Bachynski (2014) suggests that the inclusion of the sum-frequency component of both second (QTFs) and third-order (FNV) hydrodynamic loads lead to an increase in the probabilities of extreme tension in the mooring system. The results of the thesis show an increase in maximum tension of 12-30% in most of the considered designs when taking into account third-order ringing force compared to second-order modelling. Furthermore, the author found that sum-frequency second-order loads had an important contribution to the fatigue damage on both the tower base and the mooring line tendons. Finally, a comparison between the diagonal QTFs calculated on a stationary (fixed) and moving system is also presented and showed significant discrepancies between the force and moment amplitude between the two cases, especially at low frequencies. This finding suggests that the second-order non-linearities induced by the floater motion are non-negligible.

Milano, Peyrard, and Capaldo (2018) conducted a similar analysis on the DTU-TLP platform (Laugesen & Hansen, 2015; Pegalajar-Jurado et al., 2017, 2016) using EDF time domain aero-hydro-servo-elastic dynamic solver DIEGO to calculate the platform dynamic response in irregular waves. Milano used a linear potential flow model using BEM software NEMOH and a hybrid second-order model composed of a linear potential flow model coupled with Rainey's spatial derivative and axial divergence term added. These were compared against experimental results from Laugesen and Hansen (2015). The results pointed to an overestimation of the surge and pitch when Rainey's terms were considered. The paper also looked at the effect of tendon inclination showing a reduction of the extreme surge response but increasing heave and pitch response with increasing inclination. In a second paper, Milano et al. (2019)

extended his work by adding the FNV term related to the third-order potential nonlinear force while ignoring Rainey's terms based on the previous findings. The results showed that the inclusion of FNV leads to an increase in extreme surge, pitch response and mooring tensions compared to the linear model in accordance with Bachynski (2014). Furthermore, the results showed an increase in the extreme line tension when increasing the inclination of the tendons. Although not described in the paper, this effect can potentially be linked to the downshift in natural frequency of the vertical modes due to lower vertical stiffness with increasing batter angle. This results in having a more energetic bandwidth exciting the vertical modes.

Shen et al. (2016) investigated the effect of viscous forces on the harmonic springing response of the DeepCWind-TLP (See (Koo et al., 2013)). The method uses a linear potential flow hydrodynamic database and a Morison equation for the viscous drag. Whilst no high-frequency inertial forces are taken into account, the authors noted a higher level of springing response in the RAO runs when viscous forces are taken into account. The authors therefore confirmed an earlier work by Gurley and Kareem (1998) that viscous forces might have a significant impact on the high-frequency response of stiff offshore structures. Furthermore, the effect of increasing wave steepness on the springing response peak was investigated via regular wave runs showing a maximum third-order springing response at a wave steepness of around $H/\lambda \approx 7\%$ after which the springing response reduces. The authors suggest that this is due to the additional drag damping overwhelming the drag excitation force. Irregular wave cases in storm conditions using a peak period of one-third of the pitch resonance were simulated with and without steady wind aerodynamic load. Their results showed a reduction in the springing spectral peak when aerodynamic loads are taken into account due to aerodynamic damping as described in Koo et al. (2013). It is noted that a linear wave kinematic model is used in both monochromatic and multi-chromatic wave cases which is recognised as an issue by the authors. Another approach was taken by Jagdale et al. (2021) which modelled the high-order response of the DeepCWind prototype in regular waves using Rainey's theory coupled with Morison drag, which therefore represents a more consistent non-linear inertial hydrodynamic model. Three velocity fields were generated for comparison, one using a linear wave theory (Airy), one using a Fenton's based wave theory (See Stream Function in Section 3.1.2) and one using kinematics extracted from a nonlinear PF numerical wave tank. Their results showed a good agreement between the two nonlinear methods and also highlighted the springing response generated in the mooring lines by second and third-order wave loads. The importance of using nonlinear wave kinematics to capture accurate springing peaks was highlighted.

Pegalajar-Jurado et al. (2017) investigated several approaches to model wave kinematics to simulate a range of irregular sea states tested experimentally in Laugesen and Hansen (2015) including one focused wave case and two storm cases. Four approaches were used, the first three using respectively: a target signal modelled with first-order (Airy), a second-order wave theory ((Sharma & Dean, 1981)), and kinematics obtained from fully-nonlinear PF NWT. The last approach consisted in using the measured signal in the tank rather than imposing the target spectrum , by recomposing it numerically with linear waves (Airy). Interestingly, the most successful model consisted of the linear model using the measured wave spectrum which managed to generally reproduce both the linear response but also the nonlinear springing response. The second-order and fully non-linear wave kinematic models were generally successful at reproducing the storm case pitch and nacelle acceleration spectral response both in linear and nonlinear low and high-frequency responses. It is noted that as seen in several other studies, the hydrodynamic model used in this study is relatively simplified with wave loads and added mass radiation effects being modelled through the Morison equation.

Overall, numerical work on springing and ringing of FOWT-TLP is relatively limited with very few articles (Bachynski, 2014; Jagdale et al., 2021; Milano et al., 2019) having implemented a consistent non-linear inertial wave loading model. Furthermore, it appears that no thorough comparison between the different approaches has been carried out despite the multiple combinations possible such as hybrid methods combining potential flow and strip-theory equations. The effects of the tower flexibility, high-order wave kinematics and the modelling of viscous forces have been discussed above as significant parameters to take into account when simulating the nonlinear response of a FOWT-TLP. However, a significant study is required to review the significance of these parameters on the numerical simulation of springing and ringing responses.

| Study | Prototype | Wind | Cases | Code used | Wave | ME-In | ME-Dr | RE | FNV | PF-RAD | PF-LIN | PF-QTF- | PF-QTF+ |
|---|---|---|---|---|---|---|---|---|---|---|---|---|---|
| Koo et al. (2013) | DeepCWind-TLP | ✓ | MTLSIM-FAST | DT/WN/SW/WSS/WWSS | Airy | × | ✓ | × | × | ✓ | ✓ | ✓ | ✓ |
| Bachynski (2014) | Academic designs | ✓ | WWSS | Sima-Riflex-AeroDyn | Airy | ✓ | ✓ | × | ✓ | ✓ | ✓ | ✓ | ✓ |
| Laugesen and Hansen (2015) | DTU-TLP | ✓ | DT/RW/ WSS/WWSS | WAMIT | Airy | × | × | × | × | ✓ | ✓ | × | × |
| Vita et al. (2015) | Pelastar | ✓ | DT/WN/RW/WSS/WWSS | BLADED/HAWC2/SIMA/OrcaFlex | Airy Whel | ✓ | ✓ | × | × | × | × | × | × |
| Shen et al. (2016) | DeepCWindTLP | ✓ | DT/RW/WSS/WWSS | CRAFT/FAST | Airy | ✓ | ✓ | × | × | ✓ | × | × | × |
| Caillé et al. (2017) | SBM-TLP | ✓ | DT/WN/RW/WWSS | DeepLines/OrcaFle | Airy | × | ✓ | × | × | ✓ | ✓ | × | × |
| Pegalajar-Jurado et al. (2017) | DTU-TLP | × | FW/WSS | FAST | Airy/$2^{nd}$/FNL | ✓ | ✓ | × | × | × | × | × | × |
| Oguz et al. (2018) | TLPWIND | ✓ | DT/DTW/RW/RWW/WWSS | FAST | Airy | × | × | × | × | ✓ | ✓ | × | × |
| Milano et al. (2019) | DTU-TLP | ✓ | WWSS | DIEGO | Airy/FNL | × | ✓ | × | ✓ | ✓ | ✓ | ✓ | × |
| Ren et al. (2020) | TWWC | ✓ | DT/SW/RW/RWW/WWSS | AQWA | Airy | × | × | × | × | ✓ | ✓ | × | × |
| Jagdale et al. (2021) | DeepCWind | ✓ | RW/RWW | FAST | Airy/SF/FNL | × | ✓ | ✓ | × | × | × | × | × |
| Vardaroglu et al. (2022) | DHI-TLP | ✓ | DT/RW/WSS | FAST | Airy | × | ✓ | × | × | ✓ | ✓ | ✓ | × |

**Table 2.3:** Summary of numerical simulation of FOWT-TLP with aero-servo-hydro-elastic time domain codes. Abbreviations: **Environment case**: - DT: Decay tests, DTW: Decay tests+wind, RW: Regular waves, RWW: Regular waves+wind, SW: Steady wind, WN: White noise, WSS: Wave-only sea-state, WWSS: Wave+wind sea-state, WWCSS: Wave+wind+current sea-sate. **Hydrodynamic models**: Me-In: Morison inertial, ME-Dr: Morison drag, RE: Rainey equations, FNV: FNV equations, PF RAD: Potential flow radiation force, PF LIN: Potential flow linear excitation force, PF QTF-: Potential flow difference-frequency QTFs, PF QTF+: Potential flow sum-frequency QTFs

# Chapter 3

# Theoretical and experimental background

## 3.1 Numerical representation of oceanic waves

The complex hydrodynamic effects occurring in the ocean have to be simplified for the purpose of offshore engineering. This requires the segregation of ocean effects based on their origin (ie. tidal, wind-generated, thermal) and the time scale of their periodicity (ie. days, hours, seconds). In this thesis, ocean waves refer to the wind-generated periodical modification of the free surface, far-field or locally. The periodicity of such waves has an order of magnitude comprised between some seconds and some dozen seconds.

### 3.1.1 Mode-coupled approach

Whilst the behaviour of fluid in the ocean could be accurately described by complex non-linear equations, these have to be numerically solved in the time domain to remain fully nonlinear. This process is CPU intensive and can currently only realistically be used for very short time-frames, typically below an hour. Since an offshore structure is subject to several millions of waves throughout a lifetime of 25 years or over, engineers rely on a linearisation of the problem in the frequency domain to be able to simulate a wide range of sea states. This way, the ocean-free surface in the area of interest can be expressed as a linear superposition of an infinite amount of wave modes.

$$\eta = \eta^{(1)} + \eta^{(2)} + \eta^{(3)} + ... \tag{3.1}$$

The solution for the wave propagation, induced kinematics and higher-order free surface can be found in the framework of the potential flow theory, where fluid kinematics induced by waves are represented by a velocity potential field, assuming in-viscid, in-compressible fluid and irrotational flow. The fluid is expressed as a continuous velocity field represented by a potential which follows a set of boundary conditions.

$$\phi(x,z,t) = \phi^{(1)} + \phi^{(2)} + \phi^{(3)} + ... \tag{3.2}$$

**Box 1: Potential flow boundary conditions**

BC1. Laplacian continuity condition

$$\Delta\phi = 0 \text{ in } \Omega \tag{3.3}$$

BC2. Dynamic free surface condition (Bernouilli)

$$\frac{\partial\phi}{\partial t} + \frac{1}{2}(\nabla\phi)^2 + g\eta = 0 \text{ at } z = \eta \tag{3.4}$$

BC3. Kinematic free surface condition

$$\frac{\partial\eta}{\partial t} + \frac{\partial\phi}{\partial x}\frac{\partial\eta}{\partial x} + \frac{\partial\phi}{\partial y}\frac{\partial\eta}{\partial y} = \frac{\partial\phi}{\partial z} \text{ at } z = \eta \tag{3.5}$$

BC4. No-leak seabed condition

$$\Delta\phi = 0 \text{ at } z = -h \tag{3.6}$$

The Bernoulli and kinematic boundary conditions at the instantaneous free surface are combined into a single free surface boundary equation. The expansion of the potential into a Taylor series reveals a first-order homogeneous partial differential equation and a set of higher-order terms. The homogeneous free surface condition and the following in-homogeneous second and third-order conditions are given below.

$$g\frac{\partial\phi^{(1)}}{\partial z} + \frac{\partial^2\phi^{(1)}}{\partial t^2} = 0 = Q_F^{(1)} \text{ at } z = 0 \tag{3.7}$$

$$g\frac{\partial\phi^{(2)}}{\partial z} + \frac{\partial^2\phi^{(2)}}{\partial t^2} = \frac{1}{g}\frac{\partial\phi^{(1)}}{\partial t}\frac{\partial}{\partial z}\left(\frac{\partial^2\phi^{(1)}}{\partial t^2} + g\frac{\partial\phi^{(1)}}{\partial z}\right) - \frac{\partial}{\partial t}(\vec{\nabla}\phi^{(1)})^2 \tag{3.8a}$$

$$= Q_F^{(2)} \text{ at } z = \eta \tag{3.8b}$$

$$g\frac{\partial\phi^{(3)}}{\partial z} + \frac{\partial^2\phi^{(3)}}{\partial t^2} = Q_F^{(3)} \text{ at } z = \eta \tag{3.9}$$

where $Q_F^{(3)}$ can be found in the original publication of Malenica and Molin (1995).

From these equations, one can observe that the knowledge of the free surface is built up from solving the potential with increasing order of nonlinearity starting from $z = 0$. The solution to the homogenous equation, or first-order wave mode, which will also be referred to in this thesis as the linear or fundamental mode, is found to be an infinite sum of sine waves. The writing used here is for the case of uni-directional waves which is used in this thesis and which lightens the formulas. The reader will note the $e^{-i\omega t}$ convention used in this work.

$$\eta^{(1)}(x,t) = \sum_i A_i \cos\left(k_i x - \omega_i t + \Phi_i\right) \tag{3.10}$$

This implies that the first-order potential assumes a free surface at the mean sea level, $z \approx 0$, hence the name of small-amplitude wave theory also known as Airy wave theory. The knowledge of this fundamental free surface forcing enables us to derive higher-order hydrodynamic effects. The wave kinematics is then extracted from the incident potential solution.

$$\phi_I^{(1)}(x,z,t) = \sum_i \frac{A_i g}{\omega_i} \frac{\cosh\left(k_i(z+h)\right)}{\cosh k_i h} \sin\left(k_i x - \omega_i t + \Phi_i\right) \tag{3.11}$$

At second-order these models have to verify a more complex free surface condition which highlights the interaction of waves by pair (Molin, 2023).

$$\phi_{I\pm}^{(2)}(x,z,t) = \sum_i \sum_j \frac{q_{ij\pm}}{-(\omega_{ij\pm})^2 + g k_{ij\pm} \tanh k_{ij\pm} h} \frac{\cosh\left(k_{ij\pm}(z+h)\right)}{\cosh k_{ij\pm} h} \sin\left(k_{ij\pm} x - \omega_{ij\pm} t + \Phi_{ij\pm}\right) \tag{3.12}$$

where $i, j$ are the $i$th and $j$th linear components in the fundamental wave spectra.

#### Stretching models

The linear potential-flow theory which serves as the basis for the mode-coupling approach relies on the assumption of low wave steepness and a linear superposition of waves. This leads to the velocity in the wave-crest being an approximation. In monochromatic waves, the linear hyperbolic relation between kinematic velocity and depth in the water column is found to be relatively valid and very accurate when several orders of non-linearity are taken into account (Molin, 2023). However, in irregular waves, also referred to in this document as multi-chromatic waves, this approximation is found to be generally false. This is due to several factors among which the limited non-linearity of irregular wave theories and the issue with long-short wave linear superposition. For that purpose, various extrapolations of the velocity in the crest have been proposed.

- **Linear stretching** assumes that kinematics from the $z = 0$ to $z = \eta$ can be extrapolated linearly by prolonging the velocity profile above the mean water level: $u(x,y,z,t) = u(x,y,0,t) + z\frac{\partial u(x,y,0,t)}{\partial z}$

- **Vertical stretching** assumes a vertical velocity profile up from $z = 0$ to the wave crest $z = \eta$, with all kinematic values being equal to the wave kinematics at $z = 0$
- **Wheeler stretching** assumes that the kinematics at the crest, $z = \eta^{(1)}$, are equal to the kinematics found at $z = 0$ and stretches the entire velocity profile accordingly
- **Delta stretching** is a modification of the Wheeler method to provide a velocity profile extrapolation which is in between a linear and Wheeler stretching

It is worth noting that these models violate the Laplace equation mass conservation principle. Therefore, their validity can only be assessed against velocity profiles obtained through experimental measurements or high-fidelity numerical simulations (Molin, 2023). Stansberg, Gudmestad, and Haver (2008) compared LDV measurements of kinematics in an extreme irregular wave event against various methods and showed that the best-performing model was based on second-order Stokes' theory applied without Wheeler stretching. A wave-by-wave stretching approach developed in Grue, Clamond, Huseby, and Jensen (2003) also showed good results. Finally, a linear wave theory with Wheeler stretching applied on nonlinear wave records was also found to reproduce the trend of the LDV measurement better than when using filtered linear wave records. In that case, the results showed that the Wheeler Stretching leads to good results in the crest but tends to underestimate the velocities at and below the mean water level.

#### Spectral representation of ocean waves

As explained above, waves in the ocean can be modelled as an infinite sum of linear waves following a dispersion relation. It has been shown that the distribution of these components is stochastic and that the distribution of wave parameters can be assumed as a Gaussian process (Goda, 2010; Molin, 2023). These parameters include wave height, period and direction and their statistical representation is generally expressed by the peak period $T_p$, the significant wave height $H_s$ and mean direction of propagation $\bar{\beta}$ (Goda, 2010; Molin, 2023). Detailed information on the description of waves as random processes can be found in Goda (2010), a founding piece of literature on marine engineering.

In deep water it is common to consider that a sea state remains stationary over a duration of 3 hours during which the statistical distribution of wave parameters are assumed to remain constant (DNV-GL, 2010; Molin, 2023). It is therefore common to carry out stochastic numerical time domain simulations by 3-hour intervals where the stationary sea-state is described by an energy density spectrum. This spectrum represents the repartition of energy across the range of frequencies for a stationary sea-state. Several single peak spectra can be used to define an energy repartition centred around one peak frequency The most commonly used is the JONSWAP spectrum which was built in a semi-empirical manner from a campaign of

measurements in the North Sea (Hasselmann et al., 1973). This spectra can be assumed based on fetch data (wind speed, fetch length and time) or described based on stationary sea-state statistical parameters $H_s$, $\omega_p = 2\pi/T_p$ and the peak enhancement factor $\gamma$ typically equal to 3.3.

$$S(\omega) = \alpha H_s^2 \omega_p^4 \omega^{-5} \exp\left(-\frac{5}{4}(\frac{\omega}{\omega_p})^{-4}\right)\gamma^{\alpha} \tag{3.13a}$$

$$\alpha = \exp\left(-\frac{(\omega-\omega_p)^2}{2\sigma^2\omega_p^2}\right) \tag{3.13b}$$

$$\sigma = \begin{cases} 0.07 & \omega < \omega_p \\ 0.09 & \omega > \omega_p \end{cases} \tag{3.13c}$$

Once assigned to the aero-hydro-elastic time-domain solver, such spectra can be discretised into bands centered around a finite amount of frequencies to generate a set of linear waves with a given amplitude and phases assigned randomly. For a given band of frequency between the pulsations $\omega_{i1}$ and $\omega_{i2}$ and centered around $\omega_i$, the amplitude of the representative wave is found by integrating the energy density over the frequency band.

$$A_i = \sqrt{2\int_{\omega_i - \mathrm{d}\omega/2}^{\omega_i + \mathrm{d}\omega/2} S(\omega)\,\mathrm{d}\omega} \tag{3.14}$$

This method requires to cut-off the spectrum at a given low and high frequency which on top of being somewhat arbitrary, also contains some inherent issues Johannessen (2011). Furthermore, measured spectra in the ocean or laboratory flume include bound harmonics. Several methods to discretise a spectrum into frequency bands exist such as by using steps of the same frequency width (iso-frequency), of the same period width (iso-periodic), of the same energy density (iso-energetic) or even random width bands (random frequencies). Iso-periodic, iso-energetic and random frequency methods do not use a constant frequency step. Hence they allow to represent a spectrum with a reduced amount of individual components without compromising on the length of the unique time signal generated (Duarte, Gueydon, Jonkman, & Sarmento, 2014).

### 3.1.2 Highly nonlinear seas

#### Regular waves- Stream Function

A regular wave theory applicable to highly nonlinear wave cases was developed by Dean (1965). The problem is formulated using a Stream Function, $\psi$(x,y,z,t), representing the flux rather than using a potential and the same boundary conditions as in 3.1.1. The problem is linearised in the frequency domain and requires a truncation at the required number of Fourier modes, $N$, that allow convergence of the solution. Fenton (1990) extended the method although using analytical solutions based on Stokes' theory. These two methods are now used interchangeably.

#### Irregular waves

Other methods exist to simulate the propagation of highly nonlinear waves. In the fully non-linear methods, one of the most computationally intensive is to resolve the Reynolds Averaged Navier Stokes' equation typically done in Eulerian or Lagrangian CFD. An introduction of Eulerian CFD in the context of offshore structures is provided in Section 3.3. Other lighter time-domain method exists such as resolving numerically the fully nonlinear potential flow problem as seen in Liu, Xue, and Yue (2001); Xue, Xü, Liu, and Yue (2001).

Using a frequency-domain linearisation of the initial condition, the high-order spectral method (HOS) enables the calculation of the instantaneous free-surface elevation and free surface potential in the time-domain, based on a pseudo-spectral method. An implementation of this approach is presented in Ducrozet, Bonnefoy, Le Touzé, and Ferrant (2016). This methodology allows the reconstruction of the wave kinematics at specific points of the fluid individually but doing so for the full domain is computationally intensive. Therefore this method is not utilised in this thesis since the position of each element of the floater is meant to change with the platform motion.

## 3.2 Low to medium fidelity wave-structure interaction models

### 3.2.1 Frequency domain potential flow approach

#### Boundary conditions

Following the potential flow approach that is used to describe the propagation of waves in the ocean, the problem can be extended to analyse the wave pressure on an offshore structure. The potential in the near-field of the structure can be decomposed into three main components, the incident potential $\phi_I$ which defines the initial velocity potential of the wave field without structures, the scattered-potential $\phi_S$ which defines the modification of the velocity

potential due to the structure. The scattered potential is divided between the diffracted wave field, $\phi_D$ generated by the presence of the fixed structure, and the radiated potential $\phi_R$ which defines the modification of the potential due to the radiated wave field generated by the oscillatory motion of the structure.

$$\begin{aligned} \phi^{(p)} &= \phi_I^{(p)} + \phi_S^{(p)} \\ &\text{with} \\ \phi_S^{(p)} &= \phi_D^{(p)} + \text{ if motion } \phi_R^{(p)} \end{aligned} \tag{3.15}$$

Boundary conditions have to be added to the existing set shown in the Box in Section 3.1.1 to account for the body presence. The no leak condition on the hull surface ($S_{B_0}$) requires the fluid velocity on the wetted hull surface to be equal to the body velocity. Finally, the far-field condition requires the wave scattering due to the body disappearing far from the body and the total velocity potential to tend towards the incident potential.

**Box 2: Additional body boundary conditions to the potential flow problem**

BC 5 No-leak body condition

$$\vec{\nabla}\phi\vec{n} = \ddot{X}\vec{n} \text{ on } \in S_{B_0} \tag{3.16}$$

BC 6 Far-field condition

$$\lim_{R\to\infty} \phi = \phi_I \tag{3.17}$$

**Resolving the diffraction and radiation problems**

In order to resolve the diffraction problem, Green's function and Green's theorem are useful tools. The Green function defines the influence of a source $\sigma_i(\xi)$ located at a point in the fluid domain with coordinate $\xi$ on a potential $\phi_j(\mathbf{X})$ at a position $\mathbf{X}$ in the same domain. The Green's function satisfies the Laplacian, free surface and sea-bed condition.

$$\phi_j(\mathbf{X}) = \frac{1}{4\pi} \iint_{S_{B_0}} \sigma_i(\xi) G(\mathbf{X}, \xi)\, \mathrm{d}S \tag{3.18}$$

Using this identity and Green's second theorem, the scattered potential can be written using the boundary integral equation method (ANSYS Inc, 2016; Journée & Massie, 2001; Molin, 2023).

$$2\pi\phi_S(\mathbf{X}) + \iint_{S_{B0}} \phi_S(\xi)\frac{\partial G(\mathbf{X},\xi)}{\partial n}\,\mathrm{d}S = \iint_{S_{B0}} \frac{\partial \phi_S(\xi)}{\partial n} G(\mathbf{X},\xi)\,\mathrm{d}S + \frac{1}{g}\iint_{S_F} Q_F(\xi)G(\mathbf{X},\xi)\,\mathrm{d}S \quad \text{for} \quad \mathbf{X} \in S_{B_0} \tag{3.19}$$

Where $\iint_{S_{B_0}}$ represents an integral over the structure hull surface; and $\iint_{S_F}$ an integral over the free surface of the fluid domain.

Diffraction

For the integral at the body surface, the problem is linearised by assuming two separate problems, one for a fixed structure subject to wave forcing, and one for a structure in motion in a fluid at rest. Hence for the diffraction case which considers the fixed body, the velocity at the body surface is null, $\frac{\partial \phi_D}{\partial n} = -\frac{\partial \phi_I}{\partial n}$.

For the free surface integral, the free surface boundary conditions from Section 3.1.1 are used from the above equation, and using the free surface condition:

- For the first-order diffraction, the term $Q_F^{(1)} = 0$ leading the last term on the right-hand side to be removed and leaving an equation of a simpler form:
- At second-order the free surface boundary conditions in Equation 3.8b is introduced and the last right-hand side term consists of a free surface integral over the fluid domain which depends on the first-order potential solution
- At third order, the free surface boundary conditions in Equation 3.9 is introduced which includes both first-order and second-order potential quantities which leads to terms including a double integral over the free surface of the fluid domain

Resolving the diffraction problem at orders higher than one is complex due to the boundary conditions. Hence Molin (1979) split the diffracted potentials into a homogeneous and particular solution of the free surface boundary condition.

$$\phi_D = \phi_{DI} + \phi_{DD} \tag{3.20}$$

- $\phi_{DI}$, the diffraction problem due to the incident potential, which therefore assumes a homogeneous free surface condition and represents the free-wave potential
- $\phi_{DD}$, the diffraction problem due to the modified free surface which therefore assumes an in-homogeneous free surface condition and represents the locked-wave potential

As can be seen, in the free surface condition of Equations 3.8b and 3.9, the second and third-order potentials depend on the respective lower-order potential terms and incident and scattered free surface. This particular complexity can easily be illustrated by substituting the first order potential from equation 3.15 into the expression of the second order potential in equation 3.8b, one can deduce that the second order potential is described by quadratic cross-terms of the first-order potential (Pinkster, 1980) and a term, $\phi_0^{(2)}$, representing the homogeneous diffraction solution based on the linearised free surface.

$$\phi^{(2)} = \phi_0^{(2)} + \phi_{II}^{(2)} + \phi_{DD}^{(2)} + \phi_{RR}^{(2)} + \phi_{ID}^{(2)} + ... + \phi_{RD}^{(2)} \tag{3.21}$$

It is worth to add that at second-order, $\phi_0^{(2)}$, includes the term $\phi_{DI}^{(2)}$ in Molin (1979) (Equation 3.20) and the second-order radiation potential $\phi_R^{(2)}$. The remaining terms are solved through the resolution of the in-homogeneous diffraction problem with the exception of term $\phi_{II}^{(2)}$ which only depends on the first-order incident potential and as such is the second-order incident potential of Equation 3.12. As can be expected, the situation for the third-order potential is thus a lot more complex involving triple cross terms.

Radiation

For the radiation case, the fluid is considered at rest and the body is in motion. Hence at first order, the free surface condition is null and the radiation potentials of higher orders are assumed to be negligible. Hence only the body surface integral remains in Equation 3.19, with the body radiation condition, $\frac{\partial \phi_R}{\partial n} = \dot{X}\vec{n}$. The radiation potential is usually written as the sum of its six degrees of freedom components.

$$\phi_R = \sum_{j=1}^{6} i\omega x_j \phi_{Rj} \tag{3.22}$$

$x_j$ represents the unit amplitude of the body oscillatory motion in the j direction (j= 1, 2 ...6) being respectively the three horizontal directions: surge, sway, heave and three angular directions: roll, pitch, yaw. At second-order, Kim and Yue (1990) showed that the radiation condition can be solved in the same way as at first-order but as a function of the sum and difference frequency motion. For that reason, the problem remains linear and the frequency-dependent hydrodynamic coefficient solutions are identical. However, in Equation 3.21, the terms $\phi_{RR}^{(2)}$ can be found which corresponds to the cross term of the first-order radiation potential. This term, as well as all other cross terms of the free surface, intervenes in the resolution of the second-order diffraction problem and as such the first-order radiation impacts the second-order diffraction.

**Diffraction-radiation forces**

Radiation force

The radiation force is the direct integration over the hull of the linear pressure term. It can be written as $F_R = Z$ which consists of an active and a reactive component such as can be found in an electric AC circuit with impedance (Alves, 2016). The active term (or real part) represents hydrodynamic damping which is the dissipation of energy from the oscillating body to the water by the generation of the radiated wave. The reactive (or imaginary part) represents a back-and-forth transfer of energy from the oscillating body in harmonic motion to the water. The first is the hydrodynamic damping (B) and the other is the added Mass ($M_a$) such as $Z = B - i\omega M_a$. As seen in Equation 3.22, the radiation potential is composed of six individual components for the six DoFs of motion. Since each six-motion DoF results in a radiation potential which in turn results in a load vector in the six DoF, the result is a matrix expression. As such, damping and added mass coefficient are expressed as 6 x 6 matrices which are individual for each frequency of motion $\omega$.

$$F_R = \rho \iint_{S_0} \frac{\partial \phi_R}{\partial t} \vec{n} \, \mathrm{d}S = [M_a(\omega)\omega^2 + iB(\omega)]\vec{X} \tag{3.23}$$

First-order diffraction force

From the linear Bernouilli equation, the integration of the first-order potential induced pressure on the hull provides the hydrodynamic force due to wave action. As in Equation 3.2 and 3.15, the forces can also be separated into different orders and components. For example, the first-order force can be written as follows. It is worth noting that at first order, the integration is carried out on the mean wetted hull of the structure, $S_{B0}$ since the free surface elevation is a first-order quantity itself.

$$F_I^{(1)} + F_S^{(1)} = \rho \iint_{S_0} \left( \frac{\partial \phi_I^{(1)}}{\partial t} + \frac{\partial \phi_S^{(1)}}{\partial t} \right) \vec{n} \, \mathrm{d}S \tag{3.24}$$

The integration of the incident wave potential pressure on the hull represents the force generated by the undisturbed wave field which is also referred to as the Froude-Krylov force. The integration of the scattered potential provides the diffraction force which is due to the emission of diffracted waves from the structure. When a structure is infinitely large, the diffraction tends towards full reflection. The first-order incident potential is relatively easy to derive since it is a homogeneous solution of a linear equation which does not depend on the structure. On the other hand, both the diffracted potential and radiated require a more complex derivation which requires the use of Green's theorem.

Higher-order diffraction force

At second-order and above, the full Bernoulli equation pressure including its quadratic terms is used to calculate the second-order forces. With the movement of the platform, second-order quantities are also generated. The second-order component of the force can then be decomposed in terms associated with:

- Pressure integrated over the static hull up to waterline $S_{B0}$ which includes
  - the dynamic pressure due to the first-order potential integrated over the static hull (Equation 3.25)
  - the combination of first-order pressure components integrated over the static hull and rotated according to first-order motion (Equation 3.29)
  - the integration of first-order pressure components integrated over the static hull and accounting for its displacement in the domain (Equation 3.28)
  - the second order pressure component integrated over the un-rotated wetted hull (Equation 3.27)
- Pressure integrated over the oscillatory part of the hull surface comprised between the waterline and the first order free surface elevation (denoted as $wl$) which includes:
  - the static pressure term integrated over the oscillatory part of the rotated hull surface (Equation 3.26)

$$\vec{F}_{1a}^{(2)} = \frac{1}{2}\rho \int\int_{S_0} (\vec{\nabla}\phi^{(1)})^2 \cdot \vec{n} dS \qquad \text{Dynamic pressure term} \qquad (3.25)$$

$$\vec{F}_{1b}^{(2)} = \int_{wl} \frac{1}{2}\rho g (\eta_r^{(1)})^2 \vec{n} dl \qquad \text{Hydrostatic correction} \qquad (3.26)$$

$$\vec{F}_{2}^{(2)} = \rho \int\int_{S_0} \frac{\partial \phi^{(2)}}{\partial t} \vec{n} dS \qquad \text{Contribution of 2nd order potential} \qquad (3.27)$$

$$\vec{F}_{1c}^{(2)} = \rho \int\int_{S_0} \vec{X}^{(1)} \vec{\nabla} \frac{\partial \phi^{(1)}}{\partial t} \vec{n} dS \qquad \text{Inertia force correction} \qquad (3.28)$$

$$\vec{F}_{1d}^{(2)} = \mathbf{R}^{(1)} \vec{F}^{(1)} \qquad \text{Rotation of 1st ord. forces} \qquad (3.29)$$

Finally, at third-order the horizontal forces on a fixed structure as described by Malenica Malenica (1994); Malenica and Molin (1995) are provided below.

$$F_{x1}^{(3)} = \frac{i\omega\rho}{8g}\int_{wl}\left[\nabla\phi^{(1)}(\nabla\phi^{(1)})^2 + \frac{\omega^2}{g}\phi^{(1)^3}\right]\vec{n}\,\mathrm{d}l \tag{3.30}$$

$$F_{x2}^{(3)} = -\frac{\rho}{2}\iint_{S0}\nabla\phi^{(1)}\cdot\nabla\phi^{(2)}\vec{n}\,\mathrm{d}S - \frac{\rho\omega^2}{g}\int_{wl}\phi^{(1)}\phi^{(2)}\vec{n}\,\mathrm{d}l \tag{3.31}$$

$$F_{x3}^{(3)} = 3i\omega\rho\iint_{S0}\phi^{(3)}\vec{n}\,\mathrm{d}S \tag{3.32}$$

The higher-order forces consist of multiplication of the first-order potentials, quadratic at second-order and cubic at third-order. The first-order potential is a sum of sinusoidal functions for each fundamental wave frequency, its quadratics term generates sum-frequency and difference-frequency terms for each pair of frequencies. The forces generated by each pair can be expressed by the quadratic force transfer functions (QTFs) which are normalised by the amplitude of each individual fundamental wave in a pair. Each force vector component can be represented as a matrix and plotted in 2D space.

$$\begin{aligned}\vec{F}_{ij}^{(2)} = a_i a_j\{&\vec{R}^{+}\cos[(\omega_i+\omega_j]+(\Phi_i+\Phi_j)]\\ &+\vec{I}^{+}\sin[(\omega_i+\omega_j]+(\Phi_i+\Phi_j)]\\ &+\vec{R}^{-}\cos[(\omega_i-\omega_j]+(\Phi_i-\Phi_j)]\\ &+\vec{I}^{-}\sin[(\omega_i-\omega_j]+(\Phi_i-\Phi_j)]\}\end{aligned} \tag{3.33}$$

At third-order, the problem becomes much more complex with the addition of a third frequency resulting in multiple combinations of sum and difference cross terms. In the current form, the theory is therefore limited to the sum-frequency monochromatic wave case.

#### BEM - Boundary Element Method

The Green's function representation of the scattered potential and its integral over the body can be understood as a mix of sources and dipoles. For complex structures, the panel method is used where the total scattered potential is emitted by the sum of the sources represented by the body's mesh panels. The boundary integral equation (Equation 3.19) is written as a sum of the panel potentials and the solution is found numerically. At second-order, a mesh of the free surface is required to directly integrate a portion of the free surface potential. More details on the Boundary Element Method are provided in ANSYS Inc (2016); Babarit and Delhommeau (2015) and for second-order in Lee (1995). In most industrial codes, the sources are calculated on 2D panels with a centroid. A higher-order BEM method exists which uses a nonlinear panel method for which information can be found in Liu, Kim, and Lu (1990).

### Semi-analytical methods

With simpler axisymmetric geometries such as a vertical cylinder, the potential flow equations can be written in polar form and expanded into Fourier series about the polar angle $\theta$.

$$\phi^{(p)} = \sum_{n=0}^{\infty} \varepsilon_n \phi_n^{(p)} \cos n\theta \tag{3.34}$$

where $\varepsilon_0 = 1$ and $\varepsilon_n = 2$ for $n > 0$. This way, the diffraction problem can be solved using a semi-closed form solution and domain decomposition. Due to the simplification possible to the Laplace and radiation condition problem with a cylinder in polar coordinates, quasi-analytic solutions can be found in the form of Bessel functions. The advantages of these semi-closed form solutions are multiple. Firstly they avoid reliance on a second-order BEM solver which requires a detailed mesh and can demand significant computational time to reach convergence of results. Secondly, they are parametric which allows for better optimisation at early design stages. However, since in their derivation, they forego interaction between multiple objects, these are not reliable for assemblies of columns Kim (1991) and would mostly be suited to simple geometries with a single diffracting surface piercing element which is often the case in FOWT-TLP design. In this thesis, these semi-analytical solutions are used as a reference when analysing the high-frequency force transfer functions. Furthermore, an attempt is made to showcase their relevance to the dynamic simulation of FOWT-TLP by testing them in a monochromatic wave case.

#### First-order solution for bottom-fixed vertical cylinder

The first of its kind use was published by MacCamy and Fuchs (1954) providing the solution for the first-order diffraction potential by fixed vertical bottom-seated cylinder in water with homogeneous depth.

$$\phi^{(1)} = \phi_I^{(1)} + \phi_D^{(1)} \tag{3.35a}$$

$$\phi^{(1)} = \sum_{n=0}^{\infty} \varepsilon_n [\phi_{I,n}^{(1)} + \phi_{D,n}^{(1)}] \cos n\theta \tag{3.35b}$$

$$\phi^{(1)} = -\frac{iAg}{\omega} \frac{\cosh k(z+h)}{\cosh kh} \sum_{n=0}^{\infty} \varepsilon_n i^n \left[ J_n(kr) - \frac{J'n(ka)H_n(kr)}{H'_n(ka)} \cos n\theta \right] \tag{3.35c}$$

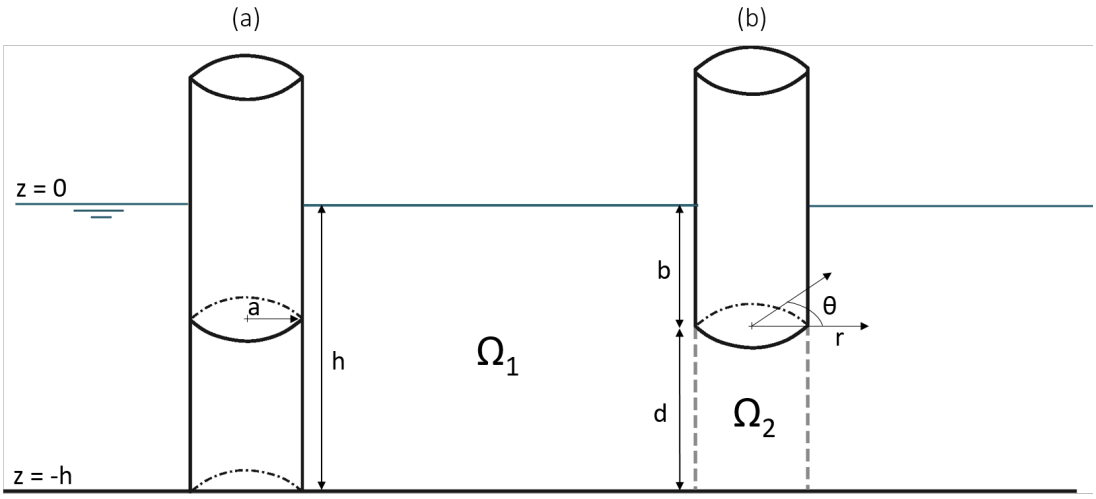


**Figure 3.1:** Vertical cylinder domain geometry (a) bottom-seated, (b) truncated cylinder

Such that the integral of the first-order pressure due to the first-order potential gives

$$F_x^{(1)} = \Re\{\int_0^{2\pi} a \int_{-h}^{0} \phi^{(1)}(a,\theta,z)\,\mathrm{d}z\,\mathrm{d}\theta e^{-i\omega t}\} \tag{3.36a}$$

$$F_x^{(1)} = \Re\{-4\rho\omega a^2 \frac{\tanh(ka)}{(ka)^2}\left(\frac{1}{H_1'(k_0 a)}\right) e^{-i\omega t}\} \tag{3.36b}$$

(3.36c)

Second-order diffraction solution for bottom-fixed vertical cylinder

For the second-order diffraction problem over a fixed vertical cylinder, the simplified boundary integral in Equation 3.19 and the free surface condition in Equation 3.8b can also be expressed in Fourier series (Chau & Eatock Taylor, 1992; Kim & Yue, 1989).

$$Q_D^{(2)} = \sum_{n=0}^{\infty} \varepsilon_n q_n(r)\cos n\theta \tag{3.37}$$

$$2\pi\phi_{D,n}^{(2)} = \int_0^{2\pi} a \int_{-h}^{0} (\frac{\partial \phi_{I,n}^{(2)}}{\partial r} G_n(a,r) + \phi_{D,n}^{(2)} \frac{\partial G_n(a,r)}{\partial r})\,\mathrm{d}\theta\,\mathrm{d}z - \int_a^{\infty} r \int_0^{2\pi} G_n(a,r) q_n(r)\,\mathrm{d}\theta\,\mathrm{d}r \tag{3.38}$$

where the expression for the modal free surface forcing $q_n$ and Green's function $G_n$ are provided in detail in Annex A. The Green's function is constructed based on the added assumption that $\partial G/\partial r = 0$ on $r = a$ (Chau & Eatock Taylor, 1992). This simplifies the boundary value integral by removing the second term on the right-hand side of Equation 3.38. As per (Molin, 1979), the second-order diffraction potential is divided into two parts. The homogen-

eous term, $\phi_{DI}^{(2)}$, that is the solution of the boundary integral problem on the body due to the second-order incident potential and the in-homogeneous term, $\phi_{DD}^{(2)}$, that resolves the boundary integral problem on the body due to the integral of first-order free surface forcing. The equations listed below are the equations published in Huang and Eatock Taylor (1996) with some corrections made from the original publication which contained misprints.

$$\phi_{DI,n}^{(2)}(r,z,\theta) = \sum_{n=0}^{\infty} \varepsilon_n i^n \cos(n\theta) \sum_{m=0}^{\infty} \frac{1}{k_m} \frac{3iA^2\omega}{8} \frac{2kJ_n'(2ka)}{\sin kh^4} \alpha_m \frac{U_n(k_m r)}{U_n(k_m a)} Z_m(k_m,z) Z_m(k_m,0) \tag{3.39}$$

$$\phi_{DD,n}^{(2)}(r,\theta,z) = \sum_{n=0}^{\infty} \varepsilon_n \cos(n\theta) \sum_{m=0}^{\infty} Z_m(0) Z_m(k_m,z) \int_a^{\infty} \xi q_n(\xi) G_{nm}(r,\xi) d\xi \tag{3.40}$$

These potentials can be solved directly by reaching numerical convergence on the eigenfunctions series and the direct integration of the free surface. Once, the potentials are solved, these can be integrated over the hull of the vertical cylinder to obtain the force. These equations have been extended to the bi-chromatic case and therefore can be applied to obtain the full QTFs which has not been attempted here.

Second-order forces on vertical cylinder

The equations published by Huang and Eatock Taylor (1996) for a truncated vertical cylinder provide a solution for the second-order force components from a monochromatic wave train. It also provides an approximation consisting of integrating the potential calculated on the outer domain without accounting for the bottom domain contribution.

The first terms consist of the quadratic forces of the first-order potential equivalent to the terms in Equation 3.25 and 3.26.

$$\begin{aligned}\frac{F_{x1a}^{(2)}}{\rho g a A^2} =& \Re\left\{ \frac{2i}{\pi(ka)^2} \sum_{m=0}^{\infty} \frac{(-1)^n}{H_n'(ka)H_{n+1}'(ka)} \left( \left[ 1 + \frac{sinh(2kh) - sinh(2kd)}{sinh(2kh)} - \frac{2kb}{sinh(2kh)} \right] \frac{n(n+1)}{(ka)^2} \right.\right. \\ & \left.\left. \left[ \frac{sinh(2kh) - sinh(2kd)}{sinh(2kh)} + \frac{2kb}{sinh(2kh)} \right] \right) e^{-2i\omega t} \right\}\end{aligned} \tag{3.41}$$

$$\frac{F_{x1b}^{(2)}}{\rho g a A^2} = \Re\left\{ \frac{2i}{\pi(ka)^2} \sum_{m=0}^{\infty} \frac{(-1)^n}{H_n'(ka)H_{n+1}'(ka)} e^{-2i\omega t} \right\} \tag{3.42}$$

Then the following term consists of the approximated second-order force due to the incident potential, $\phi_I^{(2)}$.

$$\frac{F_{x2I}^{(2)}}{\rho g a A^2} = \Re\left\{ -\frac{3i\pi\tanh(kh)}{4\sinh^4(kh)} J_1(2ka)(\sinh(2kh) - \sinh(2kd))\, e^{-2i\omega t} \right\} \tag{3.43}$$

Finally, the following terms are the forces due to the approximated second-order diffracted potential. The first is the term respecting the homogeneous free surface condition, $\phi_{DI}^{(2)}$ and the second is the term respecting the in-homogeneous free surface condition $\phi_{DD}^{(2)}$.

$$\begin{aligned} \frac{F_{x2DI}^{(2)}}{\rho g a A^2} = \Re\Bigg\{ \int_{-b}^{0} \Bigg\{ \sum_{m=0}^{\infty} \Bigg[ \frac{3i\pi k^2 \tanh(kh)}{\sinh^4(kh)} J_1'(2ka) \frac{i\alpha_m}{k_m} \\ \cdot \frac{U_1(k_m a)}{U_1'(k_m a)} Z_m(k_m, z) Z_m(k_m, 0) \Bigg] \Bigg\} \mathrm{d}z\, e^{-2i\omega t} \Bigg\} \end{aligned} \tag{3.44}$$

$$\begin{aligned} \frac{F_{x2DD}^{(2)}}{\rho g a A^2} = \Re\Bigg\{ \int_{-b}^{0} \Bigg\{ \sum_{m=0}^{\infty} [2\pi i\omega/g \cdot Z_m(k_m, z) Z_m(k_m, 0) \\ \int_a^{\infty} r q_1(r) G_{1m}(a, r)\, \mathrm{d}r \Bigg] \Bigg\} \mathrm{d}z\, e^{-2i\omega t} \Bigg\} \end{aligned} \tag{3.45}$$

Third-order solution for bottom-fixed vertical cylinder

At third-order, Malenica and Molin (1995) published the semi-analytical solution for the third-order force in monochromatic waves based on the same principles. These are too complex to write here and the reader is referred to the published paper Malenica and Molin (1995) and Malenica's thesis Malenica (1994) which is available in French.

Truncated cylinder case

Figure 3.1 shows the representation of vertical cylinders in the fluid domain. As seen in Using Figure 3.1b, a decomposition of the fluid domain between an outer domain, $\Omega_1$, with potential $\phi_1$ and a bottom domain, $\Omega_2$, with a potential $\phi_2$ is used to solve the case of the truncated cylinder. The basis of this method is to find the solutions to the exterior and interior potential such as:

**Boundary condition: Domain decomposition**

$$\frac{\partial \phi_1^{(n)}}{\partial r} = \begin{cases} 0 & r = a, -b \leq z \leq 0 \\ \frac{\partial \phi_2^{(n)}}{\partial r} & r = a, -h \leq z \leq -b \end{cases} \tag{3.46a}$$

$$\phi_1^{(n)} = \phi_2^{(n)} \; r = a, -h \leq z \leq -b \tag{3.46b}$$

The total potential in the exterior region,$\Omega_1$, is then written as the sum of the following terms.

$$\phi_1^{(p)} = \phi_I^{(p)} + \phi_{D,1}^{(p)} + \phi_{D,2}^{(p)} \tag{3.47}$$

$$\phi_1^{(p)} = \phi_0^{(p)} + \phi_{D,2}^{(p)} \tag{3.48}$$

where $\phi_0^{(p)}$ corresponds to the case of a bottom-seated vertical cylinder, and $\phi_{D,2}^{(p)}$ is the correction due to the presence of the interior domain potential, $\phi_2^{(p)}$. The approach then assumes that the relation defined in Equation A.38b between the two potentials at $r = a$ can be expressed as follows.

$$\phi_2^{(p)}(a,z) = \phi_0^{(p)}(a,z) + \phi_{D,2}^{(p)}(a,z) \tag{3.49a}$$

$$\sum_{n=0}^{\infty} \varepsilon_n \phi_{2,n}^{(p)}(a,z)\cos n\theta = \sum_{n=0}^{\infty} \varepsilon_n \left[\phi_{0,n}^{(p)}(a,z) + \phi_{D,2,n}^{(p)}(a,z)\cos n\theta\right] \tag{3.49b}$$

which for each Fourier mode $n$ gives the following relation

$$\sum_{m=0}^{\infty} A_{mn}^{(p)} V_n(\lambda_m a)\cos(\lambda_m(z+h)) = \phi_{0,n}^{(p)}(a,z) + \sum_{j=0}^{\infty} B_{jn} \frac{U_n(k_j a)}{U_n'(k_j a)} Z_j(k_j, z) \tag{3.50}$$

where $A_{mn}$ and $B_{jn}$ are potential coefficients which are found by solving the boundary condition of the domain decomposition. Annex A provides detail on the semi-analytical resolution of the diffraction problems using domain decomposition. The end force on a truncated cylinder is found by integrating the interior domain potential pressure directly on the circular end of the cylinder which gives for the first and second-order potential:

$$F_z^{(1)} = \Re\{2i\omega\pi\rho e^{-i\omega t}\left[\frac{A_{00}^{(1)}}{4}a^2 + \sum_{m=1}^{\infty} \frac{A_{00}^{(1)} a(-1)^m I_1(\lambda_m a)}{\lambda_m I_0(\lambda_m a)}\right]\} \tag{3.51}$$

$$F_{z22}^{(2)} = \Re\{4i\omega\pi\rho e^{-i\omega t}\left[\frac{A_{00}^{(2)}}{4}a^2 + \sum_{m=1}^{\infty} \frac{A_{m0}^{(2)} a(-1)^m I_1(\lambda_m a)}{\lambda_m I_0(\lambda_m a)}\right]\} \tag{3.52}$$

And the quadratic force due to the dynamic pressure can be found in the original publication (Huang & Eatock Taylor, 1996).

### 3.2.2 Strip theory approach

Due to the complexity of extending the potential-flow approach to higher orders, several authors have attempted to simplify the wave-body problem by ignoring the free surface scattering by the body. This is done by assuming that the body is infinitely small with regard to the wavelength and considering that radiation effects are negligible. This way, only the incident wave field is considered. The structure is then approximated as an assembly of circular cylinders (although a square section can also be used in some cases). The force is then calculated based on an integration of averaged wave kinematics on the longitudinal discretised cylinder sections (transverse force on strips) and on the exposed cylinder end (axial). These methods are therefore referred to as the slender-body approach and the strip-theory.

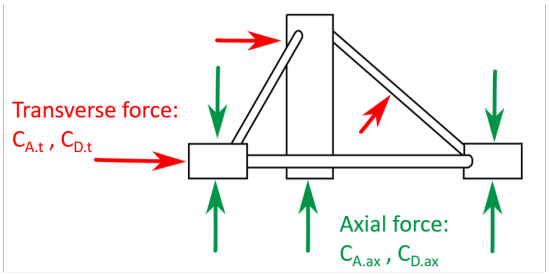


**Figure 3.2:** Strip-theory transverse and axial forces

#### Morison equation

The Morison's equation (Morison et al., 1950) combines the linear inertial force and the quadratic viscous forces in a single formula which for the transverse force per unit length on a stationary circular cylinder is as follows:

$$\mathrm{d}f_x(\mathbf{X},t) = (1+C_{A.t})\rho\pi a^2\dot{u}(\mathbf{X},t) + C_{D.t}\rho a u(\mathbf{X},t)\cdot|u(\mathbf{X},t)| \tag{3.53}$$

and with motion.

$$\mathrm{d}f_x(\mathbf{X},t) = (1+C_{A.t})\rho\pi a^2\dot{u}(\mathbf{X},t) - C_{A.t}\rho\pi a^2\ddot{X} + C_{D.t}\rho a(u(\mathbf{X},t)-\vec{\dot{X}})\cdot|u(\mathbf{X},t)-\vec{\dot{X}}| \tag{3.54}$$

Based on the linear pressure field computed from the incident wave kinematics, the inertial end effect on the exposed base of a vertical cylinder of circular cross-section can also be accounted for as shown on the left term of the equation below and the axial drag effect as shown on the right-hand term:

$$F_z = (1+C_{A.ax})\pi a^2 \rho \frac{\partial \phi_I(t)}{\partial t} + \frac{1}{2} C_{D.ax} \rho \pi a^2 (w(\mathbf{X},t) - \dot{\vec{X}}) |w(\mathbf{X},t) - \dot{\vec{X}}| \tag{3.55}$$

The inertial part of the force is made of an equivalent to the distributed Froude-Krylov force and the body diffraction which is approximated using an added mass coefficient, $C_{A.t}$. Both added mass and drag coefficients are chosen based on empirical data, standard recommendations or calibrated using CFD. It is worth noting that the Morison inertial part provides some high-order forces due to the:

- integration of the force in the oscillating wave crest
- and if using high-order wave kinematics and free surface elevation

**Rainey load model**

Rainey (1989, 1995) and Manners and Rainey (1992) derived based on an energy argument and a slender-body approximation a formula akin to Morison's equation but taking into account the convective acceleration and an axial divergence term. For a circular cylinder in two dimensional flow, two terms cancel from Rainey's original formulation to give out the following equation.

$$F_{xID}(t) = \int_{-b}^{\eta} \rho \pi a^2 \left[ (1+C_{A.t}) \left( \dot{u} + u\frac{\partial u}{\partial x} + w\frac{\partial u}{\partial z} \right) + C_{A.t} u \frac{\partial w}{\partial z} \right] dz \tag{3.56}$$

For a fixed vertical cylinder, the axial divergence term, $u\partial w/\partial z$, cancels out with the term $u\partial u/\partial x$ multiplied by the added mass. This reduces the original formulation further to the following expression leaving only part of the convective acceleration terms on top of the classic Morison's expression.

$$F_{xID}(t) = \int_{-b}^{\eta} \rho \pi a^2 \left[ (1+C_{A.t}) \left( \dot{u} + w\frac{\partial u}{\partial z} \right) + u\frac{\partial u}{\partial x} \right] dz \tag{3.57}$$

On top of the distributed forces, Rainey (1995) derived several point load terms. The first one is generated at the free surface intersection with the cylinder and is due to the uneven distribution of the fluid on the wetted hull. Chaplin et al. (1997) noted that there is a third-order error in this solution in comparison to the FNV method and proposed a corrective term. However as noted by the authors, this correction term is inconsistent with Rainey's theory.

$$F_{xS}(t) = -\frac{\rho \pi a^2}{2} u(t)^2 \frac{\partial \eta}{\partial x} \tag{3.58}$$

The second is a representation of the load distribution around the submerged end of cylinders generating both a vertical and horizontal load component. This approximation is only valid for slender elements for which the pressure distribution around the bar end can be approximated as a point load.

$$F_{xEnd}(t) = \rho \pi a^2 u \cdot w \tag{3.59}$$

$$F_{zEnd}(t) = \rho \pi a^2 (u^2 + v^2) \tag{3.60}$$

A key point in Rainey's (1989; 1995) is that the derivation of his equations is based on an approximation of time-domain potential flow and therefore according to its author, consistent with fully nonlinear wave kinematics. Figure 3.3 below shows the distribution of the forces from a Rainey load model. The reader will note that the crest is made of a linear, a second-order and possibly higher-order components whilst the wave kinematics also include linear and higher-order terms. Therefore the total distributed Rainey loads on a vertical cylinder can be split into its various order components.

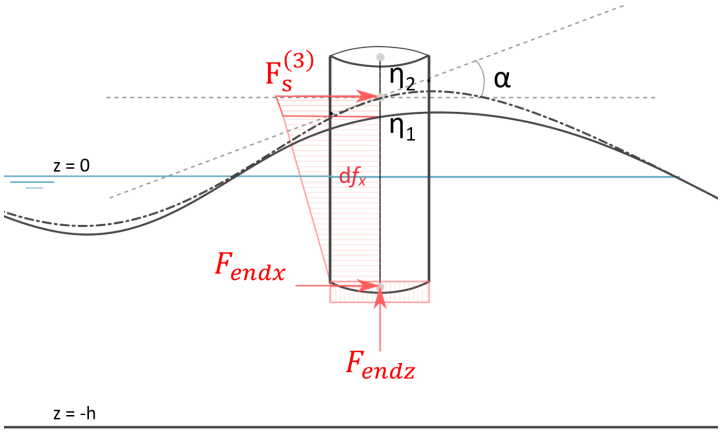


**Figure 3.3:** Diagram of Rainey loads and their point of application.

*First-order loads*

The first-order load is the integration of the Morison inertial load in the still water column using linear wave kinematics.

$$F_{x1}(t) = \int_{-b}^{0} \rho \pi a^2 (1 + C_{A.t}) \frac{\partial u^{(1)}}{\partial t} \mathrm{d}z \tag{3.61}$$

*Second-order loads*

The second-order load due to the first-order terms is generated from the integration of the convective acceleration terms in the still water column $F_{x21a}$, and the integration of the linear wave kinematics in the instantaneous free surface, $F_{x21b}$.

$$F_{x21a}(t) = \int_{-b}^{0} \rho \pi a^2 \left[ (1 + C_{A.t}) w^{(1)} \frac{\partial u^{(1)}}{\partial z} + u^{(1)} \frac{\partial u^{(1)}}{\partial x} \right] \mathrm{d}z \tag{3.62}$$

$$F_{x21b}(t) = \int_{0}^{\eta^{(1)}(t)} \rho \pi a^2 (1 + C_{A.t}) \frac{\partial u^{(1)}}{\partial t} \mathrm{d}z \tag{3.63}$$

and the second-order load due to the second-order kinematics which is limited to the integration of the equivalent Morison equation in the still water column.

$$F_{x22}(t) = \int_{-b}^{0} \rho \pi a^2 (1 + C_{A.t}) \frac{\partial u^{(2)}}{\partial t} \mathrm{d}z \tag{3.64}$$

*Third-order loads*

The third-order loads are generated from the integration of the term due to the linear wave kinematics in the instantaneous first-order free surface;

$$F_{x31a}(t) = \int_{0}^{\eta^{(1)}(t)} \rho \pi a^2 \left[ (1 + C_{A.t}) w^{(1)} \frac{\partial u^{(1)}}{\partial z} + u^{(1)} \frac{\partial u^{(1)}}{\partial x} \right] \mathrm{d}z \tag{3.65}$$

The integration of the first-order kinematics in the second-order crest, of the second-order wave kinematics in the first-order crest and the interactions between first and second-order kinematics in the still water column;

$$F_{x32a}(t) = \int_{0}^{\eta^{(2)}(t)} \rho \pi a^2 (1 + C_{A.t}) \frac{\partial u^{(1)}}{\partial t} \mathrm{d}z \tag{3.66}$$

$$F_{x32b}(t) = \int_{0}^{\eta^{(1)}(t)} \rho \pi a^2 (1 + C_{A.t}) \frac{\partial u^{(2)}}{\partial t} \mathrm{d}z \tag{3.67}$$

$$\begin{aligned} F_{x32c}(t) = \int_{-b}^{0} \rho \pi a^2 \Bigg[ & (1 + C_{A.t}) w^{(2)} \frac{\partial u^{(1)}}{\partial z} + u^{(2)} \frac{\partial u^{(1)}}{\partial x} \\ & + (1 + C_{A.t}) w^{(1)} \frac{\partial u^{(2)}}{\partial z} + u^{(1)} \frac{\partial u^{(2)}}{\partial x} \Bigg] \mathrm{d}z \end{aligned} \tag{3.68}$$

And finally, the integration of the Froude-Krylov and diffraction term due to the third-order wave kinematics in the still water column.

$$F_{x33}(t) = \int_{-b}^{0} \rho \pi a^2 (1 + C_{A.t}) \frac{\partial u^{(3)}}{\partial t} \mathrm{d}z \tag{3.69}$$

#### FNV load model

At the same time as Rainey, Faltinsen et al. (1995) derived a formula to account for higher-order wave loads on a vertical cylinder in infinite water depth based on a simplified expression of frequency domain potential flow theory keeping with the long-wave approximation. It was later extended for the unidirectional irregular wave case Newman (1996b) and then to the finite water depth case by Kristiansen and Faltinsen (2017) which provide the following equations.

$$\begin{aligned} F_{xID}(t) = \int_{-b}^{\eta} \rho \pi a^2 \Bigg[ \left( \dot{u} + u\frac{\partial u}{\partial x} + w\frac{\partial u}{\partial z} \right) \\ + C_{A.t} \left( \dot{u} + w\frac{\partial u}{\partial z} \right) \Bigg] \mathrm{d}z \end{aligned} \tag{3.70}$$

The equation has the same form as Rainey's equation for a fixed cylinder in 2-dimensional flow although the use of high-order kinematics is inconsistent between the two theories. A nonlinear wave-load term is included to account for the nonlinear contribution of the third-order potential. This non-linear term is calculated by resolving a simplified non-linear potential boundary value problem using the approximated first-order potential solution in the inner domain of the cylinder.

$$F_{x\Psi}(t) = \left[ \rho \pi a^2 \frac{\beta_{FNV}}{g} u^2 \dot{u} \right]_{z=0} \tag{3.71}$$

The coefficient $\beta$ is found in an analytical manner by integrating the inner nonlinear potential over the cylinder length. Based on Newman (1996a) results, the coefficient tends to $\beta = 4$ for cylinders longer than $b/a = 4$. However, Kristiansen and Faltinsen (2017) reports that this value could be overestimated and Milano et al. (2019) proposes to treat it more in an empirical manner and calibrate it.

## 3.3 High fidelity CFD models

### 3.3.1 Eulerian Reynolds Averaged Navier-Stokes theory

The Navier-Stokes' equations are obtained by considering the conservation of mass and momentum in a Newtonian fluid and using the respective continuity equations.

$$\frac{\partial \rho}{\partial t} + \vec{\nabla} \rho \vec{u} = 0 \tag{3.72}$$

$$\frac{\partial \rho \vec{u}}{\partial t} + (\vec{\nabla}\vec{u})\rho\vec{u} = -\vec{\nabla}P + \rho g + \vec{\nabla}\left( \mu \left[ \vec{\nabla}\vec{u} + \nabla\vec{u}^T - \frac{2}{3} tr(\vec{\nabla}\vec{u}) Id \right] \right) \tag{3.73}$$

The set of equations can be solved numerically by finite volume methods using a set of 2D or 3D boundary conditions. In Reynold's averaged Navier-Stokes (RANS) model, turbulence is simulated by an eddy viscosity method using Reynold's stress tensor. Such a method is appropriate for maritime applications with flow dominated by gravity waves and with the absence of breaking. In situations with significant unsteady complex flow, such as in problems concerned with vortex-induced-vibration or significant vortex-shedding around sharp-edged elements, Large-Eddy-Simulation (LES) method might be appropriate. In the context of this thesis, which concerns non-breaking waves, RANS is considered a sufficiently accurate model to represent the turbulence effect. The reader is referred to the following book for more information on CFD turbulence model and their range of applications Rodriguez (2019).

### 3.3.2 Neptune_CFD

neptune_CFD is a multi-phase flow finite volume CFD solver which has been developed at EDF R&D (owned with the CEA, Framatome and IRSN). As described in the following studies (Benguigui et al., 2018; Benguigui, Laviéville, & Merigoux, 2019; Benoit, Benguigui, Teles, Robaux, & Peyrard, 2022), the solver uses a pressure correction approach to solve a set of balance equations for each field of a multi-phase flow. This is done by volumetric averaging of the instantaneous balance equations where in a multi-phase flow of total number N, the one property of the k-phase volumetric fraction is:

$$\sum_{k=1}^{N} \alpha_k = 1 \tag{3.74}$$

To describe ocean gravity waves, the problem can be focused on an adiabatic liquid-gas flow hence simplifying the mass and momentum equations for each phase $k$ as follows:

$$\frac{\partial(\alpha_k \rho_k)}{\partial t} + \vec{\nabla} \cdot (\alpha_k \rho_k \vec{U}_k) = 0 \tag{3.75}$$

$$\begin{aligned} &\frac{\partial(\alpha_k \rho_k \vec{U}_k)}{\partial t} + \vec{\nabla} \cdot (\alpha_k \rho_k \vec{U}_k \vec{U}_k) \\ &= -\alpha_k \vec{\nabla} P + \alpha_k \rho_k \vec{g} + \vec{\nabla} \cdot \bar{\bar{\tau}}_k + \sum_{p=1 p \neq k}^{N} \vec{M}_{p \to k} \end{aligned} \tag{3.76}$$

where $\rho_k$ is the density, $\vec{U}_k$ is the flow velocity vector of phase $k$, $\tau_k$ is the Reynold's stress tensor of phase $k$, $P$ is the pressure and $\vec{M}_{p \to k}$ is the momentum transfer from phase $p$ to phase $k$.

**Wave generation**

To model ocean waves, the relaxation zone method is used through the imposition of a surface elevation and a wave velocity profile at the inlet boundary. In this thesis, the incident wave condition is determined as follows:

- Regular waves: Stream-Function which determines a nonlinear wave profile in uniform water depth based on a truncated Fourier decomposition of the signal. Associated elevation and kinematics in the water column are applied at the inlet.
- Irregular waves: Linear airy wave theory

In the wave generation zone, a momentum source term is introduced to enforce the incident solution of the free surface and/or velocity profile based on the time and spatial coordinates variables. The source term can be decreased linearly or exponentially in the generation zone.

Robaux (2022) has carried out 2D analysis in regular waves of the quality of the free surface generation and its sensitivity to the mesh and time refinement. CFD probe measurements in the working zone were compared against the analytical solutions of the Stream Function which is used to generate the waves. The computed error in the amplitude of the harmonics is plotted in Figure 3.4 as a function of the mesh refinement by the number of cells per wavelength, $N_{cells}$, and the approximate Courant number:

$$C_t = U_c \frac{\Delta t}{\Delta x} \tag{3.77}$$

where $U_c$ is the crest velocity and:

$$\Delta x = N_{cells}/\lambda \tag{3.78}$$

**Floating object definition through the time-space dependent porosity method**

As described in detail in Benguigui et al. (2018, 2019), the structure can be modelled in neptune_cfd using a geometric function or a .stl CAD interpolator to get the value of the time and space-dependent porosity which is 1 in the fluid, 0 in the solid, and between 0 and 1 at the interface. The solver finds the interface cells between the input object geometry and the fluid which are then redefined with smaller elements.

$$\varepsilon(x,t) = 1 - \alpha_s(x,t) \tag{3.79}$$

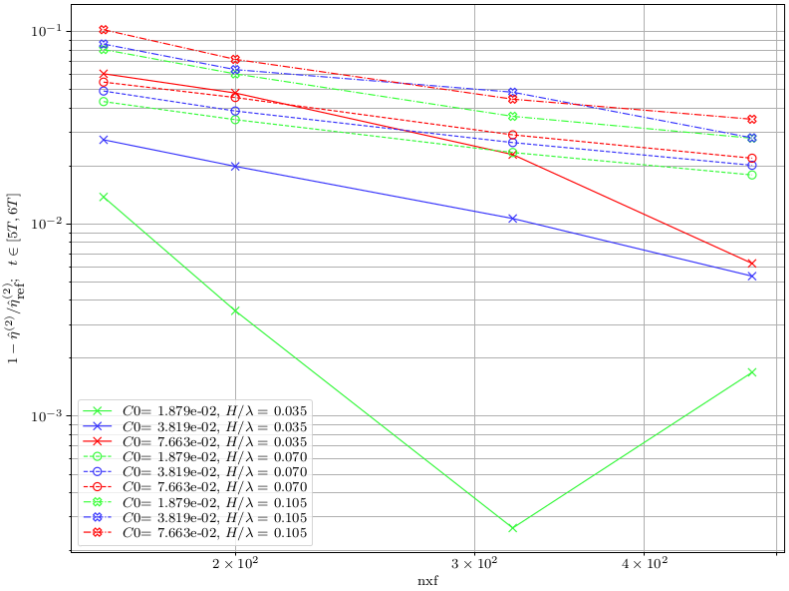


**Figure 3.4:** Convergence of the errors in amplitudes of the second free surface harmonic, $\eta^{(2)}$ as a function of the horizontal refinement of mesh cells (Robaux, 2022)

With $\varepsilon$ being the time and space-dependent porosity and $\alpha_s$ being the volumetric fraction of the solid phase. This then modifies the volumetric fraction balance described in Equation 3.74 as follows.

$$\sum_{k=1}^{N} \alpha_k = \varepsilon(x,t) \tag{3.80}$$

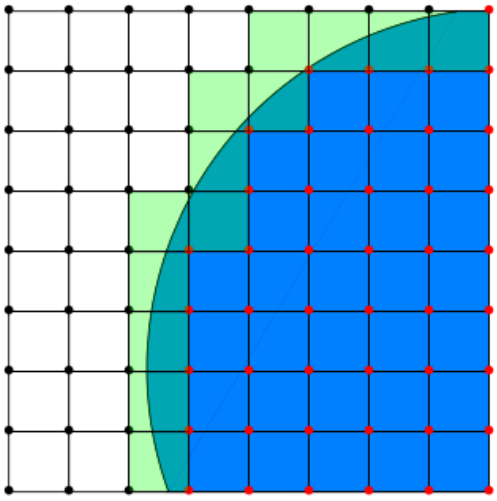

**Figure 3.5:** Computation of porosity interface as shown in Benguigui et al. (2018). Nodes in the solid domain are in red, and those in the fluid domain are in black. Fully solid cells ($\varepsilon(x,t)=0$) are shown in blue, all fully fluid cells in white while the interface is shown in green.

In the fluid-structure interface cells, the wall is reconstructed to take into account its effect on the fluid. Thus, there is no difference between a body-fitted mesh or the use of the present discrete forcing method. For the present application, the forces are computed at the immersed walls, further details can be found in Benguigui et al. (2019). This enables the user to have a single cartesian mesh for the entire fluid-solid domain and impose the solid geometry in the mesh nonexplicitly.

### Example of use

At the time of writing this thesis, various works in the field of hydrodynamics have been carried out by EDF using neptune_cfd. This includes the study of wave impact and run-up on coastal structures (Benoit et al., 2023; Peyrard, 2018; Villefer, 2022), and on the University of Maine academic Volturnus semi-submersible floater Peyrard et al. (2023); Robaux et al. (2022).

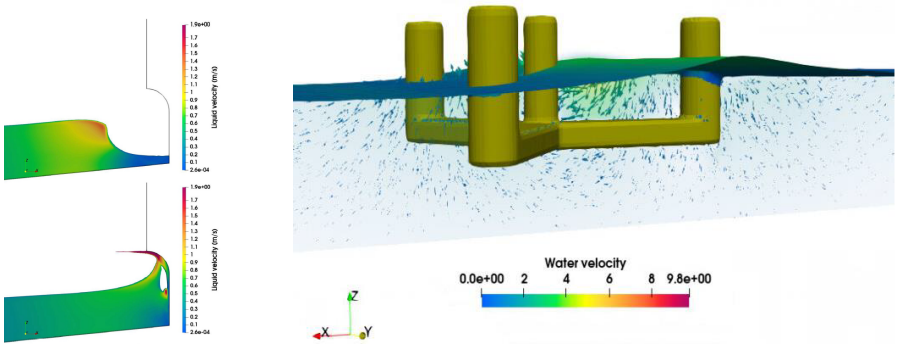


**(a)** **(b)**

**Figure 3.6:** Example of use of neptune_cfd (a) wave impact on a parapet (Benoit et al., 2023), (b) response of FOWT to focused wave (Peyrard et al., 2023)

## 3.4 FOWT-TLP Dynamics

This section provides the basic theoretical background behind the resolution of the dynamic simulation of floating offshore wind turbines in the time domain with aero-hydro-servo-elastic solvers.

### 3.4.1 Reference frame

In studying the hydrodynamics of floating wind platforms, an Eulerian reference frame is typically used. The displacement of the body in 3D space is defined by 6 degrees of freedom (DoFs) as a combination of three translations of the body reference frame from its origin in the global coordinate system and three rotations. These are referred to as surge, sway and heave for the translation along the $x$, $y$, $z$, axis and roll, pitch, and yaw for the rotation around these axes. Figure 3.7 displays the reference frame used in this document. It is worth noting that this entire thesis assumes unidirectional waves and therefore only 3 DoFs are mostly relevant with sway, roll and yaw being negligible motions. In this document, the forces and moments in the same DoFs are referred to by the same name, such as a force in the x direction will be referred to as the surge force.

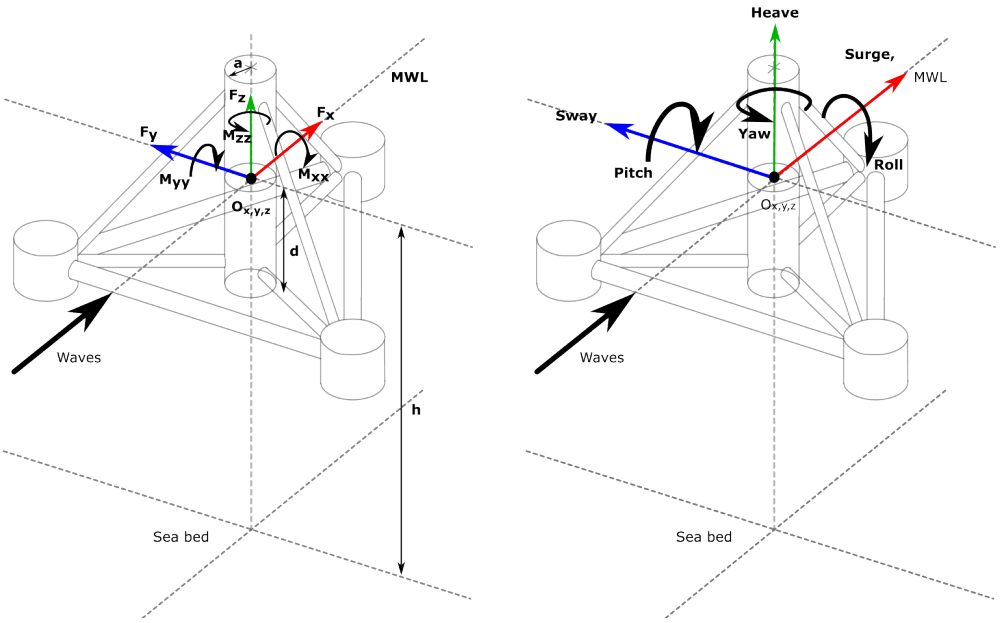


**Figure 3.7:** Reference frame and degrees of freedom for (a) forces; (b) displacements

### 3.4.2 Rigid body dynamic equation

In rigid 3D body dynamic the motion equation is derived from Newton's second law $\sum \vec{F} = \mathbf{M}\vec{\ddot{X}}$ where $\vec{\ddot{X}}$ is the body 6DoF acceleration. When accounting for the external excitation forces, $\vec{F}_e$ which include wave and wind loading, the equation of motion can be written as follows.

$$(\mathbf{M_I} + \mathbf{M_A})\vec{\ddot{X}}(t) + \mathbf{B_R}\vec{\dot{X}}(t) + (\mathbf{K_H} + \mathbf{K_M})X(t) = F_e(t) \tag{3.81}$$

where, $\mathbf{B_R}$ is the damping coefficient due to the body radiation, and $\mathbf{K_H}$ and $\mathbf{K_M}$ the hydrostatic and mooring stiffness matrix. The equation expressed this way is relatively linear since it assumes that the added mass, the radiation damping and both the hydrostatic and stiffness matrix are constant. This model is therefore only applicable to small body motion with negligible radiation-diffraction (transient waves from the body negligible) and where a linear spring-like mooring system remains a valid approximation. Large but slowly varying body motion would likely tend towards frequency-independent radiation, however, the linearisation of a mooring system would likely not hold in such configuration.

To provide a more accurate model, the following have to be accounted for:

- As mentioned in Section 3.2.1, the radiation problem is solved in the frequency domain and the terms become dependent on the frequency of motion of the body, hence requiring a memory "effect" of the body past motion in the time domain
- The hydro-static stiffness cannot be considered linear if the water displacement volume changes non-linearly with the body motion and therefore has to be considered as an external force to be calculated in real-time
- The mooring stiffness cannot be assumed to be linear with important body motion since the stiffness will vary with the instantaneous displacement of the mooring lines. Furthermore, if mooring line deformations are important these have to be resolved structurally.

Therefore accounting for the modifications of the two latter points leads to the following equation with external forces made explicit. The radiation added mass and damping in the *j*th movement of the 6 DoFs, due to forces and moments in the *i*th direction is then written as follows with frequency-dependent terms obtained from the resolution of the potential flow problem (See Section 3.2.1) Molin (2023).

$$\sum_{j=1}^{6}\left[(M_{I,ij} + M_{A,ij}(\omega))\cdot\ddot{X}_j + B_{R,ij}(\omega)\dot{x}_j\right] = F_{M,i}(t) + F_{H,i} + F_{e,i}(t) \tag{3.82a}$$

$$\sum_{j=1}^{6}\left[(M_{I,ij} + M_{A,ij}(\omega))\cdot\ddot{X}_j + B_{R,ij}(\omega)\dot{x}_j\right] = F_{M,i}(t) + F_{H,i}(t) + F_{W,i}(t) + F_{A,i}(t) \tag{3.82b}$$

where $F_{M,i}$, $F_{H,i}$, $F_{W,i}$, $F_{A,i}$ are respectively the restoring mooring force, the restoring hydro-static force, the wave excitation force and aerodynamic excitation force in the $i$th degree of freedom. Here the added mass and radiation damping are defined in the frequency domain. The Cummins' equation Cummins (1962) enables putting the pulsation-dependent radiation effect back into the time domain by the use of an impulse response radiation function (IRRF) which represents the memory-effect of the floater motion and is expressed as a convolution from minus infinity to the present time $t$. In practice, the convolution is carried out over a finite number of periods. This method requires the added mass matrix at the infinite pulsation. The IRRF function is related to the frequency-dependent added mass and radiation damping matrix by equations that are not detailed here but are available in textbooks such as in Molin (2023).

$$\sum_{j=1}^{6}\left[(M_{ij}+M_{aij}(\infty))\cdot\ddot{X}_j+\int_{-\infty}^{t}X_j(\tau)R_{ij}(t-\tau)d\tau\right]=F_{M,i}(t)+F_{H,i}(t)+F_{e,i}(t) \tag{3.83}$$

This is the equation that is solved numerically in the aero-hydro-elastic solver DIEGO using standard iterative numerical schemes such as Euler, classic Runge-Kotta or Newmark methods. At each time step the external forces have to be calculated by individual modules and the motion solved.

- $F_W$, the wave excitation forces are calculated based on models presented in Section 3.2
- $F_M$, the mooring restoring forces are calculated as explained in Section 3.4.3
- $F_H$, the hydro-static restoring forces are calculated based on Archimedes's principle which accounts for the difference between the weight of the floater and its immersed volume
- $F_A$, the aerodynamic excitation forces are calculated based on a set of modules of varying degrees of complexity as seen in 3.4.3

### 3.4.3 Hydro-aero-servo-elastic solver architecture - DIEGO

The structure of the time domain solver used in this thesis is presented in the following diagram. The reader will note the different weak or strong coupling of the various aforementioned modules that generate the external forces. Weak coupling refers to when a module generates an external force based on the motion information from the previous time-step and does not interact directly with the resolution of the motion equation. Strong coupling (red-arrows) means that the module considers the dynamic of the problem solved by the module within the same numerical scheme as the main motion equation. In that sense, weakly-coupled modules (green-arrows) can only react to the body's motion, whereas strongly coupled modules intervene directly in the resolution of the movement.

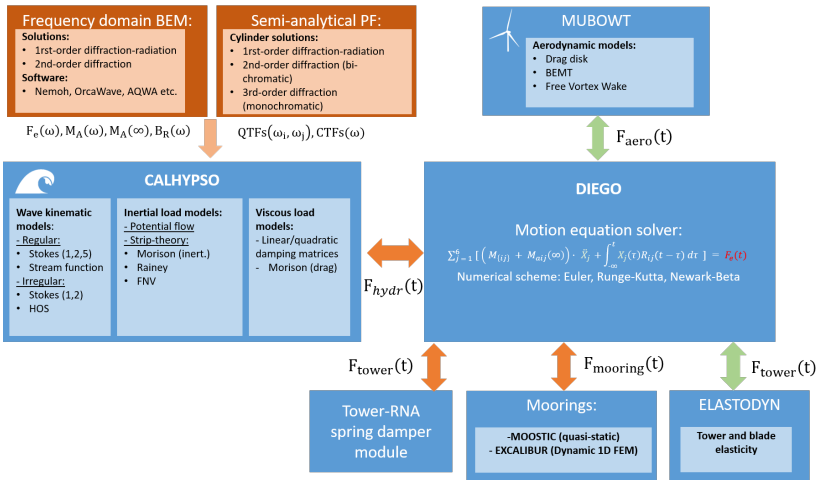


**Figure 3.8:** Schematic of organisation of DIEGO: aero-hydro-servo-elastic time domain solver. Red arrows show strongly-coupled modules and green-arrows weakly-coupled ones

### Aerodynamic

The aerodynamics of floating offshore wind is a complex question which is not considered in detail in this thesis since the high-order hydrodynamic effects are the core of this investigation. However, several experimental cases consider combined wind-wave conditions. In such cases, the aerodynamic load is only considered using a steady wind condition and approximated as a point load. This method reasonably approximates what is achievable experimentally using a thrust actuator. Therefore a simple aerodynamic load model can be used for this work. However, the existing methods available in DIEGO are briefly summarised and the theory behind the simplified model used in this thesis is provided.

Several approaches are available in the industry to model the aerodynamic effects. The simplest method which is the one used in this thesis, consists in approximating the aerodynamic thrust on the wind turbines using the actuator disk model. The basic actuator disk model approximates the rotor as a porous disk and resolves the conservation of mass in 1D using the momentum theory. The thrust on the wind turbine is found to be proportional to the square of the velocity and the thrust coefficient. In this thesis, a thrust coefficient is calibrated based on the known incoming wind to achieve a desired thrust force at the nacelle.

$$F_T = 2\rho C_T A_D U_I^2 \tag{3.84}$$

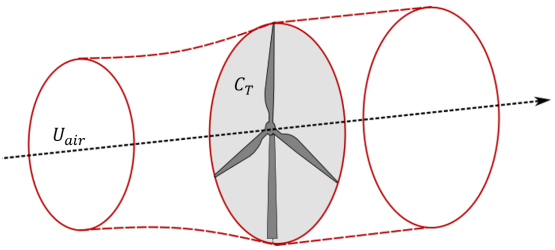


**Figure 3.9:** Schematic of the simplified aerodynamic load model

More complex methodologies exist to model the wind with a higher level of fidelity. The actuator disk model can be solved by taking into account individual blades through the blade element theory. This approach is referred to as Blade Element Momentum Theory or BEMT and is very popular for resolving aerodynamics with more fidelity and computational efficiency. More details on these methodologies are available in Burton, Jenkins, Sharpe, and Bossanyi (2011). Vortex methods using lifting lines also exist which resolve the near wake effect. It is recognised that while their interest is not necessarily crucial in the framework of this particular research project, some aerodynamic and turbine effects are expected to influence the high-frequency response such as the torque oscillation due to the three blades as noted in Wehmeyer et al. (2013). However, these are complex to reproduce experimentally and it has not been attempted within the framework of this project.

#### Hydrodynamics

The hydrodynamic module of DIEGO, CALHYPSO, generates the incident wave field based on a range of theories which are presented in Section 3.1 of this chapter. From the wave-field linear components, the module can calculate the force via the potential flow force transfer functions. The other option is to integrate the strip-theory forces directly based on the instantaneous wave kinematics computed using linear or non-linear theories. The structure is then idealised as an assembly of cylinders which are discretised into equal length segments based on a discretisation parameter. The wave kinematics are calculated at each node and forces are integrated over the discretisation length assigned to each node. At the free surface, this length is reduced based on the instantaneous position of the free surface relative to the closest surrounding node. As seen in Section 3.2.1 this ultimately leads to high-order loads being generated even when using a simple Morison equation and a first-order wave theory.

The dynamic response is then calculated based on the Cummins equation, using either the frequency-dependent added mass and radiation damping matrices from a potential flow solution, or, a simple added mass coefficient if using a full strip-theory approach.

**Mooring dynamics**

The equation of the 6DoF mooring stiffness in the static case can be found in Milano (2021). In DIEGO the mooring module contains a fully linear approach, a quasi-static approach and a dynamic approach. This section will focus on presenting the fully dynamic module, EX-CALIBUR, which is based on the 1D Finite Element Method (FEM) and resolves both the inertial effect due to the displacement of the line and its deformation.

The mooring lines are modelled as an assembly of links with a sectional area $s_a$, the material Young's modulus $E$, and a material density $\rho_l$. Links are then represented on the lump mass elements. The displacement and deformation of the line elements induced by the restoring force opposing the body motion are resolved within the framework of a dynamic motion equation. Only axial and shear stiffness are resolved in this thesis based on the assumption that for TLP pre-tensioned lines, bending effects can be neglected. A Newton scheme is then adopted to equate the external loads (Morison forces) to the internal loads: the inertial effects and internal stiffness due to the imposed displacement, velocity and acceleration computed in the dynamic equation of the floater hydrodynamics.

**Tower elasticity**

As mentioned in the literature, the structural elasticity of the turbine tower is an important factor to take into account in FOWT-TLPs dynamic simulation. For this purpose, engineers have several options from a simple mass-spring-damper system to resolving the dynamic equation using 1D Euler beam or even 1D FEM. In this thesis, a simple approach consisting of modelling the tower-nacelle as a lumped mass connected to the floater by a spring-damper system is adopted. This is due to several considerations. First, this is to limit the complexity of the numerical model and avoid longer calculation time. Secondly, this allows for a strong coupling between tower dynamics, hydrodynamics and moorings dynamics in the architecture of DIEGO which was not yet the case with more complex structural modelling options. However, one of the downsides is that the rotor inertia is approximated and blended within the RNA as a point mass. The schematic of the tower structural model used in DIEGO is shown below. The tower-nacelle structural problem is solved by a Newmark algorithm that is solved in parallel to the main hydro-mooring-aero problem.

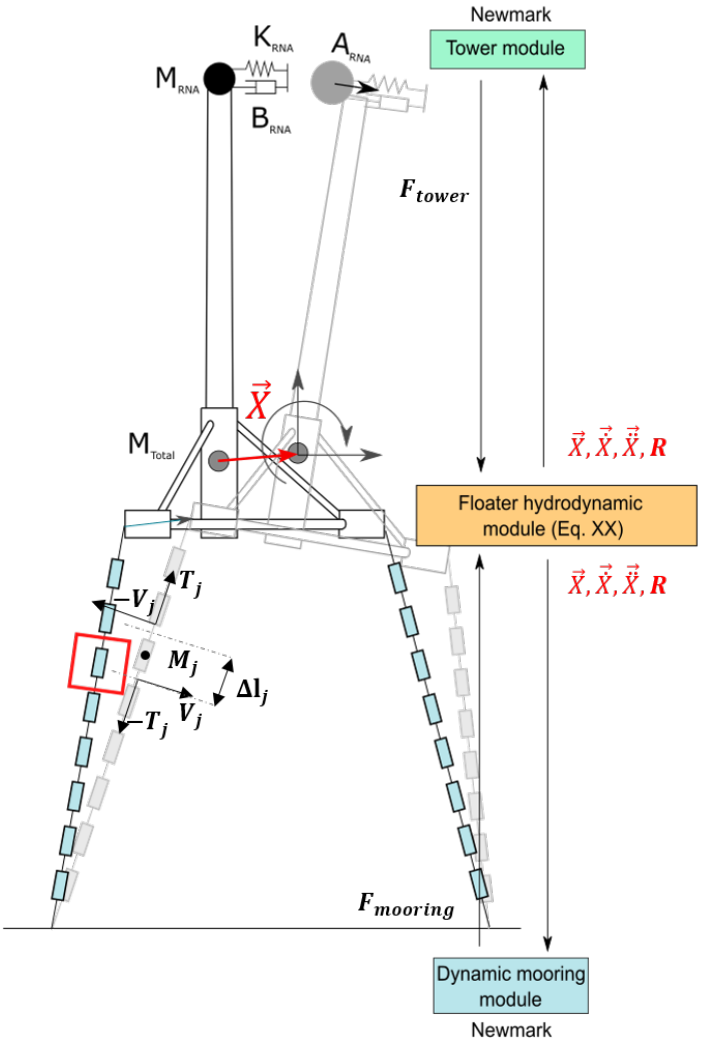


**Figure 3.10:** Schematic of tower elasticity (shown with nacelle spring) and mooring coupling with floater hydrodynamics as used in DIEGO

### Structural damping

In structural dynamics, the energy dissipation due to internal material effects is modelled using linear damping. This is usually done by ascribing a damping ratio, which is a damping proportional to the critical damping. A popular method for its mathematical convenience Orcina (2023) is to use a Rayleigh damping approach which provides a function to assign the damping ratio for each degree of freedom based on a linear relationship on both mass and stiffness of the system in that DoF. This linear relationship with damping, $\mathbf{C}$, is defined by the empirical coefficients $\alpha$ and $\beta$.

$$\mathbf{C} = (\alpha\mathbf{M} + \beta\mathbf{K}) \tag{3.85}$$

$$\zeta = \frac{1}{2}(\alpha \frac{1}{\omega} + \beta \omega) \tag{3.86}$$

In this thesis, both coefficients are kept equal which allows for a damping ratio that remains relatively within the same order of magnitude across the range of frequencies which are close to the natural mode of the structural system (See Figure 3.11). Furthermore, the tower elasticity and its damping will not influence the low-frequency rigid-body modes of surge and yaw.

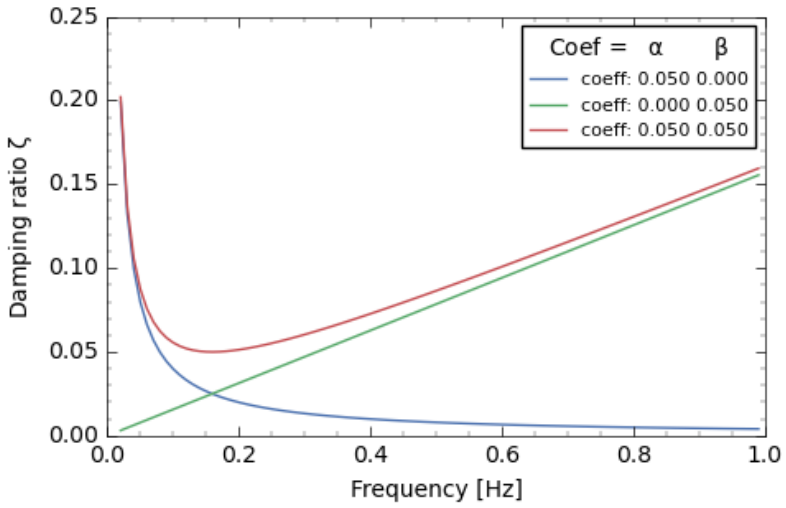


**Figure 3.11:** Example of Rayleigh damping

## 3.5 Experimental modelling

On top of the numerical modelling of floating wind systems, this thesis is also concerned with experimental methods to replicate such systems in tank testing facilities. Therefore, the following section provides some necessary theoretical and quantitative background on the experimental work carried out in EDF's facilities.

### 3.5.1 Scaling laws

Hydrodynamic similarity between full-scale and experimental models scale is achieved by keeping the non-dimensional Froude number constant. Some essential Froude scaling coefficients are functions of, $\lambda$ the length scale, and $\rho_w/\rho_{ws}$ the ratio of tank water facility density over sea water density, are briefly reminded to the reader.

| Variable | Scaling coefficient |
|---|---|
| Distance | $\lambda$ |
| Speed | $\lambda^{0.5}$ |
| Acceleration | 1 |
| Time | $\lambda^{0.5}$ |
| Mass | $\lambda^3 \rho_w / \rho_{ws}$ |
| Force | $\lambda^3 \rho_w / \rho_{ws}$ |

**Table 3.1:** Froude scaling coefficients

### 3.5.2 Tank test wave analysis

#### Tank test wave making

Wavemakers generate waves based on displacing water by mechanical action. This can be done using a piston, paddle or plunger actuator. The amplitude of displacement required to achieve a desired wave is calculated based on frequency domain potential flow theory. In this thesis, a first-order piston wavemaker is utilised with its motion amplitude dictated by linear transfer functions whose solutions were published by Fontanet (1961). The principle is the same as for a floating body and the potential solution is decomposed in the frequency domain and resolved. The required amplitude of the piston motion is then written in the form of a linear transfer function.

$$x_{0,i}(\omega_i) = A_i \frac{2k_i h + \sinh 2k_i h}{4 \sinh k_i h} \tag{3.87}$$

Waves generated at the wavemaker represent then the target linear potential. However, as the wave train propagates into the tank it is affected by complex nonlinear wave-wave interactions and dissipation due to the boundary of the tank and in the case of storm events even wave breaking. For these reasons, the wave conditions at the physical model include nonlinear effects which are not accounted for in the generation and hence represent a more nonlinear and realistic sea condition than close to the wavemaker. Notably, one significant nonlinear effect that occurs in deep water condition and which increases with wave steepness is the Benjamin-Feir instability (Benjamin & Feir, 1967). For a monochromatic wave train generated over a long relative distance to the wavelength and/or with a strong noise from the wavemaker, this effect can lead to significant modulation of the wave group and in some cases focusing event and wave breaking (Molin, 2023). This effect represents a limit for regular wave generation in this thesis. In irregular waves, it tends to modify the spectrum shape (Canard, Ducrozet, & Bouscasse, 2022; Molin, 2023). As for energy dissipative effects in a wave flume, Canard et al. (2022) showed that in non-breaking wave conditions, most losses were due to viscous interactions with the boundary wall. The wave condition at the position of the model therefore has to be measured and calibrated prior to the physical model tests as recommended by the ITTC (2017).

**Wave reflection**

Tank testing flumes absorb incoming waves using an absorbing beach. However, a certain amount of energy is reflected back and has to be quantified. The incident wave train and the reflected wave train are identified by measuring the signal between several probes. Goda and Suzuki (1976) proposed a two-point method. However, Mansard and Funke (1980) discussed the limitation of this approach due to the single probe spacing and proposed a least-square approach using a series of probes with non-regular spacing. The components are extracted on each probe using FFT and assuming a linear propagation theory. The wave elevation at each probe with distance $X_j$ from the wave-maker ($X_0$) and distance $X_{Rj}$ from the reflecting beach, can be expressed as the sum of all incident components and the sum of all reflected components.

$$\begin{aligned}\eta_{pj}(t) = &\sum_{i=1}^{N} A_{Ii}\sin(-\omega_i t + k_i(X_0 + X_j) + \Phi_i) \\ &+ \sum_{i=1}^{N} A_{Ri}\sin(-\omega_i t + k_i(X_0 + 2X_{R0} - X_j) + \Phi_i + \Theta_i)\end{aligned} \tag{3.88}$$

In the frequency domain, this can be written for each probe based on the reference phase for both incident and reflected:

$$Z_{Ii} = A_{Ii}\exp(ik_i X_0 + i\Psi_i) \tag{3.89}$$

$$Z_{Ri} = A_{Ri}\exp(ik_i(X_0 + 2X_{R0}) + i(\Psi_i + \Theta_i)) \tag{3.90}$$

leading to the following expression:

$$\eta_{pj}(\omega) = \sum_{i=1}^{N}[Z_{Ii}\exp(ik_i X_j) + Z_{Ri}\exp(-ik_i X_j k_i)] \tag{3.91}$$

At each probe, the error between the reconstructed incident and reflected frequency component and the FFT component measured at the probe, $B_{j,i}$, is expressed as follows.

$$\varepsilon_{j,i} = Z_{Ii}\exp(ik_iX_j) + Z_{Ri}\exp(-ik_iX_j) - B_{j,i} \tag{3.92}$$

A least square method is then applied to find the value of $Z_I$ and $Z_R$ that minimises the error at each probe. This method is adopted by the wave-maker software and used in this thesis to analyse the proportion of wave reflection.

#### Parasitic waves

As seen in the second-order wave theory, bound harmonics travel with the fundamental wave packet. Wave generated experimentally with a linear potential flow theory, as is the case with the wavemaker used in this thesis, generates spurious free waves also called parasitic harmonics (Schäffer, 1996). These free harmonics are especially problematic for the accurate representation of regular waves. For irregular sea-states, their effects can be considered as statistically correct. In deep water, these travel at half the velocity of the fundamental wave and therefore can be avoided by taking only the first periods of a wave packet Kristiansen and Faltinsen (2017). Huseby and Grue (2000) proposed to measure the second-harmonic by a two-point method as per Goda and Suzuki (1976) and cancel it with an opposite signal. The method is based on a similar principle as for the reflected wave presented above with the reflected component being replaced by a free harmonic double frequency component verifying the dispersion relation $(2\omega_i)^2 = gk_{2,i}\tanh k_{2,i}h$.

$$\begin{aligned}\eta_{pj}(t) = &\sum_{i=1}^{N} A_{Ii}\sin(-\omega_i t + k_i(X_0+X_j) + \Phi_i) \\ &+ \sum_{i=1}^{N} A_{Pi}\sin(-2\omega_i t + k_{2,i}(X_0+X_j) + \Phi_i)\end{aligned} \tag{3.93}$$

Schäffer (1996) developed a second-order wave-maker theory to account for the cancellation of spurious waves in the generation. Due to limited access to the back-end software of the wave-maker used for this thesis, the first method is applied for regular waves.

### 3.5.3 Hybrid coupled wind-wave testing

As explained in the literature background, several methods exist to carry out coupled wind-wave tank testing for FOWT. The system that is of interest for this thesis is the hybrid method using the software-in-the-loop (SIL) methodology. Although SIL was not implemented, an actuator is used in this thesis to generate constant wind loads and the basis from which to build a SIL system has been put in place. Therefore it is important to remind the reader of

its principles. The diagram below in Figure 3.12 displays the hybrid system that is typically put in place which consists of controlling the thrust of the brushless motor based on a numerical simulation of the wind turbine which itself can be fed with the instantaneous displacement, velocities and acceleration at the RNA measured by the instruments on the physical model. As discussed in Chabaud, Steen, and Skjetne (2013), the thrust actuator requires a feedback loop which uses an inner time-step. This inner time step must be much lower than the common time-step in order to control the force actuation within one time-step using the servo-sensors and controller. This inner time step should be as small as possible. Therefore, this requirement defines that the acquisition rate of the system should be as high as possible. In Chabaud et al. (2013) an inner time step, 100 times lower than the common time step is used.

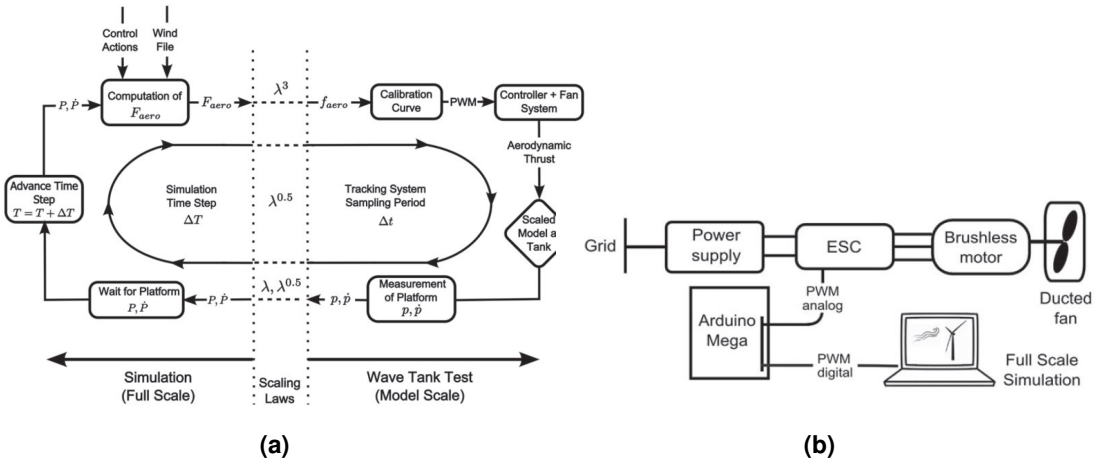


**Figure 3.12:** Software-in-the-loop (SIL) principles (Azcona et al., 2019): (a) method diagram; (b) proposed actuator control

Advantages of the hybrid method, as highlighted in Azcona et al. (2019), is that the virtual rotor allows simulation of rotor control strategies, simulation with realistic turbulent wind and gust which are complex and costly to do with the so-called "full approach" using both hydrodynamic and aerodynamic physical models. However, one inconvenience of that method is that, if a single actuator is used, a single force is generated to represent both thrust and drag in a fixed direction. Such actuation therefore is limited to fixed rotor azimuth and therefore relatively fixed wind direction. In the idling case, with no thrust dominating the aerodynamic forces and drag on the floater and tower becoming significant, the point of application of the aerodynamic force will not be correct. Simulating a realistic idling case with wind above cut-out speed might therefore require some adjustments. Furthermore, considering only the horizontal component does neglect other effects such as rotor torque, gyroscopic force and aerodynamic moments on the response which have been investigated by Bachynski, Chabaud, and Sauder (2015). This method can be improved by increasing the number and direction of actuators and by implementing more advanced actuation control leading to increased

| | DTU-10 MW | |
|---|---|---|
| Wind regime | IEC Class 1A | |
| Rotor orientation | Clockwise rotation , Upwind | |
| Control | Variable Speed, Collective Pitch | |
| Cut-in wind speed | 4 | m/s |
| Cut-out wind speed | 25 | m/s |
| Rated wind speed | 11.4 | m/s |
| Rated power | 10 | MW |
| Number of blades | 3 | |
| Rotor diameter | 178.3 | m |
| Hub diameter | 5.6 | m |
| Hub height | 119.0 | m |
| Minimum rotor speed | 6.0 | rpm |
| Maximum rotor speed | 9.6 | rpm |
| Rotor mass | 227,962 | kg |
| Nacelle mass | 446,036 | kg |
| Tower mass | 628,442 | kg |
| Tower side-side mode | 0.25 | Hz |

**Table 3.2:** Characteristics of the DTU-10 MW (Bak et al., 2013) with tower height and mass modified by Milano (2021)

complexities in designing the system. However, in contrast with Bachynski et al. (2015), the motions considered here are mostly hydrodynamic, therefore the non-thrust aerodynamic forces could be assumed to be negligible. Other constraints such as the frequency bandwidth of actuators Gueydon et al. (2020) are considered in the choice of data acquisition and control system and will be investigated as part of the experimental set-up in Chapter 6.

## 3.6 Academic EDF-TLP floater

### 3.6.1 DTU 10MW

The academic reference wind 10 MW turbine of the Technical University of Denmark (DTU 10-MW) was developed by the Wind Energy research group as part of the Light Rotor project in collaboration with Vestas (Bak et al., 2013). Whilst the original research aim of the project focused on the optimisation of blades to achieve lighter rotors (Bak et al., 2012), the conception of a whole reference wind turbine system (RWT) including supporting tower was carried out using standard practices. The wind turbine is classified as offshore with IEC class 1A. The DTU 10-MW has been used in a variety of studies (Laugesen & Hansen, 2015; Madsen et al., 2020; Milano, 2021; Milano et al., 2019; Pegalajar-Jurado et al., 2017). Details on the geometry and design characteristics of the RWT are provided in Table 3.2 and plots of the main aerodynamic properties are shown in Figure 3.13

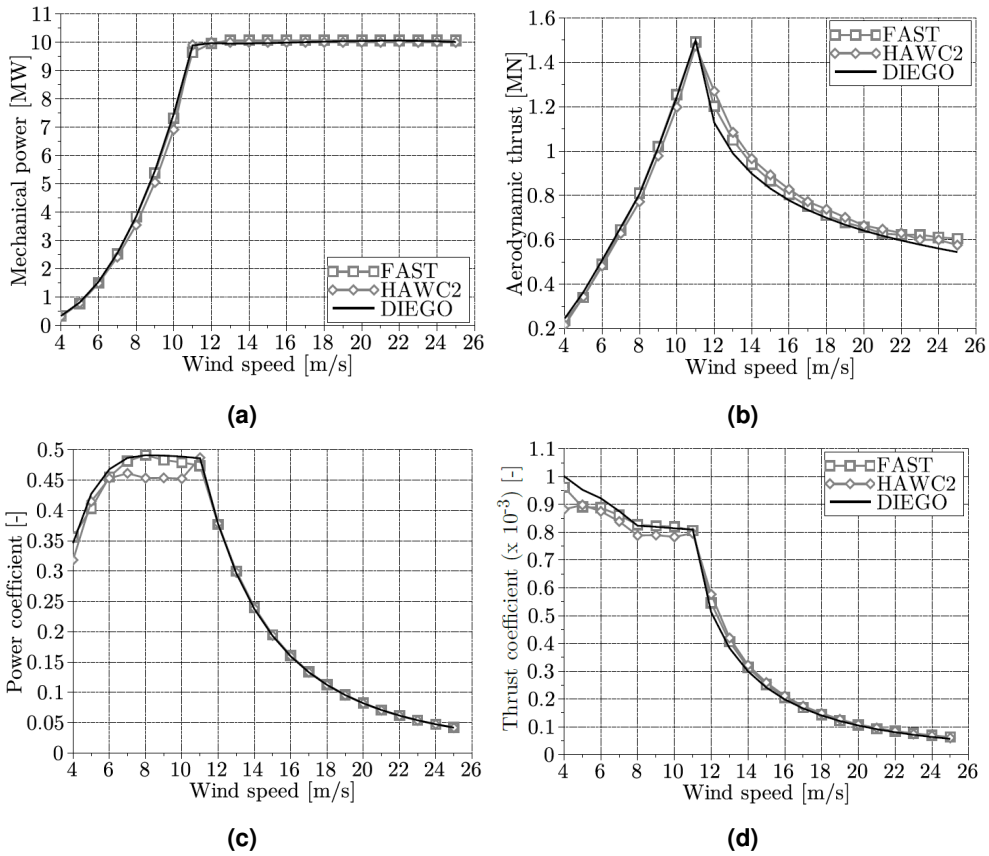


**Figure 3.13:** Aerodynamic characteristics of the DTU 10-MW per Milano (2021) based om Bak et al. (2013); Laugesen and Hansen (2015)

### 3.6.2 EDF-TLP substructure

As seen in Figure 3.14 as well as in the reference frame diagram of Figure 3.7, the EDF academic TLP prototype takes the form of a tri-floater with a central mast (or transition piece - TP) which is the main surface-piercing element and three side buoys connected by cylindrical bracings of circular cross-sections. The side buoys have been designed to provide stability during towing at which point they are only half submerged. For its moored position, the EDF-TLP is sunk by a further 14m and the side buoys become fully submerged. The main properties of the platform and geometries of its main elements are provided in Table 3.3.

**(a)** **(b)**

**Figure 3.14:** Overview of EDF academic TLP (a) DIEGO numerical model (b) physical model with aesthetic blades (removed in tank testing)

The EDF academic TLP prototype (EDF-TLP) is used in this thesis as a case study on the accuracy of the use of high-frequency load models on complex FOWT-TLPs. The platform was designed at EDF R&D to serve as an experimental physical model of a 10MW FOWT-TLP to test in EDF's tank testing facilities and to demonstrate a concept of TLP floater with good towing stability (Duchet, 2019). The EDF-TLP has also been used as case study in the EngD thesis of Milano (2021). In his work, the EDF-TLP floater served as substructure to demonstrate the feasibility of a numerical prototype of a potential future 10 MW FOWT-TLP pilot farm located in the Gulf of Lion, France.

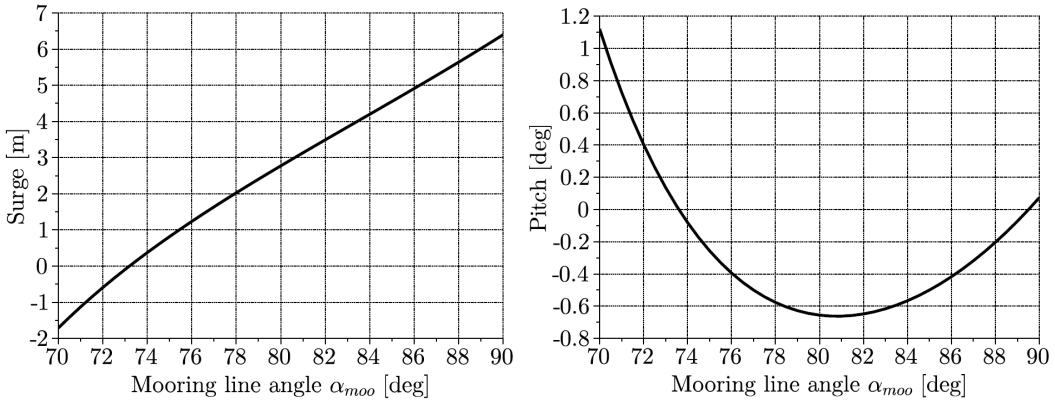


**(a)** **(b)**

**Figure 3.15:** Static displacement of EDF-TLP under maximum turbine thrust as a function of tendon angle (Milano, 2021)

From that study, elements have been re-used such as the mooring line inclination which had been optimised for counter-pitching ability against the maximum wind thrust as displayed in Figure 3.15. Furthermore, Milano (2021) slightly reduced the length of the tower of the DTU 10-MW RWT in order to keep the same hub-height when mounted on the EDF-TLP floater resulting in an increase of the first bending mode frequency. However, whilst Milano (2021) thesis was set to represent a realistic design, the present study concerns a numerical and experimental investigation of the nonlinear dynamic response of the system and in particular ringing. As such, the original design of the mooring system had to slightly be modified due to experimental constraints, notably the stiffness of the mooring lines and the resulting natural frequencies as is explained in Chapter 6. These changes are reflected in Table 3.3.

**Table 3.3:** EDF-TLP 10MW properties and resulting target physical model scale values

| Floater Geometry | | 1:1 prototype | 1:83.3 model | |
|---|---|---|---|---|
| Length | $Loa$ | 60 | 0.72 | [m] |
| Beam | $Lb$ | 60 | 0.72 | [m] |
| Draft | $b$ | 18 | 0.216 | [m] |
| Transition piece: | Ø | 8.8 | 0.106 | [m] |
| | height | 38.0 | 0.456 | [m] |
| Side buoys: | Ø | 11.0 | 0.132 | [m] |
| | height | 8.0 | 0.096 | [m] |
| Bracings A: | Ø | 1.8 | 0.022 | [m] |
| Bracings B: | Ø | 2.0 | 0.024 | [m] |
| Bracings C: | Ø | 3.0 | 0.036 | [m] |
| Mass Properties | | | | |
| Floater mass | $M_{float}$ | 1724.8 | 2.9112x10$^{-3}$ | [t] |
| Tower mass | $M_{tower}$ | 469.2 | 8.3752x10$^{-4}$ | [t] |
| RNA mass | $M_{RNA}$ | 674.0 | 1.1376x10$^{-3}$ | [t] |
| Total mass: | $M_{Total}$ | 2868.15 | 4.841x10$^{-3}$ | [t] |
| Centre of Gravity | CoG | (0.,0.,32.9) | (0.,0.,0.395) | [m] |
| Centre of Buoyancy | CoB | (0.,0.,-12.64) | (0.,0.,-0.152) | [m] |
| Displacement | $V_w$ | 4709.50 | 7.949x10$^{-3}$ | [m$^3$] |
| Mooring lines | | | | |
| Design water depth | $h$ | 100 | 1.2 | [m] |
| Draft of point of attach | $d_{moor}$ | -14.0 | -0.168 | [m] |
| No of lines | $N_{lines}$ | 3 | 3 | [-] |
| Line angle | $\alpha_{moor}$ | 80.65 | 80.65 | [°] |
| Line length (rest) | $l_0$ | 86.9 | 1.043 | [m] |
| Tendon pre-tension | $\tau_0$ | $6.605 \cdot 10^6$ | $11.148$ | [N] |
| Tendon axial stiffness | $E \cdot A_{line}$ | $2.908 \cdot 10^9$ | $4.0889 \cdot 10^5$ | [N] |
| Modes (Anchored - fixed tower) | | | | |
| Surge natural frequency | $f_x$ | 0.03 | 0.27 | [Hz] |
| Heave natural frequency | $f_z$ | 0.53 | 5.02 | [Hz] |
| Pitch natural frequency | $f_{yy.f}$ | 0.33 | 3.01 | [Hz] |
| Modes (Anchored - flexible tower) | | | | |
| Bottom-fixed tower bending mode | $f_{tower}$ | 0.35 | 3.01 | [Hz] |
| Coupled tower fore-aft + pitch mode | $f_{yy.c}$ | 0.25 | 2.82 | [Hz] |

# PART II

# Validation and application of low-fidelity wave-structure interaction models on fixed offshore structures

Chapter 4

# Definition of load models and comparative analysis on cylinders

## 4.1 Introduction

Part II of the thesis is meant to define and investigate in more detail the type of high-order hydrodynamic load models that will be applied in the following chapters on the floating offshore wind EDF-TLP system. These models have been presented in Section 3.2. However, this Chapter is dedicated to undertaking a more in-depth look into how these have been implemented for use in DIEGO as well as describing how 3D meshes are set-up for the CFD NWT. This is followed by a validation comparison of their application on vertical cylinders of circular cross-section. This is because much numerical and experimental work in the literature has been carried out on such structures. As explained in the above chapters, such simple geometry allows for semi-analytical solutions of the potential flow diffraction problem. Furthermore, the FNV strip-theory model has also been developed with vertical cylinder in mind, and more recently extended to finite water depth in the context of ringing on offshore wind mono-piles. Therefore, it appears important to start the comparison between these approaches within the original domain of their application, before applying them to more complex situations.

A portion of the validation case presented below is part of a journal article published under the title "Evaluation of second and third-order wave-structure interaction numerical models for floating offshore wind TLPs" (Rongé, Peyrard, Venugopal, Xiao, et al., 2023). Some of these results have also been presented at the Journée de l'Hydrodynamique 2022, a conference on hydrodynamic research with a short article being published in the proceedings (Rongé, Peyrard, Benoit, Robaux, & Venugopal, 2022). Additional material has been added to the thesis.

## 4.2 Preparing engineering load models

### 4.2.1 Strip theory models

The various strip-theory models presented in Section 3.2.2, had already been mostly implemented in DIEGO's hydrodynamic module, CALHYSPO, prior to this work. As explained in that Section, the distributed forces are calculated in the time-domain based on the instantaneous position of the free surface and related wave kinematics. However, some small modifications were added to the existing code structure:

- When using the FNV method, the velocity gradient terms given in Kristiansen and Faltinsen (2017) and displayed in Equation 3.70 are applied instead of those of Rainey (Equation 3.57) for consistency reason, although these give the same results for vertical cylinders of circular cross-section
- The free surface end effect of Rainey (1995), Equation 3.58 and Figure 3.3, was added to fully extend that approach to third-order

#### Refinement of cylinder at the free surface intersection

The paper by Faltinsen et al. (1995) showed that a significant portion of the third-order inertial force, up to 50% of the total amplitude, is generated at the free surface. For that reason, it is important to understand the way the free surface effect is modelled in DIEGO. As explained in Section 3.2.2, strip-theory cylinders in DIEGO are represented as a series of evenly spaced nodes. Therefore, due to the current code structure, the free surface effect is also represented as a distributed load which is integrated at the discretised section where the free surface intersects. The quality of the interpolation between velocities is then dependent on the discretisation of the cylinders with regard to the wave period and amplitude that is investigated. Assuming wave of constant steepness of $kA = 0.10$ and $0.20$, the sensitivity to cylinder discretisation of the computed total third-order force amplitude is shown in Figure 4.1 below. The discretisation $\mathrm{d}z$ is normalised by the wave number, and the convergence error is expressed based on the amplitude of the force at the highest discretisation value $a_c$.

The convergence error is found to be relatively consistent across periods when discretisation is normalised by the wave number. As expected, this signifies that the smaller the period, the higher the discretisation required. For this study, it is considered that it is important to capture well the sum-frequency forces generated for frequencies within the typical design linear ocean spectrum bandwidth, $5 - 25$ s. Therefore, an error of less than 5% for frequencies in this range is considered acceptable which coincides with a normalised discretisation of $k\,\mathrm{d}z \approx 0.05$ representing a discretisation of the cylinder by strips of $0.25 - 1$ m depending on the period considered.

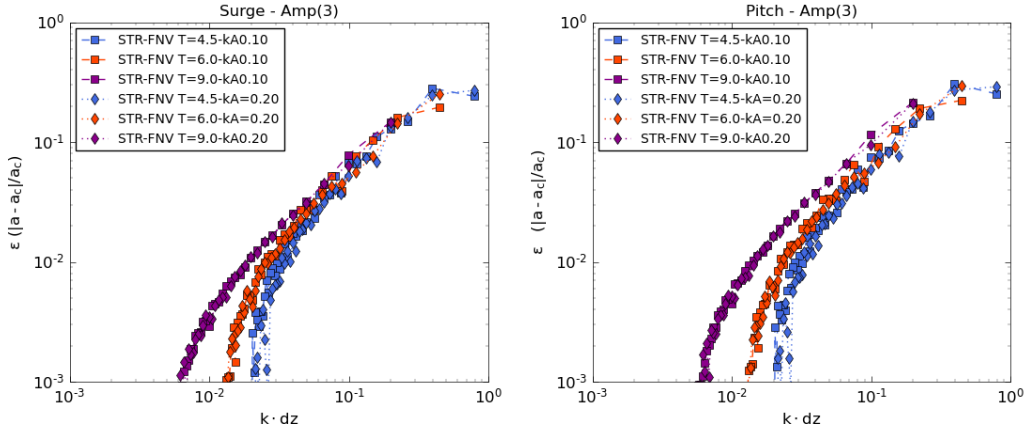


**Figure 4.1:** Convergence of free surface load with cylinder discretisation

### 4.2.2 Potential flow semi-analytical solution

For the purpose of analysing sum-frequency forces on FOWT-TLP floaters, typically taking the form of a main surface piercing vertical cylinder, it is useful to have at disposal a simpler method than BEM solvers to resolve the nonlinear diffraction problem. Hence, the semi-analytical equations presented in Section 3.2.1, are useful tools since they are entirely parametric, do not require a mesh and therefore are more time efficient. Furthermore, each term of the potential solutions is available separately which can be useful for term-to-term comparison with the strip-theory. Finally, second-order solutions are useful for understanding the nonlinear diffraction regime and the importance of the evanescent modes around the fixed structure.

#### Implementation of the second-order semi-analytical formulas for truncated cylinder

The numerical implementation of the Huang & Eatock Taylor semi-analytical formulas was carried out as part of the thesis via a Python script and more details are provided in Section 3.2.1 and Annex A about the theory. The complex element of the script is the truncation of the sum of the vertical eigenfunctions. The approach used in this study is to truncate the sum of vertical eigenfunctions based on the convergence of the free-wave second-order potential $\phi_{DI}$ which can be calculated quickly. More importantly is the approximation of the free surface integral in Equation 3.38 which for second-order case involves the second-order diffracted potential given in Equation 3.40 and repeated here:

$$\phi_{DD}^{(2)}(r,\theta,z) = \sum_{n=0}^{\infty} \varepsilon_n \sum_{m=0}^{\infty} Z_m^{\pm}(0) Z_m^{\pm}(z) \int_a^{\infty} \xi q_n^{\pm}(\xi) G_{nm}^{\pm}(r,\xi) d\xi \tag{4.1}$$

where the detail of the scattered surface forcing term, $q_n^{\pm}(\xi)$ can be found in Annex A of this thesis. A comparison of the code implementation of the evanescent modes of this forcing term against Chau and Eatock Taylor (1992) analytical and approximate solutions is provided below. The current implementation appears to be quite satisfying with regard to the asymptotic solution.

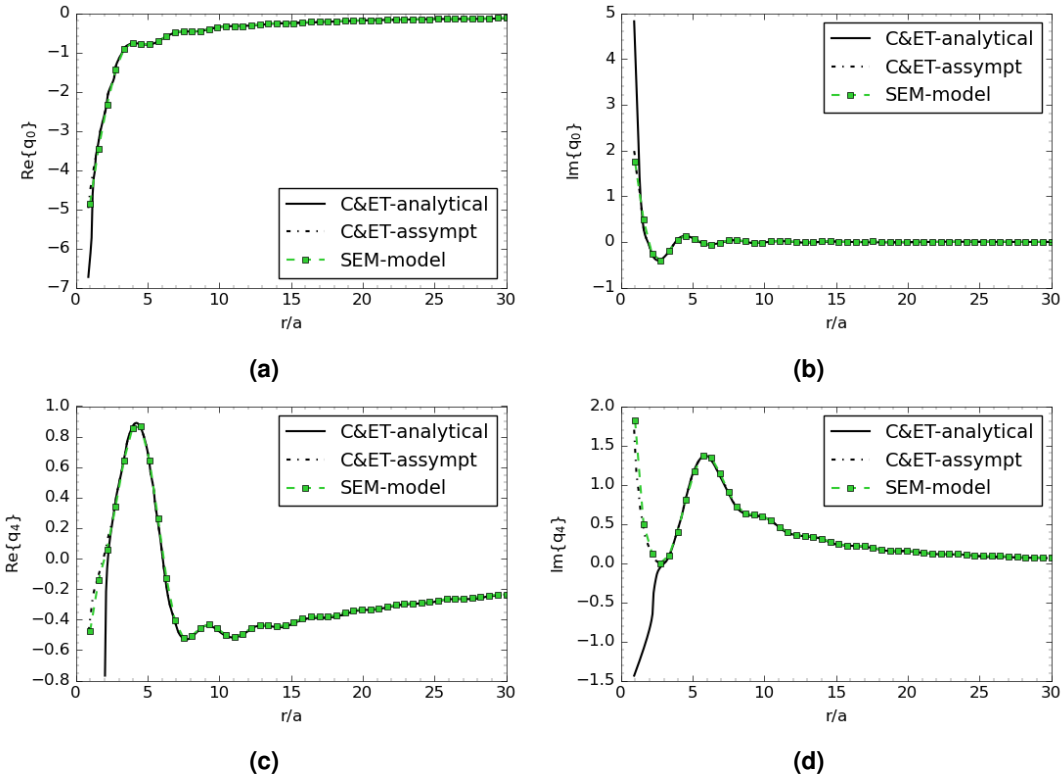


**Figure 4.2:** Fourier modes n=0 and n=4 of the free surface forcing term for the case $ka = 1$, $h/a = 3$ of Chau and Eatock Taylor (1992). The plain black line represents the analytical results, the black dashed line the approximation using the asymptotic form of Hankel functions and in green are the results using the current implementation

For the free surface integral, a Gaussian quadrature method is used to integrate the free surface function with a discretisation step of $\Delta ka = 0.02$. Similarly to Mavrakos, Chatjigeorgiou, and Lentziou (2005), a numerical convergence over a certain distance is sought instead of an analytical approximation of the infinite value of the integral as proposed in Kim & Yue, Chau & Eatock Taylor and Huang & Eatock Taylor Chau and Eatock Taylor (1992); Huang and Eatock Taylor (1996); Kim and Yue (1989). This method appears to lead to satisfying results when compared against the reference case published in Huang and Eatock Taylor (1996)

shown in dotted and dashed black line in Figure 4.3. The thesis implementation of their approximate analytical method shows a very good fit from $ka$ over 0.5. At low $ka$, the approximate method becomes less reliable as the neglected cylinder bottom boundary condition becomes important.

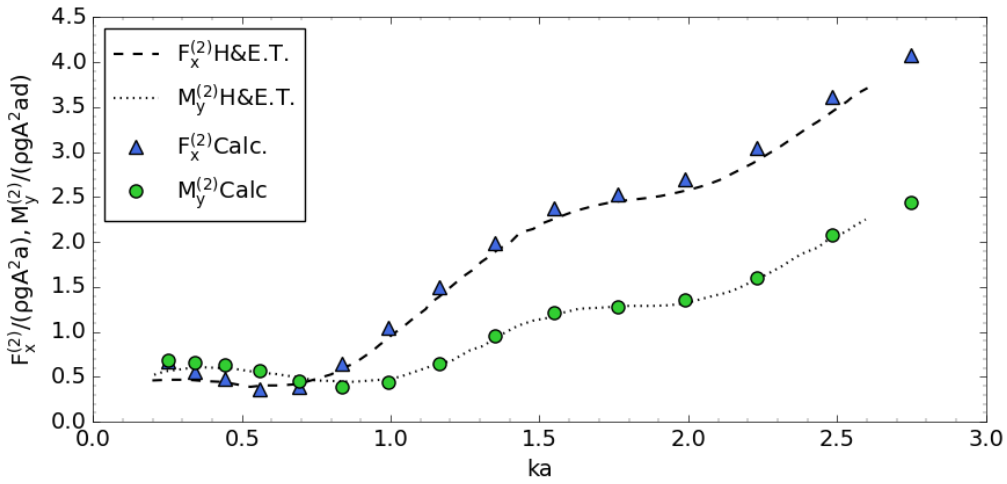


**Figure 4.3:** Comparison of the normalised horizontal force and overturning moment amplitudes over a truncated cylinder for the case $b/a = 3$, $h/a = 20$ calculated by the implementation of the approximate method and the analytical results published in Huang and Eatock Taylor (1996)

## 4.3 Methodology of comparative analysis on cylinders

### 4.3.1 Presentation of cases

Before applying the described numerical models on the academic floating platform, it is important to test the application of the engineering models in conditions that respect the assumption of their original derivation. The first step will be to validate these models against published experimental results by Kristiansen and Faltinsen (2017) which concerns ringing loads on bottom fixed offshore wind structures. The second part of the exercise will focus on a case already closer to a floating offshore wind engineering case, by analysing the high-order forces on a truncated cylinder in intermediate to deep water conditions. The truncated cylinder geometry is based on the central mast of the EDF-TLP floater referred to as the transition piece or TP. In both cases, a Navier Stokes' based CFD Numerical Wave Tank (NWT) is used to provide high-fidelity results for validation. A summary of the load models compared for the two cases is provided in Table 4.1. It is important to note that the nonlinear potential flow approach is presented as transfer functions based on fundamental amplitudes whereas the strip theory approach uses Stream Function for the kinematics.

| DIEGO Models | Elements | Inertial | | Strip theory | Coeff. | | Viscous Drag | Coeff. | Wave theory | |
|---|---|---|---|---|---|---|---|---|---|---|
| | | Potential Flow $F^{(2)}$ | $F^{(3)}$ | $F^{(2)}$ & $F^{(3)}$ | $C_{A,t}$ | $C_{A,ax}$ | $F_D$ | $C_{D,t}$ | $C_{D,ax}$ | $\vec{u}(t), \vec{\dot{u}}(t), \eta(t)$ |
| SEM | KF case | SEM: KY | None | None | - | - | None | - | - | SF |
| FNV | KF case | None | None | FNV | 1.0 | None | None | - | - | SF3 |
| Rainey | KF case | "" | "" | Rainey | 1.0 | None | None | - | - | - |
| SEM | TP | SEM: HET | SEM: MM | None | - | - | None | - | - | - |
| FNV | TP | None | None | FNV | 1.0 | -0.11 | None | - | - | SF3 |
| Rainey | TP | "" | "" | Rainey | 1.0 | -0.11 | None | - | - | SF |
| SEM+D | TP | SEM: HET | SEM: MM | None | - | - | Morison | 1.0 | 2.0 -/SF | |
| FNV+D | TP | None | None | FNV | 1.0 | -0.11 | Morison | 1.0 | - | SF3 |
| Rainey+D | TP | "" | "" | Rainey | 1.0 | -0.11 | Morison | 1.0 | - | SF |

**Table 4.1:** Engineering numerical approaches used on the truncated cylinder. HET refer to Huang and Eatock Taylor (1996); MM refer to Malenica and Molin (1995); Rain. refer to Rainey (1989, 1995); SF refers to Stream Function and SF3 a stream function with kinematics restricted up to the third harmonic (Dean, 1965).

### 4.3.2 Set-up of CFD Numerical Wave Tanks

The numerical wave tank in neptune_cfd is built from a conformal fluid mesh (no hanging nodes) obtained from the open-source mesh generator GMESH (Geuzaine & Remacle, 2009). The fluid domain is split between a working zone in the centre and two relaxation zones, one for generation and one for absorption (See Section 3.3).

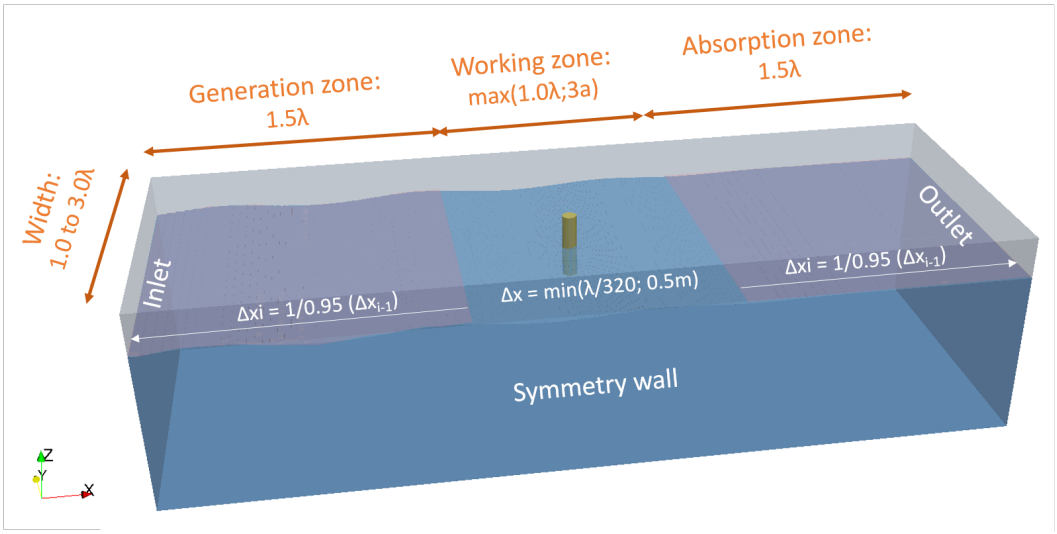


**Figure 4.4:** CFD NWT view

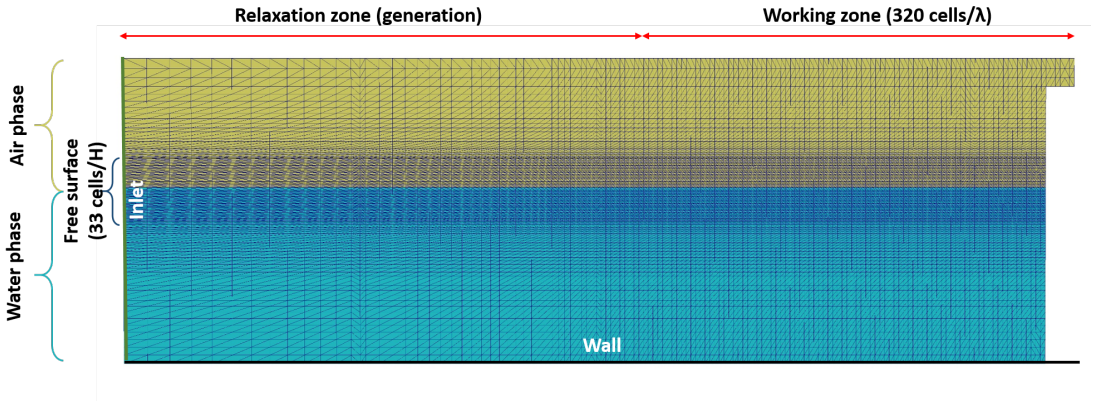


**Figure 4.5:** Mesh elevation cross-section showing: the free surface zone, working zone and the generation relaxation zone with gradual coarsening of the mesh cells towards the inlet boundary

The refinement of the mesh in the working zone is fixed to 320 cells/$\lambda$ in the $x$ direction at minimum based on the sensitivity work carried out by Robaux (2022). This refinement is increased for long wavelength waves where the diameter of any large cylinder is represented by less than 5 cells. The refinement in the $y$ direction is fixed to 200 cells/$\lambda$. Outside of the working zone, a coarser mesh is progressively obtained both in the $x$ and $y$ direction through a geometric sequence. In the $z$ direction, a free surface zone is defined around the mean water level with a height of 1.5 times the incident wave-height, $H$ and is refined with 49 cells. Outside of this zone, the mesh is also coarsened using a geometric progression with the coefficients shown in Table 4.2. Figure 4.5 below displays a cross-section through the middle of the NWT showing the central working zone, the free surface zone and the generation relaxation zone. In terms of length, a relaxation zone of 1.5$\lambda$ is used based on Robaux (2022) and the width of the tank is increased qualitatively with increasing scattering parameters so as to reduce the reflection of diffracted waves on the symmetry walls.

| | Refinement | Geometric progression |
|---|---|---|
| X | min(320 cells/$\lambda$;5 cells/$a$) | 0.95 |
| Y | min(200 cells/$\lambda$;5 cells/$a$) | 0.95 |
| Z | 33 cells/$H$ | 0.91 |

**Table 4.2:** Details of refinement of mesh in the working zone and of coarsening through geometric progression

## 4.4 Validation of load models on fixed offshore wind case

To test the accuracy of our various numerical methods, this study uses one of the bottom-mounted vertical cylinder cases of Kristiansen and Faltinsen (2017) for which experimental data on the second and third-order surge force and pitch moments amplitudes have been published. The case with $h/a = 7.83$, $H/\lambda = 1/25$ received the most attention in the original paper and therefore is considered as a validation case for the numerical tools used in this study. It must be noted that in the present work, the model has been put to a realistic fixed offshore wind turbine monopile scale using the cylinder radius of the EDFTLP-TP, $a = 4.4$ m. Considering that this case concerns steep regular waves in shallow to transitional water depth, these conditions are considered more nonlinear than the condition that will be analysed in floating wind cases which are typically in transitional to deep-water conditions. A snapshot of the CFD NWT is shown in Figure 4.6.

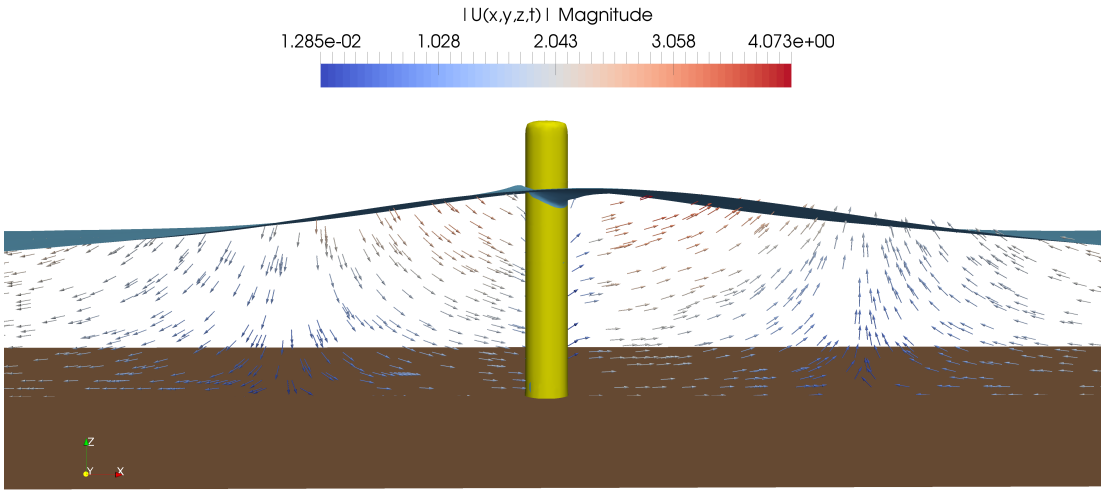


**Figure 4.6:** CFD flume Elevation showing the free surface and velocity vectors in the water column

The strip theory approaches described in the above sections are used using a wave theory based on the Stream Function (See Section 3.1.2). These models are noted DIEGO-FNV and DIEGO-Rainey.

### 4.4.1 Results of normalised force and moments

The comparison of first, second and third-order harmonic amplitudes of the surge force and pitch moment with published results of Kristiansen and Faltinsen (2017) are plotted in Figure 4.7 along with the corresponding approximated points of attack of the surge force, defined as $M_y/F_x h$. It is important to note that in the latter figures, which are normalised by the water depth, a value of one represents a point of application of the total surge force acting at the mean water line, above one in the wave crest, and under one in the water column. For reference, the red dotted line represents the maximum water elevation due to the wave amplitude.

It is observed that the CFD results match very accurately the experimental data for the first, second and third-order surge force and moments. The third-order pitch moment appears to be slightly underestimated although remaining in the lower end of the experimental scatter. It is noted that there appears to be a small error in the original paper of Kristiansen and Faltinsen (2017) where the amplitudes of the first and second-order moments have been multiplied by a factor two which has been corrected in this paper. It is attested by the fact that the published measurements of the approximated point of attack agree with the current results. In terms of the DIEGO results obtained using the two strip-theory approaches, it is surprising to observe that the DIEGO-Rainey model appears to match better the amplitudes of the third-order horizontal experimental and FNV analytical force than the DIEGO-FNV model. This is despite both models predicting the same amplitudes at second-order force. Further analysis focusing on the components of the FNV force provides some answers to this issue in the section below.

The CFD results of the approximated points of attack of both first and second-order surge force in Figures 4.7c and 4.7f seem to agree well with the original measurements. The results of the strip-theory appear to follow the published FNV analytical results. On the other hand, the point of attack of the third-order wave load in Figure 4.7i appears somehow overestimated in the experimental data compared to the CFD results. The NWT results show a similar trend to the experimental measurements with a peak at $ka \approx 0.125$ followed by a steep decline beyond. However, it is observed that the reported experimental points of attack at the peak display a high experimental scatter and values in the range of 120% to 150% of the water depth. This is way above the incident-free surface maximum elevation and suggests significant run-up

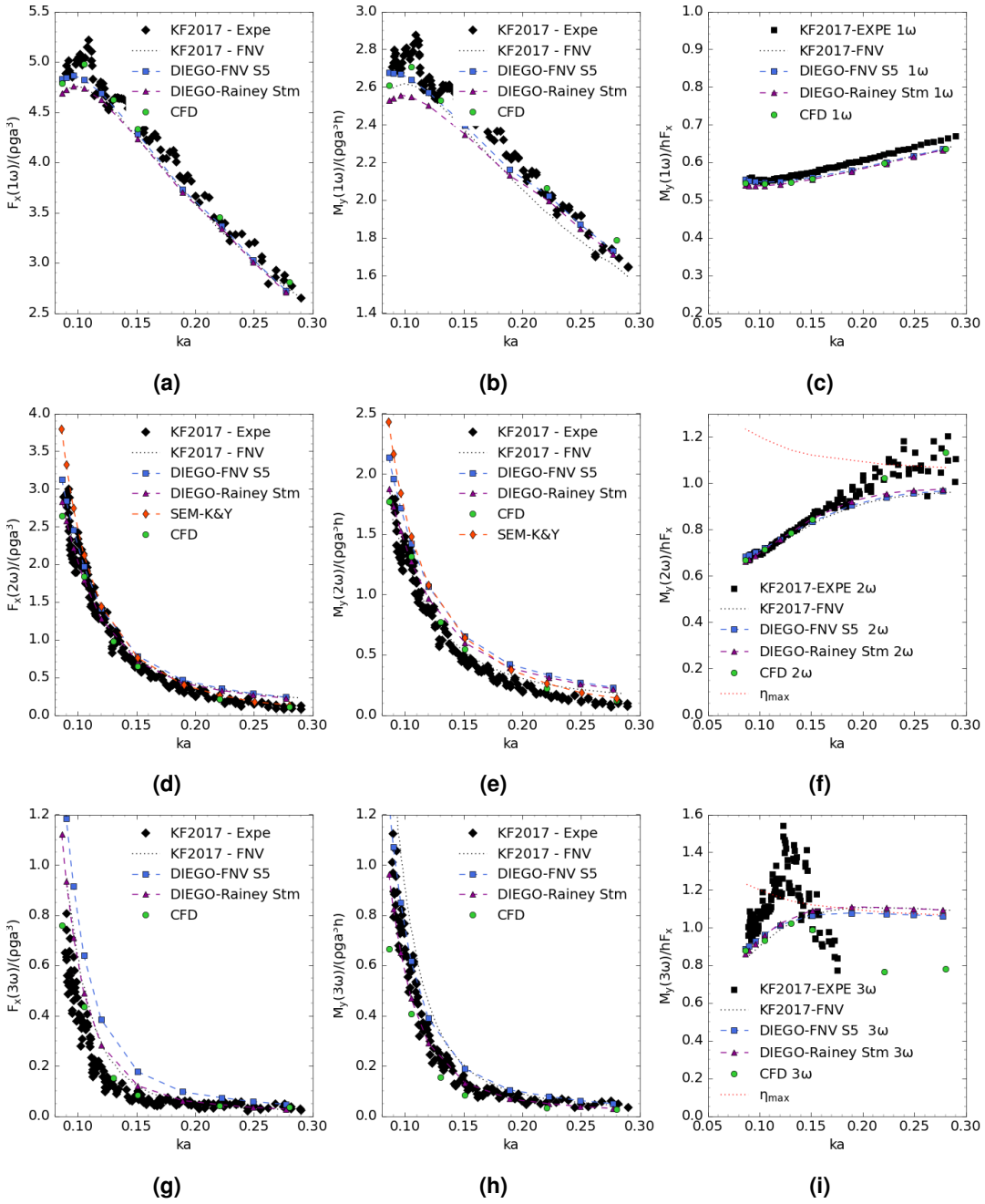


**Figure 4.7:** Comparison of normalised first, second and third-order surge force (a)(d)(g) and pitch (overturning) moment (b)(e)(h) transfer functions and the normalised approximated point of attack of the surge force (c)(f)(I).

effects on the loading not observed with CFD. The strip-theory results from DIEGO are seen to to follow the prediction of the analytical FNV solution. These seem to agree with the CFD results until the peak at $ka \approx 0.125$ beyond which the point of application is then significantly overestimated.

### Analysis of components

The components of the third-order horizontal forces calculated with the FNV approach of DIEGO are compared in Figure 4.8 against those published in Kristiansen and Faltinsen (2017). This is to understand the discrepancies observed above. The following terms are compared: $F_i$ which corresponds to the sum of the terms integrated over the still water column (Equation 3.68,3.69). The term $F_{HD}$ which corresponds to the sum of terms integrated into the first-order crest (Equation 3.65, 3.67). $F_Q$ which corresponds to the Morison acceleration term integrated between the first and second-order crest (Equation 3.66) and finally $F_\Psi$ which corresponds to the nonlinear potential term in Equation 3.71.

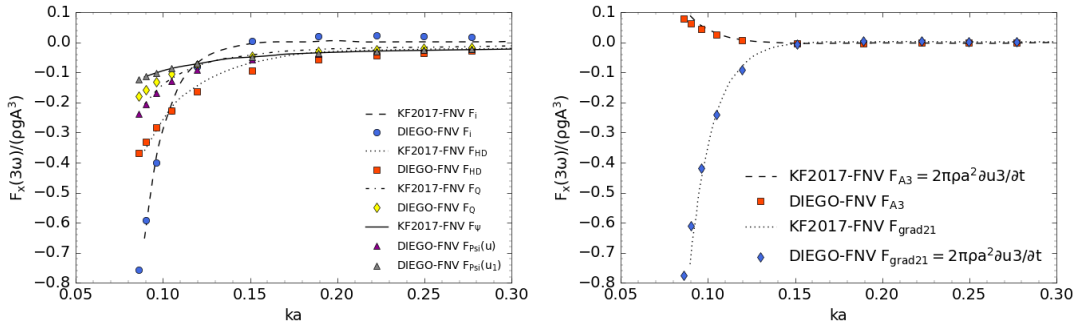


**(a)** **(b)**

**Figure 4.8:** Comparison of the components of the third-order surge force as per Figure 2 of Kristiansen and Faltinsen (2017) where amplitudes are plotted based on the phase sign. (a) all components, (b) components of term $F_i$.

Generally, it is observed that most calculated terms agree well with the published results of Kristiansen and Faltinsen (2017). However, a significant difference is observed with the free surface nonlinear term $F_\Psi$. Specifically, it is found that including higher-order kinematics from a Stream Function wave theory in the nonlinear potential term (See yellow in Figure 4.8) results in an over-prediction of its amplitude. On the other hand, if kinematics are computed from a linear wave theory (plotted in grey), this particular issue appears to be corrected meaning that it could stem from higher-order sum-difference interactions. Kristiansen and Faltinsen (2017) do mention that the generalised FNV theory can be used using nonlinear wave theories but they do stress that higher-order components should only be considered in the incident potential by which they mean the standard Morison inertial term. For this reason, Rainey's approach (Rainey, 1989, 1995) is a more consistent high-order theory for use in DIEGO.

**Signal results and rear-run-up**

The comparison of the filtered harmonics that are provided in Figure 14 of Kristiansen and Faltinsen (2017) paper are shown in Figure 4.9 below. The top graph (Figure 4.9a) displays the comparison of the filtered harmonic from the CFD results compared against the published experimental results. The second graph compares the results of DIEGO using the FNV approach against the experiments (Figure 4.9b) and against the published FNV results of Kristiansen and Faltinsen (2017) in the last graph (Figure 4.9c).

The results in Figure 4.9a show that the amplitude and phase of the harmonics are very well captured by the CFD NWT despite a slight lag of the second-order surge force. The total force appears to match well with the experimental observation although with a slightly less nonlinear profile. It is therefore possible that higher-order terms have been captured with less accuracy. The comparison of the DIEGO-FNV model against the published experimental time-series in Figure 4.9b show a good agreement of the DIEGO model for the amplitudes of the first and second-order components with also a slight visible lag for the second-order term. The third-order amplitude predicted by the DIEGO-FNV model is overestimated compared to experimental data with a slight lead of the phase. This lead is still visible when the DIEGO model is compared against the published FNV results in Figure 4.9c. On the other hand, the third-order amplitude appears there correct.

Finally, a qualitative observation of the NWT free surface around the cylinder is carried out. This is informative since the rear run-up that is mentioned in the literature and photographed in detail in Kristiansen and Faltinsen (2017) is also observed in the NWT model. As seen in Figure 4.10, a clear run-up is observed after the passage of the crest followed by a split into two side waves circling back to the front of the cylinder. Therefore, the NWT seem to capture the "Type-2" waves mentioned in the literature which brings confidence in the model's reliability.

### 4.4.2 Summary

The various models that are used further in this thesis chapter have been presented. The methods used to apply the strip-theory and semi-analytical approaches as well as details on the Navier-Stokes CFD NWT set-up have been shown. A validation exercise was carried out based on the published experimental and theoretical results of Kristiansen and Faltinsen (2017). The exercise can be considered successful considering that the CFD NWT appears to provide an accurate description of the experimental results including the drop of the point of application of the third-order force. The strip-theory approaches that are implemented in DIEGO have also been used relatively successfully. The Rainey (1995) method as currently applied in DIEGO has appeared as a potential substitute for the FNV approach, showing

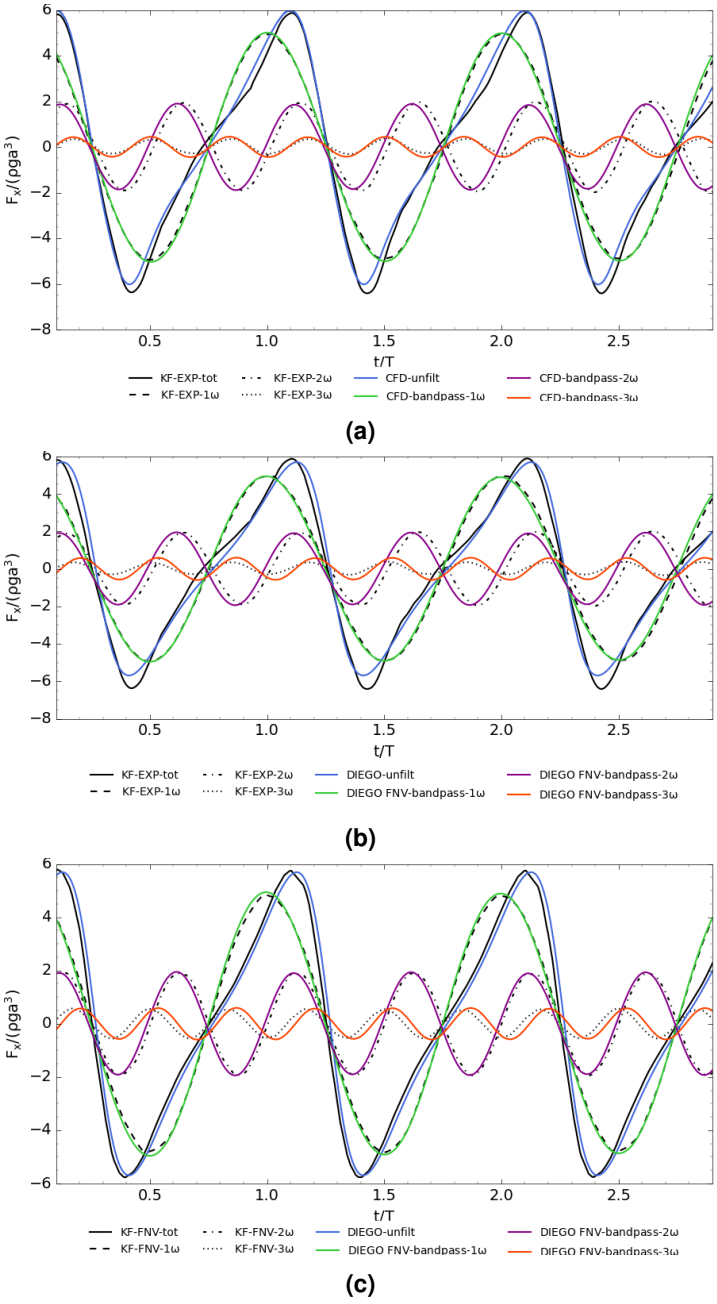


**Figure 4.9:** Time series comparison between load models and published results of experimental and analytical solution of Kristiansen and Faltinsen (2017) case $ka = 0.105$, $h/a = 7.83$, $H/\lambda = 1/25$. (a) comparison between experimental and present CFD results; (b) comparison between experimental and present DIEGO-FNV model results; (c) comparison between published FNV and present DIEGO-FNV results.

a very good agreement with the published analytical results of Kristiansen and Faltinsen (2017). The FNV method suffers from some inconsistency in its application within DIEGO. Notably, the FNV nonlinear potential term does not seem to be appropriately described when

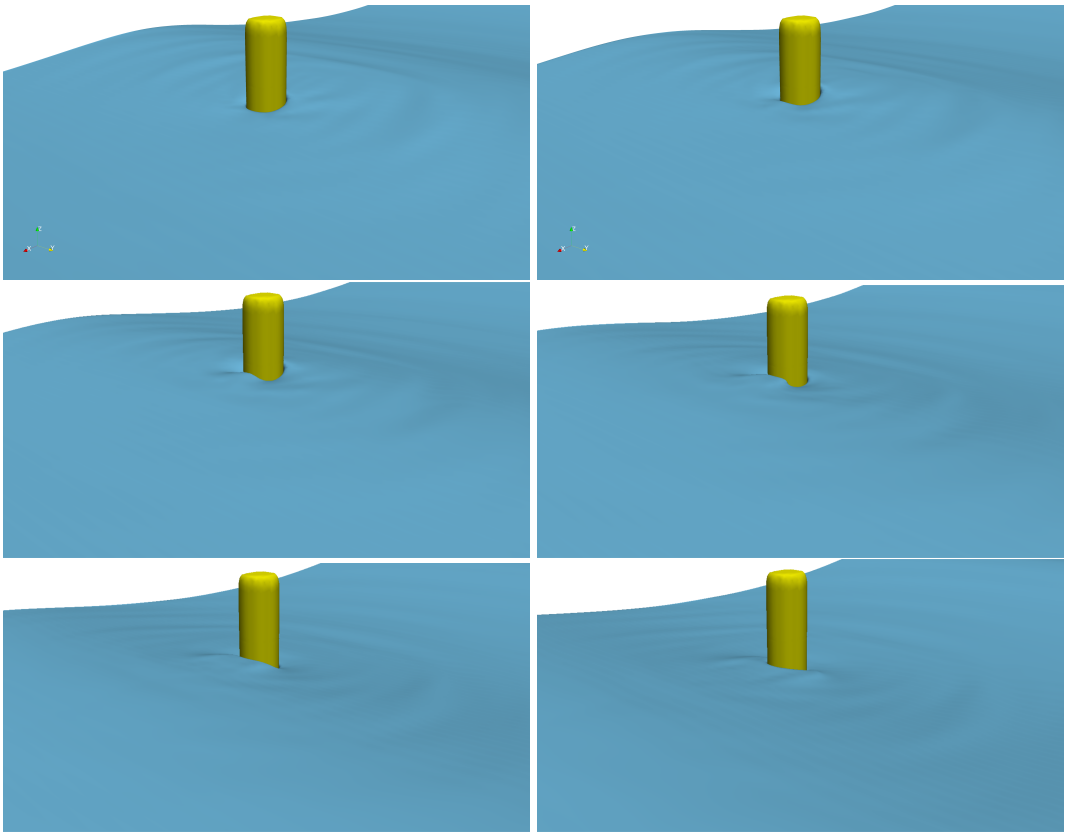

**Figure 4.10:** Rear view of the cylinder

applied with higher-order kinematics whilst these kinematics are required to compute the higher-order acceleration and advection terms. The case investigated here concerns shallow to intermediate water depth conditions with a stronger level of non-linearity. The next section continues this analysis but considers a deeper depth applicable to floating wind TLPs.

## 4.5 Truncated cylinder case

From the geometry of the EDF-TLP presented in Part I of this thesis, the central mast of the platform, referred to as transition piece (TP), is idealised as a truncated cylinder with a radius of $a = 4.4$ m, a draft of $d = 18$ m placed in water depth of $h = 100$ m ($d/a = 4.1$, $h/a = 22.7$). The cylinder is represented without the bracing connections of the TP. This is to test the application of the engineering load models in a situation where the assumptions made in their derivation remain relatively valid. The total high-order forces from the strip theory and potential flow semi-analytical models presented in Section 3.4.3 are then compared against CFD results. The various high-order load contributions are also separated into their different components and analysed. A summary of load models comparison is displayed in Table 4.1 with details on the wave kinematic theory being used for the strip theory model as well as the added mass and drag coefficients. It is important to note, that while a Stream Function wave theory is used with both strip-theory approaches, the use of nonlinear incident kinematics is restricted to the third harmonic for the FNV to stay consistent with the original theory (Kristiansen & Faltinsen, 2017) and in light of the observation seen above. On the other hand, Rainey's approach is applied with nonlinear kinematics truncated at the tenth harmonic. It is noteworthy to mention that in the Rainey approach, the Stream Function wave theory includes higher-order kinematics including corrective terms on the linear, second and third-order incident harmonics. Therefore while these effects tend to be small, these corrective terms will generate small differences between lower-order terms of the Rainey and FNV approach.

Following the validation case, the CFD NWT serve as the reference results for the force transfer functions on the cylinder. The same mesh set-up methodology is applied with the only difference being the application of a water depth limit to the mesh. It is restricted to the limit of infinite water depth at half a wavelength. A screenshot of the NWT flume is provided in Figure 4.11.

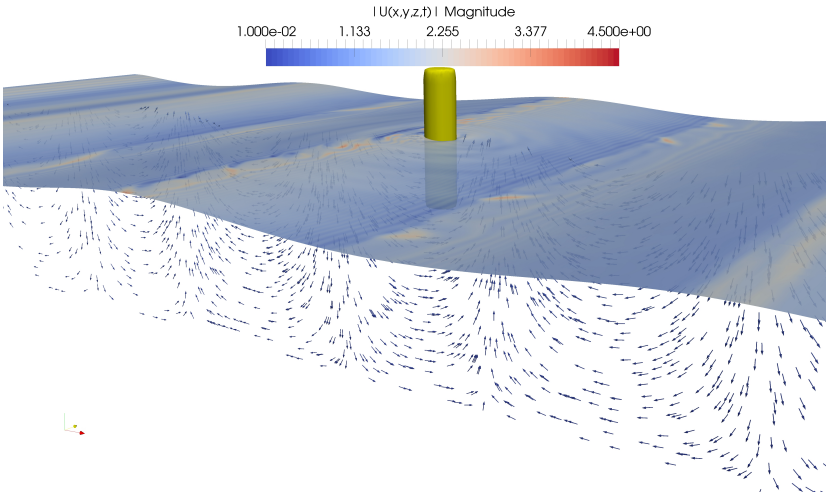


**Figure 4.11:** Screenshot of the truncated cylinder CFD NWT with free surface and velocity vectors at $T = 9.0$ s, $kA = 0.10$.

### 4.5.1 Monochromatic wave field

A monochromatic wave field is generated by the Stream function. The regular wave conditions used are provided in Table 4.3. Two constant wave steepness of $kA = 0.10$, $H/\lambda \approx 3\%$ and $kA = 0.20$, $H/\lambda \approx 6\%$, are used in this study to understand the limit of the engineering models in medium steepness conditions. The Keulegan-Carpenter $KC$ number is calculated based on the maximum velocity at the crest predicted by the Stream Function. It can be seen that all cases have generally a low KC number on the transition piece and therefore the contribution of drag on that element is expected to be low for most frequencies.

Figure 4.12a and 4.12b display the distribution of the tested wave conditions within the ranges of validity of common wave theories and of dominating hydrodynamic regimes. Figure 4.12a shows that all wave conditions necessitate a nonlinear wave theory equivalent to, at least, a Stokes second-order theory. For the steeper wave condition ($ka = 0.20$), a theory of at least third-order is required. In this case, truncating the Stream Function above the third-order kinematics, as prescribed in the generalized FNV theory, appears justified. The waves with periods ranging from $T = 12 - 18$ s appear to be in intermediate water depth, also referred to as transitional depth conditions, while the remaining waves are all within the infinite water depth range. It is therefore expected that the nonlinear Froude-Krylov load component due to the incident wave will be negligible for most wave conditions. In terms of the dominant wave force regime, Figure 4.12b indicates that inertial loads are expected to be dominant with a truncated cylinder in fixed conditions. The shorter waves are expected to include a significant portion of diffraction with scattering parameters approaching $ka = 1$. On the other hand, the longest waves are expected to include a significant drag component, especially in the steeper wave conditions.

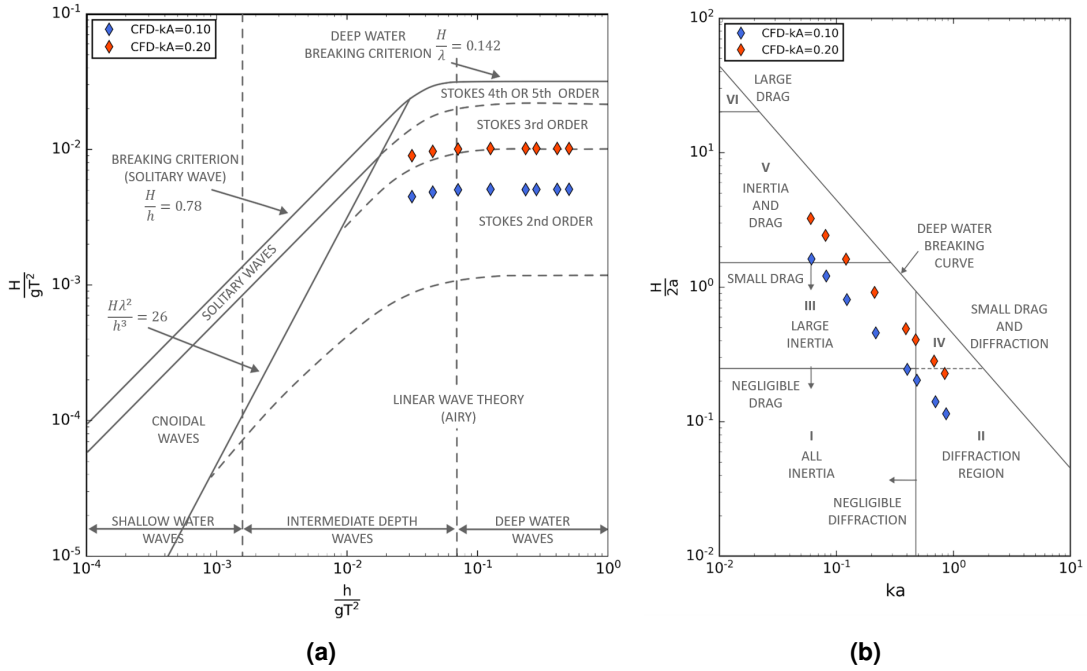


**Figure 4.12:** Distribution of tested regular wave conditions within (a) the ranges of validity for common wave theories, (b) ranges of different wave force regimes. Adapted from Chakrabarti (1987).

The comparison between the generated wave in the CFD NWT and the reference Stream Function solution is provided in terms of harmonics amplitudes in Figure 4.13 for wave steepness $kA = 0.10$. Generally, the agreement of the CFD NWT with the reference solution is satisfying. The amplitudes of the incident wave components appear to be correctly captured up to the third harmonics with a slight underestimation by the CFD over large periods.

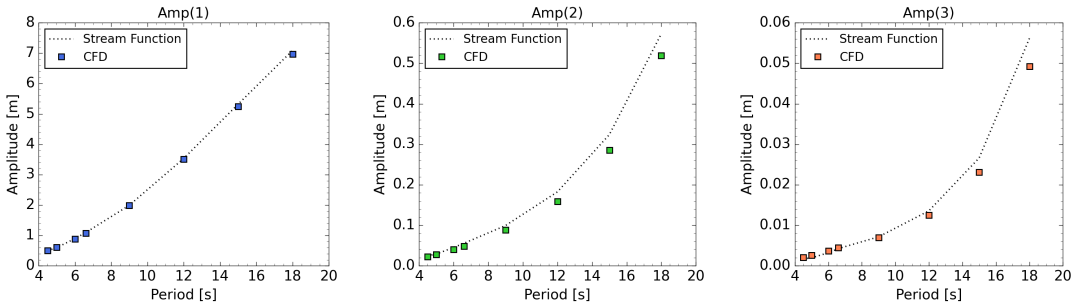


**Figure 4.13:** Comparison between harmonics obtained with the CFD and reference from Stream Function for wave steepness of $kA = 0.10$

| T $[s]$ | H $[m]$ | $\lambda_{Str}$ $[m]$ | $ka$ $[-]$ | $kA$ $[-]$ | $H/\lambda$ $[-]$ | $kh$ $[-]$ | Beta $[-]$ | $KC_{SF}$ $[-]$ |
|---|---|---|---|---|---|---|---|---|
| kA = 0.10 | | | | | | | | |
| 4.5 | 1.0 | 31.81 | 0.8744 | 0.10 | 3.18% | 19.87 | 1.7209e+07 | 0.39 |
| 5.0 | 1.2 | 39.27 | 0.7083 | 0.10 | 3.18% | 16.10 | 1.5488e+07 | 0.48 |
| 6.0 | 1.8 | 56.55 | 0.4918 | 0.10 | 3.18% | 11.18 | 1.2907e+07 | 0.70 |
| 6.6 | 2.1 | 68.43 | 0.4065 | 0.10 | 3.18% | 9.24 | 1.1733e+07 | 0.84 |
| 9.0 | 4.0 | 127.25 | 0.2186 | 0.10 | 3.18% | 4.97 | 8.6044e+06 | 1.57 |
| 12.0 | 7.1 | 224.62 | 0.1238 | 0.10 | 3.18% | 2.81 | 6.4533e+06 | 2.78 |
| 15.0 | 10.7 | 336.72 | 0.0825 | 0.10 | 3.18% | 1.87 | 5.1627e+06 | 4.35 |
| 18.0 | 14.3 | 449.99 | 0.0617 | 0.10 | 3.18% | 1.40 | 4.3022e+06 | 6.34 |
| kA = 0.20 | | | | | | | | |
| 4.5 | 2.0 | 32.76 | 0.8440 | 0.19 | 6.14% | 19.18 | 1.7209e+07 | 0.86 |
| 5.0 | 2.5 | 40.42 | 0.6839 | 0.19 | 6.15% | 15.54 | 1.5488e+07 | 1.06 |
| 6.0 | 3.6 | 58.15 | 0.4754 | 0.19 | 6.15% | 10.80 | 1.2907e+07 | 1.53 |
| 6.6 | 4.3 | 70.32 | 0.3931 | 0.19 | 6.16% | 8.94 | 1.1733e+07 | 1.84 |
| 9.0 | 8.1 | 130.32 | 0.2121 | 0.19 | 6.18% | 4.82 | 8.6044e+06 | 3.41 |
| 12.0 | 14.2 | 228.71 | 0.1209 | 0.20 | 6.21% | 2.75 | 6.4533e+06 | 6.04 |
| 15.0 | 21.3 | 341.51 | 0.0810 | 0.20 | 6.25% | 1.84 | 5.1627e+06 | 9.55 |
| 18.0 | 28.5 | 456.09 | 0.0606 | 0.20 | 6.25% | 1.38 | 4.3022e+06 | 14.23 |

**Table 4.3:** Regular wave cases tested with CFD on truncated cylinder. KC calculated based on crest particle velocity predicted by the Stream Function (Dean, 1965).

### 4.5.2 Force transfer functions comparison

The total second and third-order surge force and pitch moment transfer functions from both strip-theory approaches and potential-flow semi-analytical solution along with CFD results from neptune_cfd are provided for two wave steepness in Figure 4.14 and 4.15. The comparison between the various components to the second and third-order surge force is then provided in Figure 4.16 and Figure 4.17. This gives an understanding of the contribution of the first, second and third-order potential to the high-frequency forces as well as an indication of the importance of free surface effects. The reader will note the amplitude-phase notation used in this paper for the force transfer functions with phase referenced to the crest of the respective harmonic of the free surface elevation using the convention $e^{-i\omega t}$.

**Comparison of force harmonics total**

The comparison of the total transfer function for the second and third-order surge force and pitch moment is given in Figure 4.14 and 4.15 for the case with wave steepness of $kA = 0.10$ and $kA = 0.20$ respectively. The strip-theory models are compared against the semi-analytical solution of Huang and Eatock Taylor (1996) and Malenica and Molin (1995) and the CFD results obtained with neptune_cfd. The comparison is restricted to the horizontal (surge) force on top and overturning (pitch) moment on the bottom, with second-order transfer functions given on the right and third-order on the left. In each sub-figure, the top graph represents the normalised transfer function force amplitude and the bottom graph its phase.

The first observation is that the semi-analytical potential flow transfer functions replicate very well both the amplitudes and phases predicted by the high-fidelity CFD runs. This agreement is more pronounced at second-order where the match is almost perfect. On the other hand, at third-order, the amplitudes of the CFD results appear lower than the semi-analytical potential flow predictions. This seems to corroborate the results of Huseby and Grue (2000) which showed an overestimation of the third-order amplitudes of $20 - 30\%$ by the model of Malenica and Molin (1995) in wave steepness around $kA = 0.08 - 0.12$. However, the semi-analytical model captures well the trend both in terms of amplitudes and phases.

The strip-theory models show a relatively good agreement in the transfer functions amplitudes with both the semi-analytical solution and the CFD results at both second and third-order. The original FNV analytical solution and the generalised FNV approach appear to match the third-order semi-analytical solution until a value of $ka \approx 0.4$. The Rainey approach, on the other hand, appears to predict a lower third-order force, staying generally below the predictions of both the generalised FNV method and the semi-analytical solution of Malenica and Molin (1995) until $ka = 0.6$. It also appears to diverge less than the FNV theory at higher scattering parameters, $ka$.

Finally, an interesting observation is the comparison between Rainey's equations and the FNV theory both at second and third-order. At second-order, the agreement between the two theories is almost perfect which is expected as reported in several studies (Kristiansen & Faltinsen, 2017; Peyrard, 2018; Tromans et al., 2006). At third-order, the FNV theory becomes relatively equivalent to Rainey's if a coefficient of $\beta_{FNV} = 1$ is used as proposed for truncated cylinders in Milano et al. (2019). This is shown in Figure 4.14b, 4.14d, 4.15b and 4.15d. This can be understood easily since, in regular waves with a coefficient equal to one, the non-linear potential force term, $F_\Psi$, is equivalent to the surface intersection term in Rainey (1995). The only remaining difference between the two models is the use of higher-order wave kinematics

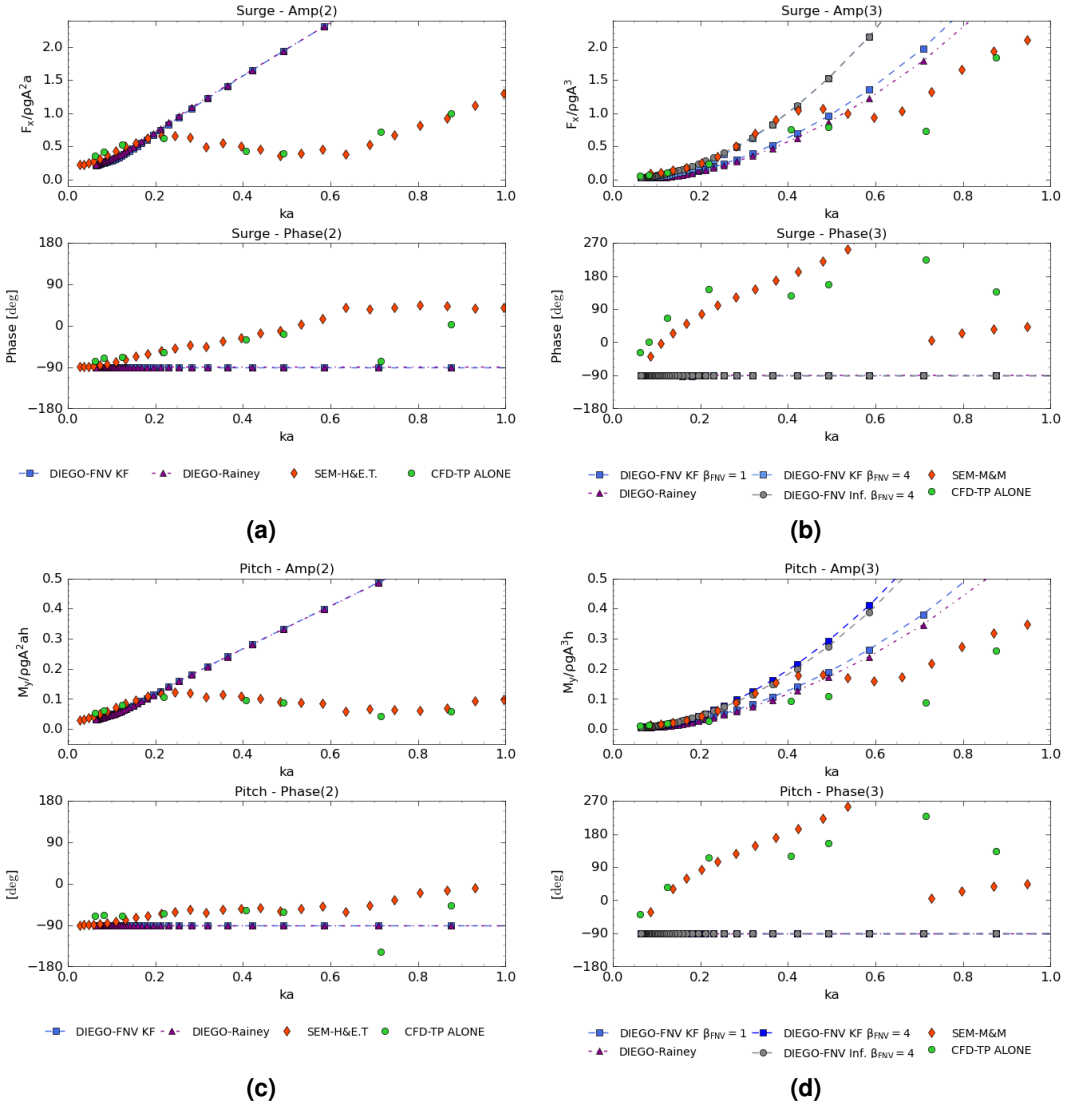


**Figure 4.14:** Comparison of normalised (a) Rainey and (b) FNV components of the surge force transfer function for wave steepness of $kA = 0.10$, $H/\lambda \approx 3\%$

which are restricted to up to third-order in the Kristiansen and Faltinsen (2017) theory whereas Rainey (1989, 1995) allows for fully nonlinear wave kinematics. If the generalised FNV theory (FNV KF) is used with higher-order kinematics and a coefficient of one, it would be exactly equivalent to the Rainey theory.

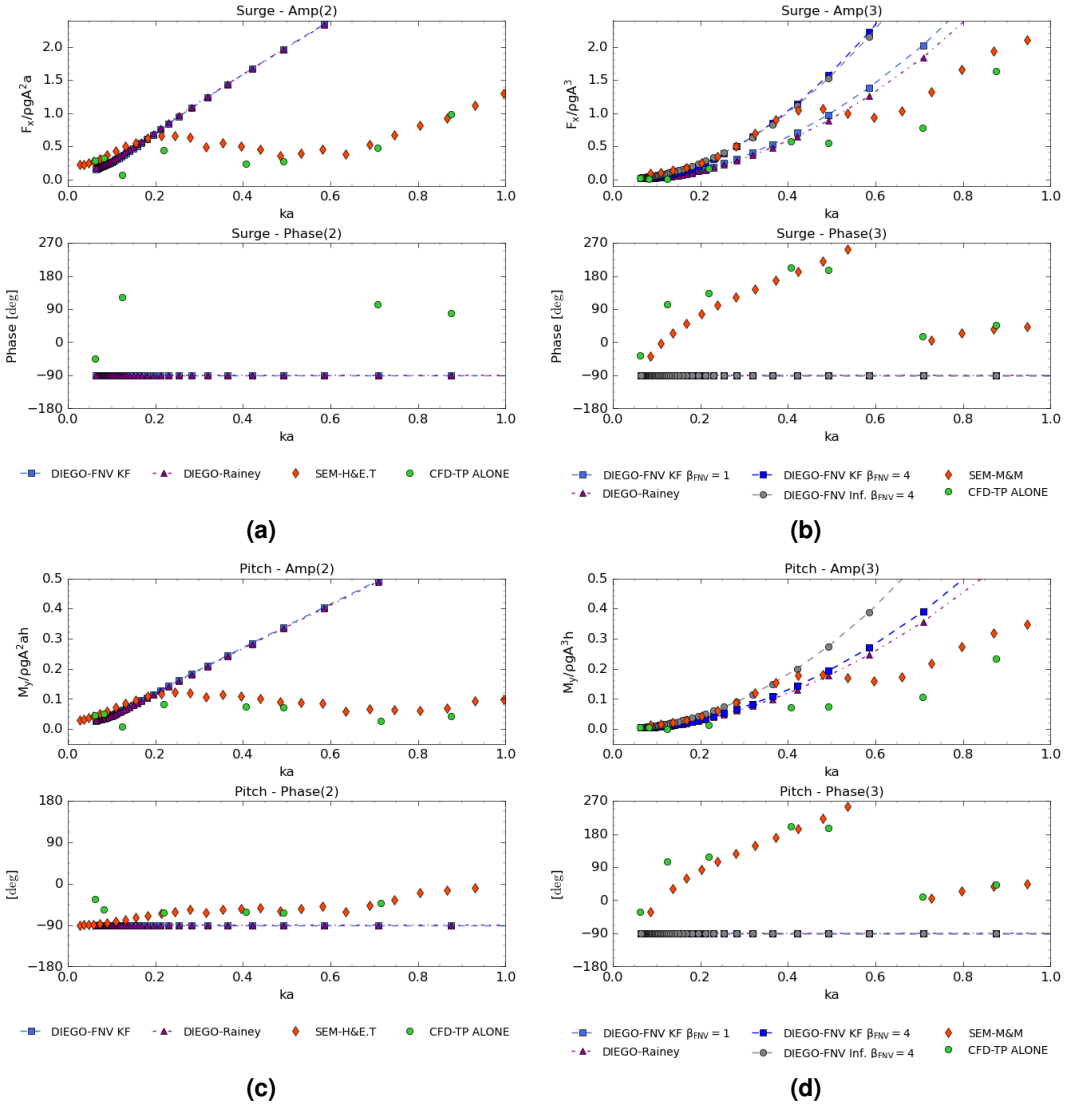


**Figure 4.15:** Comparison of normalised second and third-order (a)(b) surge force and (c)(d) pitch moment transfer functions for wave steepness of $kA = 0.20$, $H/\lambda \approx 6\%$

The original FNV formulation (Faltinsen et al., 1995) for infinite water depth and the generalised formulation of Kristiansen and Faltinsen (2017) appear to fully agree except for the frequencies which are under intermediate water depth conditions. As mentioned above, these FNV formulae display a very good agreement with the semi-analytical surge force amplitude up to $ka = 0.4$ but then diverge at a high rate. Rainey's approach on the other hand seems to match better the CFD NWT results which predict lower amplitudes than the semi-analytical solution. Furthermore, the CFD NWT correctly captures the decrease in amplitude of the third-order force transfer functions with increasing steepness which is reported in the literature and visible here by comparing Figure 4.14b and 4.15b. In higher steepness, Rainey's approach appears to match better with the CFD. It is worth noting that the opposite effect is true for the

SEM method which overestimates wave loads in increasing wave steepness since it is based on a transfer functions approach. Generally, the model using Rainey's theory appears to show a satisfying approximation of the general trend of the third-order force in the considered range of frequencies and wave steepness. Therefore, based on this observation, the Rainey model is taken forward for the analysis on the full platform that was published in Rongé, Peyrard, Venugopal, Xiao, et al. (2023) and presented in Chapter 5.

**Comparative analysis of force harmonic components**

The comparison between strip-theory and semi-analytical potential flow components of the second-order harmonic of the surge force is provided in Figure 4.16 showing the second-order forces due to first and second-order contributions. Only the Rainey components are compared against the semi-analytical equation at second-order since, as confirmed above, Rainey's and FNV's approaches are exactly equivalent. For the components of the third-order harmonic of the surge force, both FNV and Rainey approaches are compared against the semi-analytical components in Figures 4.17.

The reader will note that components are sorted based on the order of the quantities at play in their derivation following the notation used in Malenica and Molin (1995). More specifically, this means that force components that only mobilise first-order quantities (velocities, acceleration, free surface elevation) are ascribed to the component, $F_1^{(n)}$, corresponding to terms, $F_{x1a}^{(2)}$ and $F_{x1b}^{(2)}$ in Equation 3.62 and 3.63 for the second-order harmonic. The term $F_{x22}^{(2)}$, corresponds to the second-order force component mobilising the second-order quantities only, 3.64. For the third-order force harmonic due to linear kinematics only, this is limited to term $F_{x1}^{(3)}$ shown in Equation 3.65. Then, $F_{x2}^{(3)}$, correspond to the sum of terms mobilising both first and second-order quantities including those in 3.66, 3.67 and 3.68. Finally, the third-order strip theory component due to the third-order potential, $F_{x3}^{(3)}$, consists of the Morison term in Equation 3.69 and the free surface point load in either Equation 3.58 or 3.71 for the Rainey and FNV approach respectively. The choice of adding the free surface term in the third-order potential load despite being calculated from first-order quantities is based on the FNV theory which refers to $F_\Psi$ as the force due to the approximated third-order scattered potential.

The comparison of the components of the second-order force shown in Figure 4.16 gives an interesting account of the accuracy of the strip theory. It can be seen in Figure 4.16b that the equivalent of the Morison force due to second-order kinematics, STR-$F_{x22}^{(2)}$ matches very well with the semi-analytical solution for the Froude-Krylov and diffraction force due to the second-order incident wave potential, SEM-$F_{x2IH}^{(2)}$, of Huang and Eatock Taylor (1996) as mentioned in Rongé, Peyrard, Venugopal, et al. (2022). This term dissipates quickly as wave conditions move to infinite water depth conditions. For the remaining second-order load

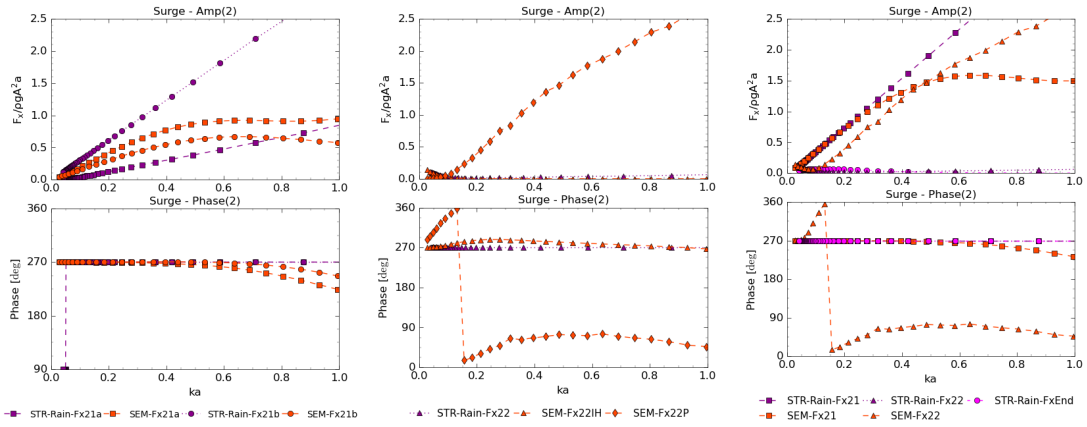


**Figure 4.16:** Normalised second-order surge force components: (a) from first-order contributions; (b) from second-order contributions; (c) comparison between total first and second-order components

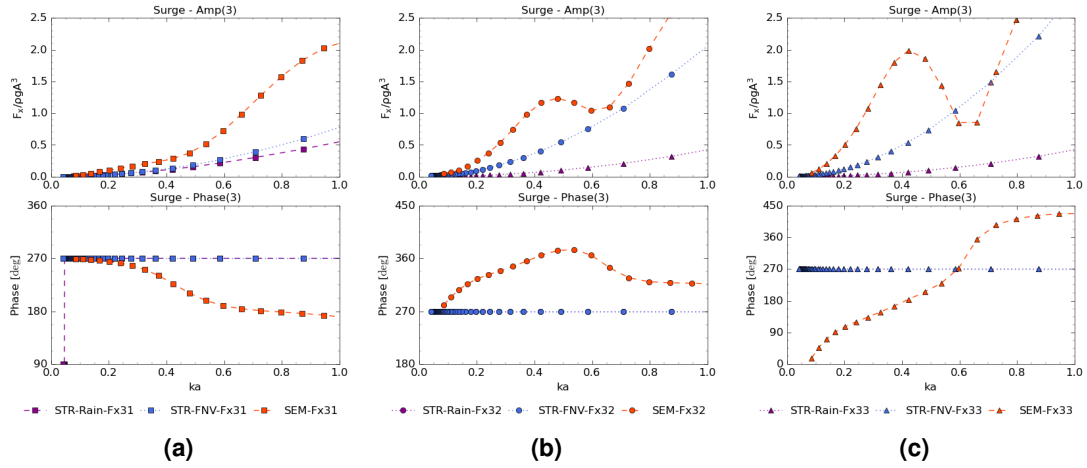


**Figure 4.17:** Normalised third-order surge force components: (a) from first-order contributions; (b) from second-order contributions; (c) from third-order contributions

contribution from first-order quantities in Figure 4.16a, the strip-theory velocity gradient and axial divergence terms, STR-$F^{(2)}_{x21a}$, and the Morison force integrated into the crest, STR-$F^{(2)}_{x21b}$ do not match in terms of amplitude the roughly corresponding term in the potential flow theory. This is despite the strip-theory component, STR-$F^{(2)}_{x21a}$ (Equation 3.62), appearing as a sort of linear approximation of the potential flow dynamic pressure for the vertical cylinder case. As for the Morison term integrated into the crest, STR-$F^{(2)}_{x21b}$, it is hardly a representation of the semi-analytical force due to the quasi-hydrostatic waterline integral. However, Figure 4.16c shows that considering the total amplitudes of the combined second-order force due to first-order quantities, STR-$F^{(2)}_{x21}$, a very good agreement is reached with the second-order potential flow solution until $ka \approx 0.2$ which is the dominant factor for the agreement seen in Figure 4.14a and 4.14c.

In terms of the phases of the different force components, it is seen that the strip-theory models conform to the long-wave approximation and predict a constant phase of $-90\,\mathrm{deg}$ for positive inline force and $90\,\mathrm{deg}$ for negative inline force. It is seen that the Morison force due to the integration of the first-order acceleration in the first-order crest undergoes a change of sign around $ka = 0.05$. On the other hand, the potential flow solution takes into account the wave scattering around the cylinder and the respective phase shift. Interestingly, at second-order it appears that the phase of quadratic forces, SEM-$F^{(2)}_{x21a}$ and SEM-$F^{(2)}_{x21b}$ remain relatively close to $-90\,\mathrm{deg}$.

Moving on to Figure 4.17, it is observed that generally, the third-order components of the force on the truncated cylinder predicted from the two strip theory approaches show a low agreement with the semi-analytical force components derived by Malenica and Molin (1995). The third-order term STR-$F^{(3)}_{x31}$, due to the linear quantities alone appears to underestimate significantly its semi-analytical equivalent. The component due to the combination of first and second-order quantities, STR-$F^{(3)}_{x32}$ appears as a good approximation of its SEM counterpart for the FNV approaches but diverges significantly for the Rainey approach. The reason for such strong divergence between the two strip-theory approaches is due to the order of wave kinematics used. Whilst, the FNV only uses kinematics up to the third-harmonics, the Rainey approach uses all harmonics of the Stream Function including higher-order terms which influence lower harmonics. As for the term due to the third-order potential, $F^{(3)}_{x33}$, it is dominated almost in its entirety by the free surface term since the incident potential term, represented by the Morison equation using third-order kinematics, tends towards zero in infinite water depth. This term is the most significant difference between the FNV and Rainey approaches, with the former method approaching better the semi-analytical solution amplitudes of the equivalent term whilst the latter appears to underestimate it. However, it is important to take into account the phases of these terms and to note that whilst all the strip theory components remain in phase with the incident wave-particle acceleration, the semi-analytical potential flow terms display significant frequency shifts across the range of frequencies considered. For that reason, a pure amplitude-to-amplitude agreement between terms is not a guarantee of an agreement in the amplitude of the total force.

**Morison drag effect on third-order force**

To understand the effect of the viscous drag on high-order loads, the same models are analysed with the addition of the viscous drag component which is estimated using the standard Morison equation integrated up to the instantaneous free surface. Figure 4.18 displays the change in third-order force transfer functions when viscous drag is included for wave steepness case $kA = 0.10$ using a transverse drag coefficient of $C_{D,t} = 1.0$ as detailed in Table 4.1.

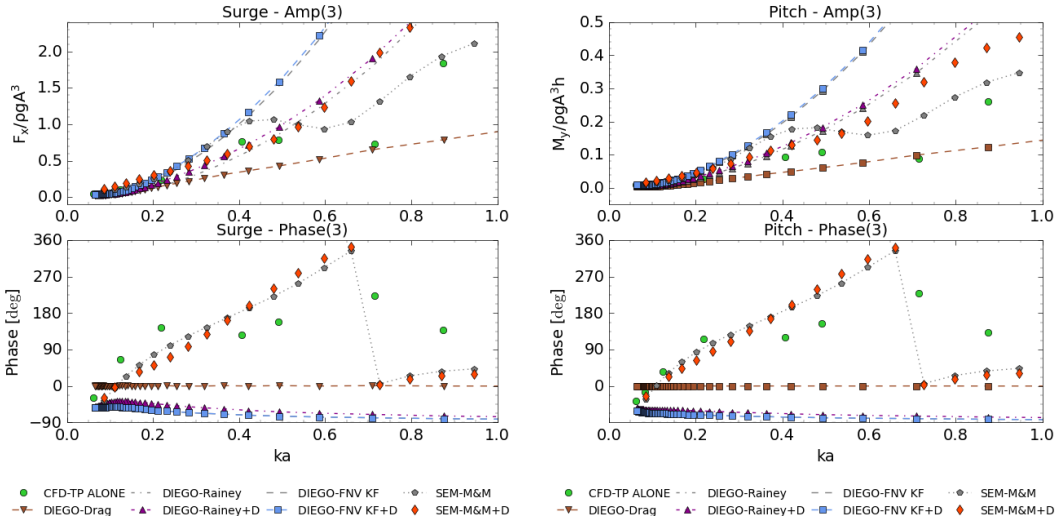


**Figure 4.18:** Comparison of normalised second and third-order surge force with the addition of viscous drag (a) surge force and (b) pitch moment transfer functions for wave steepness of $kA = 0.10$, $H/\lambda \approx 3\%$

Interestingly, the drag force does not seem to drastically impact the strip-theory models whereas the amplitudes of the semi-analytical solution appear strongly modified. This is because the strip-theory models remain at a constant $-90°$ phase shift from the drag force which remains in line with the crest. On the other hand, the third-order semi-analytical solution displays a significant phase shift and therefore undergoes much more area of increased positive and negative interaction with the drag force. Around $ka = 0.4 - 0.5$, the addition of drag seems to have a benefit on the amplitude predictions. However, for other frequencies, the addition of drag does not appear to be beneficial. Better results could be obtained by making the drag coefficient $K_C$ dependent since it was found to change significantly in the low range of $K_C$ number at high $\beta$ number (Sarpkaya, 1986).

### 4.5.3 Summary

The current results have shown that the semi-analytical potential flow diffraction solutions of Huang and Eatock Taylor (1996) and Malenica and Molin (1995) give a pretty good prediction of both amplitudes and phases of the high-order force transfer functions. The agreement between the CFD NWT and the semi-analytical method is better at second than at third-order where the semi-analytical solution over-predicts the amplitudes as reported in the literature. However, the agreement in the force phase is very satisfying in both cases. The influence of drag is also expected to be the highest on third-order loads, and therefore further calibration

of its coefficient can also influence this comparison. Finally, the increase in steepness results in an over-prediction of the normalised amplitudes of these solutions which is in line with the findings of previous experimental and numerical studies (Huseby & Grue, 2000; Shao, 2010; Xiong et al., 2020).

The strip-theory solutions appear to approximate relatively accurately the wave load amplitudes up to a scattering parameter of around $ka = 0.2$ at second-order and $ka = 0.4$ at third-order replicating the findings of Krokstad et al. (1998). It is interesting since the limit for the slender-body approximation method had been put at $ka = 0.12$ at second-order and $ka = 0.05$ at third-order in Malenica and Molin (1995) based on an analysis of the complex amplitudes. However, these limits can be understood when observing the phases which follow these limits. This is to say that while the strip theory models appear to provide a decent estimate of the high-order force amplitudes, the assumption of a constant phase value is unrealistic and reduces these models' accuracy.

Generally, the application of high-order engineering models has shown to be pretty successful at predicting the force transfer functions measured in the CFD NWT in their domain of validity. The question remains on how these models perform while transferred to a more complex offshore structure which is the subject of the next chapter.

Chapter 5

# Analysis of high-order wave loads on EDF-TLP

## 5.1 Introduction

In the previous chapter, the engineering load models have been tested relatively successfully on simple offshore structures which could be represented analytically without pushing the limit of the original theories. In this chapter, the load models are applied to the full EDF-TLP floater in fixed conditions to test these model applicability in a more realistic FOWT case and outside of those theories' assumptions.

This study formed the core of a journal article submitted to Ocean Engineering under the title "Evaluation of second and third-order numerical wave-loading approaches for floating offshore wind TLPs" (Rongé, Peyrard, Venugopal, Xiao, et al., 2023). The original target of the article was to verify if third-order transfer functions that were designed for vertical cylinders, and used in the floating offshore industry as such (Bachynski, 2014; Jagdale et al., 2021; Milano et al., 2019), remain relatively valid for the central mast (or TP) of a complex floater when bracing connection and the remainder of the structure are included around it. However, the article expanded into a deeper analysis of the high-order transfer functions elements by elements. In fact, the analysis of the nonlinear force contribution emanating from the remaining elements of the floater such as the side buoys and the bracings enables us to qualify their contribution to the nonlinear forces on the platform. This information helps answer if third-order inertial forces on other elements than surface piecing cylinders can be neglected, if strip-theory assumptions are sufficient or if new theories should be developed to fill that gap. Furthermore, the addition of viscous drag helps quantify the dominant regime at play in the high-order loads. Finally, the comparison of the total forces on the structure serves to validate the calculation of the QTFs using a frequency domain BEM approach. As a foundation for this study, the full preparation of the EDF-TLP floater load models is also presented here which includes the preparation of first and second-order BEM models and selecting the appropriate added mass and drag coefficient for the strip-theory.

## 5.2 Application of numerical approaches

A range of engineering models are applicable to the EDF-TLP floater. For first and second-order loads, resolving the potential flow problem via BEM would be usually considered robust and sufficient. However, due to the complexity of the second-order diffraction problem, this solution can be expensive to put in place in early design stages. For example, simpler models such as strip-theory models or semi-analytical potential flow ones might give relatively accurate predictions on individual elements. Furthermore, when expanding to third-order loads a range of generally unsatisfying options are available as is illustrated in Figure 5.1. This is because to capture third-order forces on elements which do not conform to vertical cylinders and hence to either the FNV or the semi-analytical approach of Malenica (1994), only Rainey's approach can provide a third-order estimate of their inertial loads with a low computational cost. However, since Rainey's model is resolved in the time-domain using the instantaneous free surface and instantaneous nonlinear kinematics, it generates first and second-order loads which therefore cannot be combined with an underlying BEM model of the full floater as this would lead to double counting these effects. This is why the FNV approach is useful in its original form as it provides a third-order analytical formula which can be applied in a hybrid QTF+FNV model as done by Bachynski (2014) and Milano et al. (2019) for FOWT-TLP based on Krokstad et al. (1998). This option is shown as highlighted in blue and green in Figure 5.1. However, Rainey's approach is compatible with a hybrid model which would consist of a semi-analytical solution for the central mast and a strip-theory approach on the remainder elements. This approach is highlighted in orange and green. It is not certain that such a model would work but the exploration of diverse models is considered worthwhile as part of this exercise.

For that purpose, it is important to both prepare BEM models of the full platform but also calibrate the added mass coefficient of our individual elements of the floater based on linear potential flow. For the transition piece, the semi-analytical potential flow solution and strip theory have been validated in Chapter 4.

### 5.2.1 Set-up of the full potential flow approach

#### BEM model

This research has only considered one wave direction along the symmetric plane of the floater. A half hull mesh (Figure 5.2) was used to reduce computational time. The hull mesh consists of 10,466 panels with a discretisation of around 0.5m on the transition piece and braces. The discretisation of the hull is dominated by the requirement for resolving the second-order diffraction.

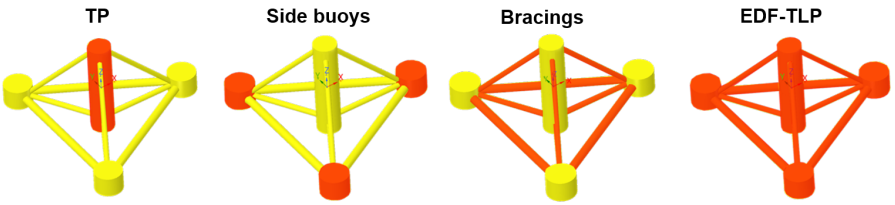


| Load order | TP 1 | TP 2 | TP 3 | Side buoys 1 | Side buoys 2 | Side buoys 3 | Bracings 1 | Bracings 2 | Bracings 3 | EDF-TLP 1 | EDF-TLP 2 | EDF-TLP 3 |
|---|---|---|---|---|---|---|---|---|---|---|---|---|
| **Frequency domain potential flow** | | | | | | | | | | | | |
| Semi-analytical potential flow | ✓ | ✓ | ✓ | ✓ | ? | ? | x | x | x | x | x | x |
| BEM | ✓ | ✓ | x | ✓ | ✓ | x | ✓ | ✓ | x | ✓ | ✓ | x |
| **Strip-theory / Slender-body approximation** | | | | | | | | | | | | |
| Rainey | | ✓ | | | ✓ | | | ✓ | | | ✓ | |
| FNV | ✓ | ✓ | ✓ | x | x | x | x | x | x | x | x | x |

**Figure 5.1:** Elements of the EDF-TLP floater and applicable engineering hydrodynamic models at first, second and third-order

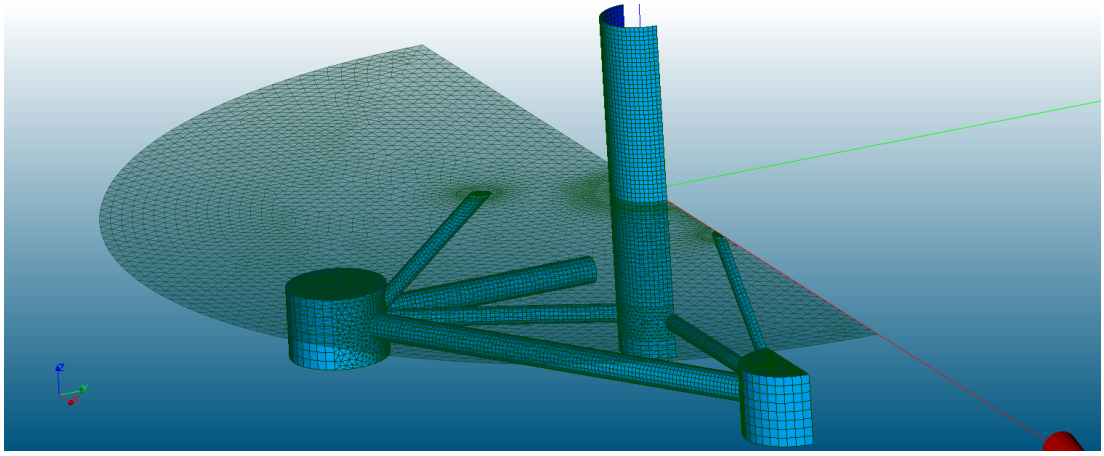

**Figure 5.2:** View of the BEM panel mesh of the EDF-TLP half hull and free surface

### Linear hydro database

A hydro-database has been constructed using both open-source BEM solver NEMOHv2.02 and commercial software OrcaWave both based on the same hull mesh. Due to the availability of NEMOHv2.02 on the cluster computer of EDF R&D, whereas OrcaWave is on a shared license set-up on a desktop of the University of Edinburgh, 600 frequencies could be generated on the former and only about 60 frequencies on the latter. The linear load transfer functions, added mass and radiation damping for the relevant three degrees of freedom are provided in Figures 5.3, 5.4a and 5.4b respectively. The agreement between the two codes is excellent in the linear transfer functions (LTF) and radiation damping, and the added mass value shows a

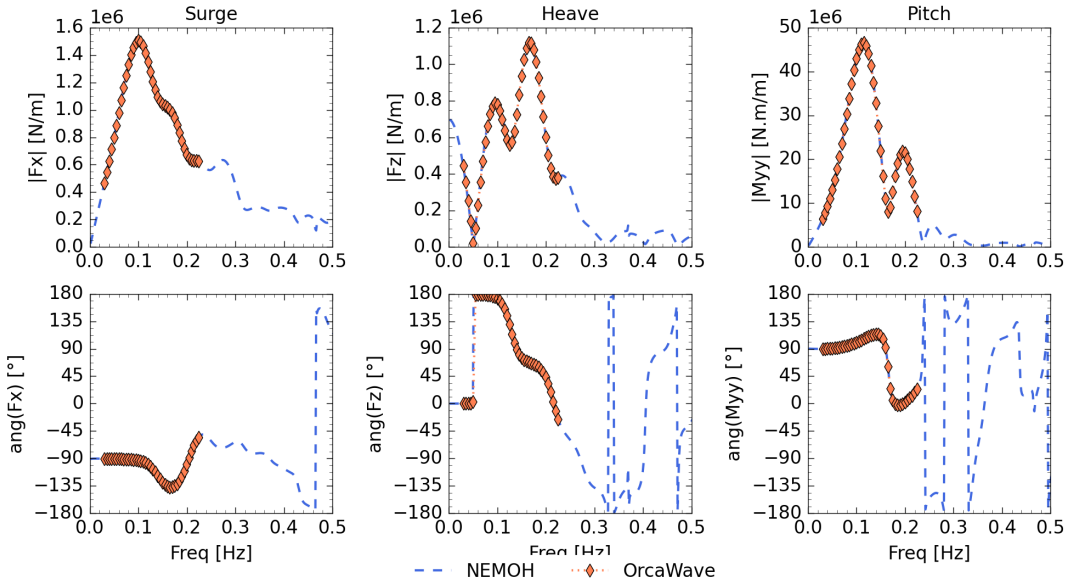


**Figure 5.3:** Comparison of linear force transfer functions (LTF) between NEMOH and OrcaWave with amplitude (top) and phase (bottom) for (left) surge, (middle) heave force and (right) pitch moment

slight reduction by around $4\%$ using OrcaWave instead of NEMOH. There is one instance of irregular frequency visible around $f = 0.47$ Hz in term $B_{R1,1}$ (Figure 5.4b) which is removed subsequently by interpolation. The location at high-frequency of this numerical artifact is therefore not a cause for much concern.

### Quadratic Transfer Functions

At the time of carrying out the bulk of the numerical work for this research, NEMOHv3.0.0 update which includes second-order diffraction had not been released. The second-order diffraction solution is therefore calculated using OrcaWave, the BEM solver integrated with OrcaFlex. Figure 5.2 does not only display a snapshot of the hull mesh but also the panelled free surface which is required to integrate directly the potential due to the scattered free surface and resolve the second-order diffraction. As mentioned above, the discretisation of the hull is based on the recommendation by DNV-GL (2019c) of around 6 hull panels per second-order wavelength. The free surface mesh is made of 7140 panels and serves for the direct integration of the scattered potential on the free surface. It extends to a radial distance of 60 m from the centre of the floater with a discretisation of 0.5m near the structure and 2m at the outer perimeter. Past that limit, Orcawave uses radial lines with points to continue the integration of the evanescent mode by Gaussian quadrature up to a limit where the asymptotic expression of the potential at infinite can reasonably be used. In this case, 120 points are used per radial line with a discretisation of one point every 2 m and 50 radial lines. The quadrature

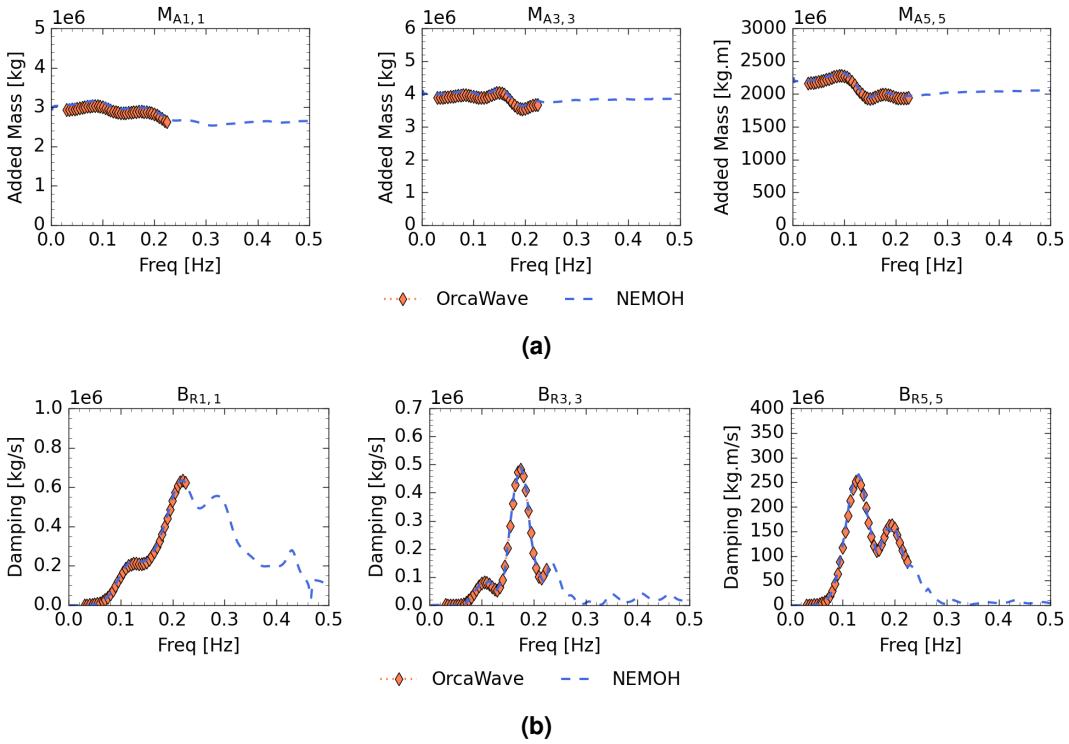


**Figure 5.4:** Comparison of added mass and radiation damping main diagonal term between NEMOH and OrcaWave (a)(d) surge-surge, (b)(e) heave-heave and (c)(f) pitch-pitch

zone extends to a radius of 300 m from the floater centre which is the radial distance at which convergence on the surface integral is achieved using the semi-analytical equation of Huang and Eatock Taylor (1996) for the frequency displaying the strongest scattering and showing satisfying convergence for the longer wavelength which do not generate strong evanescent modes. In that sense, the semi-analytical approach serves as a useful tool to provide a reference order of magnitude for the limit of direct integration of the free surface. The details of the free surface panels, quadrature and asymptotic limit are displayed in Figure 5.5.

Figure 5.6 shows the QTFs matrices for the difference and sum-frequency terms in the three dominant degrees of freedom. The QTFs have been calculated on a platform in fixed position. This is because OrcaWave in the version that was used can only account for movement by being fed a mooring stiffness matrix and calculate motion RAOs in this way instead of using an external RAO input. This is a constraint of the software which does not work well for TLPs with angular lines, since the mooring system cannot be fully linearised around the rest position, and with a flexible tower which has an impact on the high-frequency resonant response. Instead, the methodology adopted in this thesis is to apply QTFs loads in the time-domain solver on the instantaneous position of the floater. This generates quadratic forces due to the rotation of the rigid body (Equation 3.29) as well as indirectly provide the inertia correction due to the

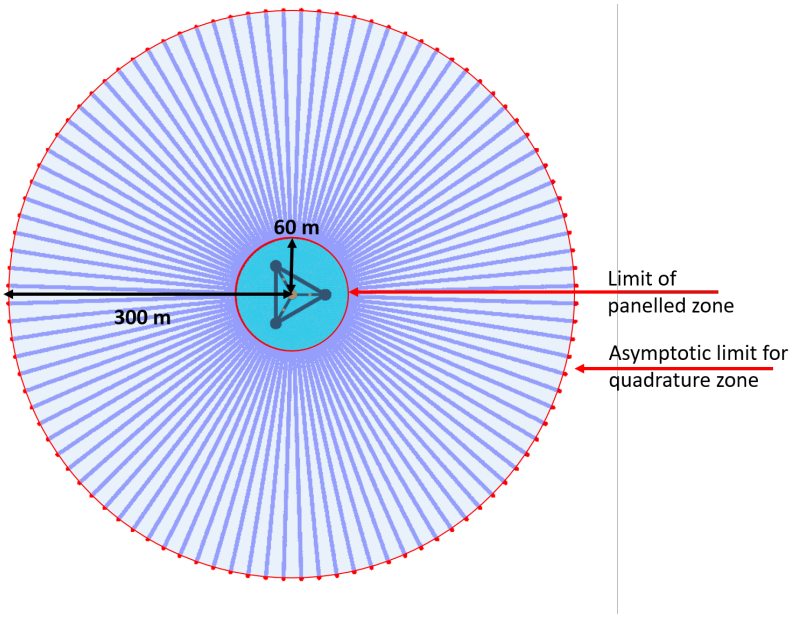


**Figure 5.5:** Plan of the free surface panelled zone and quadrature zone

movement of the floater (Equation 3.28). It will also create some third-order effects with the same principles. The only motion effect that is ignored in this methodology is the impact of radiated waves on the first-order potential and the free surface integral. However, considering that the TLP remains a relatively non-compliant structure with a slender hull shape compared to barge or semi-submersible FOWT, these effects can be assumed to be less significant. Furthermore, this method is resilient to changes in the mooring system or other parameters that can affect the RAOs without changing the static position of the floater. This is a useful approach for designs that have not converged yet since obtaining full QTFs can be time-consuming.

### 5.2.2 Full strip theory approach

#### Calibration of added mass coefficients

The added mass coefficients used for the strip-theory are kept constant in this thesis instead of using $K_C$ dependent values based on empirical data (Sarpkaya, 1986). Instead, the coefficients have been calibrated against the linear transfer functions calculated by BEM on individual elements. The transverse added mass coefficient for the transition piece and bracing are kept to a typical slender element value of $C_{A,t} = 1.0$ as these coefficients appeared to perform relatively well. On the other hand, the side buoys with their low aspect ratio required a lower added mass coefficient. The calibration of the coefficient against simple cylinders is successful as attested by Figure 5.7 which shows the good performance of the calibrated Morison model against a BEM model of the side buoys without considering the bracings

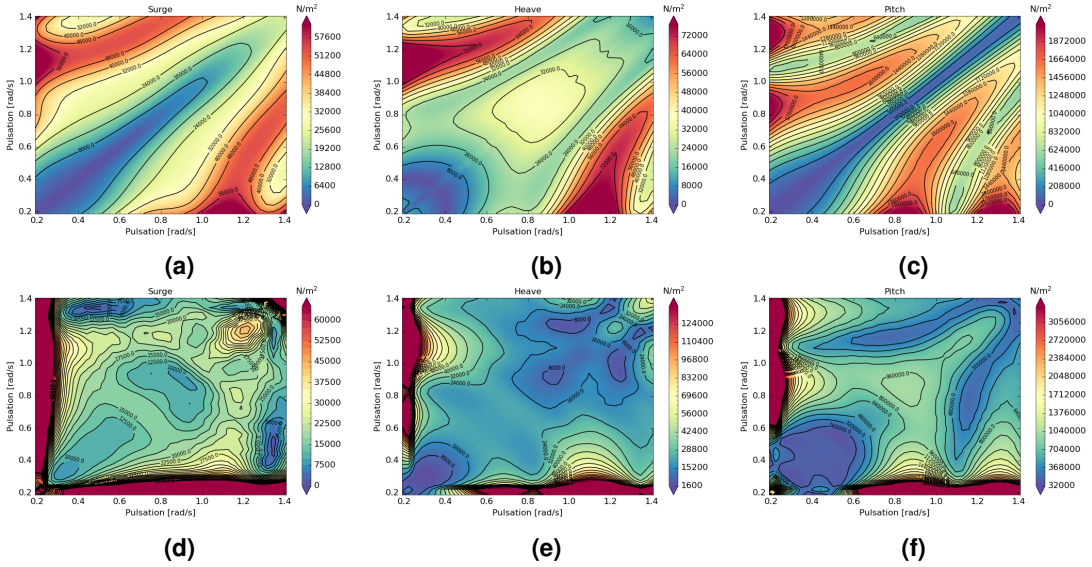


**Figure 5.6:** Quadratic Transfer Function matrices obtained with OrcaWave for the (a)(d) surge, (b)(e) heave force and (c)(f) pitch moment for the difference (top) and sum-frequency (bottom) components respectively

connection. The presence of the large bracing connections reduces the total vertical surface of the cylinder by around 10% which results in a significant increase of the surge force around $f = 0.10$ Hz. This is observed in the same Figure 5.7 where the blue dashed line represents the result from a BEM model considering the "holes" created in the hull by these bracings.

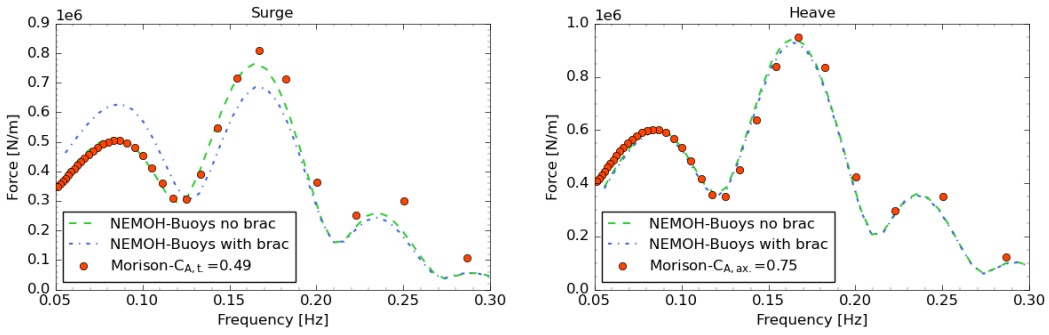


**Figure 5.7:** Result of the calibration of the transverse and axial added mass coefficients for the side buoys against BEM models with and without inclusion of the connection to bracings

### Selection of drag coefficients

The transverse drag coefficients for the transition piece and bracing are based on typical values for slender cylinders (Chakrabarti, 1987; DNV-GL, 2010; Molin, 2023). These values have been reduced for the side buoys based on their low-aspect ratio as per guidance provided in DNV-GL (2010). For the axial drag generated on the end of the cylinders, values have been roughly estimated based on current numerical and experimental measurements on various sharp angle sections (Keulegan & Carpenter, 1958; O'Brien & Morison, 1952; Thilleul, 2014; Venugopal, Varyani, & Westlake, 2009). It is recognised that, in the future, specific KC dependent drag coefficients should be used for each individual sections and wave condition.

## 5.2.3 Summary of engineering load models

A summary of load models is displayed in Table 5.1 and Figure 5.8 with details on the wave kinematic theory being used and on the elements being compared along with their respective added mass and drag coefficients. Added mass coefficients used in the strip-theory models have been calibrated based on BEM solution for individual elements as explained above.

| Model | Elements | Potential Flow | | | Strip theory | Coeff. | | Drag | Coeff. | | Wave theory |
|---|---|---|---|---|---|---|---|---|---|---|---|
| | | $F^{(1)}$ | $F^{(2)}$ | $F^{(3)}$ | $F^{(2)}$ & $F^{(3)}$ | $C_{A,t}$ | $C_{A,ax}$ | $F_D$ | $C_{D,t}$ | $C_{D,ax}$ | $\vec{u}(t), \vec{u}(t), \eta(t)$ |
| EDF TLP | Transition piece | SEM: HET | SEM: HET | SEM: MM | Rain. | 1.0 | -0.11 | Mor. | 1.0 | 2.0 | SF |
| | Side buoys | BEM LTFs | BEM QTFs | - | Rain. | 0.49 | 0.75 | Mor. | 0.6 | 4.0 | SF |
| | Bracings | BEM LTFs | - | - | Rain. | 1.0 | N/A | Mor | 1.0 | N/A | SF |

**Table 5.1:** Parameters of engineering numerical approaches used on the EDF TLP. HET refer to Huang and Eatock Taylor (1996); MM refer to Malenica and Molin (1995); Rain. refer to Rainey (1989, 1995); SF refers to Stream Function (Dean, 1965)

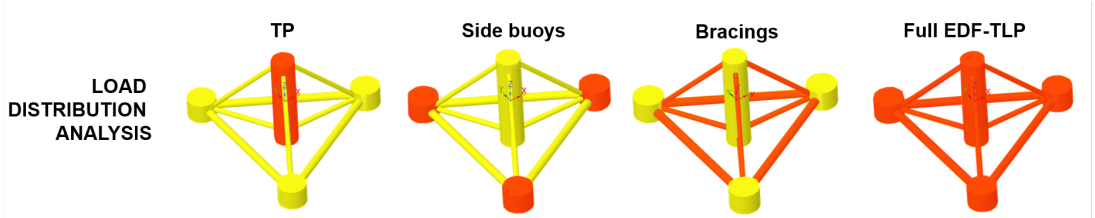


| ENG. MODELS | Inertial | Drag | Inertial | Drag | Inertial | Drag | Inertial | Drag |
|---|---|---|---|---|---|---|---|---|
| Potential flow | SEM: $1^{st}$,$2^{nd}$,$3^{rd}$ | - | BEM[1]: $1^{st}$,$2^{nd}$ | - | BEM[1]: $1^{st}$ | - | BEM (+TP SEM) $1^{st}$,$2^{nd}$ ($+3^{rd}$) | - |
| DIEGO-Rain | Rainey | - | Rainey | - | Rainey | - | Rainey | - |
| DIEGO-Rain+D | Rainey | Morison | Rainey | Morison | Rainey | Morison | Rainey | Morison |

**Figure 5.8:** Summary of engineering load models applied on elements of the platform

## 5.3 Set-up of CFD model

The same set-up methodology has been used for the neptune_cfd NWT as is presented in Section 4.3.2 with a minimum of 320 cells per wavelength in the $x$ direction. The EDF-TLP is represented in the CFD model with the same porosity wall approach presented in Section 3.3.2. In this situation, instead of defining a geometric function, the CAD mesh of the EDF-TLP is imported into neptune_cfd. The code then removes the solid body cells from the Cartesian mesh and the interface cells are identified and are sub-meshed along the solid wall border. Due to the small diameter of some of the bracings, and as the method requires a minimum of 2 to 3 cells per bar element, it results in a minimum discretisation of 0.5 m per cell in the working zone. Since the method uses a Cartesian mesh with a geometrical progression outside of the working zone, this can result in a large number of cells for high-period waves. Similarly, due to the increased size of the platform, the working zone length and width have been limited to a minimum of 2.5 structure length. This also can lead to an increase of the number of cells at low wave periods. On top of that as stated in Section 4.3.2, the width of the tank is increased qualitatively with increasing scattering parameters so as to reduce the reflection of diffracted waves on the symmetry walls. The summary of the tank flume geometry is provided in Figure 5.9 and a detail of one simulation is provided in Figure 5.10.

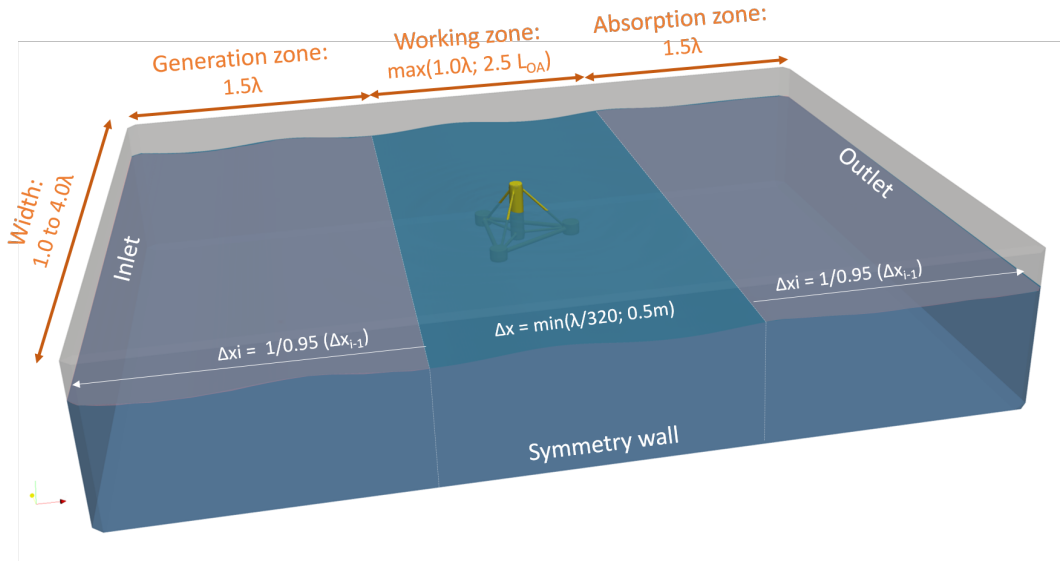


**Figure 5.9:** Geometry of the CFD NWT for the EDF-TLP

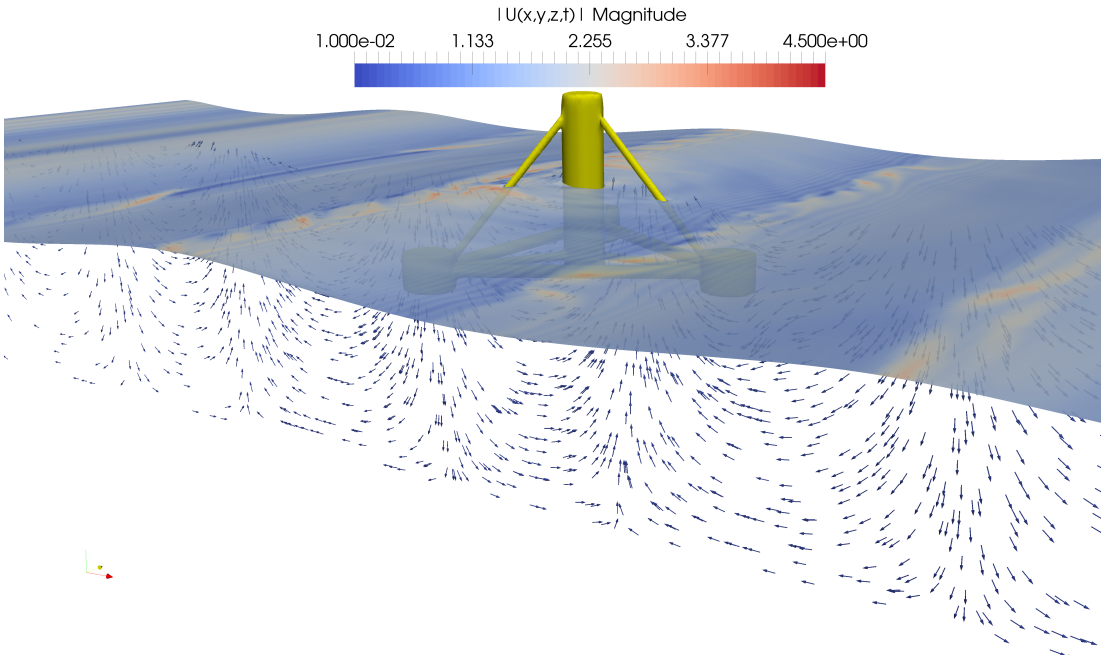


**Figure 5.10:** Screenshot of the EDF-TLP neptune_cfd model in wave of period $T = 9$ s

## 5.4 Comparison of linear and high-order load models in regular waves

Originally, the paper that was submitted focused on high-order loads and, as such, it only presented and discussed the second and third-order harmonic force transfer functions. For the purpose of this thesis, the linear force transfer functions have also been added in Figures 5.11, 5.12, 5.13 and 5.14. These are on the left-hand side of each row with one row per load DoF. This addition to the original paper is to showcase both the relatively good calibration of added mass coefficients for individual elements against BEM models and to validate the linear potential-flow and strip-theory approaches against the CFD results. Therefore a short commentary on the performance of the linear engineering load models against the CFD is given. Then, the high-order sum-frequency force transfer functions are analysed on the whole platform. The forces generated on the main elements are first analysed to understand their respective contributions to the total transfer function of the platform. Particular attention is given to the addition of the viscous Morison drag to the strip theory model.

### 5.4.1 Force transfer functions on the transition piece

The force transfer functions on the transition piece are presented in Figure 5.11a-i. The strip theory numerical models (dashed and dotted lines) are compared against existing potential flow semi-analytical solutions (red diamonds), and the CFD results (green circles) for the transition piece of the EDF-TLP floater. The previous CFD results for the truncated cylinder alone are also shown for reference in grey circles. The difference between grey and green circles highlights the impact of having a complex structure built around the truncated cylinder on the force harmonics. The first-order force transfer functions are provided respectively for surge, heave and pitch in Figures 5.11a, 5.11d and 5.11g, for second-order in Figures 5.11b, 5.11e and 5.11h and for third-order forces in Figures 5.11c, 5.11f and 5.11i with normalised amplitudes on top and phases on the bottom. The $x$-axis at all-order uses the scattering parameters based on the fundamental frequency of the carrier-wave.

Starting with the linear force transfer functions, Figure 5.11a,d,g shows that all models agree relatively well in surge and pitch until first-order diffraction becomes significant at $ka = 0.6$. For the heave linear force, all models agree in amplitudes including the strip theory models due to the good calibration of the added mass coefficient. For higher orders, a first general observation which can be extended to all figures presented in this section is that the phase prediction of the strip theory inertial models is inadequate. As reported in Section 4.5.2, these approaches assume a force in phase with the incident wave field kinematics, an approximation only valid at low frequencies, below $ka = 0.10$ for second-order forces and $ka = 0.05$ for third-order forces. The addition of the drag component improves the prediction in surge (Figure 5.11a) at very low frequencies but tends back to the inertial model as frequency increases. On the other hand, both amplitude and phases of the force transfer functions predicted by the various semi-analytical solutions show trends very similar to the CFD results.

As seen in Section 4.5.2, the results of the second-order force on the transition piece in surge and pitch (Figure 5.11b and 5.11h) show that the CFD results tend to follow very well the semi-analytical prediction. The results of the hydrodynamic interaction between the transition piece and the remainder of the structure, submerged buoys and bracings, do not fundamentally change the force amplitude trend. In Figure 5.11b and 5.11h the CFD amplitude results on the TP (in green) seem to oscillate around the CFD results of the truncated cylinder alone (in grey). Differences in amplitudes of up to 50% are observed as seen at $ka = 0.72$. In terms of the surge and pitch force phase, the buoys and bracing do not appear to lead to a large shift when compared to the CFD results on the truncated cylinder although larger discrepancies are observable at higher frequencies.

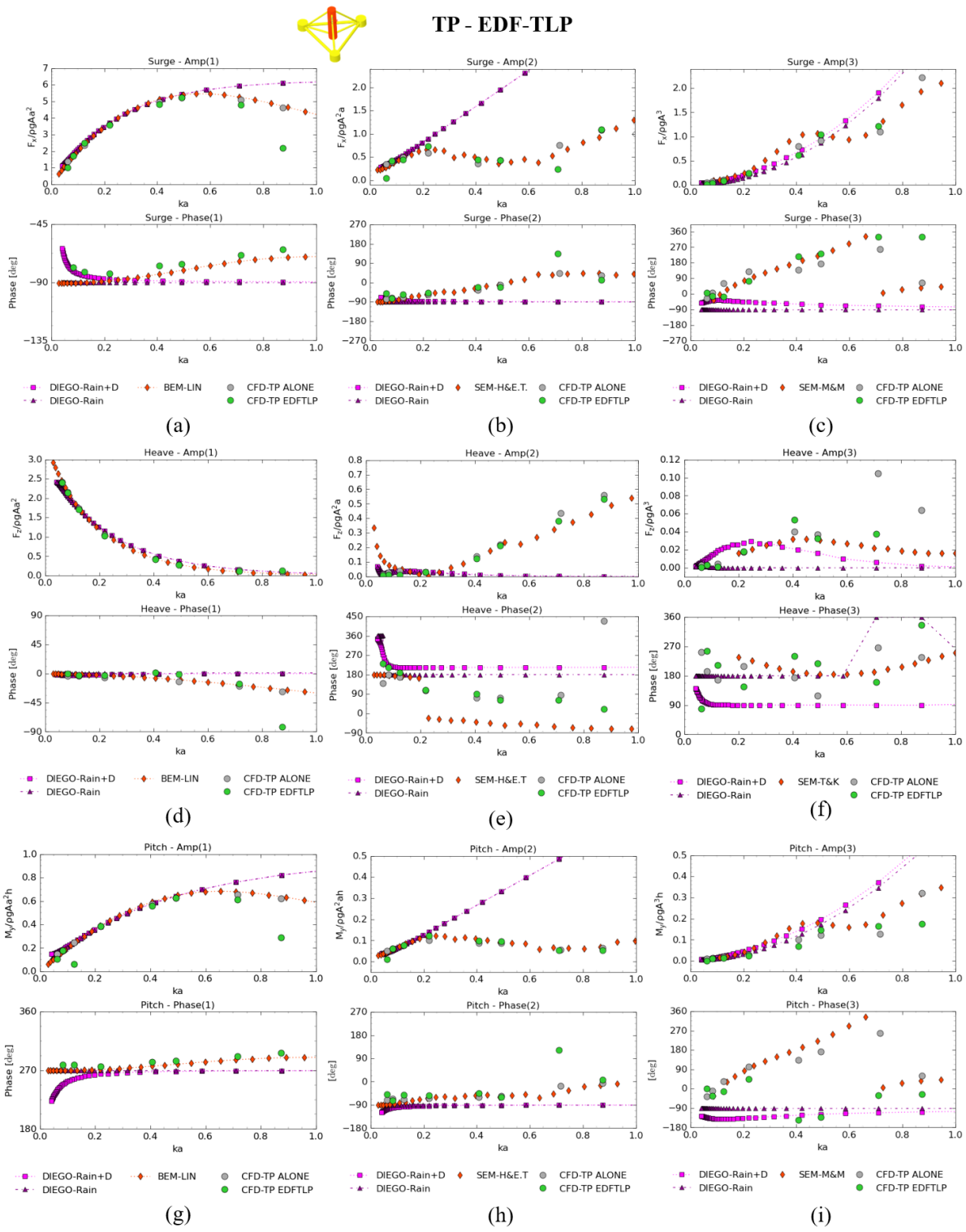


**Figure 5.11:** Comparison of normalised first, second and third-order surge (a)(b)(c), heave force (d)(e)(f) and pitch moment (g)(h)(i) transfer functions on the **TP** of the EDF-TLP

The second-order heave force transfer heave functions are also compared in Figure 5.11e. The amplitudes predicted by the CFD appear to follow very well the potential-flow semi-analytical results beyond $ka = 0.2$. Below that value, the second-order heave amplitudes predicted by both CFD model results tend towards zero while the semi-analytical potential flow predicts increasing amplitudes. Considering the relative agreement between the two CFD results (grey and green), it seems that the presence of the buoys and bracings does not significantly impact the amplitude of the heave force on the TP above $ka = 0.2$. The CFD results for the second-order heave force phase show a much less significant phase shift at $ka \approx 0.2$ than the semi-analytical predictions. Finally, comparing these results with the strip-theory models predictions highlights the significant underestimation of the heave force amplitudes by the Rainey approach beyond $ka \approx 0.2$ although the agreement with the truncated cylinder CFD model seems to be good under that value.

A similar observation to the second-order transfer function case can be made for the third-order surge and pitch force transfer functions. Similarly, the addition of the other elements of the structure does not seem to impact significantly the trend of the force amplitudes on the TP. The TP CFD model (green) follows the semi-analytical solution of Malenica and Molin (1995) (SEM-M&M), and oscillates around the truncated cylinder CFD results (grey). The CFD results on the TP actually appear in several cases to be coincidentally closer to the semi-analytical solution possibly due to the complex hydrodynamic interactions with the remainder of the platform. Looking at the strip theory models, the predicted amplitudes appear to provide still a good estimate of the CFD results up to $ka = 0.5$ with or without drag. The addition of the drag force improves slightly the results of the amplitudes at very low frequencies below $ka = 0.10$ and as expected its effect is negligible at higher frequencies for $KC \leq 1.0$. As mentioned in the case of the truncated cylinder, the phase error on the third-order horizontal and resulting moment force is significant even at low frequencies. The addition of the drag force appears to improve the results on the surge force phase in Figure 5.11c at low frequencies. However, this match could be entirely coincidental, considering that semi-analytical potential force also matches well with the CFD despite being purely inertial.

Looking at the third-order heave force, Figure 5.11f, the inertial strip theory model on its own does not appear to predict significant heave amplitudes in comparison to the CFD results. The CFD results of the truncated cylinder and the TP appear to match relatively well, although the difference increases with increasing $ka$ which could be due to increasing hydrodynamic interaction with the remainder of the platform structure in the full EDF-TLP model. The addition of drag to the strip-theory model appears to improve the match with the CFD at frequencies below $ka = 0.2 - 0.7$. However, using Teng & Kato's published semi-analytical references for a vertical truncated cylinder of dimension $d/a = 3$ and $h/a = 10$,

a similar match in transfer function is found from their purely inertial potential flow model. Therefore, whilst the horizontal force and the induced moment are relatively well captured by strip-theory engineering methods, the inertial heave force prediction appears as a weakness and might only partially be compensated by taking into account the drag force.

### 5.4.2 Force transfer functions on submerged buoys

Here the force transfer functions contribution of the buoys to the surge, heave force and pitch moment (referred to at the keel of the TP) is provided in Figure 5.12. As per above, the predictions of the strip-theory models are compared against the CFD results. For first and second-order, the LTFs and the QTFs diagonal are calculated using a BEM model containing only the submerged buoys (red diamond). This provides partial information on the potential flow diffraction solution. This is done since OrcaWave does not allow access to the second-order potential on individual panels. Therefore, the potential flow model (BEM-QTFs) does not take the interaction of the buoys with the TP into account and hence serves as an indication of the Froude-Krylov and diffraction forces generated by the buoys alone. At third-order, no reference solution exists since no semi-analytical model has yet been developed for such geometry.

Starting with the linear forces, given in 5.11a,d,g, these transfer functions are akin to the results of Figure 5.7 with the same small under-prediction by the strip-theory model of the amplitude of the surge force predicted by BEM and CFD around $ka = 0.16$. On the other hand, the phase angles predicted by the CFD agree with the phases predicted by the strip theory models, highlighting that on these submerged elements, the wave force is dominated by the incident potential pressures without a significant impact of wave scattering.

Moving on to the higher-orders and starting with the second-order forces in Figure 5.12b, 5.12e and 5.12h, it can be observed that at low frequencies, the amplitude of the transfer function of the CFD results (green circles) and the potential flow (BEM-QTFs in red squares) model tend to agree up to $ka = 0.25$. Over this value, it appears that diffraction induces stronger interaction between the TP and the buoys leading to an increase in load. The strip-theory predictions for the second-order surge amplitudes in Figure 5.12b also appear to be relatively in good agreement with the CFD at low frequencies, until $ka = 0.20$. Beyond this value, the strip-theory models significantly underestimate the surge force transfer functions compared to the QTFs and CFD solution. However, the validity limit for the second-order surge amplitude predicted by these models appears similar to that of the TP. This is relatively surprising for buoys with an aspect ratio close to $a/b = 1$ which do not respect the slender element assumption. However, their diameter does not diverge much from that of the TP and hence the long-wave approximation appears to remain valid. Furthermore, when looking

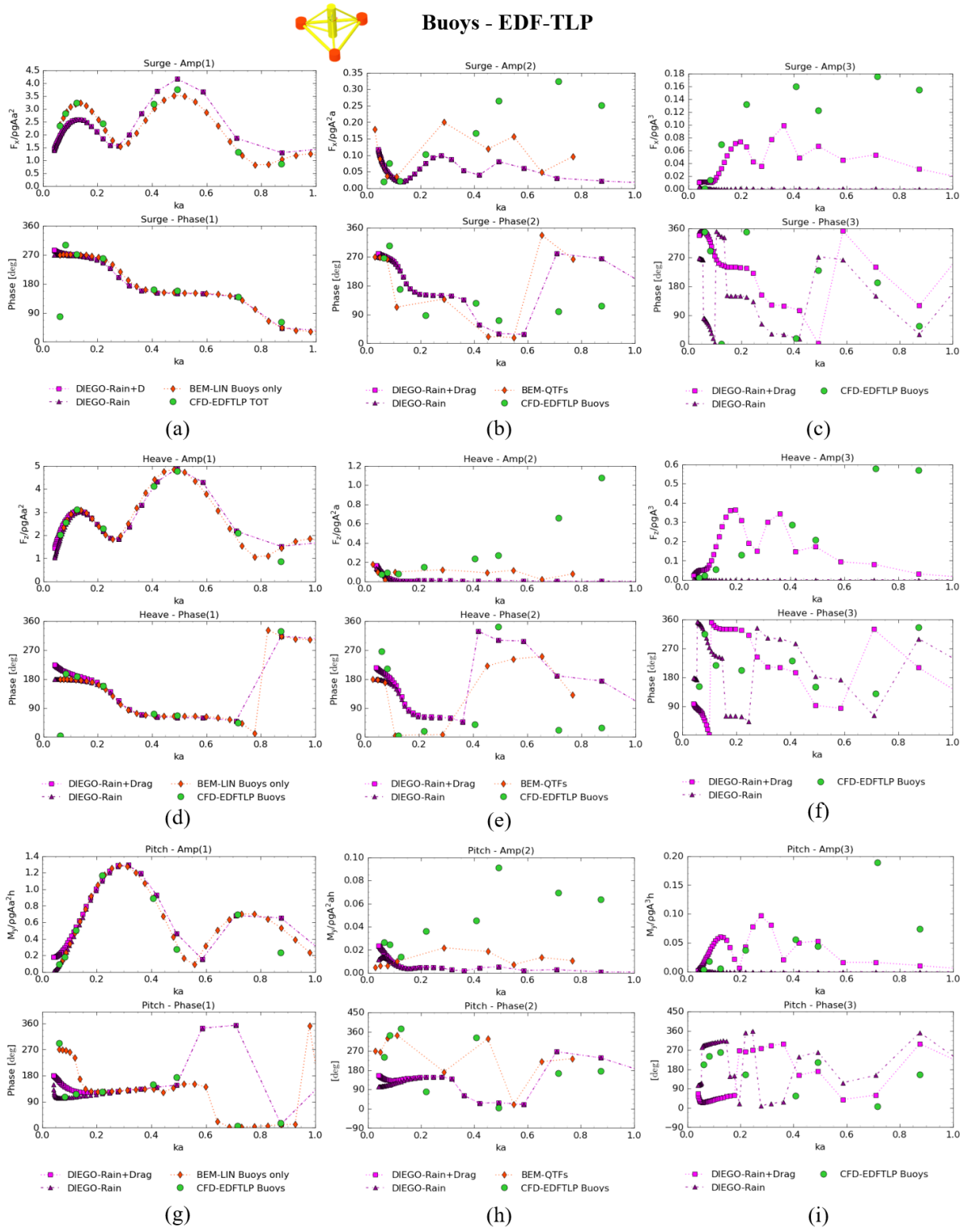


**Figure 5.12:** Comparison of normalised first, second and third-order surge (a)(b)(c), heave force (d)(e)(f) and pitch moment (g)(h)(i) transfer functions on the **side buoys** of the EDF-TLP

at the phase of the transfer functions, it is observed that the strip theory results remain relatively in good agreement with both the CFD and QTFs results until $ka = 0.5$. The picture is similar for the second-order heave force, and the pitch moment which, in the case of the submerged buoys, is dominated by heave contributions. The strip theory model predictions for the amplitudes appear valid at lower frequencies, below $ka \approx 0.15$. On the other hand, beyond that value, the phases predicted by the strip theory do seem to maintain a similar trend to the CFD and QTF reference. The benefit of adding drag to the strip theory model is not very noticeable at second-order. However, it appears to improve the predictions at low frequencies between $ka = 0.05 - 0.015$ in Figure 5.12h showing the pitch transfer functions. The addition of drag results in a similar upward trend in the pitch moment amplitudes than predicted with the CFD whereas both the purely inertial strip-theory model and the reference QTFs suggest decreasing amplitudes with decreasing frequency.

Looking at the third-order surge force transfer functions on the buoys of Figure 5.12c, 5.12f and 5.12i, it is clear that the strip theory inertial model strongly underestimates all the third-order force amplitudes which are clearly negligible in comparison to the CFD predicted amplitudes. However, an interesting observation is the relatively good agreement in all of the phases between strip theory predictions and CFD, similar to what is seen at second-order. The addition of drag to the strip theory model appears to lead to a significant increase in force and a better match with the CFD results. This is especially visible in the third-order heave and pitch force transfer functions, which are strongly correlated, between $ka = 0.2 - 0.6$. Furthermore, the addition of the drag force appears to correct the strip theory model surge phases to match with the CFD at low frequencies below $ka = 0.2$ in Figure 5.12c.

### 5.4.3 Force transfer functions on bracings

This section concerns the analysis of the force transfer functions on the platform bracings provided in Figure 5.13. In Figure 5.13a,d the surge and heave linear transfer functions calculated with strip-theory and the reference BEM model with the bracings structure only agree moderately with the CFD results at higher frequencies. The simple drag model adopted here can probably explain this discrepancy with $K_C$ numbers on the surface piercing bracings elements expected to be around one order of magnitude higher than for the TP. On the other hand, the agreement between the BEM reference model and the CFD is surprisingly good on the pitch moment in Figure 5.13g. Without further analysis, the assumption is that the heave force on the large horizontal bracings is the dominating contribution to the pitch moment which leads to better results in pitch than surge and heave.


**Figure 5.13:** Comparison of normalised first, second and third-order surge (a)(b)(c), heave force (d)(e)(f) and pitch moment (g)(h)(i) transfer functions on the **bracings** of the EDF-TLP

From the results of the second and third-order force generated on these elements, it is observed that the strip-theory models inertial component provide a decent estimation of the second-order surge force and a very approximate prediction of the second-order heave force. The addition of drag has a major impact on third-order forces as is observed previously on the buoys. Although the drag coefficients have not been calibrated and are kept constant, the addition of drag appears to yield a significant improvement in the prediction of third-order force amplitudes. Specifically, the prediction of the third-order surge force and resulting pitch moment in Figure 5.13c and 5.13i matches relatively well with the CFD results between $ka = 0.2 - 0.6$. The trend of the phases is less clear but the addition of drag still appears to provide a better estimation. For the third-order heave force, the addition of drag also leads to a better trend.

### 5.4.4 Force transfer functions on entire platform

The total first, second and third-order surge, heave force and pitch moment transfer function for the whole EDF-TLP floater are shown in Figure 5.14. The potential flow diffraction solution on the full platform is obtained at second-order using full QTFs calculated by BEM and at third-order, using the semi-analytical solution on the TP alone as the only potential flow reference.

Overall, it is observed that the linear force transfer functions' amplitudes predicted by the strip-theory for most elements are relatively representative of the BEM and CFD results. The CFD and BEM results on the full platform are in agreement which validates the BEM approach with the exception of small phase shifts at low frequency. This can likely be explained by the increasing influence of viscous effects at low frequency as corroborated by the visible influence of the Morison drag on the strip-theory model between $ka = 0.05 - 0.2$. For all submerged or mostly submerged elements (buoys and bracinsg), CFD, BEM and strip theory predict the same phase angle with the force being dominated by the incident potential pressure. Therefore, despite the relatively crude assumption of representing the structure as an assembly of cylinders, the results of the strip-theory linear models on the full EDF-TLP platform in Figure 5.14a,d,g appear relatively successful. Apart from the underestimation of the surge force by the buoys which is reflected on the total surge force amplitude at $ka = 0.16$ in Figure 5.14a, and from the diffraction parameters at high scattering parameters, the strip-theory transfer functions provide a relatively good prediction of the BEM linear force amplitudes and phase angles.

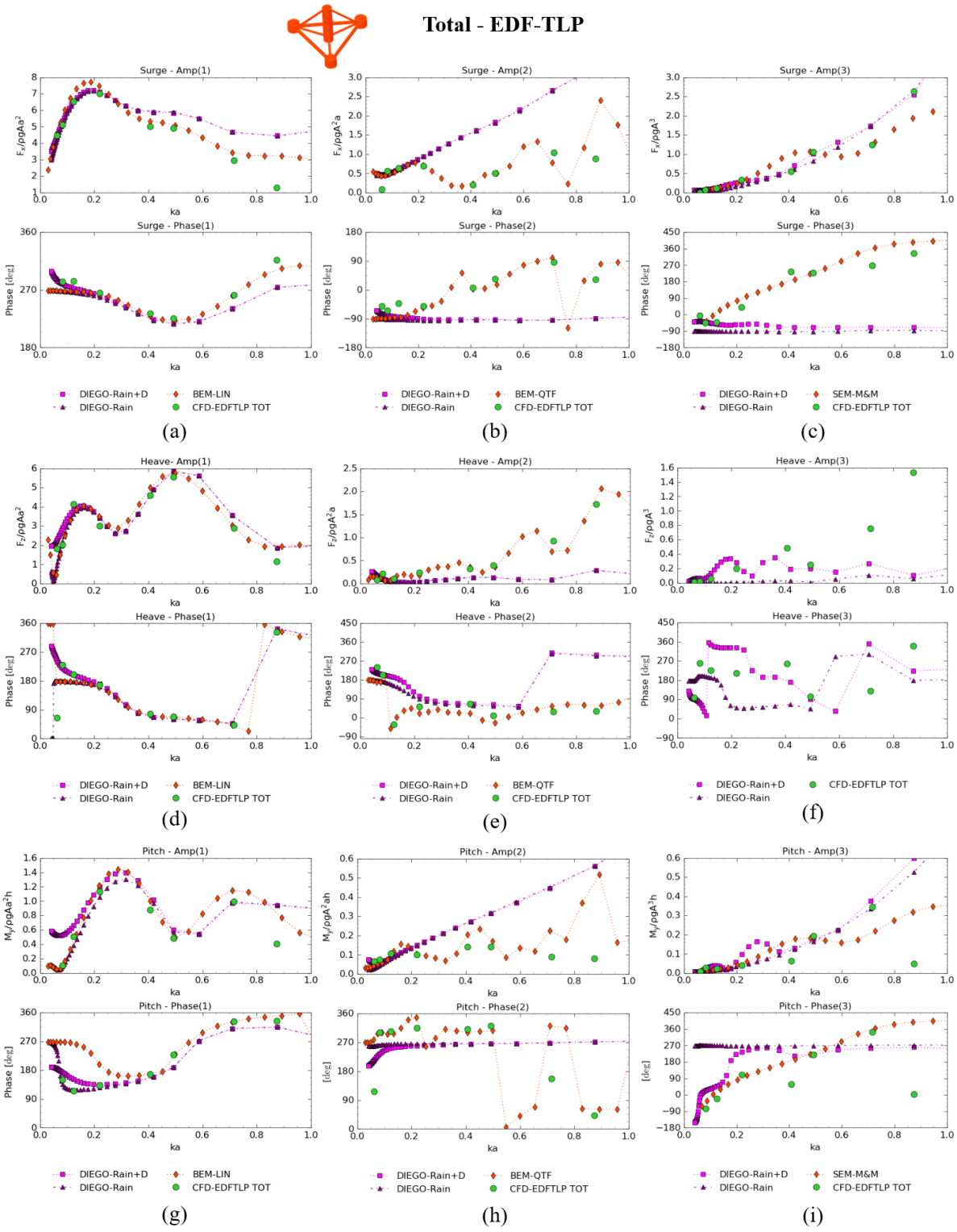


**Figure 5.14:** Comparison of normalised first, second and third-order surge (a)(b)(c), heave force (d)(e)(f) and pitch moment (g)(h)(i) transfer functions on the **full** EDF-TLP floater

Looking then at second-order transfer functions, it can be seen that the results of the CFD transfer functions agree well with the sum-frequency QTFs diagonal for all forces and moments. The amplitudes of the surge force and pitch moment of the strip-theory models agree well with the QTFs and the CFD results at low frequencies similar to what is reported above on the other platform elements. The heave force predictions appear to follow what is observed on the submerged buoys. The force is underestimated by the strip-theory models while the phases appear to be relatively correct. The addition of viscous drag appears to correct slightly the phase prediction of the inertial strip theory model in both surge and heave at low frequencies.

Analysing the third-order transfer functions in Figure 5.14c and 5.14i, it can be observed that the semi-analytical results for the third-order diffraction force on the TP on its own still provides a decent estimate of the amplitudes of both the surge force and pitch moment on the entirety of the floater. As observed above in the case of the submerged buoys, the third-order heave force is significantly underestimated by the strip-theory models. However, the addition of the viscous drag to the strip theory model has a major impact on the prediction of the heave and pitch force transfer function amplitudes. Similar to the buoys, the addition of drag appears to lead to a better estimate of the third-order heave force. There also appears to be a noticeable improvement in the predicted phase of the strip theory model third-order surge force and pitch moment at low frequencies when compared to the CFD. However, the potential-flow semi-analytical model which is purely inertial provides a similar phase prediction. Therefore, without a full calibration of the drag coefficients on the platform and a reference third-order potential flow model for the submerged buoys, it remains unclear how physical this drag effect is.

### 5.4.5 Analysis of load distribution for two cases

Overall it appears that the CFD results tend to agree with potential flow solutions, whether these are semi-analytical or based on the panel method (BEM). Generally, the second-order force transfer functions on the transition piece appear quite different from the transfer function on the full platform. This is due to a significant contribution from the remaining elements of the platform. At third-order, the transfer functions on the transition piece predicted by the semi-analytical solution of Malenica and Molin (1995), restricted to surge and pitch, appear to be relatively representative of the transfer functions on the entire floater. This suggests that the dominant horizontal force is generated by the main surface piercing element which also dominates the pitch response. However, when looking at the distribution of high-order loads on the different structural elements of the EDF-TLP, the problem appears more complex. For that reason, a side-by-side comparison between the second and third-order high-frequency force amplitudes contributed by each element is undertaken.

Figure 5.15 and 5.16 display the normalised amplitudes of the second and third-order forces and moment on the different elements of the platform for the case, $T = 9$ s, $ka = 0.22$, and $T = 5$ s, $ka = 0.71$ respectively. The results of the CFD results and strip-theory models with and without drag are provided. The semi-analytical solution for the truncated cylinder is also provided in light red for reference. First, the second-order load distribution on the floater is analysed by looking at the upper half of Figure 5.15 and 5.16. This is followed by an analysis of the third-order load distribution shown in the lower half of those figures.

**Analysis of the distribution of second-order wave loads**

The distribution of second order-forces for both periods is analysed first. At period $T = 9$ s (top of Figure 5.15), the graph shows that, overall, the second-order surge force and relative force distribution appear rather well predicted by the strip theory models. The CFD results show that the TP dominates the surge force while the bracings and submerged buoys contribute equally to the remainder of the force. The strip theory models capture this tendency while slightly overestimating the TP contribution and underestimating the contribution of the bracings and buoys by a small margin. When the period decreases to $T = 5$ s (top of Figure 5.16) the contribution from the TP is largely overestimated by strip theory models as expected from a long-wave approximation approach. In comparison, the semi-analytical formulation appears to give a better prediction although still slightly overestimated. The force predicted at $T = 5$ s by the CFD shows that the buoys and bracings contribute almost equally in terms of amplitudes to the surge force than the TP with a slight dominance from the buoys. The strip-theory models predict again with good accuracy the bracings surge contribution but neglect those from the buoys.

For the second-order heave force at $T = 9$ s, the CFD results show that the buoys dominate the total amplitudes. The Rainey strip-theory model appears to estimate correctly the heave force on the TP but the most important contributions generated on the buoys and bracings are underestimated with drag having a very small effect. At period $T = 5$ s, the CFD predicts dominant contributions emanating from the buoys and TP. Both of these are however neglected by the strip theory models with or without drag. The contribution of the bracings is the only one to be captured with relative accuracy. The semi-analytical prediction appears again valuable with a good estimation of the heave force on the TP. Finally, looking at the second-order pitch moment amplitude distribution at period $T = 9$ s, it is observed from CFD results that the horizontal force on the transition piece dominates the moment, contributing to around two-thirds of the total amplitudes. On the other hand, at $T = 5$ s, the buoys replace the TP as the dominant contributor to the pitch moment. The contribution of the TP is significantly

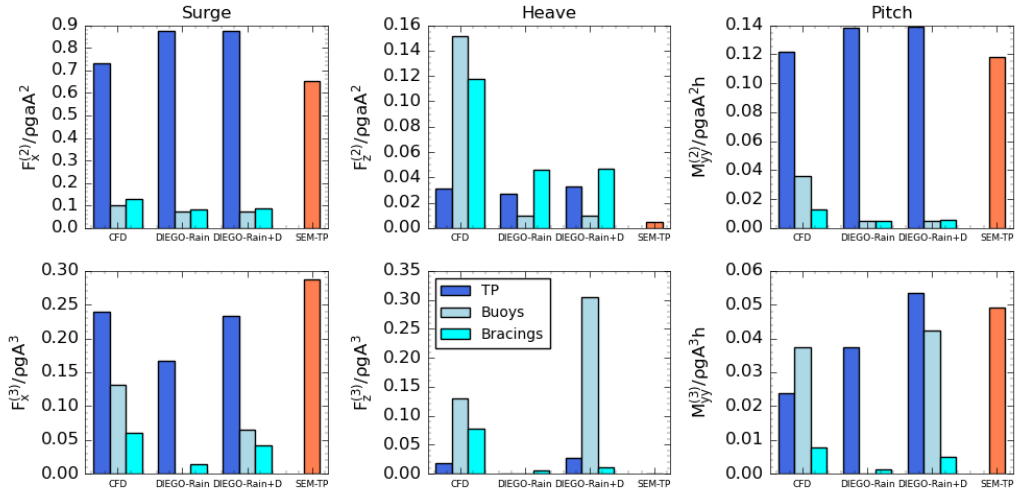


**Figure 5.15:** Normalised amplitude of the second and third harmonic forces for the different elements of the platform as predicted by CFD, Rainey and FNV models at period $T = 9$ s, $ka = 0.22$

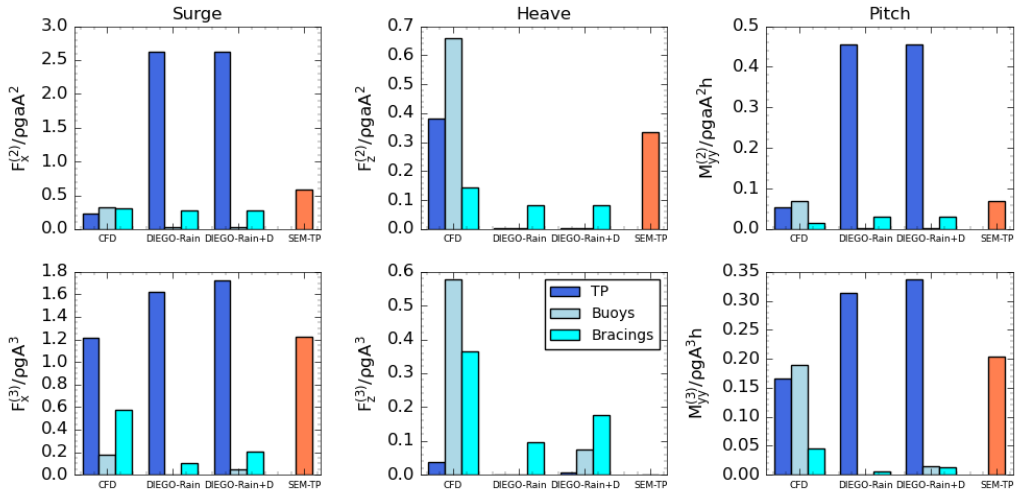


**Figure 5.16:** Normalised amplitude of the second and third harmonic forces for the different elements of the platform as predicted by CFD, Rainey and FNV models at period $T = 5$ s, $ka = 0.71$

overestimated by the strip-theory models as expected from the horizontal load predictions. Furthermore, as expected from the surge and heave results, negligible load contribution emanates from the buoys. Therefore, only the contribution from the bracing appears to be captured relatively well by the strip-theory at that period.

**Analysis of the distribution of third-order wave loads**

For the third-order force harmonics at $T = 9$ s (bottom of Figure 5.15), starting with the distribution of the surge amplitudes, it is observed that the CFD predicts that the TP dominates this force. The inertial strip-theory model predicts a slightly underestimated surge force on the TP, neglects completely the third-order surge contribution from the buoys and significantly underestimates the contribution of the bracings. However, the addition of drag leads to a significant improvement of the third-order surge force predictions with the capture of some of the contribution of the buoys and a better estimation of the contribution of both the TP and bracings. A similar observation is made at $T = 5$ s (bottom of Figure 5.16), with the addition of drag also improving the prediction on the buoys and bracings. It is interesting to note that the contribution of the bracings to the third-order surge force predicted by the CFD at that period is significant with an amplitude of around half of the contribution of the TP. Finally, as expected, the strip-theory inertial model overestimates the surge force amplitudes on the TP at that period due to the lower accuracy of the long-wave approximation whereas the semi-analytical potential flow model provides a better estimate.

For the third-order heave force, the CFD results show that the buoys dominate largely the contribution at both periods. The strip theory inertial models appear incapable of predicting a realistic third-order heave load with the only predicted but underestimated contribution emanating from the bracings. The addition of drag leads to a better approximation of the heave force on the TP and a small improvement of the prediction of the contribution of the bracings at $T = 9$ s. However, the dominant contribution of the submerged buoys is overestimated at $T = 9$ s and underestimated at $T = 5$ s.

The dominance of the buoys' contribution to the heave force amplitude is visible in the distribution of the third-order pitch amplitudes. Contrary to what could be concluded from the figures in the previous sections, the dominating elements contributing to the third-order pitch moment appear to be the buoys followed by the transition piece and then the bracings. This shows that in the case of a platform with large submerged elements, it might not be the horizontal force on the TP that dominates the third-order pitch excitation force. The inertial strip theory prediction of these contributions is rather poor. Another observation is that the contribution of the TP to the third-order pitch moment is overestimated both in Figure 5.15 and 5.16. This is despite the horizontal force being captured relatively accurately at $T = 9$ s. This suggests that the strip theory model might over-predict the contribution of the horizontal forces in the higher part of the water column leading to a longer lever arm than predicted

by the CFD. this would be a situation potentially similar to what is shown in the results of Kristiansen and Faltinsen (2017) for $ka > 0.2$ and reproduced in Figure 4.7i. The addition of the drag force to the strip-theory model significantly improves the prediction of the submerged buoys and bracings contribution at $T = 9$ s whilst mildly improving those at $T = 5$ s.

### 5.4.6 Discussion

From the results presented in the above sections, several points are to be discussed. The first one concerns the general accuracy of load models on the submerged buoys and bracings. The second point looks at the accuracy and usefulness of the potential flow approach, both semi-analytical and BEM-based, with regard to the CFD results.

#### Inertial and drag force on submerged buoys and bracings

A point of attention arising from the submerged buoy transfer functions results presented in Section 5.4.2 and the analysis of the high-order loads distribution on the EDF-TLP presented in Section 5.4.5, is that the third-order loads on these stocky elements are not well captured by the strip-theory inertial model. This is expected partly because their low-aspect ratio does not respect the slender element assumption. The CFD analysis also shows that these elements contribute significantly to the sum-frequency forces, being even the dominant contribution to the third-order pitch moment in the range of frequency likely to generate springing responses. Since TLPs' high-frequency resonant responses are generated in the vertical degrees of freedom, these elements of the EDF-TLP are a source of significant inaccuracies in the engineering load models. Whilst this is not a major issue at second-order due to the availability of industry BEM solvers capable of computing full QTFs, at third-order no such models exist. However, the close match between the phase predicted by the CFD and the phases predicted by the inertial strip-theory model in all directions leads us to suppose that the diffraction effects might not be as important on these submerged elements and that the dominant inertial high-order contribution could stem from the incident potential and dynamic pressure terms. The analysis of the second-order components in Section 4.5 shows that the phase of the second-order dynamic pressure term on the surface piercing truncated cylinder remains in fact close to the strip-theory (See Figure 4.16). Furthermore, the linear transfer functions results corroborate findings from Li and Liu (2019) who demonstrated through a semi-analytical solution that the first-order force could be estimated relatively well using Froude-Krylov theory for such fully immersed geometries. This means that without large first-order scattering, the force contribution from the third-order scattered potential is likely mostly negligible. If that hypothesis happens to be accurate at third-order, this inaccuracy in the model could be partially solved by

developing a second-order semi-analytical solution for submerged truncated vertical cylinders using the work of Abul-Azm and Williams (1988) and Huang and Eatock Taylor (1996). This would allow for the computation of the terms $F_{x1}^{(3)}$ and $F_{x2}^{(3)}$ which include the third-order dynamic pressure terms involving the first and second-order potentials.

As for the bracings, it appears that their contribution to the third-order force is also not negligible albeit smaller than the buoys. Whilst at second-order they are reasonably represented by the strip-theory model due to their slenderness, the third-order inertial strip-theory model does not appear very accurate. However, the trend of the force transfer functions remains relatively respected and with a lack of other alternatives, it provides for a decent approximation. The addition of the viscous drag force to Rainey's strip-theory model results in significant changes in terms of predicted third-order force amplitudes, especially for the bracings and the buoys.

Generally, the addition of drag seems to improve significantly the predictions on the bracings and the submerged buoys although the accuracy on the buoys is not as clear. Both transverse and axial drag coefficients have been kept constant in this study, and the author recognises that ideally this coefficient should be calibrated to improve comparisons.

**The usefulness of the semi-analytical solution**

From observing the results of the semi-analytical solutions for the TP and their relative accuracy with regard to the CFD results, it appears that these solutions constitute useful references for engineering models of truncated cylinders. At second-order, since most BEM solvers can already calculate QTFs for complex structures, the solution of Huang and Eatock Taylor (1996) does not constitute a major addition to the engineer's toolbox. In situations involving early-design stages and optimising loops, this method could however be beneficial by removing the need for meshing and convergence studies that are needed in the BEM approach as discussed in Rongé, Peyrard, Venugopal, et al. (2022). At third-order however, the semi-analytical solution of Malenica and Molin (1995) constitutes an important benchmark to assess harmonic loads on surface piercing truncated cylinder structures due to the absence of other frequency domain potential flow models. Furthermore, the transfer function results for the full platform suggest that at high frequency, this semi-analytical solution constitutes potentially a better approximation than the strip-theory with regards to both amplitudes and phases. This can serve as a calibrating tool for choosing the strip-theory approach to be used in irregular sea-states as their respective accuracy with regards to the CFD results or the semi-analytical formulation varies depending on the range of frequencies considered as discussed

above. However, as seen in Section 5.4.5, this does not solve the issue of capturing the high-frequency loads on the buoys, meaning that in our case the accuracy of the semi-analytical solution with regards to the CFD is also somewhat coincidental and due to an amplitude and phase combination that is unique to the platform geometry.

## 5.5 Summary

This chapter followed the proposed methodology presented in Chapter 4 and investigated the accuracy of engineering methods (Rainey's equations and potential flow semi-analytical or BEM solutions) by comparing the force harmonics transfer functions predicted by these engineering load models on the full EDF-TLP floater in fixed position against results from the Numerical Wave Tank. The CFD NWT solver used for this research allowed the representation of the complex hull structure and its boundary conditions using a porosity wall method instead of using an explicit mesh. The following concluding remarks are derived.

In terms of the linear force, the calibration of the strip-theory added mass coefficients appears relatively successful at representing the hydrodynamic loads on a complex EDF-TLP floater by using a simple assembly of cylinders. This is especially true for the side buoys' for which the BEM linear force transfer functions remain in phase with the strip-theory force predicted by Morison's equation, therefore in phase with the incident potential. This suggests that there is limited first-order hydrodynamic interaction between these immersed elements and the surface-piercing TP. Furthermore, the BEM solution for the linear and quadratic transfer functions on the full floater is in good agreement with the CFD results. This is with the exception of a phase shift at the lower fundamental frequencies observed in the LTF which is most likely due to the increasing importance of viscous drag. At second-order, the strip-theory Rainey model generally proves to be inadequate for the large elements of the platform beyond $ka = 0.2$, that is the TP and the side buoys.

Moving to third-order loads, the application of the semi-analytical solution of Malenica and Molin (1995) provided a relatively accurate estimate of the third-order force on the transition piece both in terms of amplitudes and phase when compared to CFD results. However, the amplitudes are found to be generally overestimated, similarly to the observation of Huseby and Grue (2000) and as pointed out in Section 4.5. The strip theory models also showed good predictions of force amplitudes but were less accurate in predicting phases of the high-order forces. This showed that the semi-analytical solution represents a useful benchmark and calibration tool for the strip theory inertial approaches in monochromatic wave cases. The heave forces on the submerged buoys were found to contribute significantly to the third-order pitch moment. This is an effect that is neglected by the strip theory inertial models. Although

the addition of the Morison axial drag force improved the results, this remains a source of inaccuracy since strip-theory methods are the only engineering approaches available to calculate third-order inertial effects for complex geometries. On the assumption that most of the high-frequency forces are due to dynamic pressure effects, a second-order semi-analytical potential flow solution following the same method as in Huang and Eatock Taylor (1996) could provide partial third-order solutions for the heave force and resulting pitch moment. This also shows the design advantage of a simpler floater geometry such as a truncated vertical cylinder with legs, which can be approximated well using calibrated strip theory models or semi-analytical potential flow diffraction solutions.

This chapter therefore demonstrated the relative accuracy of the various engineering approaches on the EDF-TLP floater in fixed condition. With the next part of this thesis dealing with testing the system in dynamic condition, the combination of high-order models to choose from appears clearer. As much as Rainey's strip-theory manages to capture the linear transfer functions relatively correctly and seems to provide a decent estimate for the third-order loads on the TP, at second-order it proves to be significantly inaccurate. For that reason, a QTF model combined with third-order FNV or semi-analytical solution is definitely preferable. On the other hand, it is still worth testing how simpler models which can be implemented at early design stages would perform in dynamic conditions such as full strip theory models or a hybrid model using a mix of semi-analytical and strip theory approaches.

# PART III

# Model application to a floating offshore wind TLP in dynamic condition

# Chapter 6

# Setting up the experimental model

## 6.1 Introduction

Investigating the full dynamic response of a complex system such as a floating offshore wind TLPs is a task that requires both numerical and experimental research. The numerical front allows researchers to test different theories in a controlled numerical environment where certain parameters can be investigated with numerous iterations. On the other hand, the experimental front allows testing of a physical model in more realistic conditions which include fully non-linear hydrodynamic effects at a fraction of the time that is achievable nowadays using high-fidelity numerical models. However, physical model tank testing includes a range of errors including geometrical asymmetries, measurement errors, and wave flume blockage effects. In that sense, a physical model can be considered as another attempt at understanding the real behaviour of a full-scale FOWT system. The comparison between both numerical and experimental data allows us to understand the error of each method which is a crucial part of hydrodynamic research. The third part of this thesis focuses on the experimental validation campaign which serves to test the accuracy of the non-linear load models presented above, this time on the EDF-TLP dynamic condition.

The present chapter deals with the experimental set-up and the method used to calibrate the physical model mass properties. Tank testing of physical models of FOWT had not been carried out in EDF-R&D at the start of the research project. A physical model had been built by Duchet (2019) as part of a Master's thesis internship based on a local initiative of the EDF R&D LNHE department. However, the experimental system had not been put in place and it represented the main task at the early stage of the research project.

## 6.2 Presentation of EDF academic FOWT-TLP physical model

The EDF-TLP 10MW FOWT was scaled down to a 1/83.3 physical model according to the hydrodynamic Froude scaling rule by Duchet (2019). The properties of the full-scale prototype are given in detail in Table 3.3 and the target mass properties of the physical model are provided in Table 6.1. All the large components of the floater: side buoys, transition piece and nacelle were 3D printed using Polylactic Acid (PLA) whilst the bracings and the tower are made of carbon fibre tubes. The 3D-printed parts have a honeycomb structure to reduce the density and final weight of the model and are coated on the outside with an epoxy resin for waterproofing. The assembly is carried out by fitting the carbon tubes to the protruding toric joint connections which were designed as part of the 3D-printed pieces. The assembly needs to be tightened progressively to avoid any fracture of the carbon tubes. The side buoys include a hollow area covered by a 3D-printed lid which can be used for placing ballasting weights. The CAD model of the EDF-TLP physical model is shown in Figure 6.1a with a detail on the side buoys. These serve as receptacles for the ballast weights.

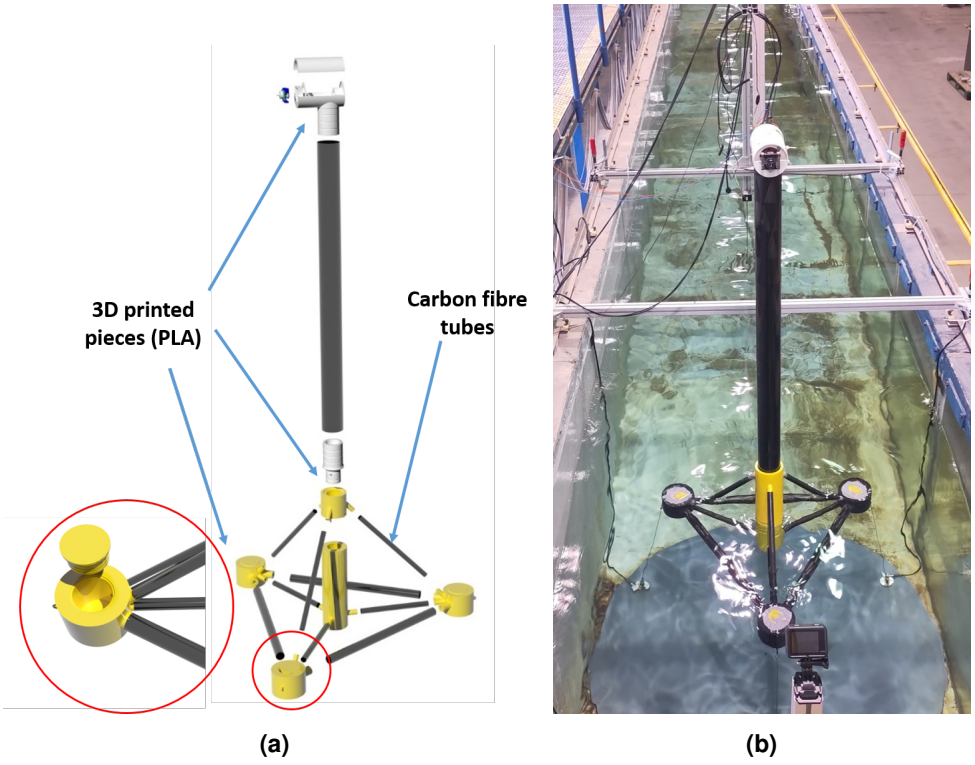


**Figure 6.1:** EDF-TLP physical model (a) Exploded view of the physical model components; (b) assembled model in tank

Several modifications from the original model of Duchet (2019) had to be carried out. First, we modified the original side buoys with a new design for the mooring line-floater connection since these were found to be fragile in the former model. Finally, a waterproof silicon paste was added around the lid of the side buoys after each opening and closing. The side buoys being fully submerged in anchored position and with wear and tear of the lid joint over many opening and closing actions, the lid system was found to be a weak point for water leakage over a long period of submerged time.

| Properties | 1:1 prototype | Froude scale | 1:83.3 model |
|---|---|---|---|
| Draft | 18m | $\lambda$ | 216mm |
| Float height | 38m | $\lambda$ | 456mm |
| Vertical Position of CoG from waterline | 32.9m | $\lambda$ | 395mm |
| Floater Mass | 1725t | $\lambda^3/1.025$ | 2985g |
| DTU tower[1], nacelle, rotor mass | 1143t | $\lambda^3/1.025$ | 1929g |
| Total Mass | 2,868t | $\lambda^3/1.025$ | 4962g |
| Roll/Pitch inertia | $1,269.73 \cdot 10^7$ kg.m2 | $\lambda^5/1.025$ | 3.09 kg.m2 |
| Yaw inertia | $1,092.22 \cdot 10^6$ kg.m2 | $\lambda^5/1.025$ | 0.26 kg.m2 |

1. Mass of tower from reference turbine Laugesen and Hansen (2015) is reduced based on height above water of floater

**Table 6.1:** EDF-TLP physical model target mass properties based on original design by Duchet (2019)

## 6.3 Tank testing facilities

The EDF-TLP physical model was designed for tank testing at the EDF LNHE-LHSV hydrodynamic lab in wave flume No. 5. The main dimensions of the flume are summarised below:

- Length: 80m
- Width: 4.5m
- Max water depth: 1.3m
- Height above channel: 4m

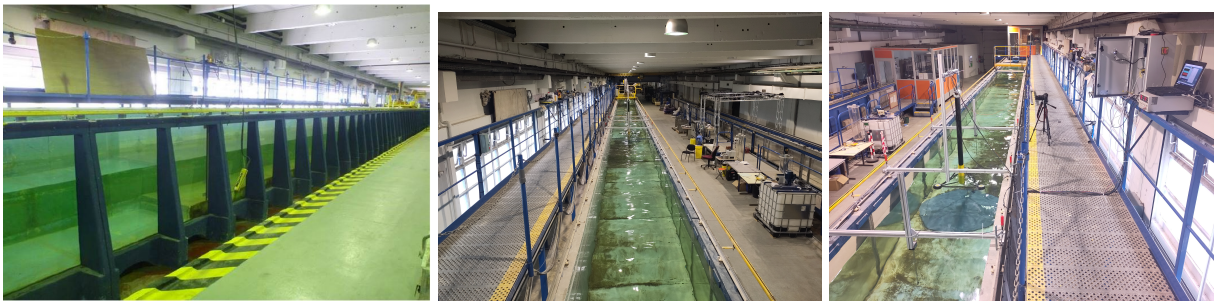

**(a)** **(b)** **(c)**

**Figure 6.2:** Wave Flume no 5

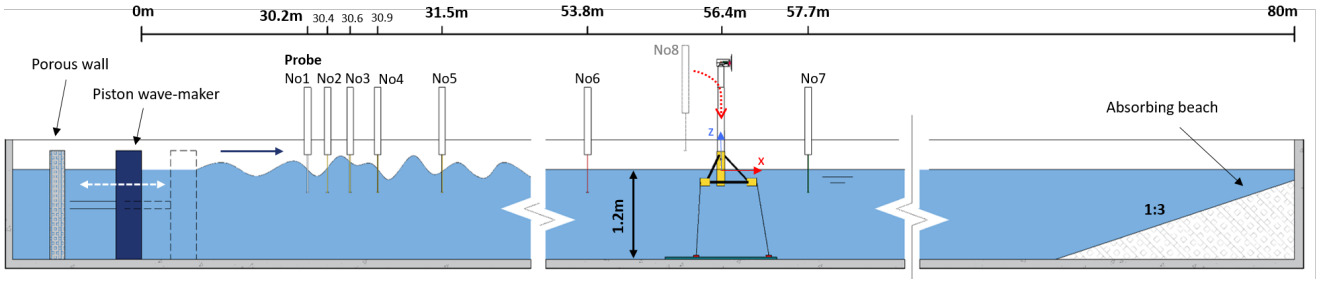


**Figure 6.3:** Elevation of wave flume No5 showing alignment of wave probes and physical model

Sketch of the elevation of the flume is shown in Figure 6.3 and photographs of key elements are shown in Figure 6.2. The wave generation is done using a piston wave-maker based on linear potential flow theory. The control of the actuation and the acquisition of free surface elevation by the twin-wire wave probes is carried out using the software WaveGen_Studio and its integrated DaQ system by Akamina Technologies.

Five twin-wire wave probes are located just upstream of the wavemaker to measure incident and reflected wave field. Two wave probes are installed just downstream and upstream from the model and an eighth one is installed at the location of the model before its installation to calibrate and measure the incident wave field that the EDF-TLP will experience as per ITTC guidelines (Ocean Engineering Committee of the 28th ITTC, 2017). An absorbing beach made of porous metal mesh with a linear slope of $1:3$ steepness is located at the end of the flume. It is worth noting that this beach was originally designed for coastal application and its efficiency in offshore conditions is questionable since it is fully submerged in this case.

## 6.4 Choice of sensors

At the start of the project, the physical model had only been tested with three low-quality 1 DoF accelerometers connected to a Rasperry-pi acquisition system, the drone motor generating the wind thrust connected to two bending strain gauges to measure the force and three Omega fully immersible tension strain gauges to measure the line tension in the mooring lines with no stiffness considered. However, the set-up had to be improved for several reasons. Firstly, the accelerometers and bending strain gauges of the drone motor had to be replaced since these were not of sufficient quality. It was also necessary to add gyroscopes to the three accelerometers in order to obtain an angular reading. The choice of the new sensors was constrained by several factors listed below:

- Total mass and inertia of the model had to be respected which favoured light instruments

- Available full-scale-output (FSO) of instruments had to match the expected measured range as well as their accuracy and bias
- The high acquisition rate required favoured analogue to digital conversion at the data acquisition end
- Reduction or elimination of the cable connection between model and data acquisition as per ITTC recommendations Ocean Engineering Committee of the 28th ITTC (2017) as these add non-existing stiffness and damping
- Budgetary constraints

### 6.4.1 Numerical studies

In order to determine the FSO of the instrumentation, prior knowledge of maximum displacement, acceleration, velocity and forces were required. Duchet (2019) carried out a previous numerical analysis in a storm case as part of his master thesis. The run did not result in a slacking event although very low tension was recorded at around 15% of the line pre-tension. Therefore, further numerical runs were carried out at the early phase of this thesis using the same model, this time with an assumed extreme storm of $H_s = 15m$ and $T_p = 20s$. On the other hand, the maximum aerodynamic force was obtained from a numerical test simulating the turbine at rated speed.

The results are compared below against similar studies on 10MW turbine Laugesen and Hansen (2015); Milano et al. (2019) as benchmark (Table 6.2). The variables listed in Table 6.2 have to be directly measured or calculated by integration of other variables during the tank tests. The resulting physical model range of forces is represented. The scale model range then informed the full-scale-output (FSO) of the instrumentation.

### 6.4.2 6DOF Motion and Acceleration

To capture the 6DoF motion of an object, it is typical to use the following methods:

- A combination of accelerometers and gyroscopes with filter and integration method
- An optical tracking system using cameras, targets and dedicated algorithms

Optical tracking systems, more specifically Qualisys, are widely found in Floating Offshore Wind Turbine (FOWT) physical testing literature (Azcona et al., 2019; Laugesen & Hansen, 2015; Oguz et al., 2018; Vita et al., 2015). Using this method has the advantage of eliminating cables connected to the model in measuring displacement. Commercial high-quality systems such as Qualisys are costly due to the need for high-resolution cameras and licences providing the real-time 6DoF tracking software. However, they become attractive for tracking large

| **Variables** | Milano[1] | DTU[1] | Duchet 1:1[1] | **1:1 range**[2] | **Froude scale** | **1:83.3 range** |
|---|---|---|---|---|---|---|
| **Max. Displ. at the CoG or nacelle** | | | | | | |
| Surge DX | 10.5m | 18m | 16m | 25m | $\lambda$ | 300mm |
| Heave DZ | 0.7m | 2.34m | 2.4m | 5.5m | $\lambda$ | 66mm |
| Pitch DRY | 5 | 6.5 | 8deg | 12.5deg | 1 | 12.5deg |
| **Max. Velocity at the CoG or nacelle** | | | | | | |
| Pitch Velocity | | | | 2.7deg/s | $\lambda^{-0.5}$ | 25.32deg/s |
| **Max. accel. at the CoG or nacelle** | | | | | | |
| Surge AX | | 3.2 m/s2 | 2.6m/s2 | 2.6m/s$^2$ | 1 | 2.6m/s$^2$ |
| **Max. tension in moorings** | | | | | | |
| Max tension | 30MN | 22MN | 16MN | 26MN | $\lambda^3/1.025$ | 44N |
| **Max Aerodynamic force - in the direction of the wind only** | | | | | | |
| Horizontal aerodynamic force | | 1.7MN | 1.18MN | 1.9MN | $\lambda^3/1.025$ | 3.3N |

1. Approximated maximum absolute values from Duchet (2019); Laugesen and Hansen (2015); Milano et al. (2019)

2. Estimated maximum absolute values from preliminary DIEGO runs

**Table 6.2:** Dynamic response variables and 1:1 / 1: 83.3 range

amounts of targets. At the start of this project, due to budgetary constraints and the original purchase of high-quality IMUs, it was decided that a simple 2D point tracking system could be developed using open-source software. Therefore object tracking was carried out at the post-processing stage using the open-cv Python library and the video data from the test.

Optical tracking is usually combined with accelerometers which directly measure nacelle acceleration (Laugesen & Hansen, 2015; Leroy, Delacroix, Merrien, Bachynski-Polić, & Gilloteaux, 2022; Oguz et al., 2018). Considering the fact that accelerometers are to be fitted to the model and that the assumption of rigid body motion only requires knowledge of the displacement at one or two points (rigid tower or not), the choice of instruments turned to Inertial Measurement Units (IMUs). IMUs combine 3DoF accelerometers with 3DoF gyroscope using time integration to return the displacement signal. Since IMUs combine the power supply, the amount of cable connections for a 6DoF IMU or for 3 separate 1DoF accelerometers is comparable. Therefore the former was originally considered a suitable alternative to optical tracking that enables both measurement of 6DoF motion and acceleration.

However, a common issue with IMUs is the drift of their gyroscopes. The gyroscope drifts in pitch and roll can be corrected using the accelerometer and a low-pass filter to detect the gravity vector. Drift in yaw angular velocity requires a reference in the horizontal plane, typically through the use of a magnetometer. It is unlikely that the magnetometer would provide accurate readings in the hydrodynamic lab of the LNHE due to the presence of electronics. Therefore a high-quality 6DoF low noise analogue MEMS IMU was originally chosen based on its FSO (provided in Table 6.3) and a low in-run bias instability. However, during the first trial, it was found that the integration of accelerometer data into displacement data is a tricky issue. This is caused by the measurement of both displacement acceleration and earth gravity pull. The latter is useful in static conditions to measure the trim of the platform. However, that information has to be removed in dynamic conditions so as to only integrate the displacement-related acceleration. The gravity pull can be removed based on the instantaneous angular position of the system which is obtained from the integration of gyroscopes measurements. Finally, the acceleration is measured in the body reference frame and has to be rotated back into the global reference frame using again the gyroscope's angular reading. However, with oscillatory motion of small amplitudes, and drift of the gyroscopes, it was found that the margin of error of this method was significant. Fusion algorithms exist to carry out the task of merging measurement of gyroscopes and accelerometers using filtering and optimisation routines such as the Madgwick algorithm Madgwick, Harrison, and Vaidyanathan (2011). However, with these added complexities and uncertainty regarding the efficiency of the approach and the availability of a simple camera tracking system, it was decided that such work was outside of the scope of this thesis.

### 6.4.3 Tension in mooring lines

The tensions in the three mooring lines are measured using tension load cells, the main constraint being the need for fully submersible instruments. A model with suitable FSO (Table 6.3) and IP68 protection class (submersible) was found in the OMEGA Series and selected by Duchet (2019). Strain gauge load cells provide a differential voltage reading in the range of a couple of mV through a Wheatstone Bridge. Conditioners for the load cells of each mooring line are used to amplify the signal from a few MV towards a higher voltage reading usually in $\pm$ 10V signal. The conditioners, OMEGA TXDIN1600S, had been bought with the load cells.

The range of the load cells was considered suitable with the ultimate capacity being three times higher than the maximum considered load. Unfortunately, it was found too late that the load conditioners enforced the measurable range based on the instrument FSO and truncated the signal over this value limiting the range of extreme tension that could be measured.

### 6.4.4 Representation of wind thrust

The LHSV-LNHE facilities cannot currently simulate a realistic wind field above the flume and considering the complexities associated with the design of a coupled hydro-aerodynamic model due to the incompatibilities between Froude and Reynold scaling, the EDF-TLP model was designed for real-time hybrid testing in mind (See Section 3.5.3). A brushless DC drone motor is placed in the nacelle to simulate the thrust force connected to the nacelle via two bending strain gauges which measure the applied load (See Figure 6.4). Two load cells were chosen as opposed to a single one in order to increase the rigidity of the system and reduce possible torsional effects or movement of the load cell around the frame. The chosen model based on the expected range of loads shown in Table 6.2 is the ME KD45 5N. The drone motor is supplied by the 24V DC supply and is controlled by a pulse-width-modulation (PWM) channel linked to the acquisition system.

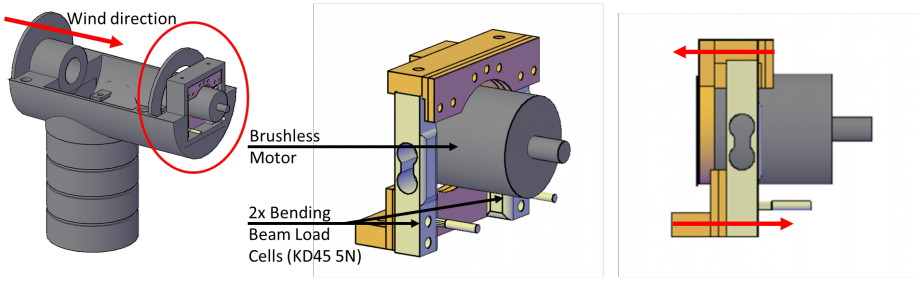


**Figure 6.4:** Brushless motor frame and connection to the nacelle via the load cells

A calibration of the PWM channel to achieve a steady thrust representative of the DTU 10MW thrust curve for the required wind-speed is done by fixing the frame on a flat surface. Figure 6.5 displays the PWM channel thrust load calibration that was carried with the new load cells and compares it with the calibration carried-out by Duchet (2019) using lower accuracy strain gauges. The agreement between the two calibrations is very satisfying.

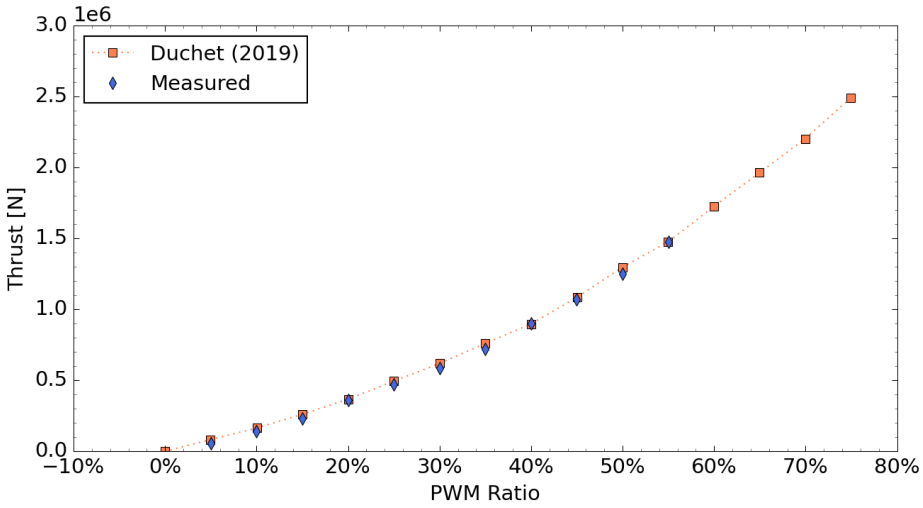


**Figure 6.5:** Relation between pulse-width-modulation opening ratio and obtained drone thrust at 10MW scale. The calibration obtained compared to calibration by Duchet (2019)

In this thesis aerodynamic modelling was limited to applying a constant wind condition. This is because of the complexities involved with implementing a full software-in-the-loop system. The reader is referred to Section 3.5.3 for details of software-in-the-loop systems in coupled-wind-wave testing. One particular issue for the implementation of the said system with the current set-up is the measurement of the instantaneous displacement of the model.

### 6.4.5 Summary of instruments

Table 6.3 provides a summary of the chosen instruments, their location in the model and shows their full-scale-output (FSO) against the expected range of measurements.

| **Variables** | Expected range | Instrument model | FSO |
|---|---|---|---|
| | | **ASC IMU 7-LN** | |
| Surge Acceleration | ±2.6m/s2 (0.26g) | Accelerometer | 19.62m/s2 (2g) |
| Pitch Angular Velocity | ±24.6 $\deg/s$ | Gyroscopes | 75 $\deg/s$ |
| | | **ME KD45 - 5N** | |
| Horizontal Aero. Force | ±3.3N | Load Cells | 2 x 5N |
| | | **OMEGA LSHD 5lbs** | |
| Max tension | 44N | Load cells | 20N - 34N - 67N (Rated) - (Safe) - (Ultimate) |

**Table 6.3:** Measured variable range and choice of instruments

## 6.5 Choice of Data Acquisition and Control System

All instruments described above are analogue systems. Therefore, they require an analogue to digital conversion using a data acquisition system in order to be saved, read and visualised digitally at a required sampling rate. Data acquisition can be carried out either from a desktop-based system digitally linked to separate analogue to digital converters or from a controller or micro-controller which is independent and transmits the data to the desktop which only serves for the visual interface. At the start of this research project, a new acquisition was required since the conversion of analogue to digital data on Rasberry-pi for the number of instruments risked to be poor. Finally, in order to provide the basis for a future SIL system, it was necessary to ensure a fast acquisition and control rate. The selection of the DAQ system was therefore influenced by the integration requirement of a range of instruments and the future need for real-time control.

### 6.5.1 Considerations

In terms of acquisition rate, the real-time hybrid method requires the choice of a step size common to all the sensors. Chabaud et al. (2013) suggests that the step size should consider the following:

- A maximum value based on the sampling frequency required to be above the Nyquist frequency of the highest frequency component in the system
- The time-lag required to compute the required force which has to be subtracted from the original time-step
- And a minimum value defined by the time required for the actuated force to settle around its reference value

Furthermore, as discussed in Chabaud et al. (2013), the thrust actuator requires a feedback loop which uses an inner time-step. This inner time step must be much lower than the common time-step in order to control the force actuation within one time-step using the servo-sensors and controller. This inner time step should be as low as possible. Therefore, this requirement defines that the acquisition rate of the system should be as high as possible. In Chabaud et al. (2013) an inner time step, 100 times lower than the common time step is used. Using the assumptions listed below, it can be assumed that the acquisition rate for SIL should be in the order of magnitude of 3.7kHz:

- Highest frequency considered: 2Hz at 1:1 - 18.2Hz at 1:83.3
- Sampling frequency of highest frequency considered: 36.5Hz
- Servo feedback-loop sampling frequency at 100 times the general sampling frequency: 3650Hz

The requirement for a high sampling rate and a minimum time lag between the instrument acquisition and the control of the drone points to an independent data acquisition (DAQ) and control system (CS) rather than a computer-based one.

### 6.5.2 Selected DAQ and CS system

An integrated National Instruments (NI) system with LabVIEW interface had been proposed for the DAQ by Duchet (2019). NI DAQ systems are recognised for their high performance, high acquisition rate and the integration of data acquisition, data post-processing and real-time control through a programmable graphical user interface (GUI). Furthermore, NI DAQ chassis (Figure 6.6) are flexible in that they provide slots for various input and output, analogue or digital with a choice of preferred connectors. Therefore, it has obvious advantages for implementing a hybrid testing method with SIL since it already integrates data acquisition and real-time control of the drone motor in a common platform. For that reason, such a system has been used in hydrodynamic tank testing of FOWT with SIL (Azcona et al., 2019; Chabaud et al., 2013; Vittori, Bouchotrouch, Lemmer, & Azcona, 2018).

After a private conversation with NI representatives in France, a National Instruments compactRIO (cRIO) controller was recommended and eventually purchased by EDF to perform the data acquisition, processing and real-time control of the drone motor. As briefly mentioned above, independent controllers are more efficient systems than desktop-based ones since they have their own processors dedicated to the task. Furthermore, cRIO have field-programmable gate array (FPGA) capacities which are programmable circuit gates enabling highly-efficient routines. This ensures a faster reaction time as well as parallel channel acquisition. A high-performance cRIO was chosen to allow for some extra processor and RAM to be available for future DAQ such as digital camera input for multi-cameras optical tracking.

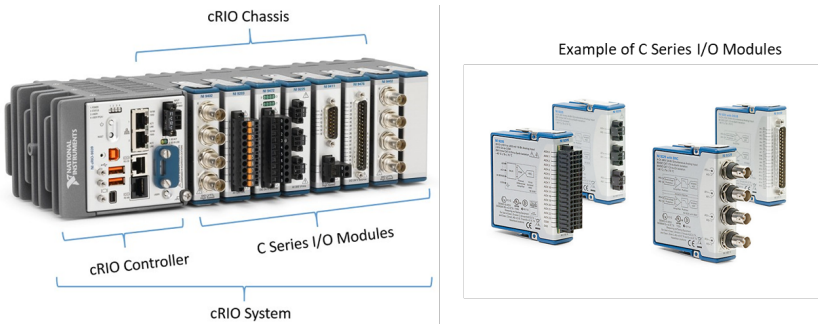


**Figure 6.6:** cRIO and C-series modules. Adapted from National Instruments (n.d.)

On top of the controller frame, the modules to mount were chosen so as to match the list of instrument and control connections displayed in Table 6.4. Two analogue input (AI) cards were selected to acquire analogue single-ended measurements and differential voltage measurements separately. This is to avoid short circuits between channels with floating and referenced mass as recommended by NI representatives and instrument suppliers. One digital output module was also selected to provide Pulse-Width-Modulation control (PWM) for the Electric-Speed-Controller (ESC) of the brushless drone motor.

### 6.5.3 Summary of sensors and acquisition

Details on the sensor to DAQ connection are provided in Table 6.4 and in Figure 6.7a with a particular focus on the nacelle. An elevation view of the EDF-TLP physical model set-up is shown in Figure 6.7b.

| Instrument connected | No | Power supply | Cable function | I/0 signal | NI Acquisition Module |
|---|---|---|---|---|---|
| 5* **Thrust load cells (KD45 - 5N) and conditioners (GSV 6K)** | 5***2** | 5* 12-24V DC - 22mA | Supply | 5* 2 x single ended in +- 10V (need reference ground) | 10* **1 x NI 9205 (32 x spring entries)** |
| | | | Analogue Output Ground Tare Scale | | |
| 11* **6DoF IMU (ASC IMU 7-LN )** | 11***2** | 11* 6-40VDC - 30mA | Supply - | 5* 6 x single ended in +- 120mV (need reference ground) | |
| | | | Supply + Gyro - X - Signal Gyro - Y - Signal Gyro - Z - Signal | | |
| | | | Accel X - Signal + | 6* 6 x differential in +-2.7V | 10* **1 x NI 9220 (32 x spring entries)** |
| | | | Accel X - Signal - Accel Y - Signal + Accel Y - Signal - Accel Z - Signal + Accel Z - Signal - | | |
| 4* **Mooring load cells (OMEGA LSHD) and conditioners (TXDIN1600S)** | 4*3 | 4*10-48 V DC | Supply + | 4* 3 x differential in +-10V | |
| | | | Supply - Signal + Signal - | | |
| 3* **Drone ESC (T Motor AIR 15A)** | 3*1 | 3*15 or 20A | Supply | 3* 1 x PWM Digital Output | 3***1 x NI 9401** |
| | | | Ground PWM Signal | | |

**Table 6.4:** Summary of sensors connection to DAQ

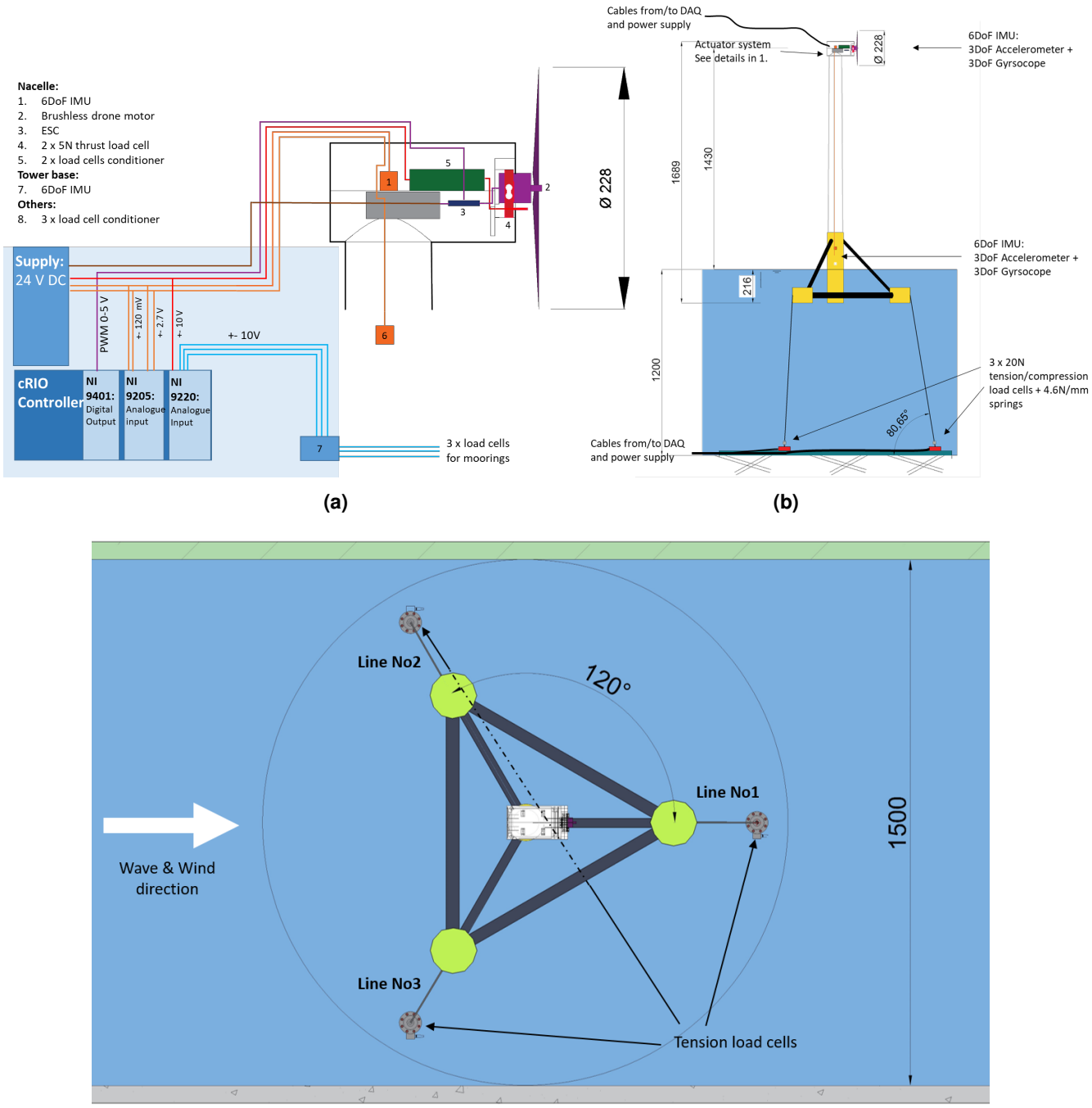


**Figure 6.7:** Details of physical model set-up (a) Detail of nacelle and of instruments to DAQ connection; Details of physical model in tank testing position (b) Elevation ; (c) Top view

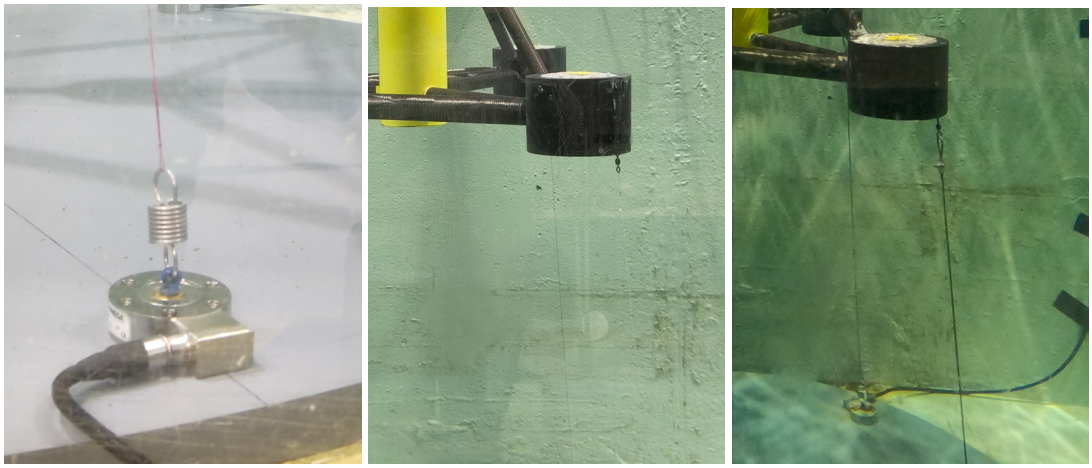

(a) (b) (c)

**Figure 6.8:** View of experimental mooring system; (a) fish-line mooring and spring connected to tension load cell; (b) fish-line mooring connection to floater; (c) steel-wire mooring connected to floater

## 6.6 Representing mooring lines

Representing mooring lines in a floating offshore wind physical model can be a complicated process. This is because of the limits in finding a material with a Young's modulus matching the scaled-down stiffness of steel wires, chains or polypropylene/polyester lines while respecting the ultimate load capacity. For TLPs with their pre-tensioned lines mobilising the axial and geometrical stiffness, these can be represented relatively accurately as a linear spring. In turn, the lines can be assumed to be infinitely rigid. This methodology was adopted for this project.

Custom-made linear springs were ordered with the required linear stiffness of $4.8$ N/mm, a pre-tension load of around $1$ N and a maximum loading capacity of $33$ N. A picture of the spring is provided in Figure 6.8a. The mooring lines could then be modelled using a strong material with a relative infinite stiffness for the load range considered. It is important to add here that it was decided to reduce the mooring lines' sectional area in the numerical model from the original value by around half for the experimental and numerical campaign. This was to reduce the vertical stiffness of the system and achieve a pitch natural mode at a lower frequency than in a realistic design. The reason lies in the limits of the wave tank capacity to generate regular waves below $T = 7$ s at 10-MW scale due to both a wave-maker actuation limit and the Benjamin-Feir instability leading to unstable wave-packet over a certain distance. Therefore, to ensure that the second harmonic of the smallest wave achievable in the tank would hit the springing resonance in pitch, it was necessary to introduce this change. This resulted in a shift of the rigid-body pitch mode from $T_{yy} = 2$ s to $T_{yy} = 3$ s.

At first, tests were carried out using fishing lines ballasted with small weights. These tests included the first monochromatic wave tests which are presented in Section 7.2 and referred to as *Exp-old* in the legend label. However, these were found to be impractical for several reasons:

- First they tended to entangle themselves when slack as the flume was filling up. Secondly, fishing weights used as ballasts tended to fall
- Secondly, the order of magnitude of their linear mass and diameter were not representative of the steel wires of the numerical model.

Therefore, these were replaced with simple off-the-shelves stainless steel wires. Using steel is advantageous since Froude scaling works with equal density and therefore the linear mass is respected if the cross-section dimension is respected. The smallest diameter wires available in the market, $2$ mm, were luckily very close to those of the numerical mooring lines at model scale, $1.86$ mm. A picture of the two types of mooring lines is shown in Figure 6.8b and 6.8c. It is noted that the change of mooring lines did not affect the frequency of the natural of te system.

## 6.7 Summary of the final experimental set-up

The instrumentation used in this experiment in the physical model is summarised in Figure 6.9. Inertial Measurement Units (IMUs) are used to provide information about the 3D acceleration of the platform. Displacement is also measured in the $x, z$ plane by camera tracking using image recognition with the open-source Python library OpenCV. Three tension strain gauges are placed at the bottom of the tank to measure the tension in the mooring lines, represented using "infinitely" stiff wires (fishing lines then changed to steel wires) connected to springs with scaled linear stiffness. Finally, two wave probes are located around the physical model and a third one at the location of the physical model to measure the incident wave field prior to the experiments during which it is removed.

## 6.8 Correcting mass and inertial properties

Once a physical model is built, its inertial properties will be different than the target scaled properties due to several factors such as the choice of material selected for building the physical model, the addition of sensors and their cables plus in this case the removal of the rotor from the nacelle. The centre of mass and inertia of the physical model therefore have to be measured. Then once these properties are known, the position and the mass of the ballast weights required to correct the model can be estimated. The method presented below is the fruit of the first few months of research carried out with the help of the EDF R&D experimental team.

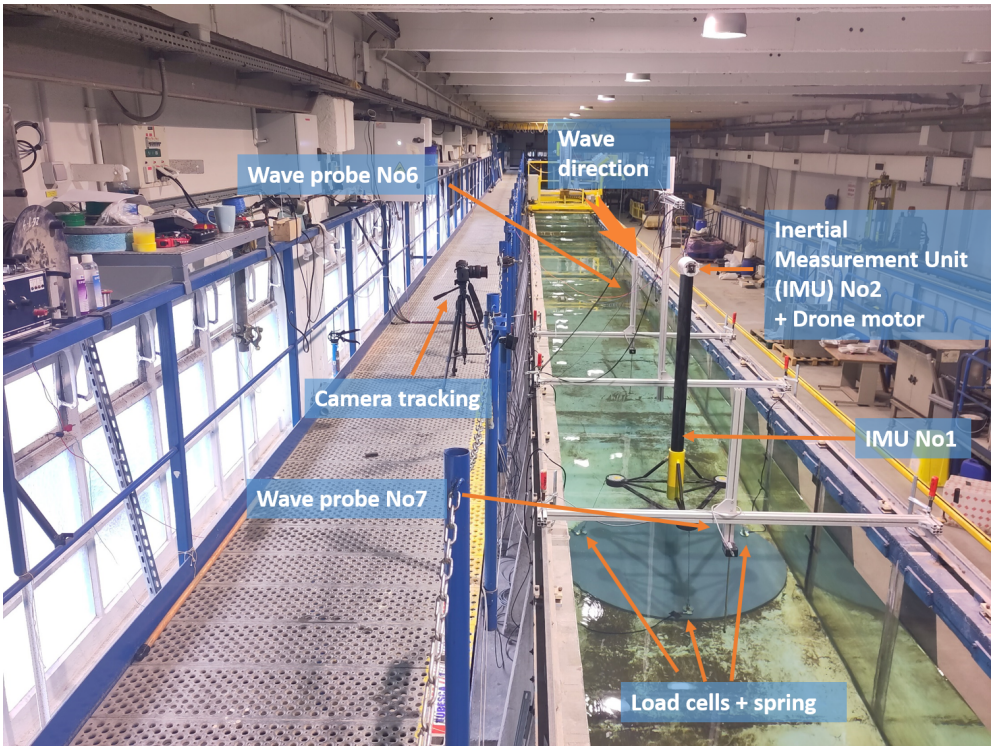


**Figure 6.9:** View of the experimental set-up with summary of instruments

### 6.8.1 Measuring the physical model mass properties

The two main methods for measuring the mass properties of a physical model are the use of an approximate/detailed CAD model or physical measurements. The first method has to include the estimation of the density of each material and the position and mass distribution of instruments and other added weights. Although few articles detail the approach used, to the knowledge of the author, several studies have relied solely on a numerical model (Ransley et al., 2022).

Considering the complexity of ensuring that the CAD model is representative of the actual mass distribution including cables, screws and added ballast weights, we decided to rely on a physical measurement method. Following the purchase order of instruments and the DAQ system, an experimental protocol was devised to measure both the centre of gravity and the mass moment of inertia. The approach which is described below is based on simple physics and inspired by the following documents Delefortrie, G.; Geerts, S.; Peeters, P.; Mostaert, F. (2017); Hinrichsen (2014).

### Horizontal position of CoG

The total mass of the model can easily be measured using a scale. A method using several scales can then be used to find the centre of gravity in the horizontal plane using the reading of each of the scales as inputs in the 2D equation of static to return the lever arm in $x$ and $y$ of the centre of gravity. This provides the position of the CoG. A set of 3 scales positioned in a circle formation, 120° apart is used. The disposition of the scale is selected to follow the position of the floaters of the tri-floater as shown in Figure 6.10. The fully equipped physical model with sensors and cables is then weighted and the centre of gravity is provided by equations 6.1 and 6.2.

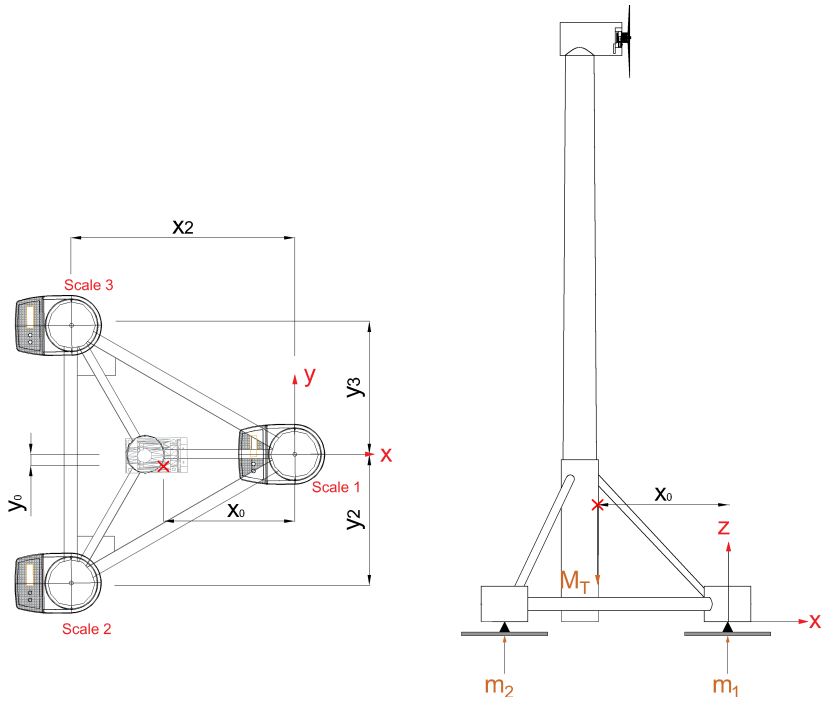


**Figure 6.10:** System of scales for horizontal plane CoG determination

$$X_0 = \frac{m_{scale1} \cdot x_1 + m_{scale2} \cdot x_2 + m_{scale3} \cdot x_3}{M_{total}} \tag{6.1}$$

$$Y_0 = \frac{m_{scale1} \cdot y_1 + m_{scale2} \cdot y_2 + m_{scale3} \cdot y_3}{M_{total}} \tag{6.2}$$

where $X_0$, $Y_0$ are the coordinates of the CoG in the horizontal plane, $x_1, ..., x_3$ and $y_1, .., y_3$ are the coordinates in the horizontal plane of the point of application of the mass for each of the measuring scales, $m_1, .., m_3$ are the measured mass at each scale and $M_{total}$ the total.

### Vertical position of CoG

The vertical position of the CoG can be found using the inclined test which consists of fixing the system vertically with freedom of rotation in roll or pitch, hanging a known mass from one of the extremities of the system and measuring the resulting inclination (See Figure 6.11). This method is proposed in a report by the Flanders Hydraulic Institute for ballasting physical models of ships (Delefortrie, G.; Geerts, S.; Peeters, P.; Mostaert, F., 2017) as well as in a paper by Hinrichsen (2014) describing methods used to measure the mass properties of full-scale hulls of sailboats.

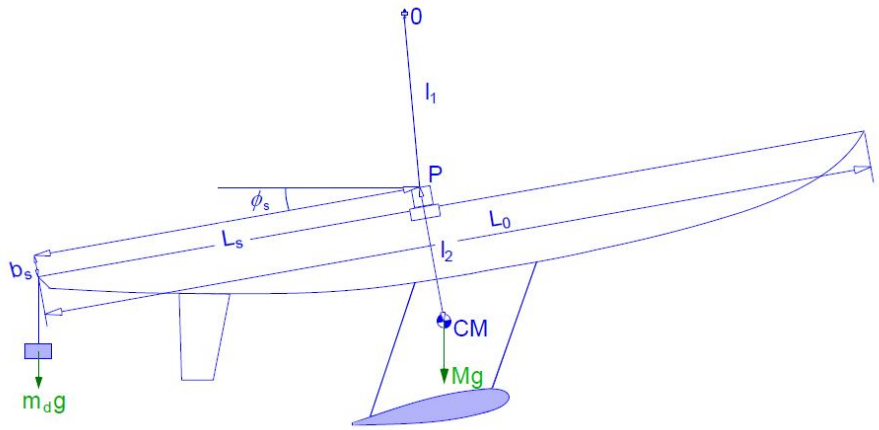


**Figure 6.11:** Inclined test example from Hinrichsen (2014)

This method was followed by designing the concept of a pendulum system and adapting the equations from Delefortrie, G.; Geerts, S.; Peeters, P.; Mostaert, F. (2017); Hinrichsen (2014) to conform to its geometry. The proposed system is shown in Figure 6.12 which includes a bar which serves as the rotation axis to which a frame hangs. The design of a frame was reduced to the minimum footprint to ensure a small mass while having structural integrity. For that reason, the frame could not extend far from the rotational axis. The floater section of the physical model being the most rigid, the model was then to be hung upside down with some kind of restraints.

The pendulum could be fitted with an accelerometer to measure the acceleration signal or the accelerometer inside the model can be used. Measuring the angle to the gravity acceleration vector yields the inclination. However, video tracking or electronic inclinometer were also an option. A simple back-up method to check the result of the measurement consisted of placing the physical model horizontally on an edge and finding the rough balance position.

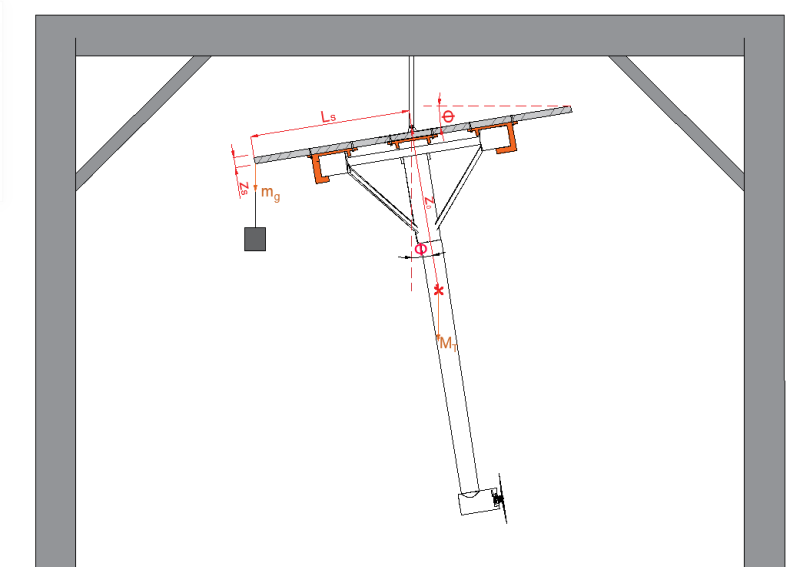


**Figure 6.12:** Inclined test set-up for the vertical position of CoG determination

The static moment equation around the axis of rotation as displayed in Figure 6.12 can be written as follows:

$$m_g(L_s\cos\phi - z_s\sin\phi) = m_{pendulum}\cdot z_{pendulum}\sin\phi + M_{model}\cdot(Z_0\sin\phi + X_0\cos\phi) \tag{6.3}$$

where $m_g$, $L_s$, $z_s$ are respectively the mass of the test weight, the horizontal and vertical distance from the rotation axis to the point of application of the test weight, $m_{pendulum}$, $z_{pendulum}$ are the mass and the vertical position of the CoG of the pendulum from the axis of rotation, $M_{model}$ and $Z_0$ are the mass and the vertical position of the CoG of the model from the axis of rotation and $\phi$ is the measured inclination angle. Finding the vertical position of the CoG of the physical model is then possible.

$$Z_0 = \frac{m_g}{m_{model}}\left(\frac{L_s}{\tan\phi} - z_s\right) - \frac{m_{pendulum}}{M_{model}}\cdot z_{pendulum} - \frac{X_0}{\tan\phi} \tag{6.4}$$

This equation requires the determination of the vertical coordinate of the pendulum frame CoG. Assuming the horizontal position of the said CoG is known, the same method could be used without the model simplifying the equation to the following.

$$z_{pendulum} = \frac{m_g}{m_{pendulum}}\left(\frac{L_s}{\tan\phi_0} - b_s\right) \tag{6.5}$$

However, the lever arm from the pendulum CoG to the axis of rotation is very small and an accurate measurement was found to be very difficult. Therefore, considering the simple geometry of the pendulum system and the relative homogeneity in material, the vertical coordinate of the pendulum CoG was determined using a CAD model.

**Roll and pitch inertia**

A common method for measuring rotational inertia for ships or plane physical models is the pendulum test. This test is explained in detail in a report by Flanders' Hydraulic Research Delefortrie, G.; Geerts, S.; Peeters, P.; Mostaert, F. (2017) and mentioned in Hinrichsen (2014). It uses the pendulum equation to relate the oscillation period and rotational inertia of the system. The physical model is fixed to a rigid frame that is free to rotate around a single axis. The inertia of the system (here assuming roll), at the axis of rotation, is then measured from the linear pendulum equation:

$$T = 2\pi\sqrt{\frac{I}{mgl_s}} \tag{6.6}$$

where $I$ is the pendulum inertia around the axis of rotation, $m$ is the lumped mass of the pendulum and $l_s$ is the distance of the string connecting the point mass to the axis of the rotation. Which in this case, leads to the following equation:

$$I_{xx/yy} = \frac{T_{xx/yy}^2}{4\pi^2} \cdot mgl_s \tag{6.7}$$

where, $T_{xx}$ is the measured period of oscillation of the system, $l_s$ is the distance between the axis of rotation and the CoG of the model-pendulum system and $m$ is the combined weight of the pendulum system and the physical model $m_{pendulum} + M_T$

The inertia in roll and pitch could then be measured using the pendulum system also devised for the inclined test described above. Several runs have to be carried out and an average of the measurement is taken following these steps:

- The inertia of the pendulum frame on its own is measured
- The model is fixed to the frame of the pendulum and the oscillation period of the whole system is measured
- The inertia of the physical model is found by subtracting the inertia of the frame from the total frame + model inertia

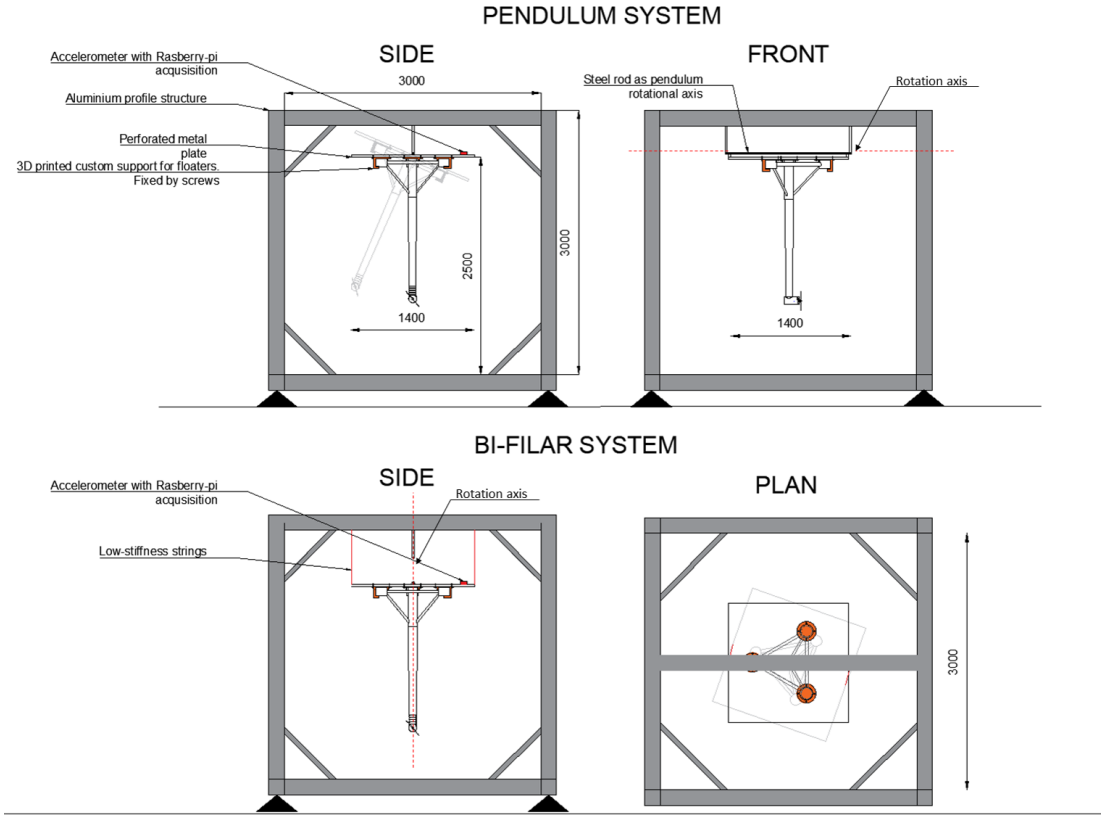


**Figure 6.13:** Oscillation tests set-up

The measurement of the oscillation period is done by a Fast Fourier transform of the accelerometer signal fitted on the pendulum and of the object tracking. The damping in the system is measured by analysing the logarithmic decrement $\delta$ of the signal.

$$\delta = \log \frac{A_i}{A_{i+1}} \tag{6.8}$$

where $A_i$ and $A_{i+1}$ are the amplitudes at following peaks in the acceleration signal. From free vibration theory, we know that the damping ratio $\zeta$ can be calculated from the logarithmic decrements as follows:

$$\zeta = \sqrt{\frac{\delta^2}{4\pi^2 + \delta^2}} \tag{6.9}$$

The measured damped free vibration frequency, $f_d$, is then modified to take into account the damping.

$$f_{n_{xx/yy}} = \frac{f_{d_{xx/yy}}}{\sqrt{1-\zeta^2}} \tag{6.10}$$

So the full equation of the measured inertia to the reference point (here CoG) can be expressed as follows:

$$I_{xx/yy} = \frac{\sqrt{1-\frac{\delta^2}{4\pi^2+\delta^2}} \cdot T^2_{d_{xx/yy}}}{4\pi^2} \cdot mgl_s \tag{6.11}$$

The model inertia is then determined by subtracting the measured inertia of the full system from the measured inertia of the pendulum system without the physical model. The model inertia, measured at the rotation axis, then should be referenced to the model target CoG or waterline using the parallel axis theorem equation shown below. the relation between the inertia at CoG and at the new reference axis is as follows:

$$I_{cog} = I_{ref} - ml^2 \tag{6.12}$$

Where, $l$ is the distance between the CoG and the new reference axis

**Yaw inertia**

Due to the geometry of a FOWT, a pendulum test in yaw is not ideal as this would require the model to be placed exactly horizontally. However, a second method using the same pendulum equation exists. It is the bi-filar test which consists of hanging model with two strings (or ropes for bigger tests). Then an initial rotational displacement in the horizontal plane is applied and the resulting oscillation is measured. This method is explained in detail in Hinrichsen (2014). The inertia around the axis passing through the CoG of the model-pendulum system can then be calculated from the following expression:

$$I_{zz} = \frac{T^2_{zz}}{4\pi^2} \cdot \frac{mgd^2}{l} \tag{6.13}$$

where, $T_{zz}$ is the measured period of oscillation in yaw of the system, $d$ is the distance between the two filars and $l$ is the length of the filars. Using this method, the inertia in yaw could have been measured similarly to the section above. However, due to the complexity of ensuring a pure yaw motion and since it was assumed that yaw motion could be neglected in the wave flume which mostly mobilise surge, heave and pitch, this method was not implemented.

### 6.8.2 Correcting properties

Knowing the measured and required mass and rotational inertia properties, the aim is then to correctly ballast the physical model in order to get as close as possible to the target properties. This is done by solving a set of 7 equations. The inertia equations assume the rotational inertia of the ballast weights around their own axis to be negligible and therefore these are represented as point masses.

**Equation of total mass:**

$$M_{required} = M_{measured} + \sum_{i=1}^{n} m_i \tag{6.14}$$

**Equations of Centre of Mass:**

$$M_{required} \cdot x_0 = M_{measured} \cdot X_0 + \sum_{i=1}^{n} m_i \cdot x_i \tag{6.15}$$

$$M_{required} \cdot y_0 = M_{measured} \cdot Y_0 + \sum_{i=1}^{n} m_i \cdot y_i \tag{6.16}$$

$$M_{required} \cdot z_0 = M_{measured} \cdot Z_0 + \sum_{i=1}^{n} m_i \cdot z_i \tag{6.17}$$

**Equations of rotational inertia:**

$$I_{xx_{required}} = I_{xx_{measured}} + \sum_{i=1}^{n} m_i \cdot (y_i^2 + z_i^2) \tag{6.18}$$

$$I_{yy_{required}} = I_{yy_{measured}} + \sum_{i=1}^{n} m_i \cdot (x_i^2 + z_i^2) \tag{6.19}$$

$$I_{zz_{required}} = I_{zz_{measured}} + \sum_{i=1}^{n} m_i \cdot (x_i^2 + y_i^2) \tag{6.20}$$

Where, $x_0$. $y_0$ and $z_0$ are the target coordinates for the centre of mass according to the defined reference frame, $X_0$, $Y_0$ and $Z_0$ are the measured coordinates for the centre of mass according to the defined reference frame and, $m_i$ is the mass of each ballast and $x_i$, $y_i$ and $z_i$ their respective position according to the defined reference frame.

The different locations in the physical model where a set of ballast weights can be placed are represented by 7 individual point masses with fixed coordinates. This is to avoid an overdetermined system. Then equations 6.14 to 6.20 can be rearranged into a linear matrix equation as follows:

$$\mathbf{m} \cdot \mathbf{A} = \mathbf{C} \tag{6.21}$$

$$\begin{bmatrix} m_1 \\ m_2 \\ \dots \\ m_7 \end{bmatrix} \cdot \begin{bmatrix} 1 & 1 & \dots & 1 \\ x_1 & x_2 & \dots & x_7 \\ y_1 & y_2 & \dots & y_7 \\ z_1 & z_2 & \dots & z_7 \\ (y_1^2+z_1^2) & (y_2^2+z_2^2) & \dots & (y_7^2+z_7^2) \\ (x_1^2+z_1^2) & (x_2^2+z_2^2) & \dots & (x_7^2+z_7^2) \\ (x_1^2+y_1^2) & (x_2^2+y_2^2) & \dots & (x_7^2+y_7^2) \end{bmatrix} = \begin{bmatrix} M_{required} - M_{measured} \\ M_{required} \cdot x_0 - M_{measured} \cdot X_0 \\ M_{required} \cdot y_0 - M_{measured} \cdot Y_0 \\ M_{required} \cdot z_0 - M_{measured} \cdot Z_0 \\ I_{xx_{required}} - I_{xx_{measured}} \\ I_{yy_{required}} - I_{yy_{measured}} \\ I_{zz_{required}} - I_{zz_{measured}} \end{bmatrix} \tag{6.22}$$

This linear set of equations can either have a single, a null or an infinite number of solutions. A symmetric system in the vertical plane will yield the same equation in pitch and roll. Furthermore, the solution can include negative masses which are not realistic solutions to the problem. This means that unless a unique solution with non-negative masses is found, the problem becomes an optimisation exercise.

A solution is, therefore, to use the Non-Negative Least-Square (NNLS) method to find a non-negative solution leading to the smallest value for the sum of squares of residuals. The method is expressed mathematically as follows. To solve this problem, an optimisation module based on the NNLS method of the Numpy library published in Lawson and Hanson (1995) is used.

$$\arg\min_{m} = \| \mathbf{A} \cdot \mathbf{m} - \mathbf{C} \|_2 \text{ for } \mathbf{m} \geq 0 \tag{6.23}$$

This method can then be used in conjunction with a loop through combinations of ballast weights coordinates to minimise the overall residual. Depending on the study some properties could also be targeted in priority such as achieving an almost correct inertia in pitch and roll whereas a bigger residual could be accepted in yaw. The algorithm that was designed is based on fixed X and Y coordinates since the location of the ballast weights are constrained to the side buoys, the central mast, the tower and nacelle. The planar coordinates can be therefore fixed to the CoG of these host structures. The NNLS problem is then solved repeatedly in loops of various combinations of coordinate positions along the vertical axis. The reference

frame $(O,x,y,z)$ at which inertia is calculated and to which CoG and ballast weights positions are referenced, is the same point as the point of resolution of the equation of movement in the numerical model (See Figure 3.7) located at the intersection between the waterline and the centre-line of the TP cylinder.

Figure 6.14 shows a flowchart showing the proposed protocol for ballasting the physical model detailed in the above sections.

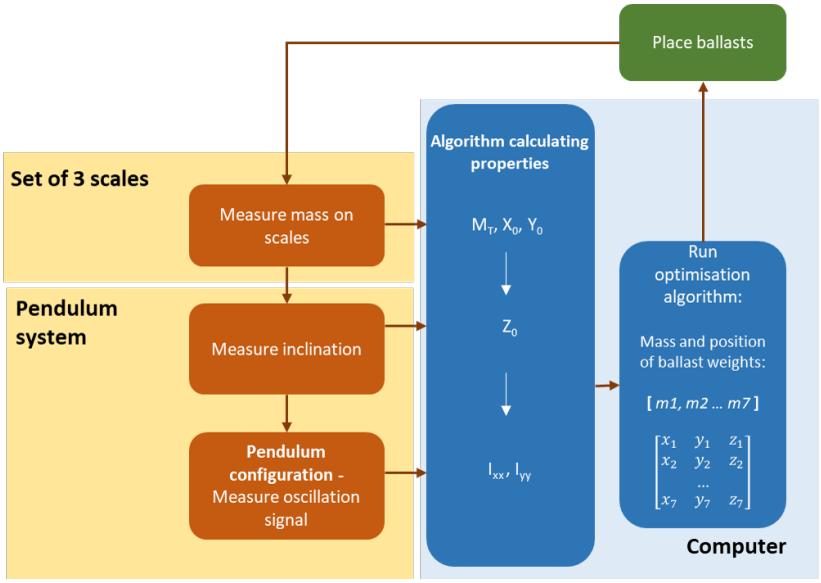


**Figure 6.14:** Proposed Ballasting Process

### 6.8.3 Implementation of the method

#### As-built design of pendulum frame

The proposed inertia pendulum system shown in the Figure 6.13 was built by the laboratory technicians of EDF R&D. The structure is made of profiled aluminium and the pendulum frame is built from a multiplex plywood board which takes the shape of a planar ring with two side supports connecting to the structure via roller bearings. These provide rotational freedom around a single axis. The dimensions and mass properties of the ring are given below. The CoG is measured in the horizontal direction using the scale system shown above, and in the vertical using a CAD model assuming homogeneous density. The coordinates are given with the rotational axis as the origin in the vertical direction with the positive direction pointing downward since the physical model is placed upside down.

- Outer diameter: 1000 mm
- Inner diameter: 700 mm
- Thickness: 15 mm

- Mass: 3.805 kg
- $X_{CoG}, Y_{CoG}, Z_{CoG}$: -1.25, 0.00, 110.0 mm

**(a)** **(b)**

**Figure 6.15:** View of (a) pendulum system supporting aluminium structure; (b) pendulum frame connection to rotational axis

### Testing accuracy of inertia pendulum

Once built, it was then necessary to verify the accuracy of the measurement method. The validation of the pitch/roll moment of inertia measurement system was carried-out using a simple geometry element made of a homogeneous material for which the inertia could be estimated analytically with good accuracy. For that purpose, a cast-iron cylinder was fixed to the pendulum frame with the help of an aluminium bar. The cast iron cylinder measured dimensions, mass and the analytical moment of inertia around its horizontal axis are as follows:

- Diameter: 154 mm
- Height: 46 mm
- Mass: 5.850 kg
- Mass moment of inertia 9.703e-03 kg.m$^{-2}$

The mass and thickness of the tubular aluminum bar of square section is given below with its vertical CoG assumed to be in the middle of the cross section.

- Section: 20 x 20 mm
- Mass: 0.917 kg

An accelerometer was placed on one edge of the frame. The inertia of the frame with the aluminium bar was measured first, and then the total inertia with the addition of the cast iron cylinder was measured. The periods measured with the accelerometer are shown in Table 6.5. The median is used rather than the mean of measurements due to the presence of outliers.

| Case | Variable | Measure No1 | No2 | No3 | No4 | No5 | Median | $\sigma$ |
|---|---|---|---|---|---|---|---|---|
| Frame | $T$ [s] | 1.820 | 1.771 | 1.811 | 1.818 | 1.806 | 1.811 | 0.017 |
| alone | $\delta$ | 0.0114 | 0.0097 | 0.0062 | 0.0113 | 0.0116 | 0.0113 | 0.0020 |
| Frame | $T$ [s] | 1.273 | 1.277 | 1.286 | 1.279 | 1.282 | 1.279 | 0.004 |
| + cylinder | $\delta$ | 0.0334 | 0.0332 | 0.0333 | 0.0318 | 0.0278 | 0.0332 | 0.00215 |

**Table 6.5:** Results of validation test for pendulum measuring inertial system

Applying Equation 6.11 with the measured values gives the following mass moment inertia around the rotational axis:

- Frame+aluminum bar: 3.9168e-01 [kg.m2]
- Frame+aluminium bar+cylinder: 4.9390e-01 [kg.m2]
- Cylinder alone: 0.1025e-01 [kg.m2]

which can be converted back to the moment mass inertia along its own horizontal axis using the parallel axis theorem in Equation 6.12, giving the following inertia:

- Measured inertia: 1.009e-02 [kg.m2]
- Analytical inertia: 9.703e-03 [kg.m2]
- Error on measurement: 3.953 %

The results being in good agreement, the validation test gave confidence in the reliability of the method to provide a decent estimate of the mass moment of inertia. An uncertainty over the mass and inertia measurement of the model below 5% is considered to be satisfactory. This is because the uncertainty on added mass which represents approximately 50% of the inertia term, is likely to be smaller with geometrical details of the platform being well controlled.

### 6.8.4 Calibration of physical model

#### Centre of Gravity

The process for ballasting the model follows the described method. Figure 6.16a shows the scale system for the horizontal position of CoG whilst Figure 6.16b shows the pendulum system used for the vertical position of the CoG and pitch and roll inertia measurements.

(a) (b)

**Figure 6.16:** Mass properties measurement of the physical model using (a) horizontal scale system (b) inertial pendulum

The initial properties of the physical model with the instruments were measured. The results of the measurements are provided in Table 6.6 for the mass measurement and estimation of the horizontal CoG, Table 6.7 for the inclined test estimation of the vertical CoG and Table 6.8 for the mass moment of inertia measurement.

| | S1 [g] | S2 [g] | S3 [g] | Total [g] | $X_{CoG}$ [mm] | $Y_{CoG}$ [mm] |
|---|---|---|---|---|---|---|
| No1 | 1244.7 | 1264.2 | 1252.9 | 3761.8 | -1.6 | 1.1 |
| No2 | 1229.1 | 1271.5 | 1268.2 | 3768.8 | -4.6 | 0.3 |
| No3 | 1236.6 | 1259.4 | 1270.9 | 3766.9 | -3.2 | -1.1 |
| No4 | 1235.5 | 1260.6 | 1265.6 | 3761.7 | -3.1 | -0.5 |
| No5 | 1240.5 | 1251.7 | 1267.1 | 3759.3 | -2.1 | -1.5 |
| No6 | 1248.9 | 1257.0 | 1256.4 | 3762.3 | -0.9 | 0.0 |
| No7 | 1245.5 | 1258.9 | 1259.2 | 3763.6 | -1.5 | 0.0 |
| No8 | 1245.3 | 1268.1 | 1251.1 | 3764.6 | -1.6 | 1.6 |
| Mean | 1240.8 | 1261.4 | 1261.4 | 3763.6 | -2.3 | 0.0 |
| $\sigma$ | 6.2 | 5.9 | 7.0 | 2.8 | 1.1 | 1.0 |

**Table 6.6:** Results of measurements of the total mass measurement and the horizontal position of the CoG for the physical model prior to ballasting

The results of the horizontal scale system shown in Table 6.6 can be read alongside Figure 6.17. The results show that the method is coherent and converges quickly towards an estimation of the horizontal CoG within a range of $\pm 1$ mm. For the vertical CoG, Table 6.7, the issue appears more complex. As masses are increased, the angular rotation becomes sufficient for a decent estimation of the CoG using the inclined test approach. Whilst a certain convergence can be observed, the accuracy falls slightly behind the accuracy of the three-scale system. Due to a lack of a sufficient variety of masses that could be used for hanging safely and time constraints, an additional check was carried out by finding the balance position when placing the physical model at the horizontal. The method appeared repeatable and results were coherent with the last two inclined test measurements. Only these three measures are taken, albeit slightly arbitrarily. In the future, a higher level discretisation is recommended to verify the convergence of the method.

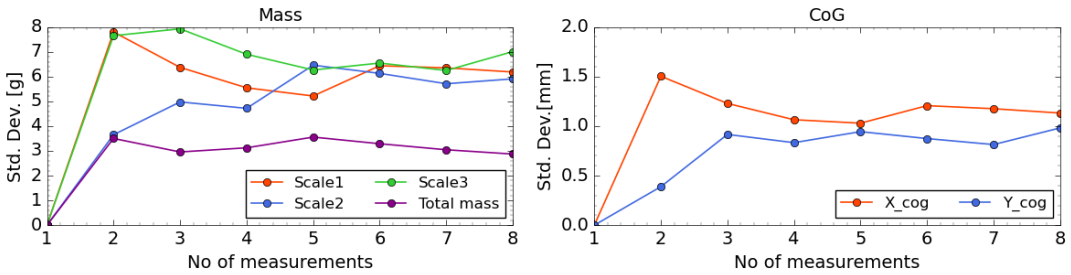


**Figure 6.17:** Convergence of the measurement standard deviation for the horizontal scale test

| | M1 | M2 | M3 | M4 | Horizontal balance | Mean |
|---|---|---|---|---|---|---|
| Applied mass [g] | 500 | 3695.5 | 5955.6 | 7849.5 | - | |
| Measured angle [deg] | 4.5 | 25.0 | 37.5 | 43.5 | - | |
| $Z_{CoG}$ [mm] | 583.5 | 498.4 | 420.4 | 426.1 | 420.9 | 422.4 |

**Table 6.7:** Results of inclined test measurement of vertical CoG

### Mass inertia

Using the measured value of the mass and coordinates of the CoG, the moment of inertia and pitch and roll were measured. The oscillation periods are measured both using the object tracking method (cv2) and the accelerometers placed inside the physical model (IMU). The median measurement of the oscillation period of the pendulum frame on its own was found to be of $T = 1.98$s, therefore slightly higher than what was measured in the validation case (Table 6.5) which is coherent since the aluminium bar was removed leading to lower mass. The resulting inertia around the rotation axis is then $I_{xx,yy,s} = 3.7955e^{-}1$ [kg.m$^2$]. The measured oscillations in roll and pitch for the physical model with instruments are provided in Table 6.8

| DoF | Variable | M1 | M2 | M3 | M4 | M5 | Median | $\sigma$ |
|---|---|---|---|---|---|---|---|---|
| Pitch | $T_{IMU}$ [s] | 2.225 | 2.233 | 2.225 | 2.267 | - | 2.229 | 0.017 |
| | $T_{cv2}$ [s] | 2.22 | 2.235 | 2.234 | 2.26 | - | 2.237 | 0.0152 |
| | $\delta_{IMU}$ | 0.134 | 0.164 | 0.150 | 0.189 | - | 0.156 | 0.020 |
| | $\delta_{cv2}$ | 0. 163 | 0.166 | 0.165 | 0.170 | - | 0.165 | 0.003 |
| | $I_{yy,IMU}$ [kg.m$^2$] | 1.8624 | 1.9144 | 1.9255 | 2.0506 | - | 1.9200 | 0.0691 |
| | $I_{yy,cv2}$ [kg.m$^2$] | 1.8664 | 1.9042 | 1.8664 | 2.0570 | - | 1.8852 | 0.0786 |
| Roll | $T_{IMU}$ [s] | 2.282 | 2.260 | 2.246 | 2.258 | 2.252 | 2.258 | 0.012 |
| | $T_{cv2}$ [s] | 2.273 | 2.275 | 2.242 | 2.256 | 2.254 | 2.255 | 0.012 |
| | $\delta_{IMU}$ | 0.147 | 0.179 | 0.193 | 0.193 | 0.154] | 0.179 | 0.020 |
| | $\delta_{cv2}$ | 0.153 | 0.169 | 0.152 | 0.171 | 0.172 | 0.169 | 0.009 |
| | $I_{yy,IMU}$ [kg.m$^2$] | 1.6339 | 1.5526 | 1.5018 | 1.5453 | 1.5264 | 1.5453 | 0.0446 |
| | $I_{yy,cv2}$ [kg.m$^2$] | 1.6004 | 1.6080 | 1.4893 | 1.5382 | 1.5345 | 1.5382 | 0.0445 |

**Table 6.8:** Results of pendulum oscillation tests on the EDF-TLP physical model prior to ballasting

#### Optimisation of ballast weights and positions

Table 6.9 displays the target mass properties, the measured values of the EDF-TLP physical model with the instruments and cables mounted and finally the corrected values after ballasting the model. The values of the model measured prior to ballasting have been fed to the non-negative-least-square optimisation algorithm. The proposed ballast mass and position given are shown in Table 6.10. The ballast masses were then positioned as close to these locations and the model mass properties were measured again. However, due to water tightness issues, further epoxy resin had to be applied on the submerged buoys as well as silicon paste and lubricant to properly seal the submerged buoy lid joint which resulted in some small modification of mass. Furthermore, the measured COG appeared to be shifted compared to the algorithm prediction which required shifting some of the ballast masses from position. The final ballast masses added in the floater are also shown in Table 6.10 and pictures of the preparation of the ballast weights are shown in Figure 6.18.

| **Model** | **Tyrion** | at 1:83.3 | | |
|---|---|---|---|---|
| Properties | Target | First measure | Measure with ballast ($\pm\sigma$) | Error |
| $X_0$ [mm] | 0.0 | -2.35 | 2.31 $\pm$ 1.26 | + 2.31 [mm] |
| $Y_0$ [mm] | 0.0 | 0.0 | 0.00 $\pm$ 0.1 | 0.0 |
| $Z_0$ [mm] | 395 | 422 | 414 | + 19 [mm] |
| $M_T$ [kg] | 4.8410 | 3.764 | 5.077 $\pm$ 0.0026 | +4.9 % |
| $I_{xx}$ [kg.m2] | 2.3343 | 1.9026 | 2.2929 $\pm$ 2.2923-02 | -1.8% |
| $I_{yy}$ [kg.m2] | 2.3343 | 1.5382 | 2.3915 $\pm$ 4.826e-02 | +2.6% |

**Table 6.9:** Required and measured properties of the numerically scaled model of EDF-TLP

| Location | Buoy No1 | Buoy No2 | Buoy No3 | Nacelle |
|---|---|---|---|---|
| Proposed | | | | |
| X | 0.420 | -0.210 | -0.210 | 0.00 |
| Y | 0.000 | 0.364 | -0.364 | 0.00 |
| Z | -0.182 | -0.182 | -0.182 | 1.429 |
| Mass | 0.262 | 0.241 | 0.241 | 0.339 |
| Actual | | | | |
| Mass | 0.192 | 0.360 | 0.348 | 0.373 |

**Table 6.10:** Ballast mass and position proposed by the algorithm and actual

After ballasting, the platform weight and the pitch mass moment inertia were increased, although below a 5% margin. The vertical centre of gravity of the physical model with added ballast is measured 19 mm above the target position which represents 1.6 m at full scale, a range which appears entirely acceptable considering the size of the structure. Therefore, the results of the mass calibration method appear quite successful with the physical model being very close to the target properties. The mass properties of the numerical model are then changed to match the experimental physical model.

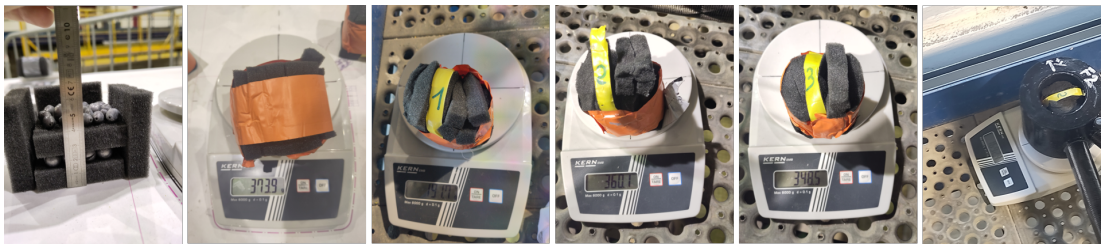

**Figure 6.18:** View of ballast weights preparation

## 6.9 System identification of floater motion

Once the mass calibration was carried-out, the physical model was placed in the wave flume and anchored to the mooring system. The next step consisted of verifying that the basic static and dynamic properties of the EDF-TLP physical model are representative of the numerical model updated with the new mass properties and vice-versa. This consists of comparing the static pitch position and mooring line pre-tension, carrying decay tests to measure the natural modes of the system in the main degrees of freedom, and finally a static thrust test to understand the excursion from the static position. The results of these checks lead to an iterative modification of the mooring system in the numerical model to achieve consistency between the physical model numerical prediction of pre-tension and decay tests modes.

### 6.9.1 Static check

The static check is relatively important for TLP since the pre-tension in the lines can inform on key differences between the numerical and physical model such as discrepancies in the mooring system geometry, in the buoyancy force or excursion of the centre of gravity. Figure 6.19 shows the comparison of the static mooring lines pre-tension and trim angle between the original numerical model, the physical model and the corrected numerical model when accounting for the experimental mass, inertia and mooring configuration. The comparison shows that the experimental model trims towards the upstream mooring line which results in a lower pre-tension in Line No1 than Line No2 and No3. Generally, all lines show a lower pre-tension than the target value due to the increased mass of the physical model. The reason for the trim angle is not clear as it could be due to discrepancies in the laying angle and length of the mooring lines. However, it could also be affected by the cables exiting from the nacelle which exert a slight weight and stiffness effect that was minimised as much as possible but potentially generating a remaining moment which is hard to quantify.

The corrected numerical model accounts for the adjusted vertical position of the anchor by considering the combined height of the foundation base and the load cells (See Figure 6.7 and 6.9). Furthermore, to achieve a lower pre-tension in Line No1 and a suitable trim angle, it was necessary to tweak the line laying angle as well as their length. Despite these modifications, a higher trim-angle by a factor of around 3 is still observed in the physical model potentially due to the presence of the instrument cables.

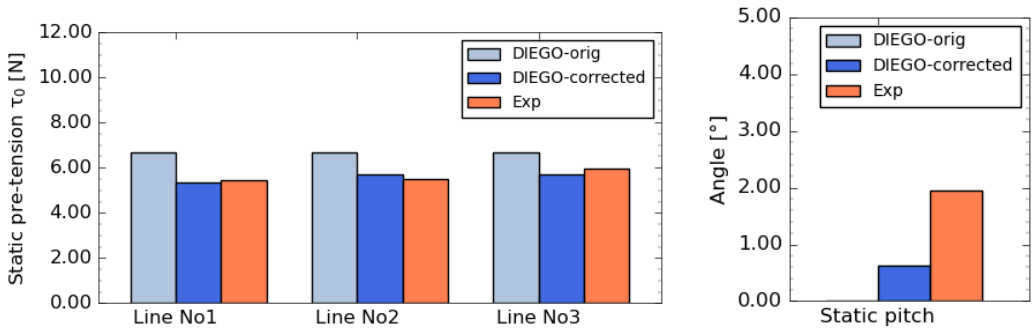


**(a)** **(b)**

**Figure 6.19:** Comparison of numerical and physical model static case (a) mooring lines pre-tension; (b) trim angle

### 6.9.2 Tower decay test

The light carbon fibre tower is designed as a rigid structure. However, with the weight of the nacelle on top of it, the tower undergoes noticeable free decay oscillation due to flexibility around the joint connection with the TP. Therefore, a decay test of the tower with RNA for the platform in clamped condition is carried out to characterise the natural period of this proxy fore-aft mode. This test was the only measurement of structural elasticity on the floater-tower structure. The FFT of the nacelle acceleration and the acceleration signal is shown in Figure 6.20 along with a time-series showing the logarithmic decrement. The natural frequency is found to be around $f_{tower} = 0.33$ Hz at 10-MW scale with a damping ratio around $\xi \approx 8\%$.

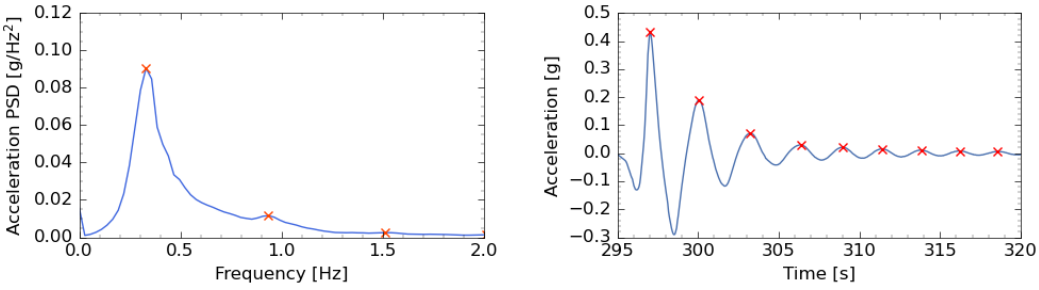


**(a)** **(b)**

**Figure 6.20:** Tower decay test (a) Acceleration FFT; (b) Acceleration signal

When comparing the decay tests of the physical model and a numerical model assuming a rigid body, the pitch natural period of the physical model is 1 s longer than predicted numerically. This result confirms that the oscillation of the tower does lead to coupling with the pitch mode as reported in the literature.

### 6.9.3 Hydrodynamic decay tests

Decay tests are carried out in four of the six degrees of freedom. This is because, with uni-directional waves, the system can be limited to surge, heave and pitch motion. A test is also carried out in yaw to verify that the horizontal distribution of mass is roughly respected since the mass moment yaw of inertia was not measured. The decay tests are done by applying a temporary steady force on the platform generating an initial displacement. The tension response is then measured in the mooring lines and analysed via Fast Fourier Transform. In the case of yaw, the oscillations of the z-axis gyroscopes are measured. A similar method is applied in DIEGO using a step force function which releases the platform at a desired time.

The comparison between the measured natural periods is shown in Figure 6.21. Generally, the results appear very satisfying with differences below 5% for the dominant degrees of freedom of surge and pitch. There appears to be an underestimation of the heave natural period by the numerical model which predicts a heave natural period of $T_{Heave} = 1.63$s whereas the physical model displays a longer mode with a period of $T_{Heave} = 1.92$ s. The definite source for this difference is unknown but likely due to the difference in static trim and resulting mooring lines laying angles. Finally, the results of the yaw decay suggest that the horizontal mass distribution in the physical model and resulting mass moment of inertia is quite representative of the original EDF-TLP design.

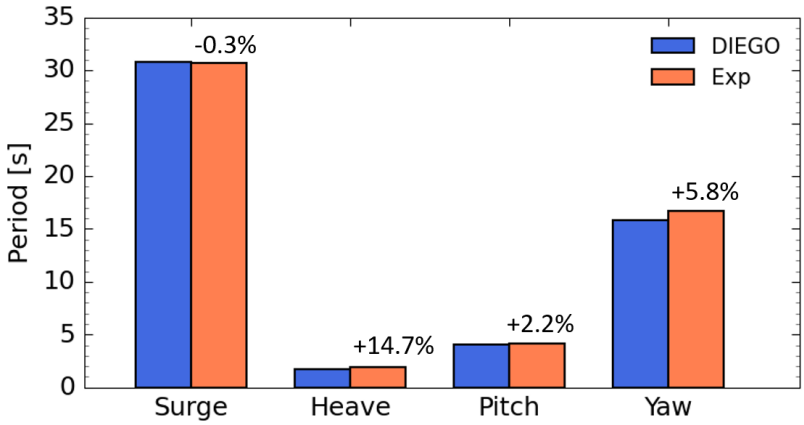


**Figure 6.21:** Comparison of natural periods between physical and numerical models

A comparison of the mooring lines' tension decay in the surge-pitch and heave test is displayed in Figure 6.22. The time scale is normalised by the natural period of the dominant mode to focus the comparison on the logarithmic decay and shape of the signal. Figure 6.22a clearly shows the strong coupling between the surge motion which appears as the underlying mode and the overlapping pitch-tower bending oscillation. In Figure 6.22b the experimental heave decay is mixed with some strong pitch oscillation due to the impossibility of generating a pure heave displacement experimentally. It is also notable that Lines No2 and No3 behave differently due to 3D asymmetries in the physical model. The Rayleigh damping coefficient of the mooring lines was calibrated in the numerical model to achieve a similar logarithmic decrement of the filtered pitch and heave oscillation. To obtain the same decay in the surge mode, it was necessary to add a linear damping coefficient. An increase of the quadratic drag coefficient was found to have negligible effects.

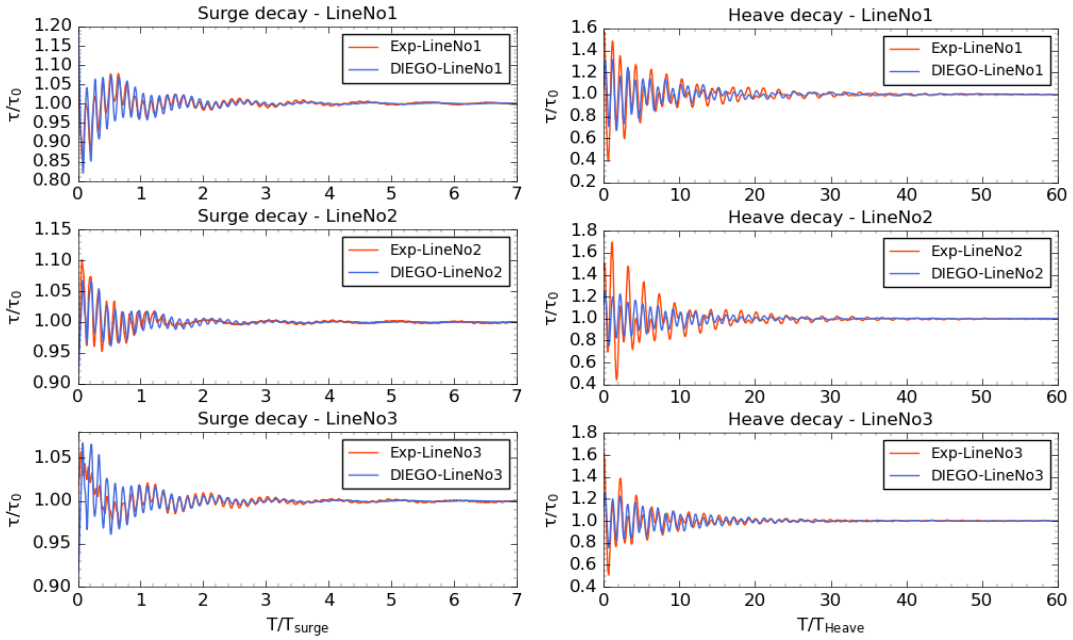


**(a)** **(b)**

**Figure 6.22:** Comparison of the line tension signal of EDF-TLP physical and corrected numerical model for (a) Surge-Pitch decay test; (b) Heave decay test

### 6.9.4 Static thrust test

The thrust test is carried out to compare the static response of the numerical and physical EDF-TLP models during steady wind production conditions. Wind speeds and thrust coefficients corresponding to the calibrated drone thrust force shown in Figure 6.5 were extracted from the DTU-10MW curves in Figure 3.13 and applied to the drag disk model. The ensuing static horizontal displacement and trim angle are then compared against tank test measurement in Figure 6.23.

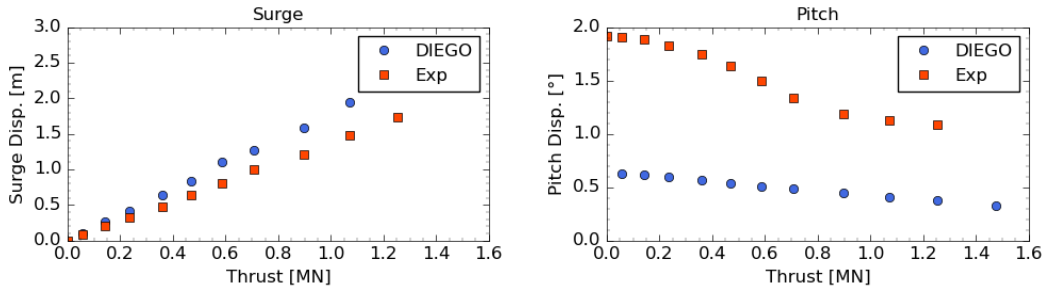


**(a)** **(b)**

**Figure 6.23:** Comparison of steady thrust displacement of EDF-TLP between physical and corrected numerical model (a) Surge, (b) Trim

The results show that the surge displacement at the nacelle, Figure 6.23a, is lower in the tank than in the DIEGO numerical model which could be due to the presence of the cables exiting the nacelle in the opposite direction. The counter-pitch behaviour of the EDF-TLP system is clearly observable in Figure 6.23b with the trim angle decreasing with increasing wind thrust as the turbine pitches into the wind. The experimental model displays a stronger counter-pitching behaviour until a thrust of 0.6 MN after which its rate of trim with increasing thrust appears to match the numerical model, although the absolute angle of trim remains different.

### 6.9.5 Results of the calibration

The original properties of the EDF-TLP presented in Table 3.3 have been modified following the subsequent calibration of the physical and numerical models. The properties at 10-MW scale of the updated numerical model are provided on the left-hand column of Table 6.11. Those of the physical model are provided on the right-hand columns at both the physical model scale and at 10-MW scale. It is worth noting that some parameters could not be measured for the physical model such as the at-rest line laying angle or the rigid body pitch natural frequency. A note is also provided to highlight parameters that remain different between the numerical and physical prototypes.

**Table 6.11:** EDF-TLP modified properties and geometry following physical model calibration. † Different values between the physical and the numerical models

| Mass Properties | | 1:1 num. | 1:83.3 phys. | 1:1 phys. | |
|---|---|---|---|---|---|
| Total mass: | $M_{Total}$ | 3007.92 | 5.077x10$^{-3}$ | " | [t] |
| Centre of Gravity | CoG | (0.,0.,35.15) | (-0.002,0.,0.422) | " | [m] |
| Mooring lines | | | | | |
| Design water depth | $h$ | 100 | 1.2 | " | [m] |
| Draft of point of attach | $d_{moor}$ | -14.0 | -0.168 | " | [m] |
| Draft of point of anchor | $d_{anch}$ | -95.83 | -1.150 | " | [m] |
| No of lines | $N_{lines}$ | 3 | 3 | " | [-] |
| Line No1 angle | $\alpha_{moor1}$ | 79 | - | - | [°] |
| Line No2/No3 | $\alpha_{moor2/3}$ | 81 | - | - | [°] |
| Line No1 length (rest) | $l_{0,1}$ | 80.92 | 0.975 | 81.22$^{\dagger}$ | [m] |
| Line No2/No3 length (rest) | $l_{0,2/3}$ | 81.61 | 0.975 | 81.22$^{\dagger}$ | [m] |
| Line No1 pre-tension | $\tau_{0,1}$ | $5.34 \cdot 10^6$ | 9.22 | $5.43 \cdot 10^{6\dagger}$ | [N] |
| Line No2 pre-tension | $\tau_{0,2}$ | $5.71 \cdot 10^6$ | 9.30 | $5.51 \cdot 10^{6\dagger}$ | [N] |
| Line No3 pre-tension | $\tau_{0,3}$ | $5.71 \cdot 10^6$ | 10.08 | $5.97 \cdot 10^{6\dagger}$ | [N] |
| Tendon axial stiffness | $E \cdot A_{line}$ | $2.908 \cdot 10^9$ | $4.0889 \cdot 10^5$ | " | [N] |
| Modes (Rigid body) | | | | | |
| Surge natural frequency | $f_x$ | 0.03 | 0.29 | 0.03$^{\dagger}$ | [Hz] |
| Heave natural frequency | $f_z$ | 0.60 | 4.74 | 0.52$^{\dagger}$ | [Hz] |
| Pitch natural frequency | $f_{yy.f}$ | 0.33 | - | - | [Hz] |
| Modes (Flexible tower) | | | | | |
| Bottom-fixed tower bending mode | $f_{tw}$ | 0.33 | 3.01 | "" | [Hz] |
| Coupled tower fore-aft + pitch mode | $f_{yy+tw}$ | 0.25 | 2.27 | 0.25$^{\dagger}$ | [Hz] |

Chapter 7

# Analysis of the high-order dynamic response of EDF academic FOWT-TLP with experimental validation

## 7.1 Introduction

After applying and validating the nonlinear engineering numerical models on the EDF-TLP floater in fixed condition, preparing the set-up of the experimental campaign and calibrating the physical and numerical model to achieve similar static conditions, this chapter presents the comparative analysis of the dynamic response of the EDF-TLP.

This analysis is split into two main parts. The first analysis focuses on the response of the system in regular waves. This is done so that harmonics of the response can be isolated and analysed separately which allows to comment on the suitability of the load models at the different order of the response. The second and most extensive comparative analysis deals with the response of the EDF-TLP in severe irregular sea-states with wave-only and combined wind-wave conditions. This way, the performance of the models to predict the nonlinear response, extreme tension and ringing events is assessed in the most realistic condition possible under this thesis' scope.

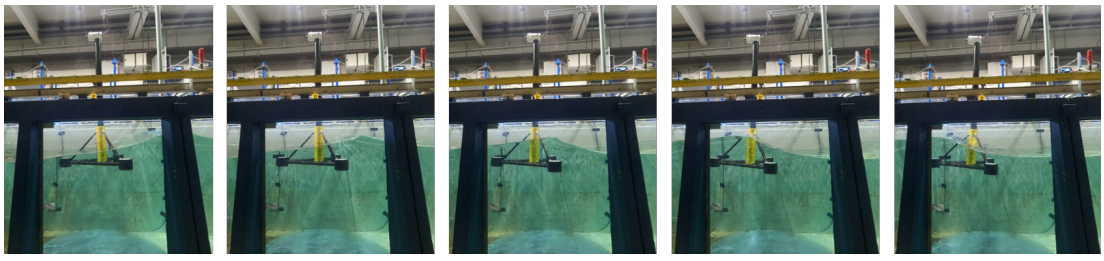

**Figure 7.1:** Time-lapse of the EDF-TLP physical model dynamic response in severe sea-state

## 7.2 Comparison of EDF academic FOWT-TLP response in regular waves

### 7.2.1 Wave generation

#### Targeted conditions

The present study is concerned with the analysis of high-frequency harmonics of the motion response and mooring tension of the EDF-TLP system. For that purpose, the system is first studied under regular waves of constant steepness $ka = 0.10$, $H/\lambda \approx 3\%$ and $ka = 0.20$, $H/\lambda \approx 6\%$. The summary of the wave cases studied experimentally is provided in Table 7.1. As seen in Figure 7.2, the wave steepnesses being tested are large enough to require the calculation of wave kinematics based on a nonlinear theory although all conditions considered remain within Stokes's theory. In terms of force regime, the tests in wave steepness of $kA = 0.10$ should be dominated by inertial forces according to Figure 7.2b, although case EOL010 is expected to have a significant contribution of the drag component. With double the steepness, half of the case move towards the region of equal dominance of inertial and drag forces. It is important to note here, that the graph considers structures which are fixed or with small movement and thus does not take into account the impact of drag damping in large motion such as resonant responses.

| | Scale 1:1 | | | Scale 1:83.3 | | | | | |
|---|---|---|---|---|---|---|---|---|---|
| Regular Test No | T [s] | H [m] | $\lambda$ [m] | T [s] | H [m] | $\lambda$ [m] | $ka$ | $kA$ | KC |
| kA = 0.10 | | | | | | | | | |
| EOL010 | 21.5 | 18.32 | 575.48 | 2.356 | 0.221 | 6.908 | 0.048 | 0.10 | 9.31 |
| EOL020 | 18.0 | 14.26 | 448.05 | 1.972 | 0.171 | 5.378 | 0.062 | 0.10 | 6.34 |
| EOL030 | 16.5 | 12.48 | 391.93 | 1.808 | 0.148 | 4.705 | 0.070 | 0.10 | 5.29 |
| EOL040 | 15 | 10.67 | 335.12 | 1.643 | 0.128 | 4.023 | 0.082 | 0.100 | 4.35 |
| EOL050 | 13.5 | 8.86 | 278.37 | 1.479 | 0.106 | 3.342 | 0.099 | 0.10 | 3.51 |
| EOL060 | 12.0 | 7.10 | 223.2 | 1.315 | 0.084 | 2.680 | 0.124 | 0.10 | 2.78 |
| EOL070 | 10.5 | 5.47 | 171.90 | 1.150 | 0.064 | 2.063 | 0.161 | 0.10 | 2.13 |
| EOL080 | 9.0 | 4.02 | 126.45 | 0.986 | 0.049 | 1.518 | 0.219 | 0.10 | 1.57 |
| EOL090b | 8.0 | 3.16 | 99.92 | 0.877 | 0.038 | 1.20 | 0.276 | 0.10 | 1.23 |
| EOL090 | 7.5 | 2.16 | 87.82 | 0.822 | 0.032 | 1.054 | 0.315 | 0.10 | 1.09 |
| kA = 0.20 | | | | | | | | | |
| EOL130 | 16.5 | 24.9 | 398.91 | 1.808 | 0.300 | 4.705 | 0.070 | 0.20 | 11.72 |
| EOL140 | 15 | 21.3 | 341.51 | 1.643 | 0.256 | 4.023 | 0.082 | 0.20 | 9.55 |
| EOL150 | 13.5 | 17.7 | 284.34 | 1.479 | 0.213 | 3.342 | 0.099 | 0.20 | 7.67 |
| EOL160 | 12.0 | 14.2 | 228.71 | 1.315 | 0.171 | 2.680 | 0.124 | 0.20 | 6.04 |
| EOL170 | 10.5 | 10.9 | 176.68 | 1.150 | 0.131 | 2.063 | 0.161 | 0.20 | 4.63 |
| EOL180 | 9.0 | 8.1 | 130.32 | 0.986 | 0.097 | 1.518 | 0.219 | 0.20 | 3.41 |

**Table 7.1:** Experimental monochromatic wave runs parameters. $K_C$ number is calculated from the crest velocity predicted by the Stream Function and the diameter of the TP of EDF-TLP

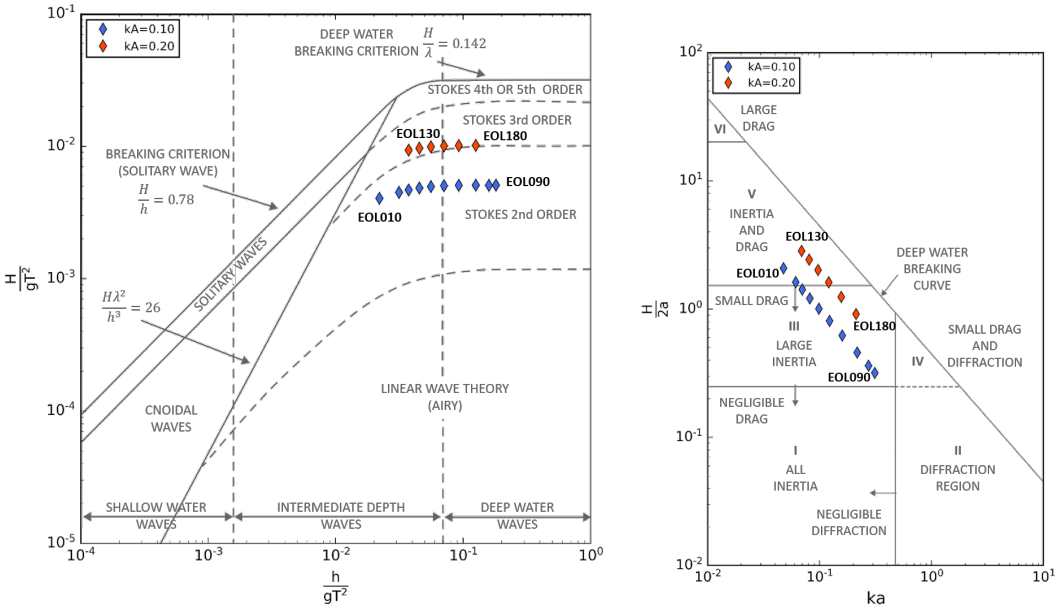


**(a)** **(b)**

**Figure 7.2:** Distribution of regular wave conditions test in wave flume within (a) the ranges of validity for common wave theories, (b) ranges of different wave force regimes. Adapted from Chakrabarti (1987)

### Measured conditions

The waves are generated experimentally using a piston wave-maker based on a linear potential flow theory. As mentioned in Huseby and Grue (2000), this leads to parasitic unbound higher-harmonics. In deep water, these waves can be avoided by analysing only the beginning of the wave train since the second parasitic harmonics travel at half the speed of the main wave group. This is the method adopted in the present paper due to restrictions on the wave-maker ends. A time window of three wave periods is selected just after the wave group front which is shown in Figure 7.5. The comparison between the regular wave amplitudes and phase measured in the wave flume and the reference values from the Stream Function is shown in Figure 7.3 and 7.4. The phases of the force harmonics are defined with reference to the crest of the main carrier wave.

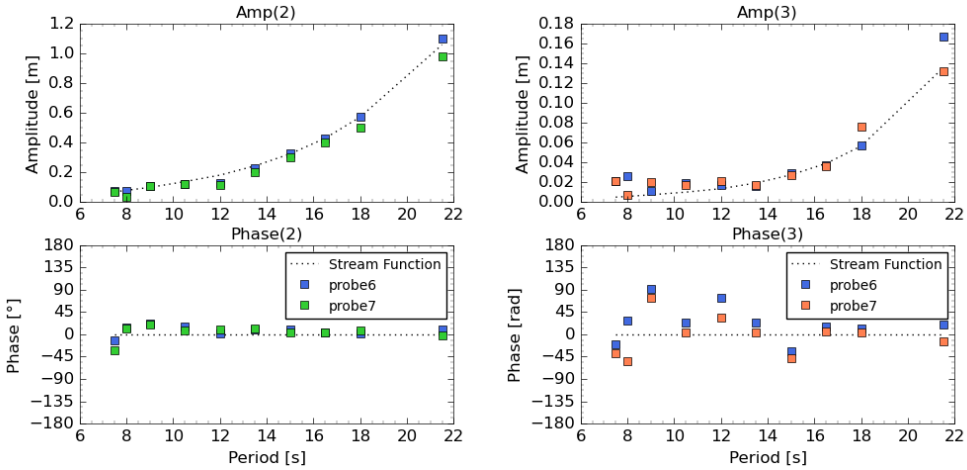


**Figure 7.3:** Comparison of measured second and third harmonic amplitudes and phase against Stream Function, kA=0.10

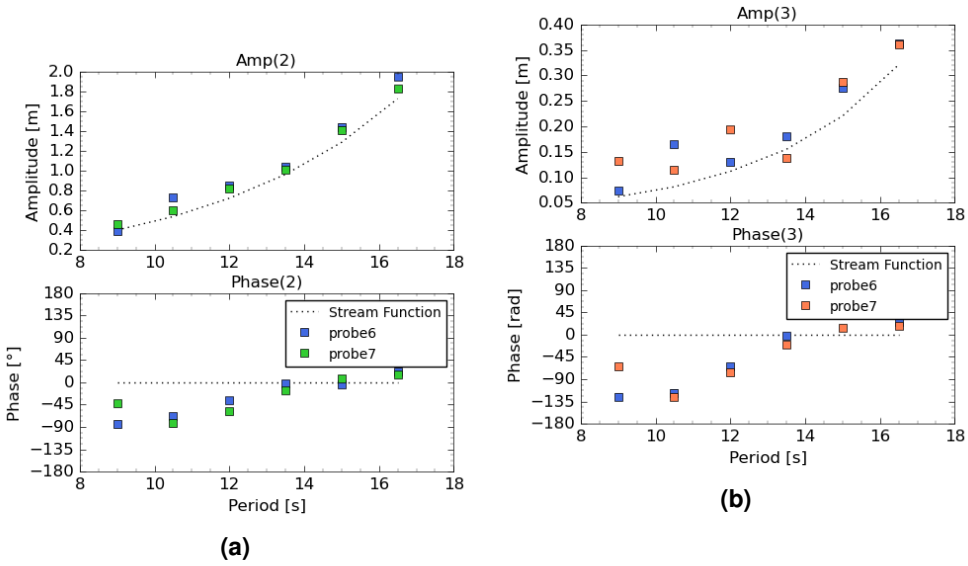


**Figure 7.4:** Comparison of measured second and third harmonic amplitudes and phase against Stream Function, kA=0.20

From a qualitative standpoint, the measured monochromatic wave records shown in Figure 7.5 appear in their majority of good quality. With reducing wave periods and higher wave steepness, the front of the wave group appears increasingly modulated as observed in cases EOL090, EOL180, EOL170 and EOL160. This modulation is due to the increasing instability of the monochromatic wave packet which is expected from Benjamin and Feir (1967) but which could also be increased by the wave-maker limits. This instability leads to strongly modulated packets with occurrences of wave breaking in lower periods tests which had to be

discarded. On the other hand, with increasing periods and also with increasing steepness, the appearance of the reflected front can be observed as in cases EOL010 and EOL130. Both of these effects increase with wave steepness and constrain the range of wave frequencies which could be tested. Hence, the case with $kA = 0.20$ has a reduced sample of waves.

It can be observed that in both wave steepness cases, the amplitudes of the second-harmonics of the incident wave, Figure 7.3a and 7.4a, are close to the reference Stream Function values which suggests that the wave field is generally free of parasitic harmonics. In terms of phase in case $kA = 0.10$, most periods agree well with the reference value. On the other hand, in the higher wave steepness case, $k = 0.20$, the lower periods below $13.5$ s appear to show increasing phase discrepancies. In terms of the third-harmonic, the amplitudes in the lower steepness case appear to be captured relatively decently. On the other hand, the quality of the third-harmonic components in the measured experimental wave field decreases significantly in the higher steepness case. The quality of the third-harmonic generation appears to decrease with reducing periods which is a similar observation than made on the second-harmonic phases. It is not known if these discrepancies are due to parasites or increasingly disturbed waves due to the wave-maker limits. However, considering that the generated free harmonics should catch up with the main wave group faster in longer waves, the wave maker limit appears a more likely culprit. This discrepancy is not of much concern since the nonlinear wave force generated by the third-harmonic of the incident wave is negligible in deep water conditions and is only dominant in shallow water conditions as seen in Section 4.4 based on prediction from FNV and semi-analytical potential flow theories.

### 7.2.2 Numerical models

The comparison of the nonlinear load transfer functions between CFD results and various engineering load models prediction in Chapter 5 has shown that a full potential load model is generally successful in capturing the second and third-order wave loads. The benefit of a potential load model versus a strip-theory model is especially visible at second-order where full QTFs transfer functions provide vastly superior predictions. At third-order, viscous drag becomes more dominant on some elements of the platform. Therefore, it is first interesting to compare the performance in dynamic condition of full potential flow models of various orders of non-linearity against the experimental results. Preliminary results of this study were compiled into a conference paper published in the Proceedings of the 33rd International Ocean and Polar Engineering Conference (Rongé, Peyrard, Venugopal, Johanning, & Xiao, 2023) whilst the updated results presented in Section 7.2.3 were presented live at the conference.

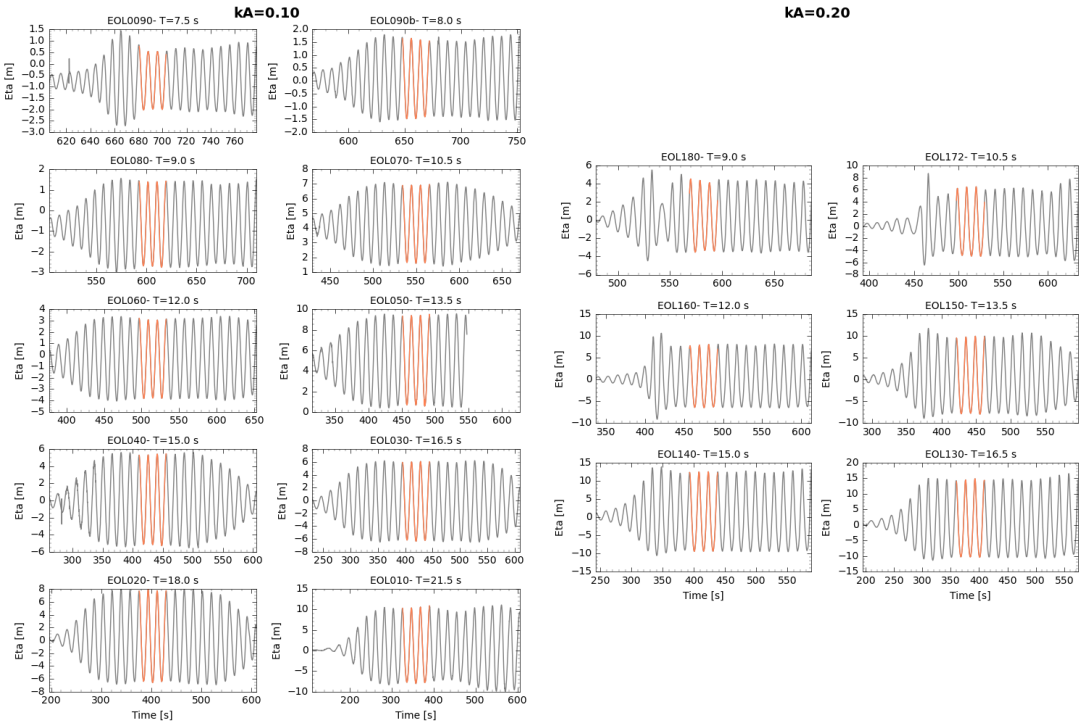


**Figure 7.5:** Wave probe recording of the monochromatic wave cases showing the time window analysed for steepness case: (a) kA=0.10, (b) kA = 0.20

As discussed in Chapter 5, strip-theory and semi-analytical potential flow formulas appear to provide relatively decent results in monochromatic waves on the transition piece. Furthermore, for the bracings, the strip-theory appears to provide a decent prediction of second-order loads. As for third-order loads, the results suggested that viscous drag plays the dominant load role on both the submerged buoys and bracings. Therefore, it is relevant to compare how various combinations of hybrid models succeed in representing the dynamic of the structure when compared to experimental results. Therefore varying degrees of hybrid potential-flow+strip theory models are also compared since, for most of them, second-order loads are simpler to calculate. The three models that are considered are detailed below. It is important to note that all models use the same linear potential flow hydrodynamic database presented in Chapter 5 to resolve the radiation problem. This way, the excitation wave loading approach is the only parameter being compared. For that reason, even a model using only the strip theory can be considered hybrid. It is also important to note that since the semi-analytical model uses a potential flow approach which includes phase shifts whilst strip-theory assumes constant phases, the combination of phases can create negative or positive interactions even if amplitudes element-wise are correct. This is an issue with using hybrid models on a structure such as the EDF-TLP which was discussed in Rongé, Peyrard, Venugopal, et al. (2022) and which is remedied here as explained below.

- HYB RAI A full Rainey model where all excitation loads are calculated based on Rainey's theory
- HYB SEM-TP: A hybrid model where the transition piece is entirely modelled using semi-analytical potential flow solutions for the linear, second and third-order forces whilst the remainder is calculated using a Rainey theory. This model is a third-order extension of the SEM model which was presented at OMAE 2022 (Rongé, Peyrard, Venugopal, et al., 2022) as a mid-range alternative between a simple Rainey theory model and a model requiring full QTF solution with a BEM solver. One key difference in the current iteration is the removal of the phase shift in the second-order semi-analytical solution to avoid the positive-negative phase interaction between the semi-analytiical potential flow and strip-theory mentioned above
- HYB QTF+FNV: A hybrid model where only the third-order loads on the transition piece are calculated using the FNV strip theory, the remainder of the loads being based on BEM potential flow. This model which is based on Krokstad et al. (1998) and Bachynski et al. (2015) is compared alongside its full potential flow equivalent using Malenica and Molin (1995) solution.

All models are detailed in Table 7.2 showing the wave load theories being used. An observation shared in Chapter 5 and highlighted in Figure 5.1 that is worth mentioning again is the fact that only some of the hybrid models are capable of taking into account the third-order inertial effects on the whole structure, although the inertial contributions from other elements than the TP have been shown to be low. Table 7.3 shows the coefficient used for the strip-theory approaches. The coefficients are kept constant as the idea is to test engineering models which typically make such assumptions. Furthermore, the calibration elements by elements and by flow condition is a task that could not be carried out during the time-frame of this thesis. The added mass coefficients are thus based on BEM calibration as shown in Chapter 5. On the other hand, the drag coefficients are based on industry standards and published work as explained in Section 5.2.2 and appeared to provide consistent nonlinear force transfer functions in comparison with CFD results presented in Section 5.4.

### 7.2.3 Results of response using potential flow method

In this section, the comparison of mooring line tension and motion response at the nacelle in a monochromatic wave regime is shown. To obtain the fundamental and harmonic responses, an FFT analysis is carried out over a window of three wave periods, and the harmonics that generate a detectable amplitude peak are then extracted. In regular waves, the experimental time window is chosen visually, based on the regularity of the signal which depends on frequencies. The comparison of fundamentals' harmonics of the surge, heave and pitch motion and mooring line tension indicates the quality of the hydrodynamic loading approach

| | Potential flow | | | Hybrids | | |
|---|---|---|---|---|---|---|
| | LIN | QTF | QTF+MAL | HYB RAI | HYB SEM-TP | HYB QTF+FNV |
| **Inertial** | | | | | | |
| Radiation | $C_m(\omega), B(\omega)$ | $C_m(\omega), B(\omega)$ | $C_m(\omega), B(\omega)$ | $C_m(\omega), B(\omega)$ | $C_m(\omega), B(\omega)$ | $C_m(\omega), B(\omega)$ |
| 1s-order | BEM LTF | BEM LTF | BEM LTF | Rainey | TP: McC.&F LTF<br>Rest:Rainey | BEM LTF |
| 2nd-order | None | BEM QTFs[1]$\pm$ | BEM QTFs$\pm$ | Rainey | TP: H&E.T. QTFs<br>Rest: Rainey | BEM QTFs$\pm$ |
| 3rd-order | None | None | TP: M.&M. H&E.T.<br>Rest: None | Rainey | TP: M.&M. CTFs<br>Rest: Rainey | TP: FNV<br>Rest: None |
| **Viscous** | | | | | | |
| Drag | Mor. drag | Mor. drag | Mor. drag | Mor. drag | Mor. drag | Mor. drag |
| Wave theories | S.F. | S.F | S.F | S.F | S.F | S.F |

**Table 7.2:** Hydrodynamic models being compared

| Elements | Added mass $C_{A,t}$ | Coeff. $C_{A,ax}$ | Drag $C_{D,t}$ | Coeff. $C_{D,ax}$ |
|---|---|---|---|---|
| Transition piece | 1.0 | -0.11 | 1.0 | 2.0 |
| Side buoys | 0.49 | 0.75 | 0.6 | 4.0 |
| Bracings | 1.0 | N/A | 1.0 | N/A |

**Table 7.3:** Added mass and drag coefficient used for strip-theory approaches

used at each frequency. Numerical results using a linear model, then adding second-order QTFs and finally adding Malenica's third-order transfer functions are shown here. The linear, second and third-order RAOs for the potential flow models in surge, heave and pitch are presented. Here, it is important to point out that the numerical prediction of the pitch response is not fully representative of the experimental measurements which measure the local pitch orientation of the nacelle. This is because the movement of the RNA is taken into account in the numerical model as a spring-mass-damper system. This does not resolve the tower bending and only provides the displacement at the centre of the hub without information on rotation. The RNA pitch angle is thus estimated by taking the full EDF-TLP rigid body pitch motion plus an additional angle calculated assuming a pin rotation of the tower+RNA around the base of the tower. The comparative analysis of the potential flow model mooring tension transfer functions is then provided for the single upstream mooring line (Line No1) and for the two symmetric downstream lines Line No2 and Line No3.

**Motion RAOs**

The harmonic motion RAOs are provided in Figure 7.6 for wave steepness $kA = 0.10$ and Figure 7.7 for $kA = 0.20$. The plots present the normalised response amplitude operators for each harmonic plotted against the fundamental frequency of the incident monochromatic wave train. As mentioned above, three runs were carried out for the lower wave steepness condition, $kA = 0.10$. One run used fish-line moorings and is referred to as Exp-old. The two more recent runs used the steel-wire moorings which are more representative of the actual geometry and weight distribution of the numerical model mooring lines. In wave steepness $kA = 0.20$, only one run with steel wire lines could be carried out due to time constraints.

Starting with the linear motion response which is shown on the left-hand side of Figure 7.6a, 7.6b, 7.6c and 7.7a, 7.7b, 7.7c, the results show that the measured experimental linear responses appear to agree relatively well with the numerical predictions. All numerical models agree since they all use the same linear force transfer functions and resolve radiation in the same manner. The addition of inertial nonlinear loads does not appear to have a significant reciprocating effect on the linear RAOs. The surge linear response predicted numerically between $f = 0.05 - 0.15$ Hz is extremely representative of the experimental measurements in the lower wave steepness case, $kA = 0.10$ (Figure 7.6). However, the numerical prediction of the peak surge response, in the frequency band considered, appears to be overestimated by around 25%. The predicted peak frequency also appears slightly shifted to the lower frequency compared to the experimental results, potentially due to the slightly higher natural period in surge predicted numerically. As for the difference between experimental and numerical prediction of the peak surge amplitude, it reduces in steeper waves as observed in Figure 7.7. This suggests a relation with the modelling of the viscous drag damping which in this thesis is modelled using a constant drag coefficient. Numerical over-prediction of the peak surge response around the resonant mode is in line with other experimental results which also observed an increased level of drag damping in experimental monochromatic wave conditions (Oguz et al., 2018; Vita et al., 2015). Moving to the heave and pitch response at the fundamental frequency, there appears to be a high experimental scatter in the heave displacement for the case with wave steepness of $kA = 0.10$ in Figure 7.6b. However, considering the small motion involved and a consistent trend between the different experimental runs, the linear numerical load model appears to perform well with a slight underestimation of the response observed in both wave steepness cases.

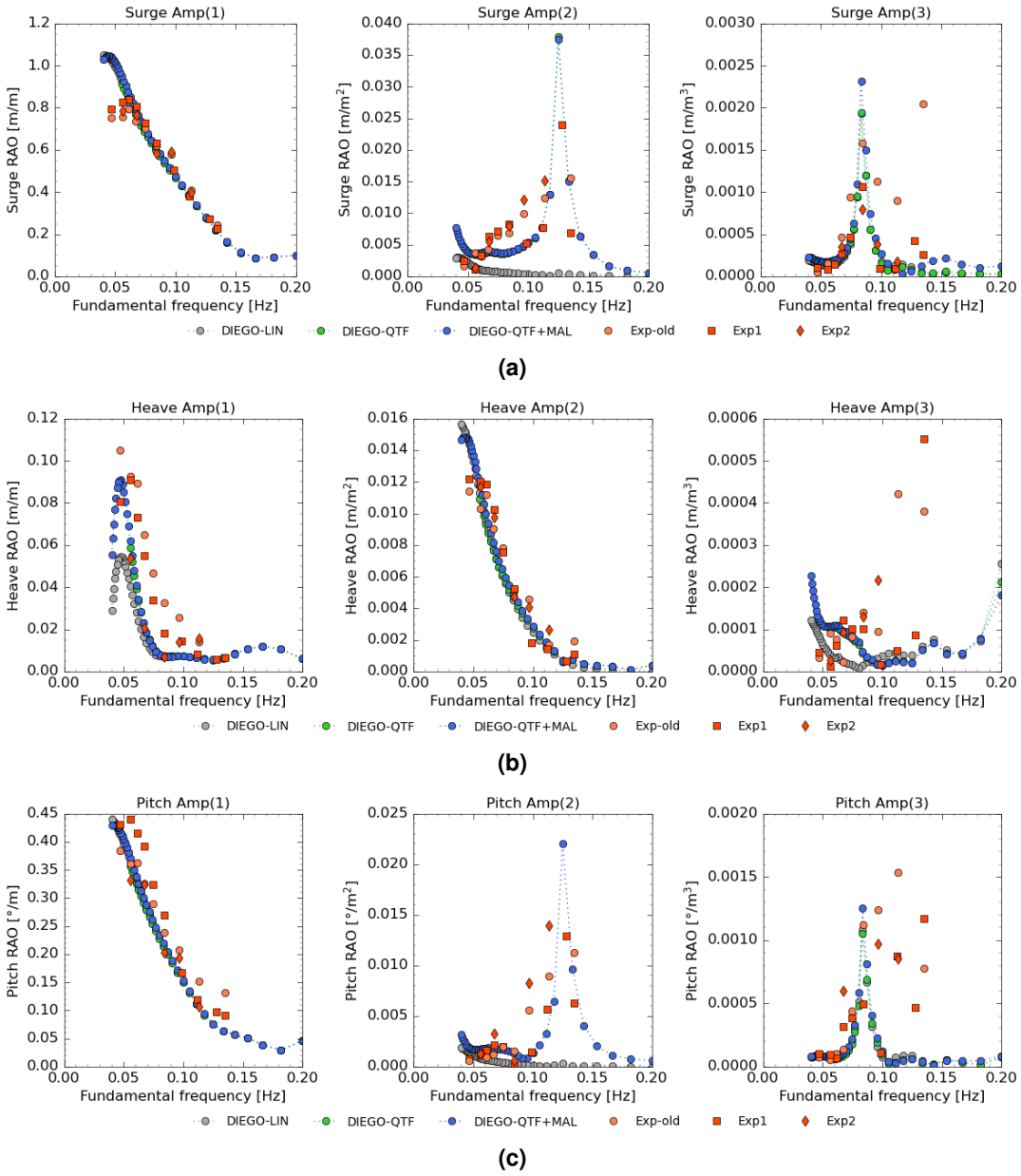


**Figure 7.6:** Comparison of the EDF-TLP harmonic motion RAOs for (a) Surge, (b) Heave and (c) Pitch DoFs - Potential flow models, $kA$ = 0.10

The results for the second-order surge and pitch response show that the nonlinear numerical models capture the springing peak at $f = 0.125$ Hz due to the resonance of the coupled pitch-tower bending mode with the second-order hydrodynamic loads. However, based on the single experimental result at that frequency for wave steepness $kA = 0.10$, the nonlinear numerical models appear to overestimate the motion amplitude. The peak response in wave steepness $kA = 0.20$ could not be captured at the resonant fundamental frequency and beyond due to the limitation of the wave tank in terms of wave reflection. At second-order,

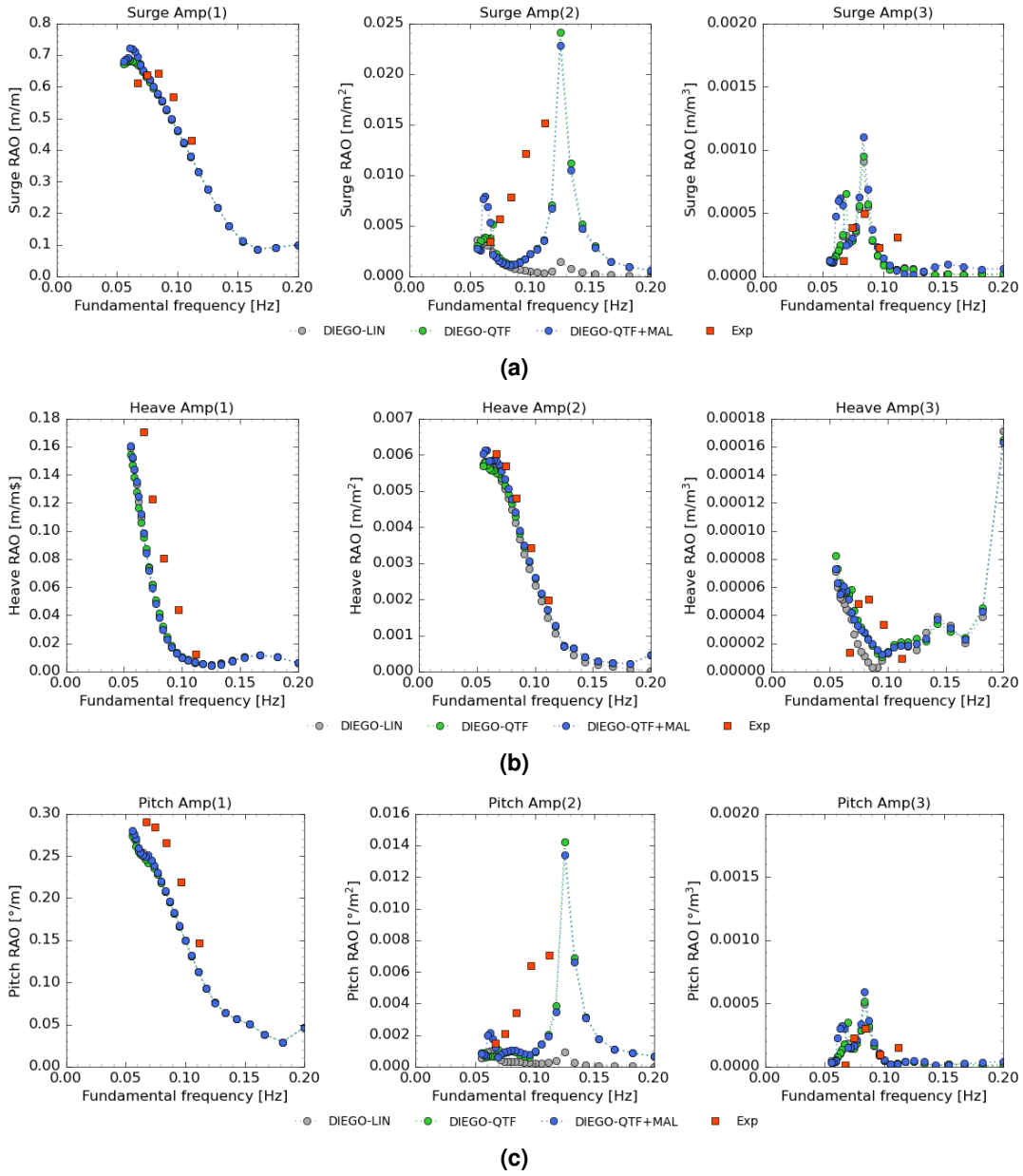


**Figure 7.7:** Comparison of the EDF-TLP harmonic motion RAOs for (a) Surge, (b) Heave and (c) Pitch DoFs - Potential flow models, $kA$ = 0.20

the linear numerical model appears to underestimate strongly the order of magnitude of the second-harmonic motion in pitch and surge and fails to capture the springing peak in the $kA = 0.10$ steepness case. This observation highlights that ignoring the second-order sum-frequency forces in the TLP system results in ignoring harmonic motions representing between 10 to 20 % of the linear response depending on the frequency and incident wave height. On the other hand, the second-order numerical heave response matches very well the experimental measurements. This is expected since, in surge motion, a TLP behaves

much like a pendulum, generating a heave motion at double the frequency of the surge-pitch motion. This effect is visible since the first-order surge and pitch RAOs and second-order heave RAOs appear almost identical in trend. In that, the second-harmonic heave motion can be considered a linear response.

Finally, looking at the third-order motion, a springing response due to the resonant excitation of the pitch-tower bending mode by third-order hydrodynamic forces is visible on the rightmost side of the surge and pitch RAOs of Figure 7.6a, 7.6c and Figure 7.7a and 7.7c. In this case, it is interesting to note that all numerical models, including the linear inertial model, predict a third-order response and a springing peak at $f = 0.083$ Hz with a nice level of consistency and agreement with the experimental results. These results therefore suggest that the third-order response is dominated by viscous rather than inertial force excitation. This dominance of drag on third-order forces was already hinted at by the results of the force transfer functions on the platform in fixed position presented in Section 5.4, the inclusion of motion possibly leading to an increase in drag dominance. In fact, the addition of the third-order inertial load only accounts for an approximate 20% increase in the springing response in both surge and pitch. Therefore, whilst neglecting second-order sum-frequency forces appears to be wholly inadequate for FOWT-TLP systems, the current results suggest that including a third-order inertial model appears here to be optional. Another noteworthy observation is that the RAOs at the third harmonic springing peak reduce in amplitude in steeper waves. This is clearly visible by comparing the third-order surge and pitch RAOs in Figure 7.6a, 7.6c and 7.7a, 7.7c, showing a reduction of around 50% in normalised motion amplitude between wave steepness of $kA = 0.10$ and $kA = 0.20$. This effect is captured numerically as well as measured physically with a similar amplitude ratio between the lower and higher wave steepness. The reason for this reduction could be due to several factors. As shown in the literature, fully nonlinear simulations and experimental tests have shown that the normalised force amplitude reduces with increasing steepness which could explain some of this reduction. However, since this effect is also captured numerically with load models based on transfer functions, it is more likely that this reduction in higher wave steepness is due to increasing drag damping.

Generally, for results in wave steepness of $kA = 0.10$, the experimental runs, Exp1 and Exp2, using the steel wire mooring lines, provide relatively consistent results outside the range of the springing peak. In the range of the springing peak, more significant scatter is observed with amplitudes varying sometimes significantly. However, results suggest that the springing motion response is overestimated by the numerical models. In pitch, the third-order numerical response in pitch is similarly as neat as the surge response. However, the experimental measurements do not show a neat springing peak but rather a very energetic bandwidth between $f = 0.083$ Hz and $f = 0.11$ Hz. It is here important to note that the fundamental frequency $f = 0.11$ Hz comes exactly at a third of the fore-aft tower "bending" of

the physical model and the predicted rigid body pitch resonance which both occur at $f = 0.33$ Hz. This probably explains the energy in this bandwidth due to the strong coupling between the tower bending and the platform pitch response. In terms of third-order heave RAOs, the points measured experimentally in Figure 7.6b are difficult to compare to the numerical results. This is partly due to the small amplitudes of the heave motion which at the third-harmonic is significantly below the limit of our video pixel resolution which lies around $0.03$ m at full 10-MW scale per pixel. However, the pitch springing peak can be observed in the experimental heave response followed by an increasing response towards the heave mode. On the other hand, the numerical model predicts a decreasing third-order response from $0.05 - 0.15$ Hz and then a sudden peak at $f = 0.20$ Hz coinciding with the third-order force excitation of the heave natural mode.

#### Line tension transfer functions

Focusing now on the mooring line normalised tension in both wave steepness, Figure 7.8 for $ka = 0.10$ and Figure 7.9 for $kA = 0.20$, it is observed that, as per the motion response, the linear mooring tension transfer functions measured experimentally and predicted numerically agree very well. There appears to be increasing experimental scatter around the peak response at $f \approx 0.10$ Hz and higher frequencies which can be related to the reduction in wave generation quality. The linear line tension response in Line No1 for both wave steepness is very well captured by all the potential flow numerical models which further confirms their performance in capturing the main response of the EDF-TLP system. Furthermore, it is interesting to note that despite the overestimation of the peak linear surge and pitch response by the numerical models, the corresponding line-tension transfer functions agree very well with the experimental results. This observation was also made by Oguz et al. (2018) and shows that while the experimental motion response is strongly affected by drag damping, this effect is less perceptible on the mooring system. This can be further shown by comparing the visible change in the linear motion RAOs against the relatively consistent linear mooring response with increasing wave steepness.

Continuing the analysis of the linear mooring response, it is observed that the line tension is at its maximum in Line No1 for a wave of $f = 0.104$ Hz and of $f = 0.12$ Hz for downstream Lines No2 and No3. These frequencies correspond to the peak pitch moment which occurs when the platform length corresponds to half the incident wavelength. A zone of low dynamic tension around $f \approx 0.06$ Hz is observed and quite discernible on the downstream lines. It corresponds to a low-frequency bandwidth where the incident waves are long enough to ensure that the forces on the platform are in phase, which reduces the pitch moment, but

located outside the range of the surge mode resonance which occurs at $f_{n,x} = 0.03$ Hz. The reader is also referred to the linear force transfer functions presented in Section 5.4. This zone appears to be slightly shifted to higher frequencies in the experimental model but the transfer function amplitude appears to be captured with reasonable accuracy.

While the first-order wave model is pretty successful at predicting the dominant linear response, the comparison of second-order normalised line tensions shows that assuming a simple linear model for inertial wave loads is wholly inadequate to the EDF-TLP system, and probably to any FOWT-TLP systems using a large central column. As observed with the motion RAOs, the linear model strongly underestimates the second-harmonic response beyond a fundamental frequency of $f = 0.06$ Hz and fails to capture the resonant springing peak. On the other hand, both models using sum-frequency QTFs predict the same peak response at the pitch-tower bending mode. The numerically predicted peak corresponds well to the one obtained experimentally at a wave steepness of $kA = 0.10$. This is despite the over-prediction of the springing motion response which leads to a similar conclusion on the effect of drag damping than made above. The peak response appears broader at wave steepness $kA = 0.20$. However, measurements could not be taken at the resonant fundamental frequency and beyond due to the limitation of the wave tank in terms of wave reflection. Outside of the peak, the second-order response predicted by the nonlinear numerical models appears to generally respect the experimental response scatter trend, especially around $f = 0.05 - 0.1$ Hz despite some asymmetry observed experimentally in the downstream lines. In wave steepness $kA = 0.10$, the experimental results obtained with the old mooring system made of fish lines, Exp-old, appear in accordance with the results obtained in the two following runs using steel wire moorings.

Taking a look at the order of magnitude of the second-order mooring line tensions, one can note that, assuming wave amplitudes of a similar size to the TP radius, such as $a \approx A$, these tensions can represent load cycles of around 20% to 50% of the firs-order mooring response, depending on frequencies, and take an even higher proportion at the springing resonance. These results go in line with the findings of Bachynski (2014) who showed that including sum-frequency QTFs could increase the total fatigue damage significantly.

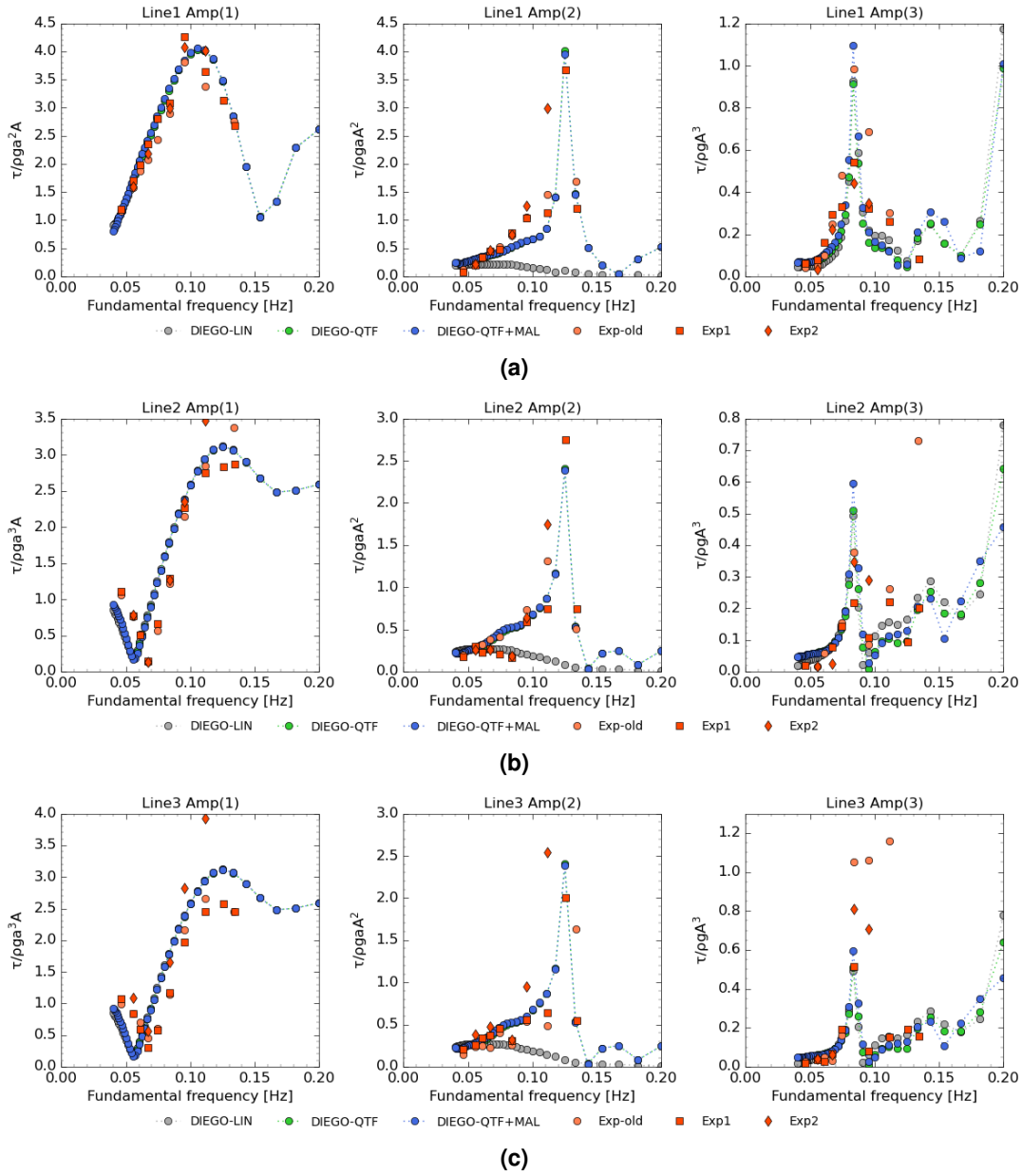


**Figure 7.8:** Comparison of EDF-TLP line tension harmonics transfer functions for (a) Upstream Line No1, downstream (b) Line No2 and (c) Line No3 - Potential flow models, $kA$=0.10

Finally, the results for the third-order mooring response confirm the observation made above, on the corresponding motion RAOs. The springing response of the pitch-tower bending mode is visible in all three lines at the fundamental frequency $f = 0.083$ Hz. The agreement between the various experimental runs and all three numerical models is very satisfying, with all appearing to perform very well in predicting the experimental third-order tension amplitudes around the springing peak. In Line No1 and No2, the amplitude of the springing

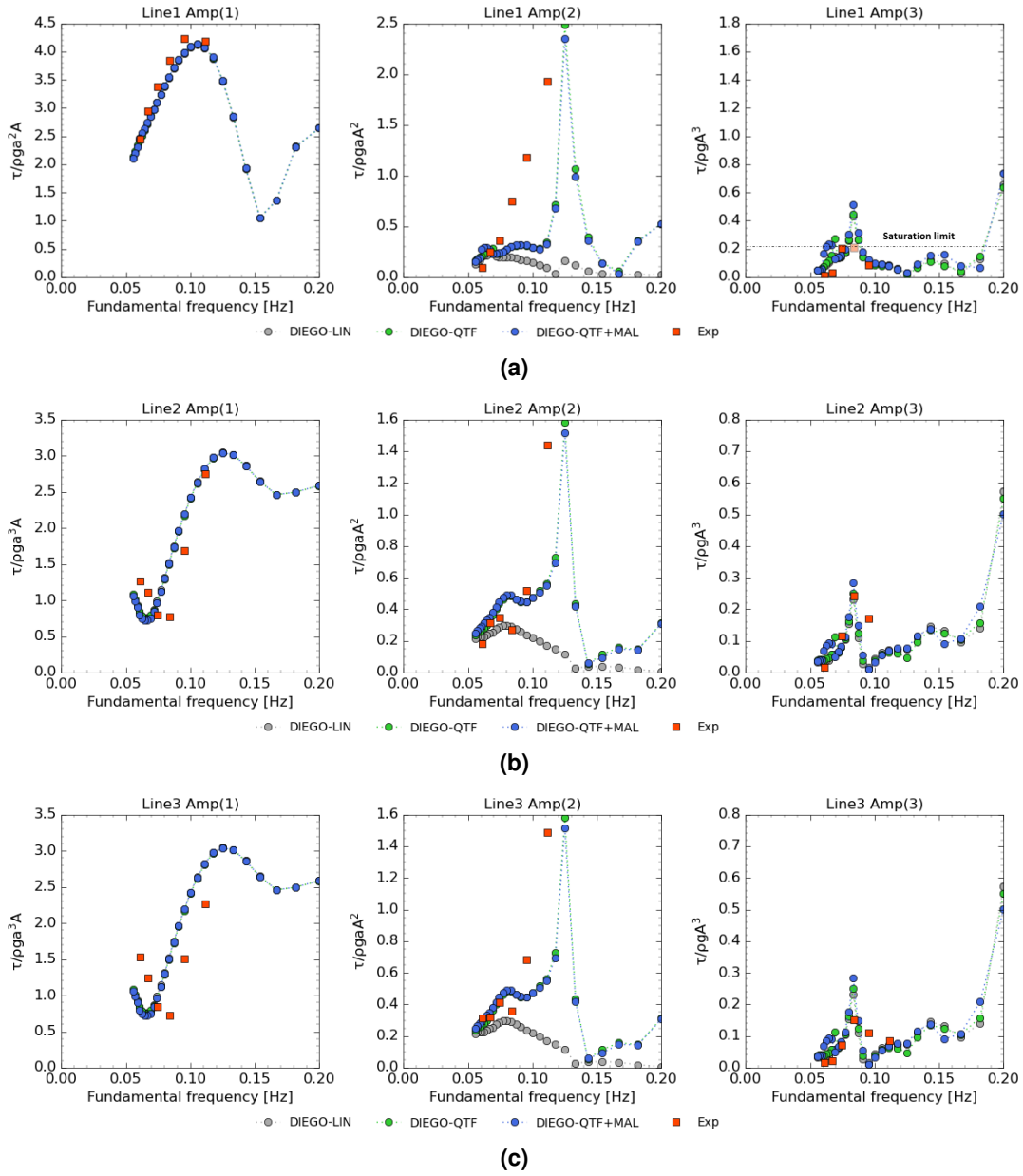


**Figure 7.9:** Comparison of EDF-TLP line tension harmonics transfer functions for (a) Upstream Line No1, downstream (b) Line No2 and (c) Line No3 - Potential flow models, $kA$=0.20

response obtained with the more recent runs using steel-wire lines appears to be over-predicted by around 50-60% by all the numerical models. In the downstream Line No3, the numerical models springing peaks fall in between the experimental scatter. The experimental runs using fish-line moorings, Exp-old, generally agree with the more recent runs in the low frequencies but predict a significantly higher resonant response and strong high-frequency harmonic response in Line No3 leading to questions on the reliability of these runs.

### 7.2.4 Results of response using hybrid and full strip theory models

The nonlinear potential flow numerical models appeared pretty successful in reproducing the linear and nonlinear harmonic response of the EDF-TLP in regular waves. The inclusion of second-order diffraction forces was found to be the leading parameter in differentiating these models with the addition of third-order forces marginally affecting the prediction of the third-order response. However, calculating sum-frequency QTFs with BEM can be a time-consuming endeavour. Therefore, it was found interesting to compare this full potential-flow approach with several ranges of hybrid strip-theory/potential flow models. Two of these, DIEGO-SEM TP and DIEGO-RAI, calculate the second-order forces in a simplified manner. The third hybrid model, DIEGO-QTF+FNV, is used for comparing the strip-theory prediction in third-order response against the full potential flow approach. This comparative analysis is only provided with the lower wave steepness condition, $kA = 0.10$.

Starting with the harmonics of motion RAOs in Figure 7.10, it is observed that the general linear motion response in all DoFs and the heave response at double wave frequency is generally consistent with the previous results. On the other hand, differences can be observed in the second-order response. Whilst, as expected, the hybrid model QTF+FNV agrees with the nonlinear full potential flow approach, the two simpler models, DIEGO-RAI and DIEGO-SEM TP, predict generally a lower second-order surge and pitch motion response that appear less representative of the experimental results. This could be tied to the under-prediction of the second-order heave force and pitch moment by the Rainey model in Section 5.4 around the relevant frequencies ($ka = 0.1 - 0.2$ or $f = 0.075 - 0.11$ Hz). However, both methods do predict the springing motion response in good agreement with the experimental result although this is probably coincidental. These approaches therefore provide a better alternative than a simple linear potential flow model. The hybrid semi-analytical model, DIEGO-SEM TP, appears to predict a similar springing response to the Rainey load model. As seen in Section 5.4, both Rainey's approach and Huang and Eatock Taylor (1996) semi-analytical approach predict similar amplitudes on the TP at the springing frequency, $f = 0.125$ Hz which corresponds to $ka = 0.24$. As for the third-order response, all models appear to agree with the previous numerical results which reinforces the conclusion that most of the third-order force is due to viscous drag. The model using Rainey's approach predicts a similar peak third-order springing response than the linear potential flow model showing that the addition of Rainey's third-order surface force and other nonlinear inertial effects on the structure including on the bracing are negligible in this situation.

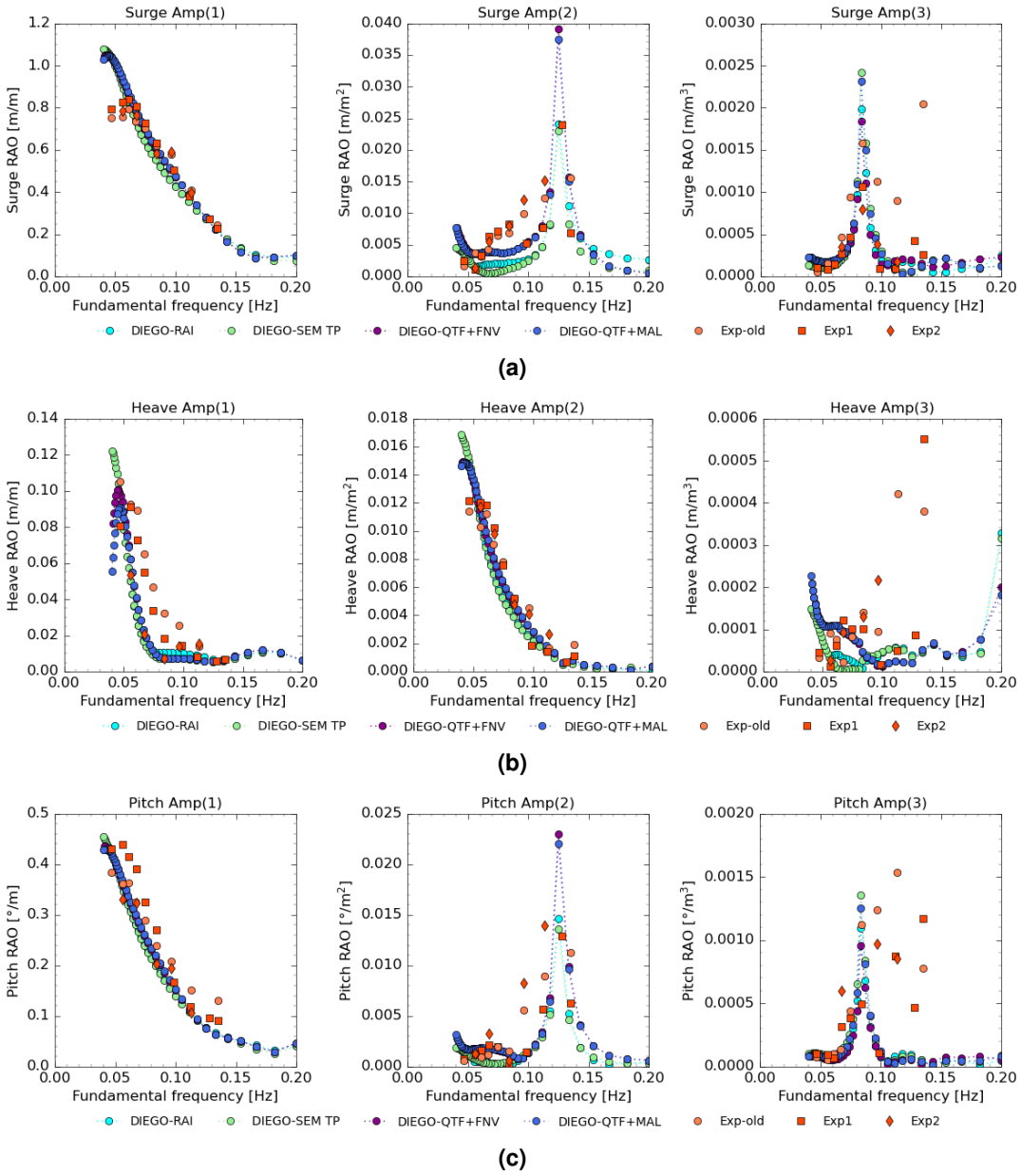


**Figure 7.10:** Comparison of the EDF-TLP harmonic motion RAOs for (a) Surge, (b) Heave and (c) Pitch DoFs - Hybrid models, $kA$=0.10

Moving to the comparison of the harmonic line tension response in Figure 7.11c, the observations made above with the motion response are generally applicable to the mooring response. The main difference lies in the inaccurate representation of the linear mooring response with the Rainey model, DIEGO-RAI, which when compared with the more accurate hybrid semi-analytical model DIEGO SEM TP, appears to be connected to the slightly inaccurate representation of the linear force transfer functions on the TP at low frequency as seen

in Section 5.4. This difference is small but visible in the heave force transfer functions. In that sense, the semi-analytical hybrid model, DIEGO-SEM TP, seems to provide a more suitable alternative than either a linear potential flow or a full strip theory model by being generally more representative of both the linear and second-order response than any of them.

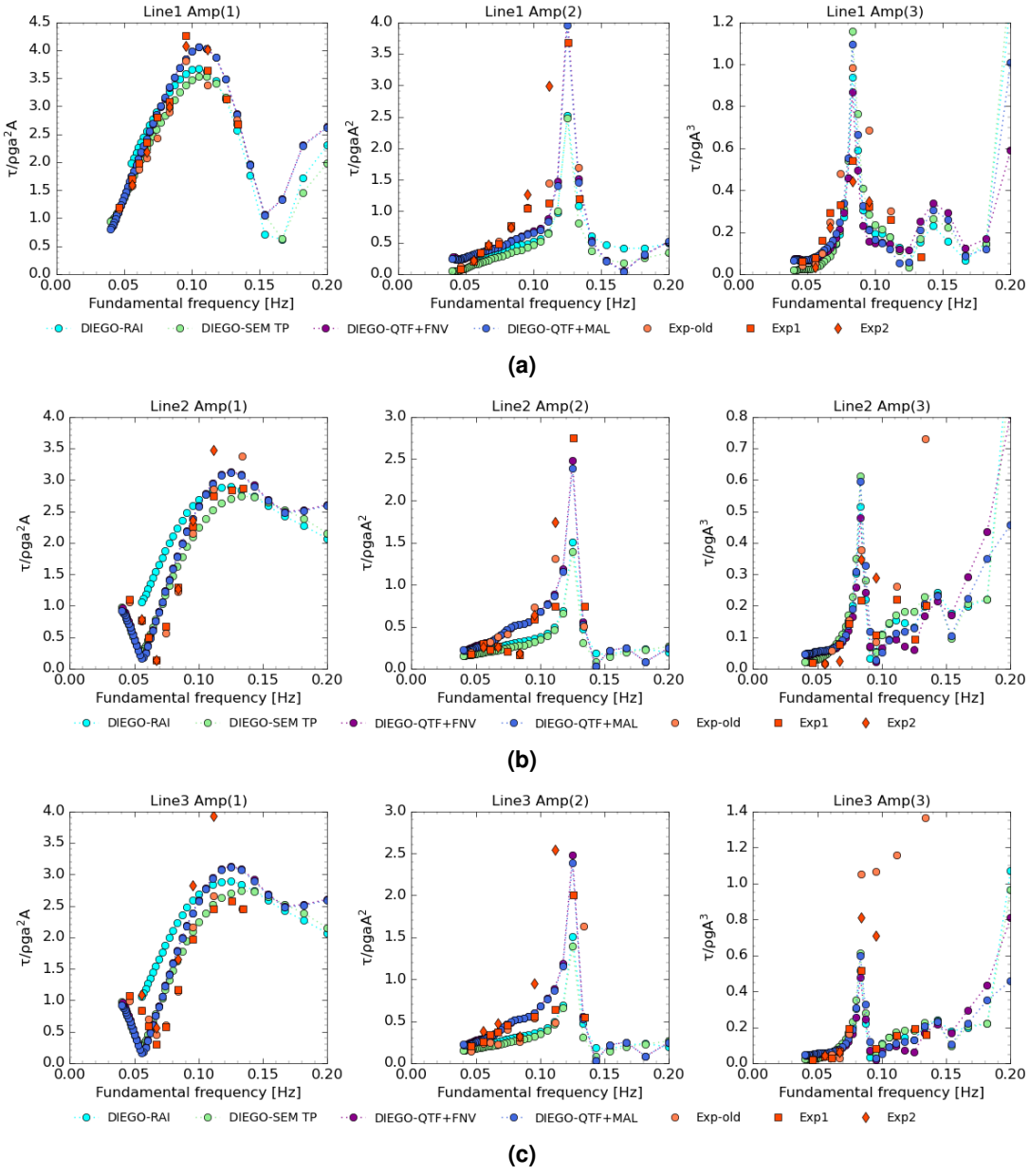


**Figure 7.11:** Comparison of EDF-TLP line tension harmonics transfer functions for (a) Upstream Line No1, downstream (b) Line No2 and (c) Line No3 - Hybrid models, $kA$=0.10

**Sensitivity to drag and damping**

As can be expected, the resonant amplitude of a system is strongly linked to damping. Damping is a factor that is difficult to replicate in physical models. Whether it is structural or viscous drag damping, both tend to be chosen based on empirical data, best practices and calibration based on decay test measurements. Therefore, to highlight potential sources of inaccuracies and errors, sensitivity analysis of the three main sources of damping on the EDF-TLP harmonic response is carried out. Figure 7.12 displays the sensitivity of the harmonic tension response of Line No1 to the axial drag on the cylinder end (excitation force and damping) in Figure 7.12a, to the structural damping in the tower flexibility model in Figure 7.12b and to the structural damping in the mooring system in Figure 7.12c. For each harmonic, the normalised amplitude of Line No1 tension for four different periods is plotted against an increasing level of drag or Rayleigh damping coefficients. The chosen periods $T = 12$ s, $T = 9$ s, $T = 8$ s and $T = 6$ s trigger resonant responses respectively due to third-order excitation of the pitch-tower bending mode, second-order excitation of the pitch-tower bending mode and third-order excitation of the heave mode.

The results show that change in the axial drag coefficient affects solely the response at $T = 12$ s, that is at the third-order springing in pitch-tower mode and at $T = 6$ s, at the third-order springing in heave. The axial drag has a significant linear correlation with the third-order springing response at $T = 12$ s with a doubling of the axial drag coefficient resulting in roughly a 20% increase in the line tension springing amplitude. This shows that the excitation effect of the axial drag dominates over the damping effect in this case, whereas at $T = 6$ s it appears that the drag switches from having mostly a damping effect to having an exciting effect with increasing drag coefficent. Tower damping is also seen to be a a significant source of inaccuracies in the numerical models since a small change in damping ratio between 0-5% can result in tension amplitudes at springing being reduced by almost half for both second-order and third-order springing response. This effect is less pronounced with structural damping in the mooring lines but remains a concern.

**Summary**

Overall, the experimental linear response appears to agree well with most of the current numerical models which confirms that both experimental and physical models are hydrodynamically representative of the same structure. The springing motion responses at both second and third-order appear to be overestimated by the nonlinear numerical models which could be related to a high influence of viscous drag damping on the resonant response of the experimental models as was observed in other studies. Generally, the match between numerical and experimental second and third-order line tension transfer functions appears very satisfying. At second-order, the results confirm the positive impact of having high-frequency hydrodynamic

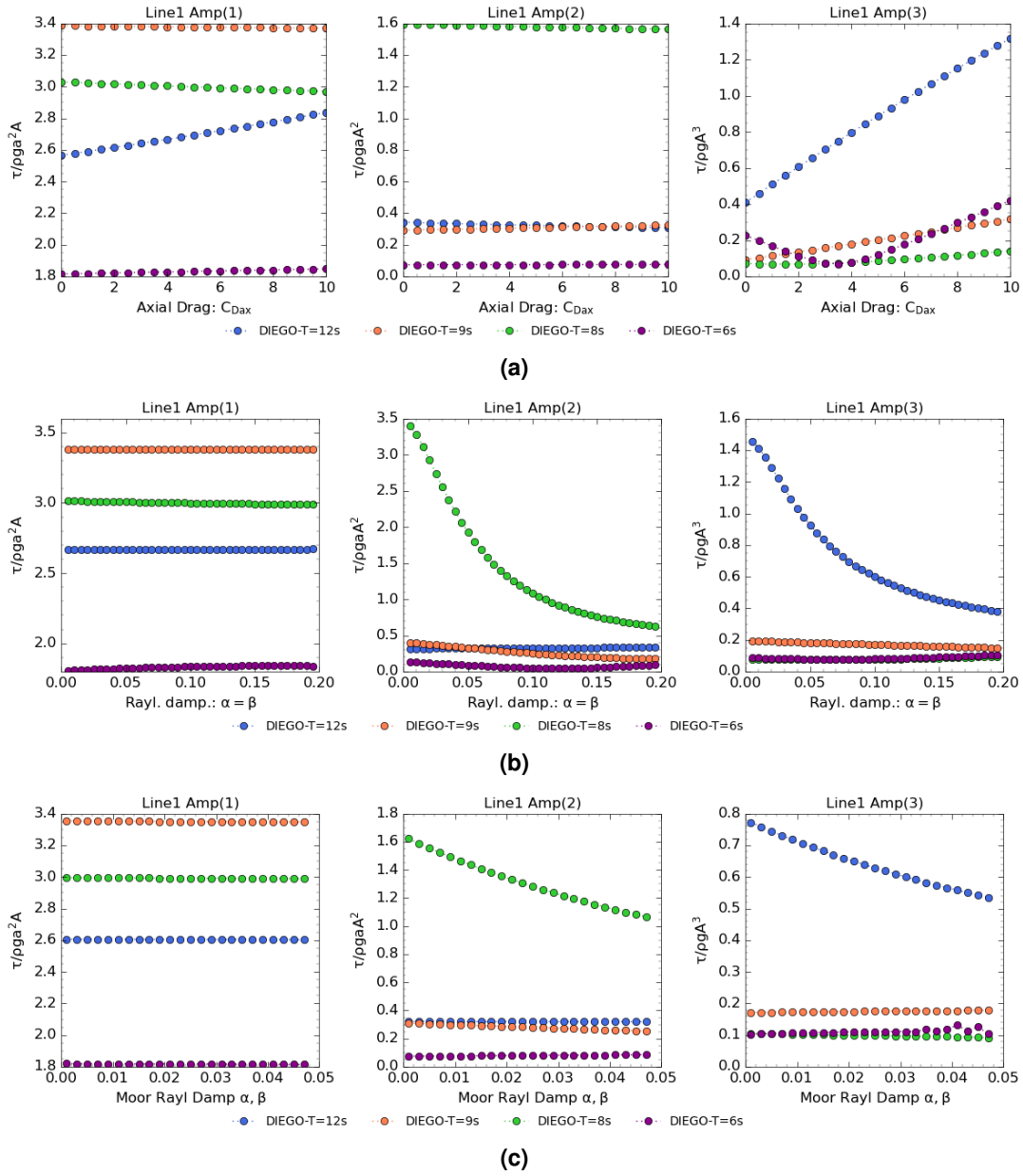


**Figure 7.12:** Sensitivity tests of resonant mooring tension response of the numerical model to (a) increasing axial drag, and increasing damping in (b) tower structure (c) mooring lines, $kA$=0.10

loading models to capture springing responses of floating wind TLP accurately. On the other hand, the third-order response and springing peak appear to be captured relatively accurately regardless of the inertial wave load model applied and seem to be dominated by viscous drag force excitation.

The tower flexibility does impact the accuracy of the numerical simulations. The experimental bandwidth between the pitch resonant frequency of the full system and the first tower bending mode appears more energetic than what is predicted by the numerical model. This could be due to the simple representation of the tower nacelle as a mass-spring-damper system rather than a more accurate structural model. Limit in the accuracy of the optical tracking method at such small amplitudes is also a possibility. However, these results confirm the importance of having a strong coupling between the mooring-platform hydrodynamic module and the turbine-nacelle-tower structural and aerodynamic modules to simulate springing response in aero-hydro-elastic time domain solvers. This is because there is a strong interaction between the tower's first bending mode and the pitch response of the TLP floater as found in previous studies (Bachynski et al., 2015; Koo et al., 2013; Molin, Remy, & Falcon, 2004).

## 7.3 Comparison of EDF academic FOWT-TLP response in irregular sea-states

The analysis of the response in regular waves highlighted the stationary resonant response of the system to the nonlinear wave load effects which is also referred to as springing. However, to investigate the capacity of the models to predict the response to realistic sea-states and specifically the transient resonant responses, the dynamic of the EDF-TLP in irregular sea-states had to be investigated. This section therefore presents this analysis, starting with explaining the range of environmental conditions (EC) that have been tested. This is followed by presenting the comparison of experimental measurements and numerical results using the measured wave field over a shorter time-window for each EC. Then an analysis is presented comparing numerical runs with randomly generated JONSWAP spectra. Finally, it was decided to focus on the accuracy of the ringing and slacking event predictions by numerical model compared to experimental data, including time-frequency analysis of some selected events.

### 7.3.1 Generation of irregular sea-states

#### Choice of Sea-states

The experimental campaign aims to test the applicability of the low to medium-fidelity load models in a range of severe wave conditions. The choice of sea-states to validate the numerical models is infinite and many parameters of irregular sea-sates could be investigated. However, due to time constraints, a limited amount of cases had to be selected. In particular and as stated above, comparing the probabilities of occurrence of extreme tensions, ringing and slacking events between experimental and numerical models is one of the main

interests of this exercise. For that purpose, it was not necessary to base it on specific site data. Therefore, combinations of $H_s$, $T_p$, $U_{wind}$ were chosen based on the original JONSWAP joint distribution of Hasselmann et al. (1973) (Figure 7.13) as done by Bachynski (2014). To facilitate the selection, the peak period was fixed at $T_p = 12$ s to concentrate the energy around the bandwidth that would generate third-order effects likely to trigger the coupled pitch-tower fore-aft bending mode as well as the individual tower mode. Then the environmental conditions shown in Table 7.4 were selected based on the $50$ year contour with increasing wind speed and hence increasing significant wave-height. The wind speeds considered were chosen based on the DTU-10MW thrust curve Figure 3.13 to have wind turbine conditions representative of (a) the peak thrust at the rated wind speed, (b) thrust above-rated wind speed, (c) idle conditions (no-wind).

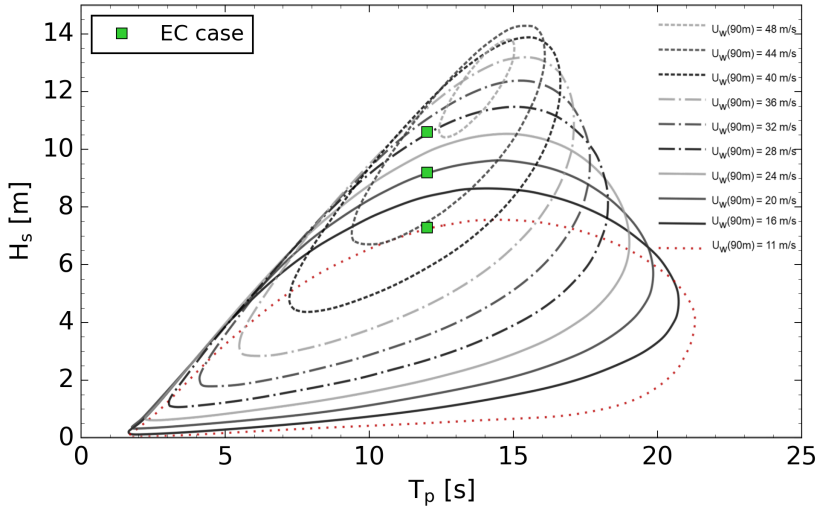


**Figure 7.13:** Selected environmental conditions based on the JONSWAP 50-year return period wind-wave joint probability contour plots adapted from Bachynski (2014) based on JONSWAP data (Hasselmann et al., 1973). The dotted red curve is an assumed extension of the joint-probability plot at lower wind speed.

| Conditions | EC No | Wave conditions No | $H_s$ [m] | $T_p$ [s] | Spectra | $\gamma$ [-] | $U_{wind}$ [m/s] |
|---|---|---|---|---|---|---|---|
| Wave only | EC1a | EOL1210 | 7.3 | 12.0 | JONSWAP | 3.3 | - |
| | EC2a | EOL1100 | 9.2 | 12.0 | JONSWAP | 3.3 | - |
| | EC3a | EOL1000 | 10.6 | 12.0 | JONSWAP | 3.3 | - |
| Wave+wind | EC1b | EOL1210 | 7.3 | 12.0 | JONSWAP | 3.3 | 11. |
| | EC2b | EOL1100 | 9.2 | 12.0 | JONSWAP | 3.3 | 20. |

**Table 7.4:** parameters of considered environmental conditions considered for wind and wind-wave cases

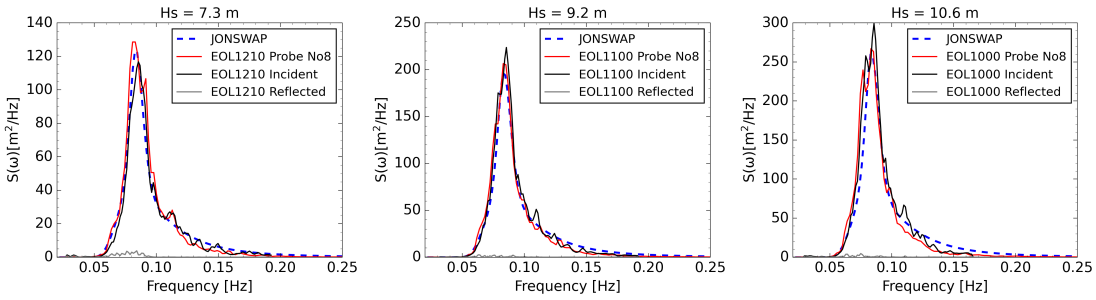


**(a)** **(b)** **(c)**

**Figure 7.14:** Measured power density spectra (a)(b)(c) comparison of spectra measured at Probe No8 for each seed draw against analytical JOSWAP spectra and measured incident and reflected spectra measured at probe No1 to No5

### Quality of generation

Using the environmental conditions selected above, three runs of 3 h at full scale (17 min model scale) for each set of wave conditions were carried out, using a different seed for the random phase, in order to verify repeatability and allow for redundancies in the campaign. The wave field was generated using the JONSWAP option of the wave-maker software. The wave-field was measured at the location corresponding to the centre of the model (Probe 8) as per guidelines of the ITTC (Ocean Engineering Committee of the 28th ITTC, 2017) both to verify the quality of wave generated at the model location as well as to have the same wave signal in the numerical model. The plots of the measured power spectral density at the location of the model for the three wave conditions are shown in Figure 7.14. The incident and reflected wave field are also measured by the probes located just downstream from the wave maker (Probe 1 to 5 in Figure 6.3). Table 7.5 displays the comparison between targeted and measured spectra including the measured reflection coefficient.

From those graphs, one can conclude that generally the targeted spectra are relatively well represented in the high energy bandwidth. However, frequencies above $f = 0.12$ Hz, $T = 8$ s appear less energetic than in the targeted JONWSWAP spectra, especially as the significant wave-height increases. Generally, there appears to be a higher concentration of energy around the peak period as the sea-states propagate to Probe No8 with a very slight shift of the peak period,$T_p$, to the lower frequencies.

| Environmental condition No | Case No | Target $H_s$ [m] | Target $T_p$ [s] | Measured $H_s$ [m] | Measured $T_p$ [s] | Reflection $C_r$ [%] |
|---|---|---|---|---|---|---|
| EC1 | EOL1210 | 7.3 | 12.0 | 7.33 | 12.04 | 15.636 |
| EC2 | EOL1100 | 9.2 | 12.0 | 9.10 | 12.04 | 9.421 |
| EC3 | EOL1000 | 10.6 | 12.0 | 10.67 | 12.04 | 9.630 |

**Table 7.5:** Comparison of targeted and measured properties of the storm spectra in full-scale units

### 7.3.2 Numerical models

The models investigated in this analysis, shown in Table 7.6, follow the same structure as those used from the monochromatic wave analysis shown in Table 7.2. From the comparison of the dynamic response in regular waves, it is found that generally, the best-performing models, all orders considered, are those using BEM-calculated transfer functions. The main difference in irregular conditions stems from the fact that the third-order Malenica and Molin (1995) model only considers forces due to each individual frequency but not due to the interaction of frequencies with each other. With that in mind, the FNV method could be considered more realistic when it comes to frequency interactions. For that reason, the main models being compared in this analysis are the three potential flow models and the hybrid model, HYB QTF+FNV, which considers the third-order FNV force on the TP. To check the performance of the most low-cost model available to engineers, the full Rainey model is also included in a short separate comparison.

The first round of models, referred to as DIEGO1 models, have been fed the time series measured at the location of the platform (Probe No8) prior to testing the physical model. This is so both a temporal and spectral comparative analysis can be carried out. However, to obtain a representative sea-state, it was necessary to include in the order of $10^3$ individual frequencies between $f = 0.02 - 0.5$ Hz therefore including some of the bound harmonics. With lookup in QTFs tables, direct integration of kinematics on the structure for the drag force on top of a non-optimised numerical scheme requiring long iterative convergence for the RNA-hydrodynamic coupling, these simulations ended up requiring heavy calculation carrying over the maximum cluster time limit. Therefore, a sea-state of one full hour is obtained for those cases and the results are compared against the equivalent experimental time window. These models assume that all the energy in the spectrum is due to individual free waves where in reality some difference and sum-frequency bound harmonics will be present. For that reason, these models use a linear wave theory with a Wheeler stretching method to avoid doubling the nonlinear effects in the incident wave field.

| | Potential flow | | | Hybrids | |
|---|---|---|---|---|---|
| | LIN | QTF | QTF+MAL | HYB RAI | HYB QTF+FNV |
| **Inertial** | | | | | |
| Radiation | $C_m(\omega)$, $B(\omega)$ | $C_m(\omega)$, $B(\omega)$ | $C_m(\omega)$, $B(\omega)$ | $C_m(\omega)$, $B(\omega)$ | $C_m(\omega)$, $B(\omega)$ |
| 1s-order | BEM LTF | BEM LTF | BEM LTF | Rainey | BEM LTF |
| 2nd-order | None | BEM QTFs$^2\pm$ | BEM QTFs$\pm$ | Rainey | BEM QTFs$\pm$ |
| 3rd-order | None | None | TP: M.&M. H&E.T.<br>Rest: None | Rainey | TP: FNV<br>Rest: None |
| **Viscous** | | | | | |
| Drag | Mor. drag | Mor. drag | Mor. drag | Mor. drag | Mor. drag |
| **DIEGO1** | | | | | |
| Wave theories | Airy+WHL | Airy+WHL | Airy+WHL | Airy+WHL | Airy+WHL |
| **DIEGO2** | | | | | |
| Wave theories | S2 | S2 | S2 | S2 | S2 |

**Table 7.6:** Hydrodynamic models being compared

The second batch of models has been generated using DIEGO's own JONSWAP spectrum using a limited amount of frequencies, random phases and a second-order wave theory with no stretching. This is to test the capacity of DIEGO to capture similar response statistics without the experimental time-series. These models are referred to as DIEGO2 models and could be carried over two full hours of sea-state realisation.

### 7.3.3 Analysis of response in severe wave conditions

#### Comparison of response power density spectra

This section presents the time and frequency comparative analysis between the numerical and experimental responses for EC1a to EC3a. The spectral analysis of the motion and line tension responses are provided both in the linear and logarithmic scale in Figure 7.15, 7.16 and Figure 7.17 and 7.18 respectively. This comparison includes all potential flow models and the hybrid, HYB QTF+FNV model.

The comparison of motion spectral response in Figure 7.15 and 7.16 displays the degrees of freedom from left to right and EC1a to EC1c from top to bottom. The main observation that appears valid for all DoFs and all models is that the surge and pitch response display clearly three peaks. This is the linear bandwidth peak between $f = 0.05 - 0.15$ Hz which dominates the response, a low-frequency peak between $f = 0.0 - 0.05$ Hz due to the resonance of the surge mode, and a high-frequency peak visible in the log scale plots between $f = 0.2 - 0.28$ Hz corresponding to the coupled tower-pitch mode. In heave, three main peaks of the same order of magnitude can be observed. The dominating peak between $f = 0.0 - 0.4$ Hz shows that significant heave motion is generated by the low-frequency excitation of the surge mode.

Two peaks corresponding to the linear wave response are found at, the linear bandwidth between $f = 0.05 - 0.15$ Hz corresponding to a true heave mode, and at roughly double that bandwidth $f = 0.12 - 0.22$ Hz due to the coupled surge-heave pendulum motion also visible in the monochromatic wave cases (See Section 7.2).

From the motion results, it appears that all the numerical models manage to capture part of the low-frequency response regardless of the use of QTFs. This suggests that a significant portion of this response is captured from applying a linear theory to the nonlinear low-frequency waves that have been included in the incident spectrum. This becomes clear when comparing these results with those of the DIEGO2 model further below. The addition of the second-order wave loads and the force non-linearities due to platform motion appear to generate higher low-frequency excitation and an over-prediction of the low-frequency response. Furthermore, the addition of the semi-analytical third-order force appears to generate an amplified resonance in surge with a strong impact on the low-frequency heave response in case EC2a. This is probably an artefact of considering low-frequency waves as part of the linear frequency bandwidth and suggests that a further filtered spectrum should be applied to the semi-analytical third-order force transfer functions. The experimental results show the low-frequency peak at the surge natural period appears slightly shifted towards lower frequencies compared to the results of the decay test, having moved from $f = 0.03$ Hz to $f \approx= 0.02$ Hz. This suggests that the surge resonant response might be influenced by drift and slowly varying loads or other nonlinear effects, although the scope of this research and the current results do not offer many opportunities for more conclusive explanations.

In terms of the linear response, the agreement of the numerical models with the experimental results appears to be the best in surge in EC1a and EC3a. In all ECs and in pitch, the numerical models display a slight tendency towards under-prediction of the peak spectral pitch response. In the heave response, the experimental results suggest that as the significant wave-height increases, the dominant response switches from a dominance of the surge-heave coupled mode at double the frequency of surge between $f = 0.12 - 0.22$ Hz, to a dominance of the pure heave mode at the linear frequency bandwidth between $f = 0.05 - 0.15$ Hz. This shift which is not captured by the numerical models could be due to some asymmetry in the experimental mooring line configuration or different viscous force excitation.

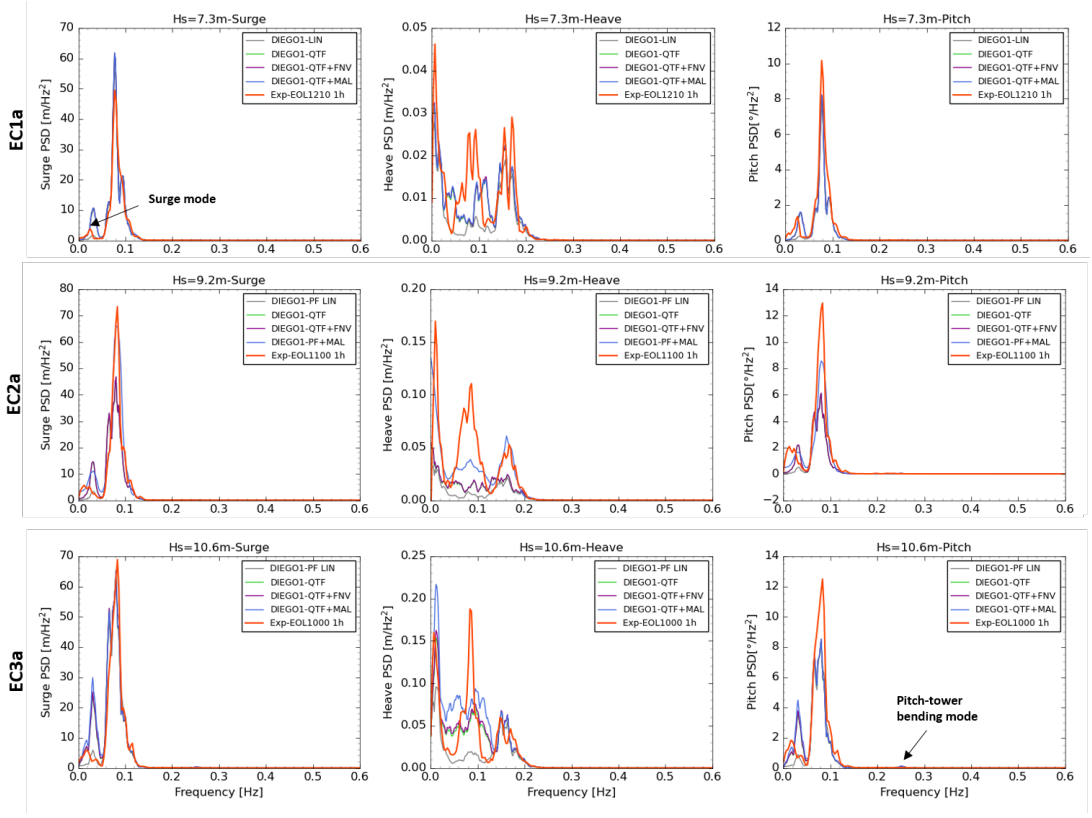


**Figure 7.15:** Comparison of Power Spectral Density of the motion response (Linear scale)

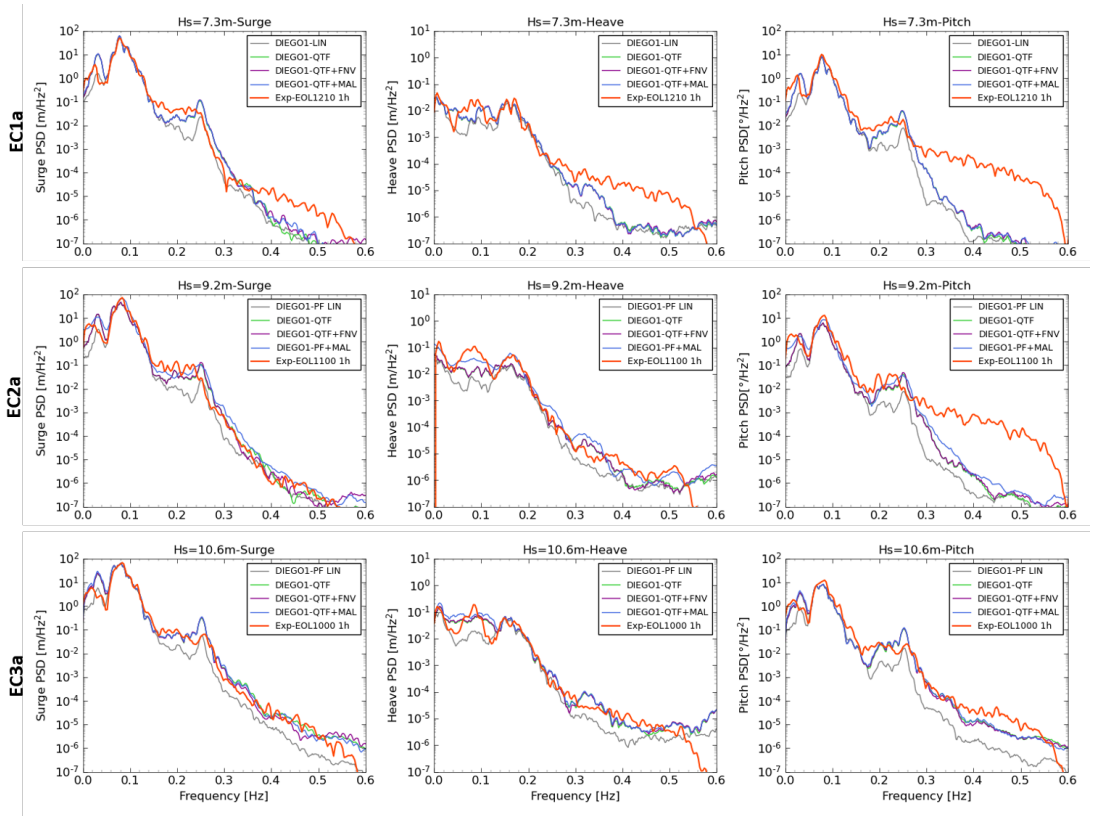


**Figure 7.16:** Comparison of Power Spectral Density of the motion response (Log scale)

Finally, although hardly visible on the linear scale plots, a high-frequency peak is visible in the surge and pitch power density spectra around the coupled tower-pitch resonant mode, between $f = 0.2 - 0.28$ Hz. The experimental results display a broader spectrum in this frequency range with a lesser-defined and slightly shifted peak compared to the numerical results. However, the numerical models which include sum-frequency QTFs and motion non-linearities are visibly better at capturing the energy in this frequency band compared to the linear model which captures only a small portion of that energy. The addition of the third-order models does not appear to generate a significant amplification of the resonant response in terms of displacement. This is thought to be due to two factors. Firstly, a significant portion of the high-frequency resonant response can be generated by second-order wave forces which possibly reduces the significance of the third-order contributions. Secondly, viscous drag, which is included in all models, is probably the dominant third-order excitation load in dynamic conditions as suggested by the observation of the comparison of the springing response in mono-chromatic wave conditions. Finally, as mentioned in the literature, in irregular sea-states third-order effects tend to be more sporadic and associated with steep wave events.

Similarly to the motion response, the comparison of the mooring lines' vertical tension response in Figure 7.17 and 7.18, shows that all three peaks of the low, linear and high-frequency response can be observed in the power spectra. The low-frequency effects on the mooring lines appear to be negligible relative to the high-frequency loads. In terms of order of magnitude, the mooring line tension is as expected dominated by the linear response which appears roughly one order of magnitude higher than the high-frequency resonant response, itself one order of magnitude higher than the response due to the low-frequency surge mode. This observation confirms that sum-frequency effects are an important consideration in the design of TLP mooring systems whereas slow varying wave loads can generally be ignored (Bachynski, 2014; Molin, Remy, & Falcon, 2004).

Generally, the tension resulting from the linear response appears to be pretty well captured by all DIEGO models. This confirms that the first-order models are accurate at capturing the dominant line tension responses as was suggested by the agreement in the transfer functions calculated in monochromatic waves. A clear asymmetry in the experimental mooring line configuration is observed when comparing the results for Line No2 and Line No3. This leads to a slightly larger experimental response on Line No2 and slightly lower on Line No3 than predicted numerically. The linear response displays a strong concentration of energy centred around the peak period at $f = 0.083$ Hz and another distinct peak after $f = 0.1$ Hz. This is explained by a concentration of energy around the peak frequency of the incident

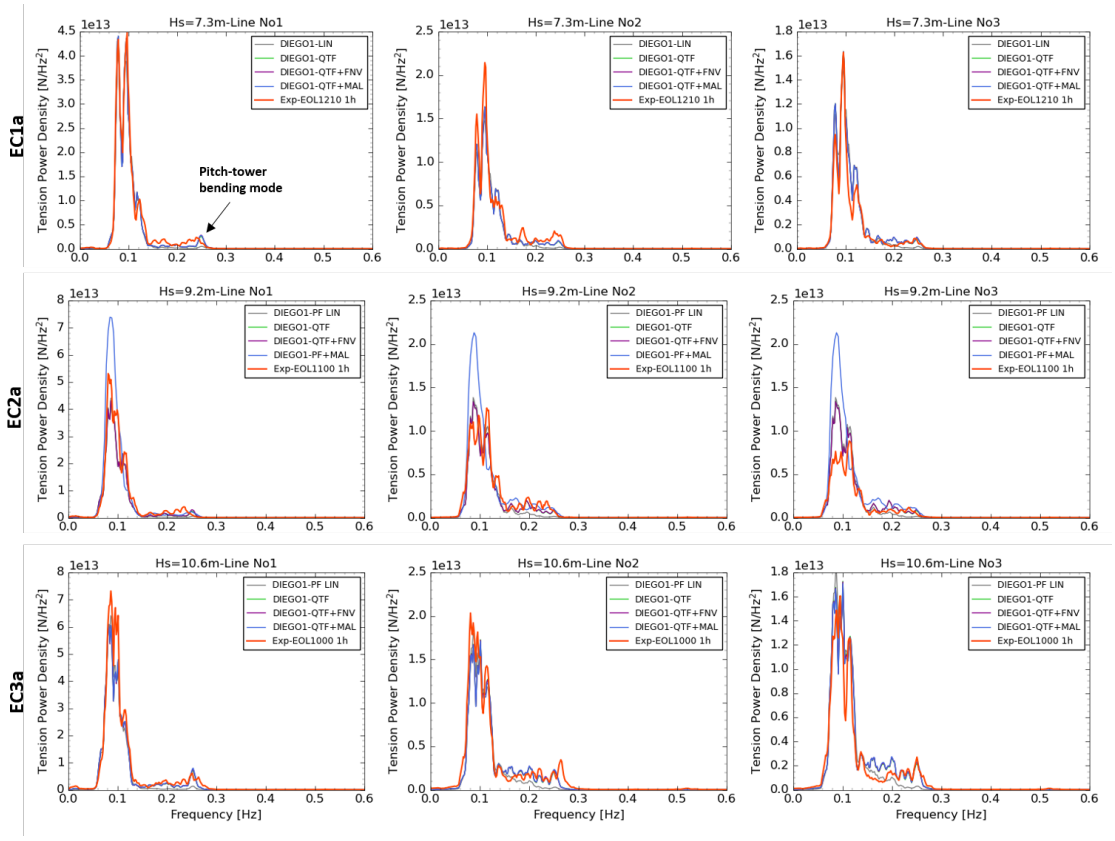


**Figure 7.17:** Comparison of Power Spectral Density of mooring line tension (linear scale) using DIEGO1 models

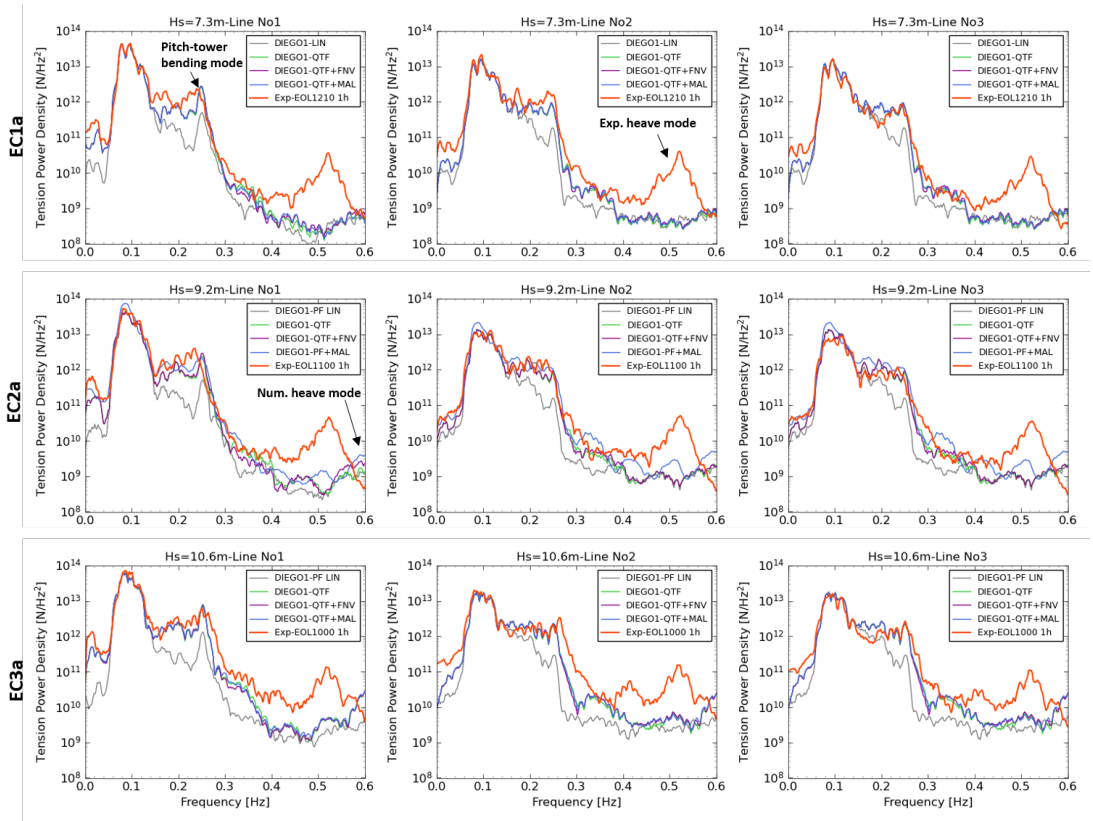


**Figure 7.18:** Comparison of Power Spectral Density of mooring line tension (Log scale) using DIEGO1 models

wave spectrum followed by a steep energy drop beyond $0.10$ Hz as observed in Figure 7.14. However, this drop in energy is compensated by the peak linear line tension response which is found at around $f = 0.12 - 0.13$ Hz as seen in the line tension transfer functions shown in Figure 7.8a, 7.8b and 7.8c.

In the high-frequency bandwidth, a clear peak is observed around the coupled tower bending-pitch mode, between $f = 0.2 - 0.28$ Hz. This resonant response is relatively distinguishable from other high-frequency effects although the experimental results suggest that the dominance of this resonant mode becomes blended with a general increase in energy in the high-frequency bandwidth $f = 0.16 - 0.22$ Hz as wave steepness increases. This effect is also observed in the numerical model in Line No2 and No3 where significant high-frequency effects are observed in that bandwidth in the more energetic sea-states EC2a and EC3a. The addition of the third-order inertial forces does not lead to a significant amplification of the high-frequency resonant response for much of the same reasons given for the high-frequency motion response. However, both the addition of the FNV and the MAL load models do appear to slightly increase the energy at the peak resonant response prediction which is barely discernible in Line No1 spectral response in sea-state EC2a. The comparison with the linear model (PF-LIN) shows that the addition of the sum-frequency QTFs and motion nonlinearities appear as key parameters for the accurate prediction of the high-frequency but also low-frequency EDF-TLP response. Generally, the order of magnitude of the peak of energy at the pitch-tower bending mode is captured by the numerical models. However, the models fail to capture the high-frequency heave response located around $f = 0.5 - 0.55$ Hz due to the difference in natural frequencies.

To finish this analysis, the line tension power density spectra comparison between the two-hour sea-state experimental results and the DIEGO2 models, which are based on the incident wave-field generated by DIEGO, are presented in Figure 7.19. It is interesting to note that generally, the results obtained with this method are very similar to those obtained using the experimental wave field. The main difference is observed with the linear model which displays much less energy in the low and high-frequency band due to the curtailment of the fundamental frequency of the JONSWAP spectrum by DIEGO. However, the energy density in the linear response and at the springing pitch-tower bending response remain relatively similar for all models although the high-frequency response appears to be strongly overestimated in sea-states EC2a and EC3a. It is worth mentioning that the DIEGO2-QTF+FNV model (purple) in sea-state EC3a crashed due to a convergence error during a slacking event and is only representative of 1.5h of simulation, hence the visible differences in the spectral plot. However, despite the curtailed fundamental frequencies, the inclusion of QTFs appears again as the dominating parameter for the accurate prediction of the total response of the EDF-TLP.

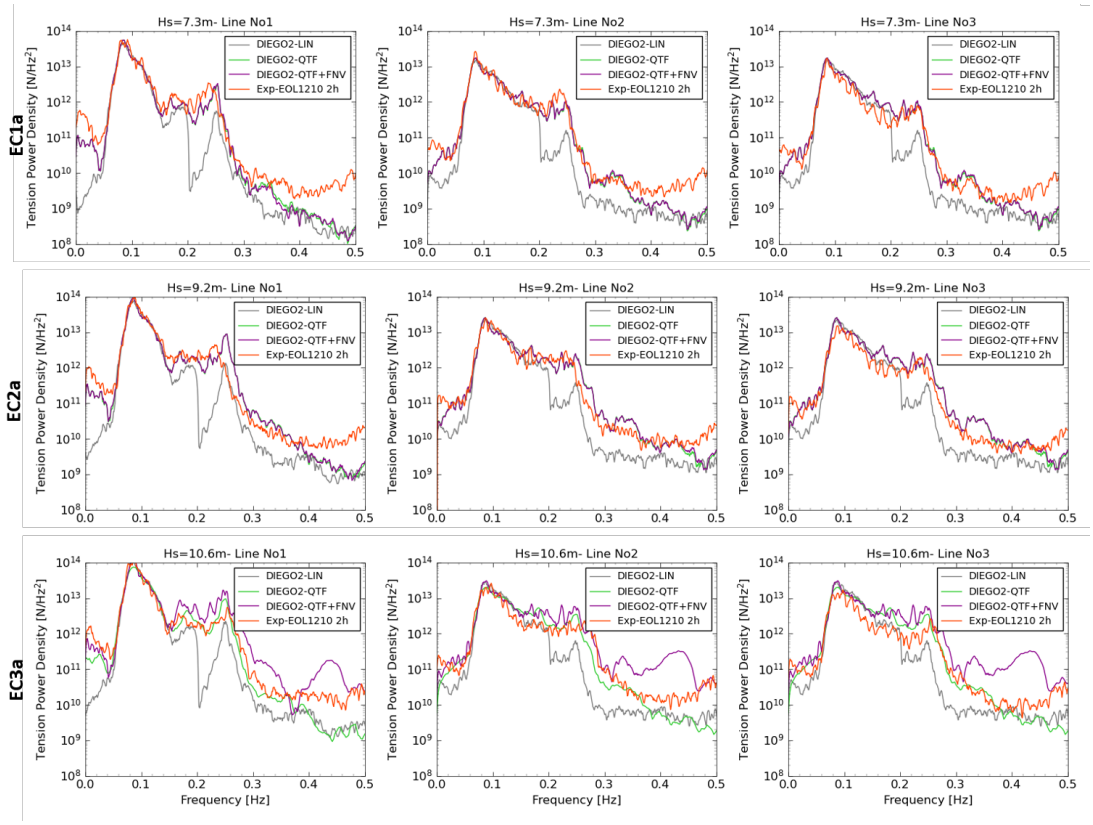


**Figure 7.19:** Comparison of Power Spectral Density of mooring line tension (Log scale) using DIEGO2 models

### Comparison of response statistics

While the comparative analysis of the power spectra informs on the distribution of energy across the frequency ranges, it does not inform on the level of accuracy of the loads and motion cycles in the time domain, including extreme cases. Since the design of floating wind systems to the ultimate design state is usually based on a stochastic estimation of extreme loads, the capacity of numerical models to capture the distribution of extreme events in a given sea-state is a primordial test of their performance in design situations. Furthermore, understanding the distribution of individual events informs on the capacity of the numerical model to represent the full load and displacement cycles accurately with an impact on fatigue load predictions. The probability of exceedance plots allows for a comparison of the statistical distribution of individual events, which are here the peaks and troughs in the system oscillatory response, with a focus on extreme events. The probability of exceedance plots of the three DoF motions for the three sea-states considered is displayed in Figure 7.20. In this case, the probability of exceedance is provided in terms of absolute displacement from the mean

position. The same plot is provided for the mooring line tension in Figure 7.21. In this case, the probability of exceedance of the tension minima and maxima normalised by the pre-tension, $\tau_0$, are presented centred around the mean tension which is typically equivalent to the pre-tension in the absence of aerodynamic thrust.

Starting with the distribution of the motion response Figure 7.20, a first observation is that the extreme displacements obtained numerically appear higher than those predicted experimentally. Another observation is that whilst the system motion ranges up to 0.35 m in heave for the sea-state of EC1a, both EC2a and EC3a sea-states display experimental heave maxima within the range of 1-1.5 m respectively. This indicates that in EC2a and EC3a, the displacement tends to a limit imposed by either the mooring system or the nacelle cables which might not be captured as well by the numerical models. Notwithstanding the observation made above, the distribution of the surge displacement in all three sea-states appears to be very well captured by the DIEGO numerical models. Generally, the lower 90-95 % of surge cycles are predicted correctly by the numerical models even using a full linear inertial approach. In the other degrees of freedom, the agreement is reduced to the lower 90 % of the heave cycles and the lower 70 % of the pitch cycles. It is worth noting that the range of pitch motion is very low with a maximum recorded angle of 3.5° experimentally and just over 4.0° numerically. Therefore, considering the method applied to measure angles experimentally, and both numerical and experimental models of the tower stiffness and bending modes being far from perfect, the results can be considered very satisfying. In the most severe sea-states EC2a and EC3a, the numerical models that include third-order inertial wave loads appear to predict well or over-predict the extreme surge, heave and pitch displacements. In EC2a in the middle of Figure 7.20 the QTF+MAL model overestimates significantly all displacement maxima which is probably due to the artificial amplification of the low-frequency response mentioned in the previous section. The model including the FNV approach, QTF+FNV, does not suffer from this issue and appears to predict slightly higher extreme displacement than the DIEGO1-QTF model. The linear model, DIEGO-LIN underestimates clearly the response in heave and pitch especially in the more extreme sea-states.

Moving to the probability of extreme tension shown in Figure 7.21, considering all lines and all ECs, the results show that all numerical models perform relatively well in predicting low tension and slacking events in Line No1. The nonlinear inertial model prediction of the extreme tension events in Line No1 is also relatively correct compared to the experimental measurements. The extremes appear clearly better predicted using nonlinear models with at least the inclusion of full sum-frequency QTFs. Unfortunately, due to the load cells limits, the maximum extreme tension events in Line No1 for sea-state EC2a and EC3a are truncated. In Line No2 and No3, the line tension maxima appear to be over-predicted. Finally, considering the distribution in the tail in all lines, it appears possible that the line tension extremes

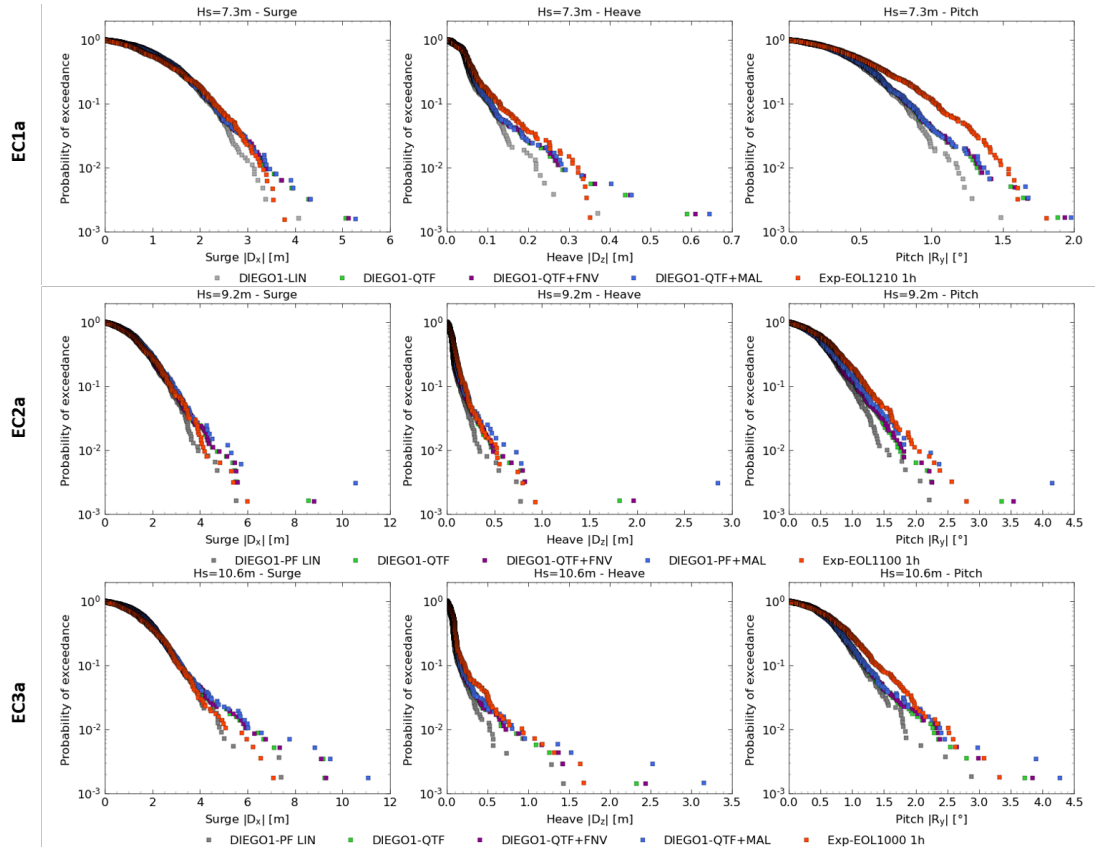


**Figure 7.20:** Probability exceedance plots of motion displacement using DIEGO1 models

are slightly overestimated by the numerical models. The inclusion of third-order inertial load models does not appear here to lead to significantly better performance. However, the hybrid QTF+FNV approach appears generally better at predicting slightly higher extremes with a slightly higher probability of exceedance bringing the prediction closer to the experimental results. Therefore, this method is potentially better suited for design purposes.

Overall, it appears that all the DIEGO1 numerical models are successful at predicting the distribution of the lower 90% of tension load cycles, which is roughly in the range of $1.0 - 1.3$ of the pre-tension $\tau_0$. This is important since these load cycles can be expected to generate a significant amount of fatigue damage in the mooring lines, winches and anchoring system. However, there is clearly an overestimation of the highest 10% of the load cycles in Lines No2 and No3 within $1.5 - 3.0\tau_0$. Extremes in Line No1 on the other hand are captured with a good accuracy within the range that was measured experimentally. Since this is the single upstream line and hence is responsible for much of the station keeping of the platform, it undergoes several events of slacking and ensuing snap loads in sea-state realisations EC2a

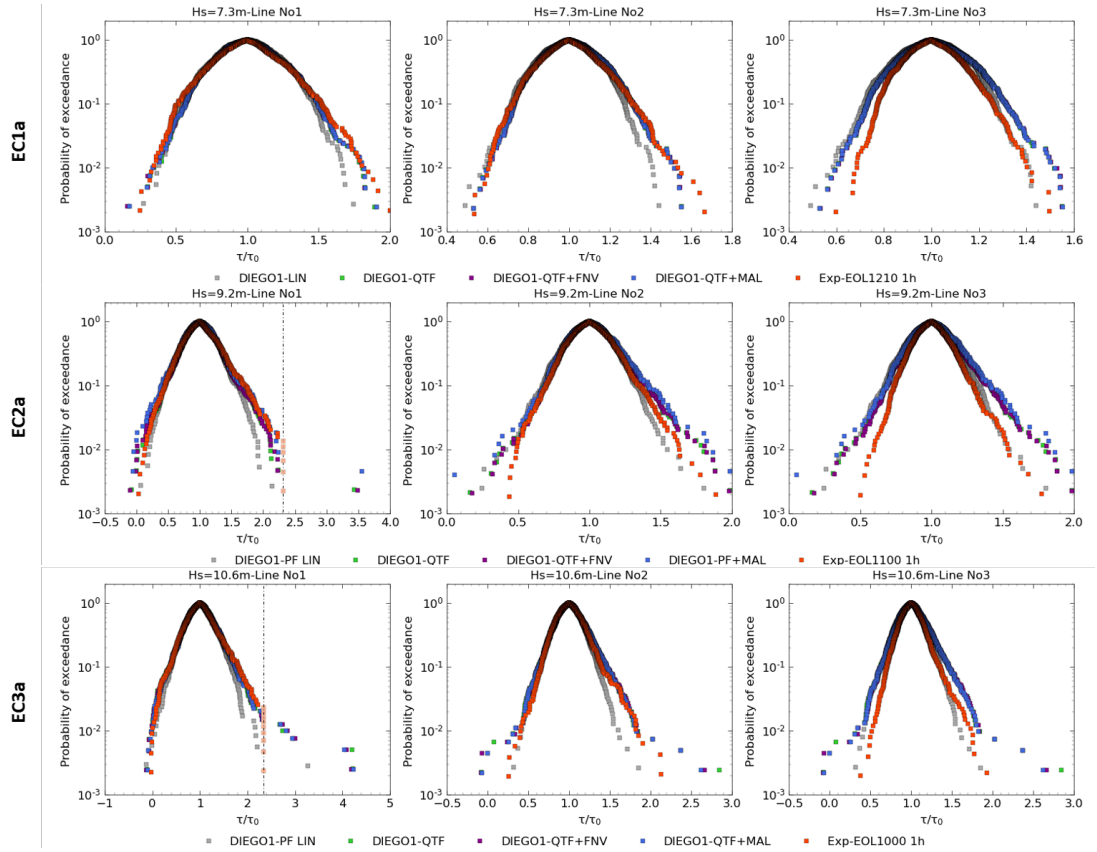


**Figure 7.21:** Probability exceedance plots of mooring line tension using DIEGO1 models

and EC3a. In fact, extreme tension outliers are clearly visible in the numerical models which are unfortunately truncated for the experimental results. It is worth noting though that with several slacking events and tension maxima between 4-5 $\tau$, sea-state EC3 appears as too energetic for the EDF-TLP system analysed in this thesis.

DIEGO1 results can be compared against the predictions made by the DIEGO2 models which use the wave-field generated by DIEGO instead of the experimental wave-field and shown in Figure 7.22. Generally, despite being a different random phase seed, the numerical results of DIEGO2 models appear very similar to those of DIEGO1 models both in the lower 90% quantiles as in the trend of the extreme tail which gives confidence in the capacity of DIEGO to model severe randomly generated sea-states. The main visible differences are between the DIEGO1 and DIEGO2 linear model in grey in Figure 7.21 and 7.22 with the former predicting a more accurate extreme tail than the latter. This is a good example of the effect of using a fully nonlinear incident spectrum with a linear potential flow model rather than with a randomly generated sea-state using a truncated JONSWAP spectrum.

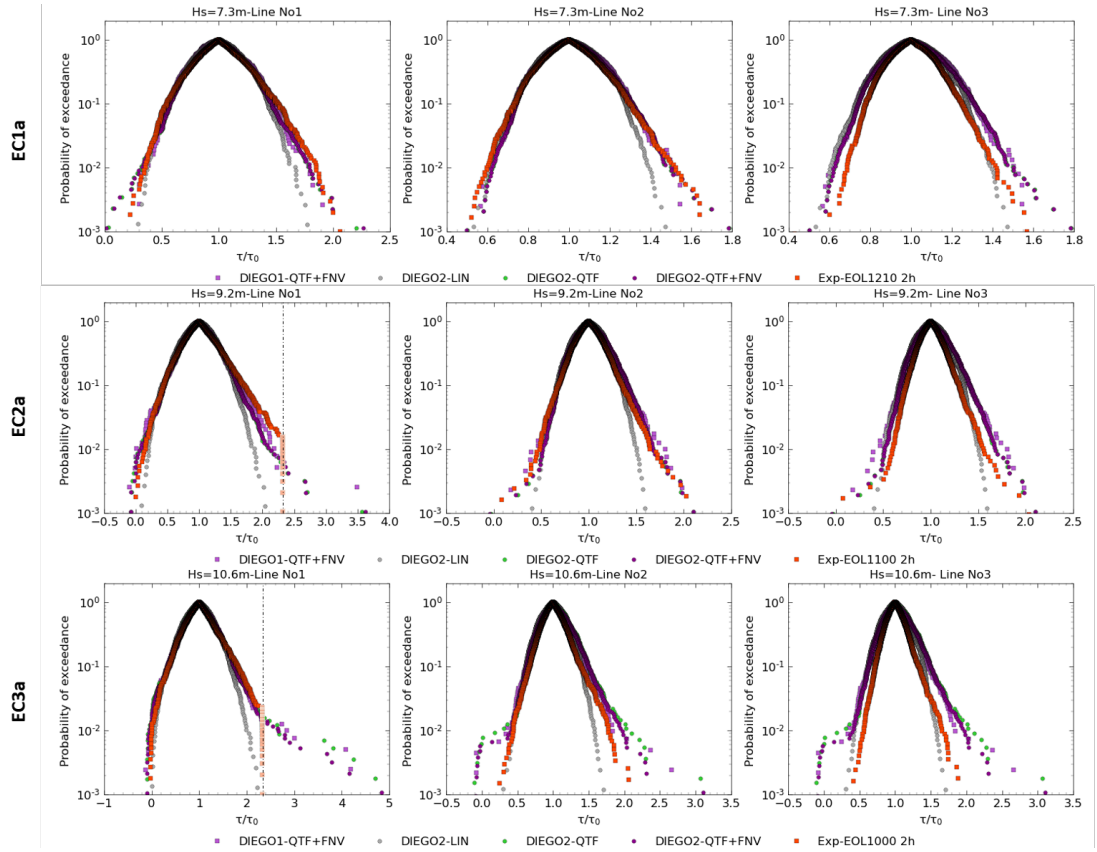


**Figure 7.22:** Probability exceedance plots of mooring line tension using DIEGO2 models

### Significance of rotation of forces

In the results shown above and as explained in Section , the nonlinear models, DIEGO-QTF, QTF+MAL and QTF+FNV use an option which applies all forces on the instantaneous position of the platform. This generates a significant amount of second and third-order load as attested by Figure 7.23 which shows the comparison of line tension spectra when forces are applied on the mean position of the platform (MEAN) or on the instantaneous position (INST). A clear increase of energy in Line No1 is visible in the $f = 0.14 - 0.24$ Hz bandwidth which most likely corresponds to the rotation of the first-order hydrodynamic forces in the energetic bandwidth $f = 0.07 - 0.12$ Hz. Although, the peak at the pitch-tower bending mode does not seem to be affected, including the non-linearities due to the platform motion results in a better agreement with the experimental model spectra in Line No1. In the upstream Line No2 and No3, it also results in a better agreement in the low-frequency bandwidth as well as in the high-frequency bandwidth around the tower bending mode $f = 0.33$ Hz.

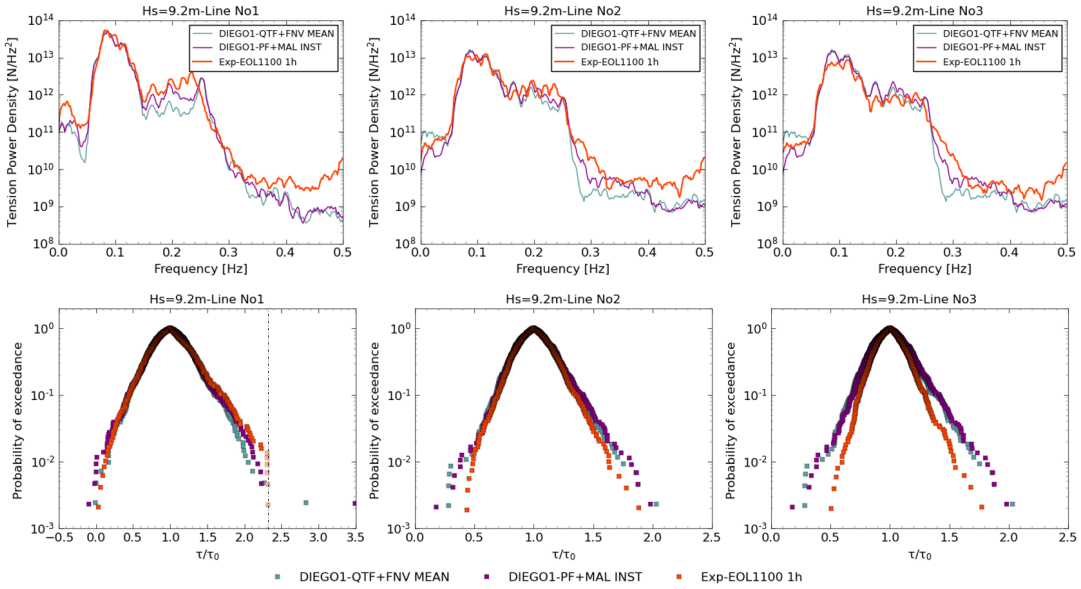


**Figure 7.23:** Effect of including motion effect on hydrodynamic forces on line tension power spectra and probability of exceedance for case EC1a

This increase in energy in the nonlinear spectra due to the inclusion of motion in hydrodynamic forces results in higher extreme tension probabilities in Line No1 in Figure 7.23 as well as an increased probability of slacking. The prediction in the amplitudes of the higher 8% tension events appears clearly improved when including the INST option. However, the agreement in the low-tension events appears to be reduced. In the lower 90% quantile, however, the two models appear to behave very similarly suggesting that these effects are most significant in extreme events when the platform motion is significant.

### Analysis of force components

Whilst this information is not available for the experimental results, the hydrodynamic force generated on the floater in the numerical models can be analysed to better understand the load regime at play. Figure 7.24 displays the pitch moment power spectra for several components of the total force in sea-state EC1a, EC2a and EC3a. As postulated, the vertical viscous component which is mostly due to the axial drag on the side buoys is a significant contributor to the high-frequency loads and a dominant contribution past $f = 0.5$ Hz. The "total drag" curve is completely overlapped by the "total drag+FNV" curve showing that in the case of the EDF-TLP, the contribution of the FNV is minimal relative to the axial viscous drag forces.

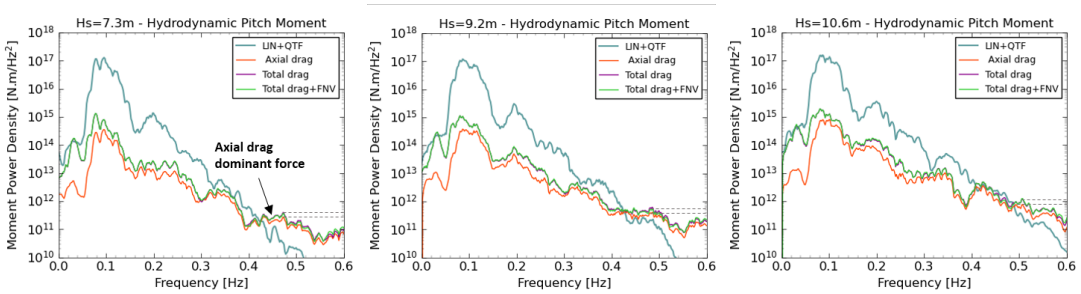


**Figure 7.24:** Comparison of pitch moment power spectra for different force components in EC1a, EC2a and EC3a

### Performance of the Rainey strip-theory model

A comparison of the power spectra and probability of exceedance of line tension predicted by the Rainey strip theory model is presented in Figure 7.25. This short analysis aims to inform on the performance of a low-fidelity model against prediction given by a more complex model using BEM-calculated QTFs. The power spectra inform that the Rainey model succeeds relatively in reproducing the low and high-frequency spectral response although it slightly under-predicts the resonance at the pitch-tower bending mode. However, it appears to be over-predicting the energy in the linear bandwidth for Lines No2 and No3. This follows the findings in regular waves in Section 7.2.4 as the Rainey model does not represent the linear line tension transfer functions very well for these lines. This translates into the exceedance probability plots, where Line No1 high tension extremes appear to be captured with similar if not higher accuracy than with the QTF+FNV model, but significantly overestimated in Line No2 and No3. Furthermore, the low tension extremes appear to be underestimated in all lines and the general behaviour of the platform does not appear correct. This is to say that the Rainey model appears to be an interesting alternative at high-level design stages to estimate extreme tension cases for a ULS case compared to a linear potential flow model. However, for general statistics of the platform response, this hydrodynamic model is not accurate enough to represent the linear response.

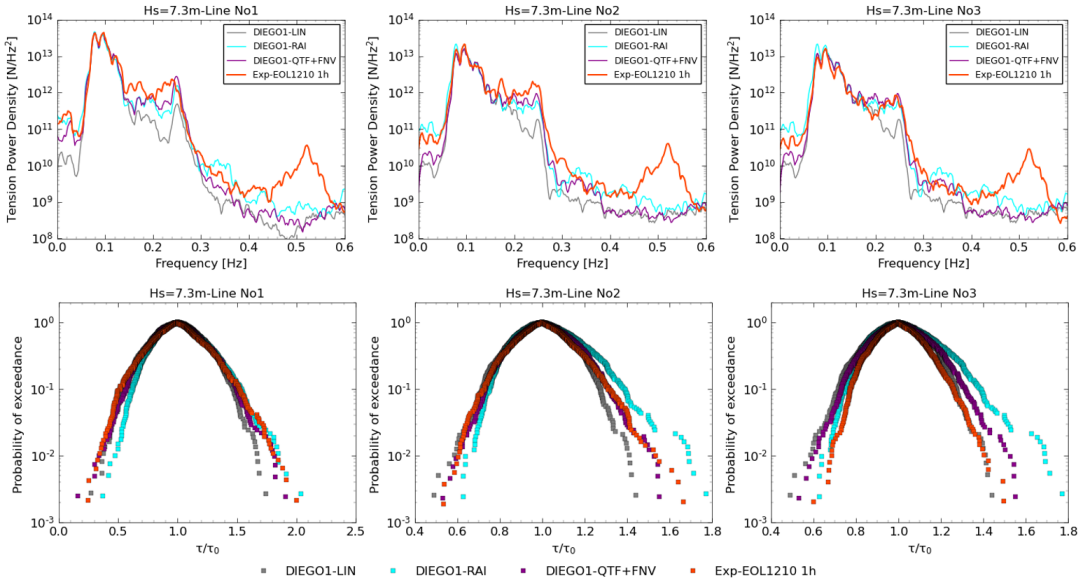


**Figure 7.25:** Comparison of line tension power spectra and probability of exceedance with full Rainey strip-theory model

### 7.3.4 Analysis of response in severe wind-wave conditions

Experiments were also carried out using steady wind conditions. As explained in Chapter 3.4.3, the wind is modelled numerically using a drag disk calibrated on the DTU 10-MW turbine and physically using a drone motor. These tests serve to verify the capacity of DIEGO and the physical model to predict the dynamic of the EDF-TLP in a production situation with severe wave conditions. The environmental setting of the test does not represent necessarily a realistic case since the selected joint wave-wind contour has a return period of 50 years in which condition the wind turbine might be expected to be parked. However, this situation could represent a conservative scenario for DLC 1.6. As explained in Section 7.3.1, production and thus wind thrust are only considered for cases EC1 and EC2.

#### Analysis of motion and vertical line tension spectra and extreme probabilities

The power spectrum for motion and line tension are presented in Figure 7.26 and 7.27. When compared to the test in waves only, the first observation is the reduced non-linearity in case EC1b. The pitch-tower bending natural mode appears to have mostly disappeared from the surge and pitch power spectra. This is probably due to the increased compliance of the system resulting from the maximum turbine thrust inducing low tension in Line No1. In this situation, the linear inertial model, DIEGO-LIN, appears in relative agreement with the nonlinear numerical model and the experimental measurements. This increase in compliance can be observed when comparing the heave motion to case EC1a. A general increase in heave motion energy is noticeable as well as a change to a dominant pure-heave behaviour from a previously largely coupled surge-heave motion. In the mooring lines spectra shown

in Figure 7.27, the resonant response in Line No1 remains visible although it appears to have decreased. On the other hand, the energy in the low-frequency band has significantly increased compared to case EC1a. Furthermore, the resonant mode in heave can be seen in the numerical power spectra of case EC1b which shows it has shifted to the lower frequencies due to an increased heave compliance. The change in the system dynamic behaviour is generally captured well by all models although the EC1b experimental results suggest that the resonant response in Line No2 and No3 remains whereas it has mostly disappeared in the numerical models.

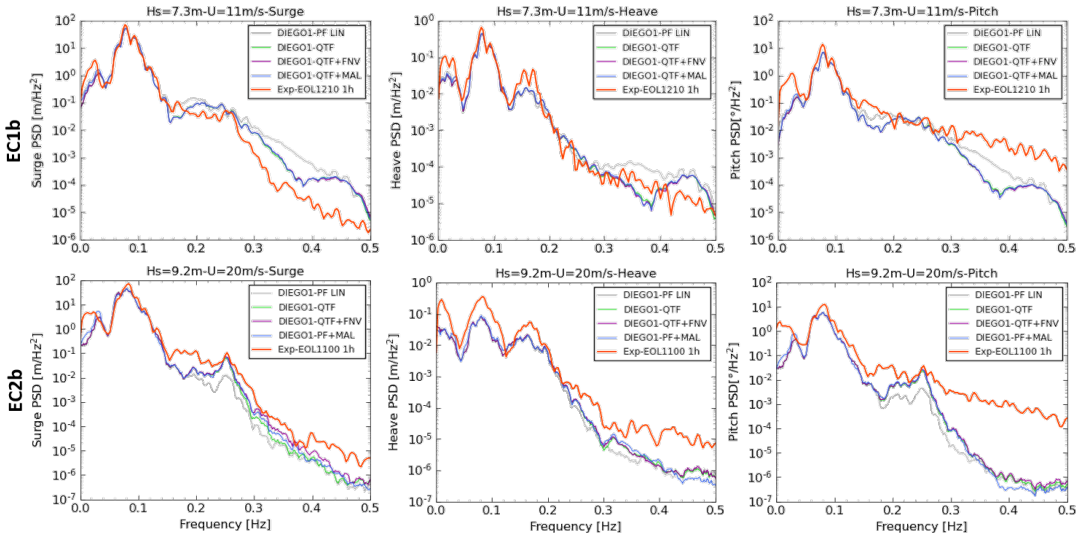


**Figure 7.26:** Comparison of Power Spectral Density of motion response (Log scale) using DIEGO1 models

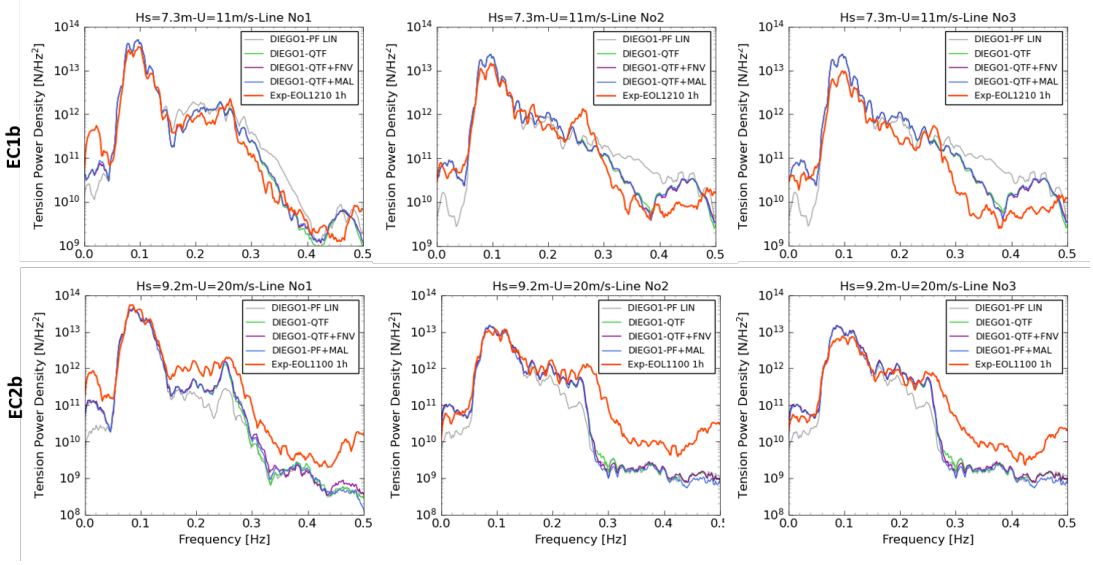


**Figure 7.27:** Comparison of Power Spectral Density of mooring line tension (Log scale) using DIEGO1 models

The effect of the inclusion of the QTFs on the estimate of the nonlinear response is more visible in case EC2b. As the turbine thrust is reduced, the EDF-TLP displays a stiffer behaviour with the pitch-tower bending mode at $f = 0.25$ Hz being visible again in the surge and pitch power spectra. The experimental surge and pitch spectra appear generally more energetic in all bandwidths than the numerical models. In terms of heave, the experimental response in case EC2b appears to be more energetic than in case EC2a and the heave motion appears again to have switched to a dominant pure heave motion. This switch is correctly captured by the numerical models but the energy in the response appears to be significantly under-estimated. Looking at the line tension spectra in Figure 7.27, the increase in energy in the low-frequency bandwidth of Line No1 is again observed as well as the slight shift to lower frequencies of the heave natural mode visible experimentally.

Generally, the linear surge, pitch motion response and dynamic mooring tension appear to be captured with reduced accuracy than in the wave-only case as confirmed by the motion probability plot. Figure 7.28 shows that the probability of exceedance of motion amplitudes predicted numerically is relatively representative of the experimental surge results, both in the 90% quantile and in the extreme values. However, compared to cases EC1a and Ec2a, the addition of the wind thrust increases the discrepancies between the physical and numerical model in the other quantities. This is probably partly attributable to the difference between the numerical and physical model in the static steady wind position. This is visible in the vertical line tension probability of exceedance plots in Figure 7.29. The plots for upstream Line No2 and No3 show that the physical model does not see the same increase in pre-tension as the numerical models, noticeable by the slight offset between them. Considering that the static surge excursion in steady wind is smaller for the physical model than the numerical model, we can posit the fact that the nacelle cable restrains a portion of the thrust force which reduces the increase of tension in the upstream lines. The stronger heave motion measured experimentally can potentially be imputed to this effect with upstream lines being less mobilised. This is to say that the addition of wind thrust exacerbates the differences between the numerical and physical model systems.

However, overall, the extreme amplitudes in surge motion, which is the dominant component for the estimation of power production and fatigue of the blade, and in the line tension appear to be reasonably predicted with a tendency for over-prediction. All things considered, the nonlinear DIEGO models remain on the safe side of design and therefore appear appropriate for application to a design under DLC1.6 for the EDF-TLP in power production during a severe sea-state.

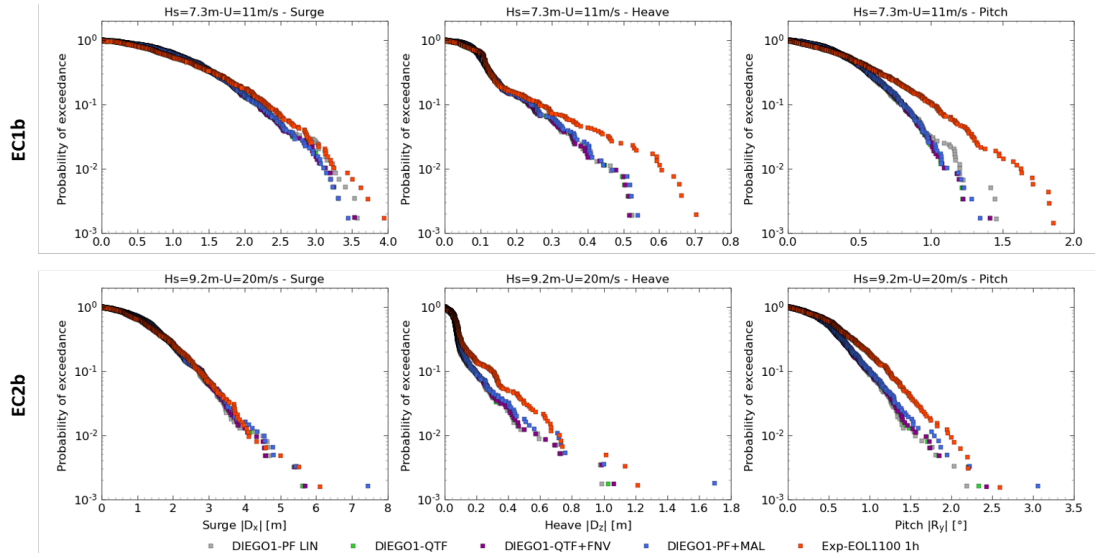


**Figure 7.28:** Probability exceedance plots of motion response using DIEGO1 models

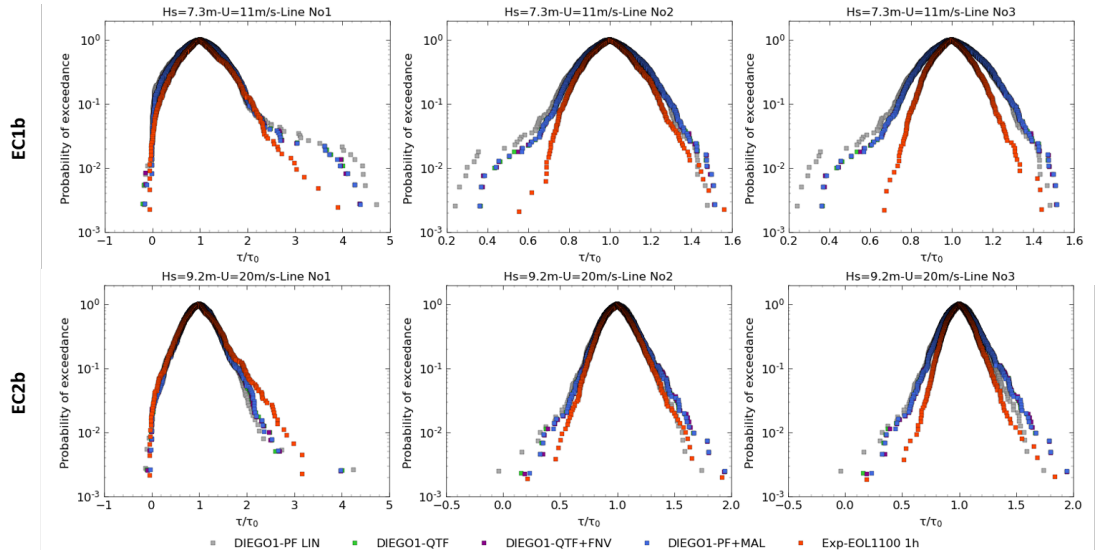


**Figure 7.29:** Probability exceedance plots of mooring line tension using DIEGO1 models

### Impact of using BEMT instead of a drag disk model

A short comparison is provided here to explore the impact of including a BEMT aerodynamic model in the analysis instead of a drag disk model. The physical model is not relevant here since these effects are not present at the same scale with the drone rotor having a much higher rotor frequency and a much lower blade mass moment of inertia. The biggest difference that can be expected by using a drag disk and BEMT aerodynamics is the addition of the rotor torque and the excitation by the rotor rotation frequency in the latter. Figure 7.30 displays the vertical line tension spectra and the respective probability of exceedance.

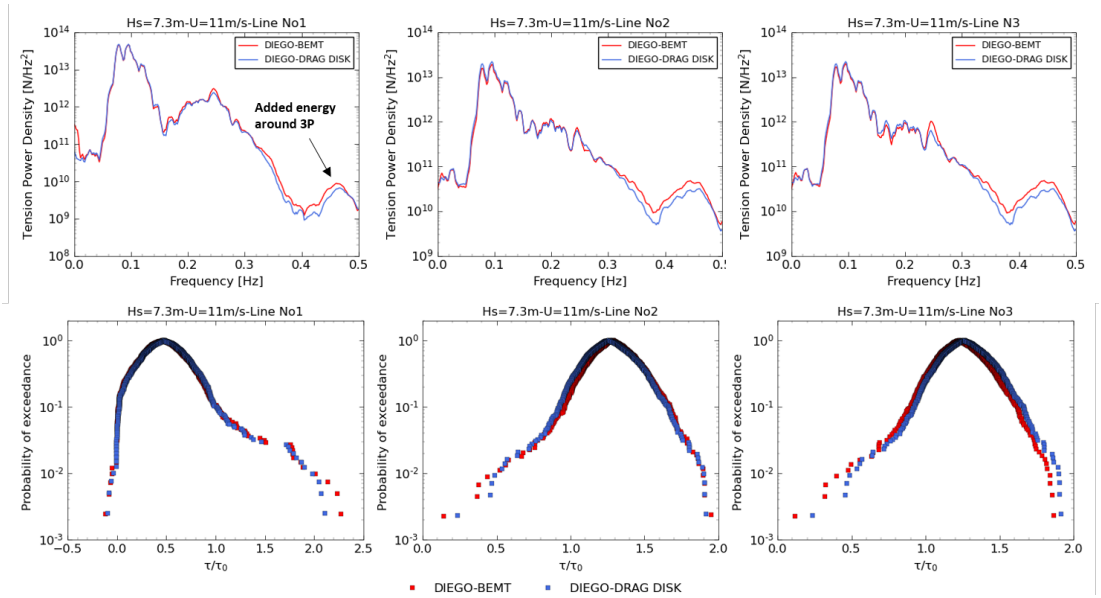


**Figure 7.30:** Effect of including a BEMT aerodynamic model on line tension power spectra and probability of exceedance for case EC1b

The addition of BEMT in this situation does not appear to result in a significantly different response of the nonlinear numerical model. However, a slight increase in energy is observed in the line tension spectra on the top graphs of Figure 7.30 around the pitch-tower bending mode, $f = 0.25$ Hz, and at the 3P frequency, $f = 0.45$ Hz which coincides with the shifted heave natural mode. Furthermore, the probability of increased tension does show an increase of around 8% of the extreme tension in Line No1 and an increased probability of slacking in Line No2 and No3. As expected, it appears advisable to use BEMT instead of a drag disk model for the realistic design of a FOWT. However, it remains to be seen if such an increase in the tension extreme would be captured experimentally using a more realistic system which would include the turbine torque.

### 7.3.5 Analysis of ringing conditions

Considering that statistically, most of the model differences appear on the extreme events, it is therefore interesting to compare in more detail the transient response of the platform during slacking and more generally, during ringing events. Analysing the performance of the ringing load prediction by low to medium-fidelity nonlinear numerical models is one of the objectives of this thesis. Ringing events being defined in codes as high-frequency transient resonant responses in an offshore structure generated by nonlinear forces.

An interesting way to capture the ringing phenomenon and compare the performance of the numerical model in predicting this transient event is to compare the time-frequency spectra by means of wavelet continuous transform. This method has previously been used to visualise ringing on fixed offshore structures (Bachynski, Pákozdi, Östman, & Stansberg, 2018; Iwanowski, Astrup, Lefranc, & Hansson, 2011; Kwon, Lee, Park, Ha, & Kim, 2001). Kwon et al. (2001) used the scalograms to identify ringing events based on experimental data and Iwanowski et al. (2011) for numerical models. Bachynski et al. (2018) used continuous wavelet transform to compare the ringing loads generated by extreme waves on a truncated vertical cylinder from experimental, CFD and strip-theory predictions. A similar method is applied here to compare the vertical line tension response of the EDF-TLP in the modelled sea-state realisation. Only a few selected cases during relatively short time windows are presented in the scalograms to allow good visualisation of the ringing events. For a comparison of the high-frequency response in the full sea-state realisation, filtered time series analysis by bandwidth is also provided. It is worth noting that due to unmitigated free-harmonics generation and relatively high level of reflection ($\approx$10%), the comparison between the numerical and experimental time series can be at time very good and, at time, relatively different. However, to the knowledge of the author, this is the first time such a study is carried out to analyse the experimental and numerical ringing response of a FOWT-TLP system. This analysis does not aim to be an extensive study on the occurrence of ringing and slacking but rather a first trial at comparing the numerical and experimental occurrence of ringing which could lead to further research.

An additional short analysis of a recorded slamming event is provided in Appendix B. This event is outside the scope of the thesis but the comparison between experimental and numerical results, especially with the FNV approach, is noteworthy.

**Analysis of scalograms for case EC1a and EC3a**

Figure 7.31 and 7.32 display a close-up of the scalogram time-frequency contour plot of wavelet coefficients expressed in power form of the free surface elevation and mooring tension of LineNo1 (downstream) and No2 (upstream) in sea-state EC1a and EC3a respectively. The time windows correspond to examples of resonant responses selected among many events as highlighted in the top graphs of Figure 7.31a and 7.32a which highlight the experimental time series of Line No2 vertical tension, including the filtered high-frequency components. The dotted lines have been overlapped on the scalograms to identify the incident spectra peak frequency(bottom), the coupled pitch-tower bending (middle) and the heave mode (top). Additional results including time-frequency comparison between the various numerical models are provided in Appendix B.

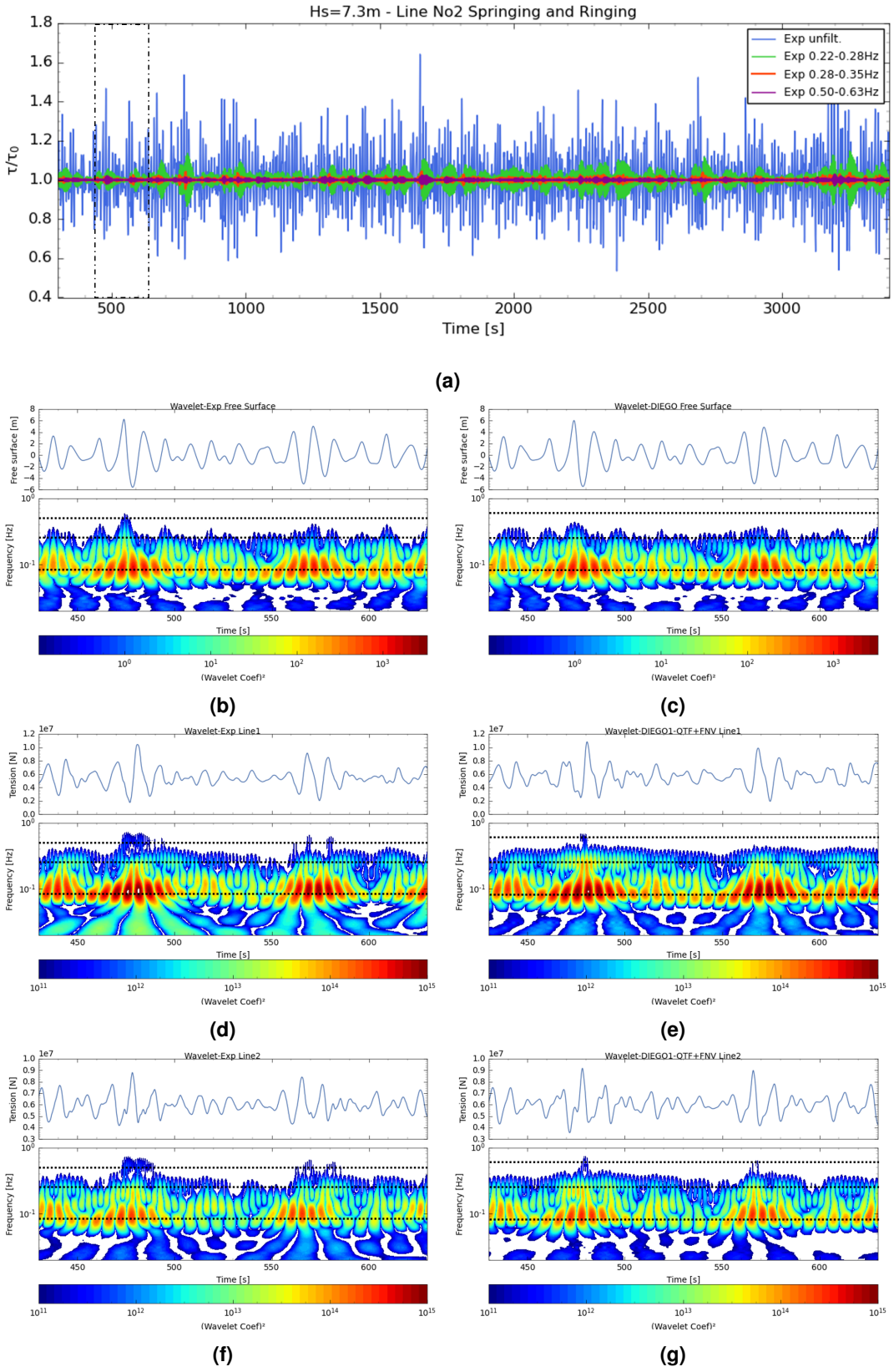


**Figure 7.31:** Springing and ringing response in case EC1a: (a) Experimental time series of Line No2 tension- including filtered high-frequency components; Scalograms of free surface, Line No1 and No2 tension during ringing events for model (b)(d)(f) Experimental and (c)(e)(g) DIEGO-QTF+FNV. Dotted lines for peak frequency, pitch-tower bending and heave mode

The first observation from both figures, is that ringing events are clearly noticeable in the line tension wavelet surface plots by the intermittent increase in energy in the high-frequency band between $f = 0.5 - 0.7$ Hz which is marked by the top dotted line. This range of frequencies includes the resonance response in heave noting that this frequency varies between the numerical and physical model. A high-frequency energy band comprised between $f = 0.2 - 0.3$ Hz (middle dotted line) displays a more steady behaviour overlapped with a burst of energy which coincides with the increase of energy in the upper bandwidth, $f = 0.5 - 0.7$ Hz. This second zone is centred around the resonant mode in pitch-tower bending and most likely shows what is commonly referred to as the springing response overlapped by ringing events. The difference between springing and ringing can be understood here by the fact the ringing response corresponds to a highly transient event in which the TLP system undergoes a resonant response in all its modes including resonance of the tower in its individual mode. On the other hand, the springing response appears as the more stationary resonance of each mode individually. In this case, this concerns mostly the pitch-tower bending mode as it is excited more often by the incident wave field. This is also visible in the top graphs of Figure 7.31a and 7.32a which display Line No2 tension time series and three filtered high-frequency components in the experimental reading, corresponding to the pitch-tower bending mode (green), the individual tower mode (red) and the heave mode (purple). Here ringing events can be identified too, where the bursts of energy in the pitch-tower bending mode (green) generally occur after a high-tension event and coincide with resonance from both the tower and the heave mode.

Observing the free surface scalograms in Figure 7.31b, 7.31c and 7.32b, 7.32c, the ringing events coincide with wave events which not only include energetic nonlinear frequencies but also consist of an energetic linear bandwidth which are the attributes of large steep waves. Qualitatively, when comparing the scalograms of the experimental reading and the nonlinear numerical model, DIEGO1-QTF+FNV, the numerical prediction of the ringing event appears overall correct. The prediction of the distribution of energy in the time-frequency space is best in the "linear" bandwidth, $f = 0.05 - 0.15$ Hz, and in the high-frequency bandwidth up to $f = 0.4$ Hz corresponding to the pitch-tower bending and individual tower mode where the burst of energy associated with the ringing response is clearly visible. Furthermore, the numerical model also captures the resonance of the heave mode, $f = 0.5 - 0.7$ Hz, during the ringing response, although generally with a decreased amplitude and a stronger decay. Unfortunately, since the natural frequency in heave of the experimental model is lower as that of the numerical model, the closer proximity of the experimental heave mode to the pitch-tower bending mode may favour an amplification of the ringing response. One significant ringing event in Figure 7.32 is captured numerically with an amplified heave resonant response compared to the experimental model. This effect is due to the occurrence of slacking in the numerical model which does not occur experimentally.

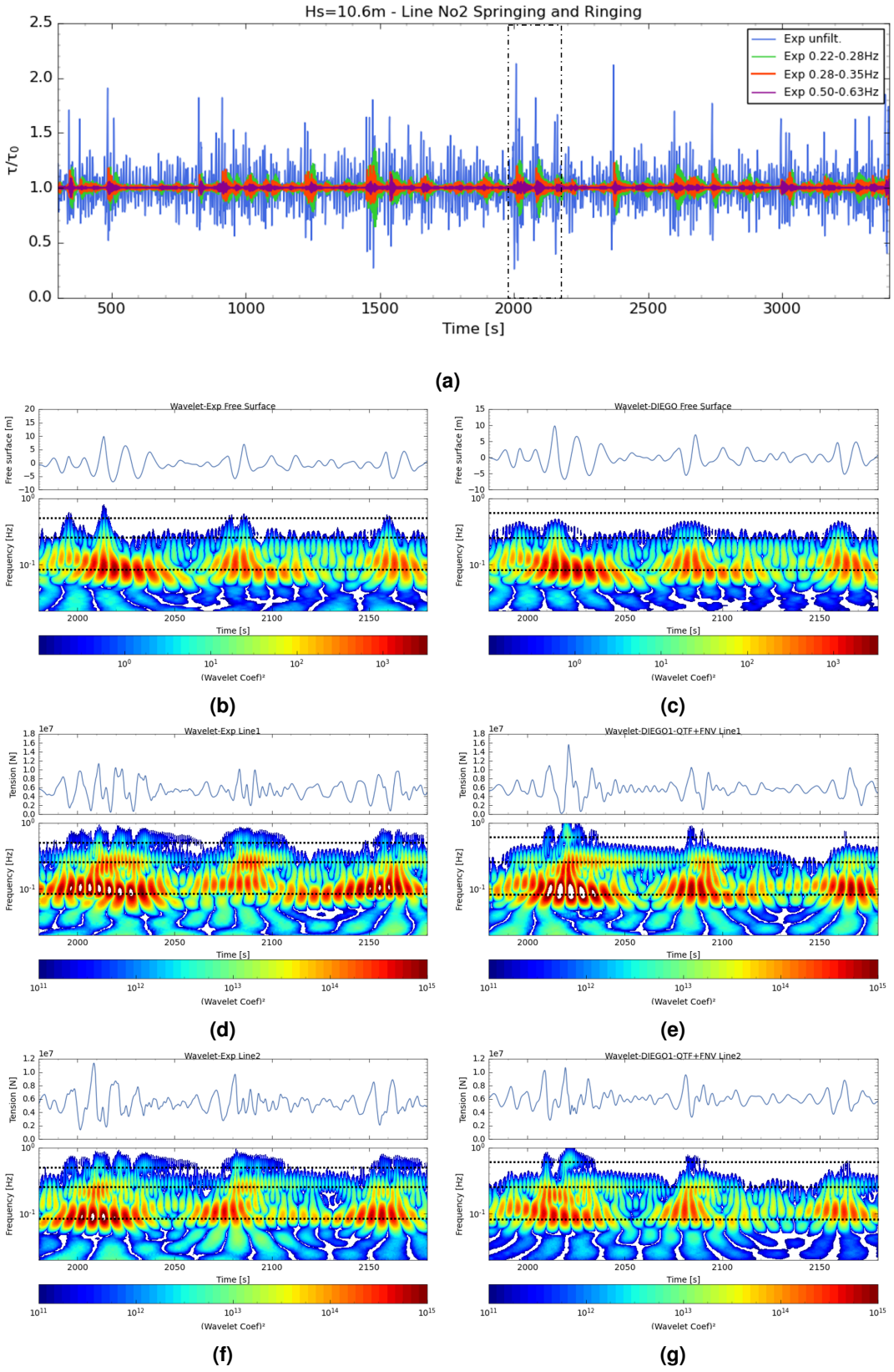


**Figure 7.32:** Springing and ringing response in case EC3a: (a) Experimental time series of Line No2 tension- including filtered high-frequency components; Scalograms of free surface, Line No1 and No2 tension during ringing events for model (b)(d)(f) Experimental and (c)(e)(g) DIEGO-QTF+FNV. Dotted lines for peak frequency, pitch-tower bending and heave mode.

**Analysis of filtered time-series for case EC1a and EC3a**

A comparison between time series experimental measurements and the various numerical models for the three filtered high-frequency bands is provided in Figure 7.33a and 7.33b for the same case EC1a and EC3a shown in the section above.

As expected, the nonlinear numerical models replicate better the high-frequency transient responses measured experimentally. Following the observation made in the analysis of power spectra and probability of exceedance plot, the dominating parameter for the accurate prediction of the high-frequency response is the inclusion of QTFs. In line with previous observations of the spectral response, the linear inertial model clearly underestimates the high-frequency response in the band $f = 0.22 - 0.35$ Hz compared to the models including QTFs. However, it is interesting to note that it manages to capture the ringing response in the heave natural mode with almost the same level of accuracy than the other numerical models with the exception of the slacking events in case EC3a where higher-order nonlinear models appear to have an impact. This can be explained by the fact that the third-order loads are dominated by viscous drag and hence present in all models and inertial third-order load models become only significant in extreme wave cases.

Overall, the occurrence of the ringing response is almost always captured numerically even with a linear inertial model. However, the high-frequency response of EDF-TLP measured experimentally is underestimated by the numerical models, although this is more significant for the highest-frequency band which includes the heave resonant mode. The significant wave reflection and the generation of free harmonics reduce our capabilities to accurately compare the systems in the time-domain since the agreement between the signals is intermittent. Furthermore, the difference in the heave natural frequency between numerical and physical models limits our capacity to conclude on the accuracy of the numerical prediction of the heave ringing response where the third-order models might have a stronger impact. However, it is clear that engineering models manage to capture the ringing response of the EDF-TLP system and that the inclusion of QTFs and viscous drag are key parameters. This signifies that, although the amplitudes might be underestimated, the wave events causing ringing responses and their occurrence can be identified numerically. With a numerical prediction of the occurrence of ringing, the time-frequency footprint of wave events that generate them could potentially be identified statistically which could have a use for numerical prototypes of TLP system or predictive failure models.

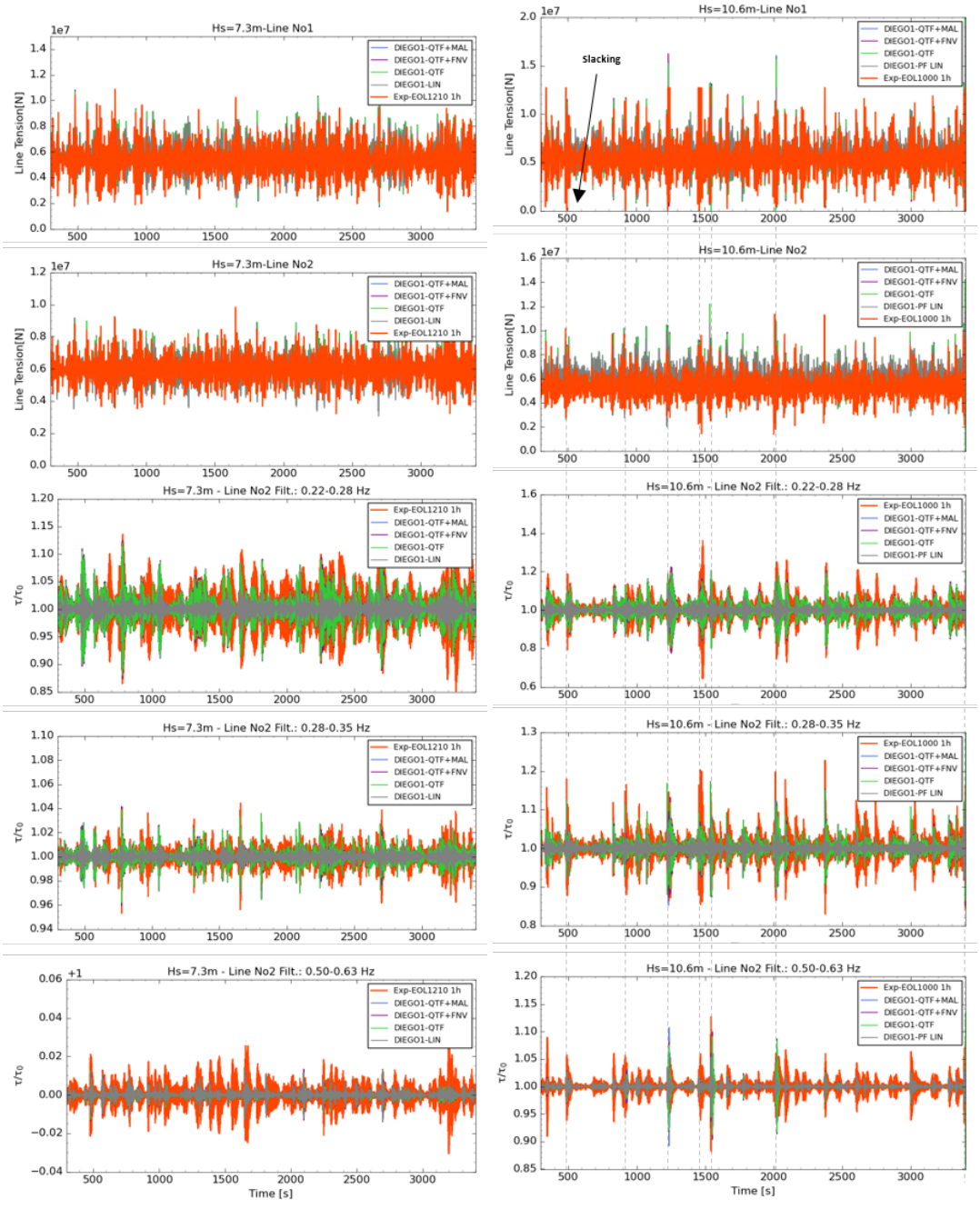


**(a)** **(b)**

**Figure 7.33:** Time series of filtered high-frequency components in Line No2 tension response for case (a) EC1a, (b) EC3a

### 7.3.6 Summary and discussion

The results of the spectral analysis have shown that generally, the DIEGO numerical models are quite successful at representing the behaviour of the EDF-TLP physical model both in the linear bandwidth as well as in the high-frequency bandwidth including the resonant behaviour of the pitch-tower bending mode. The inclusion of second-order hydrodynamic loads via the inclusion of QTFs leads as expected to a significant improvement in the prediction of the nonlinear dynamic response of the system. On the other hand, including third-order load models does not appear to be a significant parameter for the EDF-TLP. The results obtained with the DIEGO1 models calculated with fully irregular wave spectra from the tank tests and DIEGO2 models with randomly generated sea-states based on a truncated JONSWAP spectrum, generally predict the experimental spectral response with similar accuracy. These observations can be extended to the probability of exceedance plots with both DIEGO1 and DIEGO2 models predicting relatively similar extreme line tension probabilities when including the second-order wave loads in good accordance with the experimental results. Generally, the nonlinear numerical models appear to predict well the trend in the probabilities of extreme tension in downstream Line No1 although the truncation of the experimental signal does not allow for a definite conclusion on the extreme values. On the other hand, the numerical models appear to predict increased extreme response for Line No2 and No3 than measured experimentally. The inclusion of the steady wind turbine thrust results in a slight reduction of the high-frequency response and an increase in the low-frequency response as the downstream line responsible for most of the station keeping becomes more compliant. This is moderately well captured by the numerical models. The errors in the static excursion of the platform due to steady wind thrust lead to increased discrepancies in the behaviour of the system, especially at maximum thrust which reduces the accuracy of the prediction of extreme tension. However, for all cases, the lower 90% quantile of the surge and line tension response amplitudes is very well predicted by all numerical models including using a linear inertial model with viscous drag. This reinforces the confidence in the capacity of these engineering models to capture long-term statistics on the loading cycles of the EDF-TLP system.

The similarity in the high-frequency response between the various models can also be explained by the fact that the hydrodynamic component that dominates the pitch moment on the EDF-TLP beside the QTFs is the axial viscous drag on the side buoys which is included in all of them. This is in accordance with the findings of the CFD analysis in Section 5.4 and the analysis of the harmonic dynamic response presented in Section 7.2. Finally, the inclusion of non-linearities due to the motion of the platform results generally in better agreement with the experimental results. Therefore, the method applied in DIEGO which applies all forces on the instantaneous position of the platform appears to provide a suitable alternative to including

motion in the QTF calculation which can be computationally expensive during iterative design. However, this option seems to slightly overestimate the extreme surge response, although the reader must be reminded that the freedom of motion of the physical model is probably mildly hindered by the cables exiting the nacelle.

All the observations noted above translate into the prediction of the ringing response. The inclusion of the QTFs greatly improves the amplitude prediction of the ringing response in the frequency bandwidth that includes the pitch-tower bending mode and the independent tower bending mode. On the other hand, since viscous drag is the dominating high-frequency load above $f = 0.5$ Hz, and since all numerical models include viscous drag, the springing and ringing response in the heave mode is captured similarly by all of them. This is with the exception of the strong ringing responses which are triggered by specific slacking events uniquely captured with the inclusion of second-order forces. Generally, the amplitude of the ringing response is underestimated but their experimental occurrence coincides with numerical prediction. Therefore, one can conclude that low and medium-fidelity engineering models are appropriate for ULS and FLS design as well as for predicting the susceptibility of designs to ringing events and providing early estimates of the fatigue damages. The reader must be reminded that the tank test campaign presented here is the first one carried out at EDF R&D and could certainly benefit from many improvements in terms of facilities, model scale or instrumental setup. Furthermore, the numerical model also could be better tuned by carrying a deeper characterisation of drag coefficients and using a FEM tower model instead of a simple spring-mass system. In this sense, it is possible that further validation could provide better agreement between both experimental and numerical models, increase the confidence in these models and propose suitable safety factors. However, it remains important to carry out tank testing campaigns for TLP floaters since these enable the analysis of complex multi-body systems in long-sea-state realisation and can test the response to highly nonlinear events such as wave breaking and slamming impact, which are outside of the scope of this thesis, but that also will trigger ringing responses.

Overall, the comparison of experimental and numerical models in the considered environmental conditions shows that the use of second-order sum-frequency forces is absolutely critical to capture the response of the EDF-TLP to extreme events including the ringing response. In that sense, for a complex platform with large surface piercing columns, it is recommended to resolve the second-order diffraction problem in order to carry out designs to the ultimate and fatigue limit states. In the case of the EDF-TLP, the addition of third-order load models has not appeared to lead to a significant effect on the general extreme statistics with the exception of extreme wave scenarios such as the wave slamming event.

## 7.4 Conclusion of dynamic analysis

To determine the validity of the high-order engineering load models to model the extreme nonlinear response of the EDF-TLP, a tank test campaign was devised. It consisted of tank tests in regular waves to capture the high-frequency harmonics of the motion and understand the performance of the load models and the load regime at play at different harmonics. Then irregular cases were undertaken in wave-only and wave-wind conditions in order to test the application of these models to extreme design conditions similar to what could be tested for FOWT-TLP ULS design to DLC1.6 or 6.1 with occurrences of slacking and ringing.

The results of the dynamic analysis in both regular and irregular waves show that both the numerical and the physical models are mostly representative of the same structure. Notably, the regular wave cases have shown that the linear response of the two models is in very good agreement when using a potential flow approach and with reasonable agreement using a strip-theory model. This is reflected in the irregular wave cases with the spectral surge and line tension response generally agreeing the best around frequencies associated with the first-order bandwidth. This also affects the probability of exceedance plots of all numerical models which show a very good agreement with the experimental measurement for the lower 90% quantile of all the response amplitudes. The impact of the addition of nonlinear inertial load models was mostly felt at second-order. Adding potential flow quadratic transfer functions or even a simplified nonlinear strip-theory load model was shown to have a strong impact on the second-order springing response in both regular and irregular waves which is not captured when using a simple linear inertial model. In fact, the inclusion of QTFs was shown to be generally sufficient to capture the extreme response in the irregular sea-states and a significant factor for capturing ringing and slacking events. On the other hand, third-order inertial models were found to have a small impact on the high-frequency response of the EDF-TLP in comparison to second-order loads and viscous drag. The FNV approach combined with QTFs generally does lead to slightly higher peak values during the most extreme wave events and has even performed well in a breaking wave event. On the other hand, the semi-analytical third-order solution has shown to be of varying reliability in irregular waves which was to be expected.

As predicted by the CFD analysis presented in Chapter 5, viscous forces and more specifically the vertical drag component associated with the axial drag on the side buoys is found to be a dominant component of the third-order load. The third-order harmonic response of the EDF-TLP in regular waves is a good illustration of this since all inertial models, linear and nonlinear all displayed a very similar response. Furthermore, the spectral analysis of the force at play in the numerical models also confirms this conclusion. This signifies that for FOWT-TLP platforms, characterising the transverse vertical drag on pontoons and the axial drag on vertical columns which are significantly off-centred from the centre of rotation is probably at least as, if not more important than including a third-order inertial load model. This is an interesting note since few studies have published experimental or CFD NWT curves for axial drag coefficients on fully submerged and surface-piercing vertical cylinders of circular sections.

Finally, a commentary can be made on the lower-fidelity models which have been investigated in this thesis, as these can provide lower-cost alternatives to BEM models for earlier design stages and optimisation design loops. Firstly, the strip-theory model based on Rainey's approach is found to be slightly more accurate than a linear potential flow model to predict second-order loads in regular waves and hence leads to better predictions of extreme line tension values for the irregular sea-states that were tested. However, its linear response is inaccurate for our complex floater which limits its use beyond very early stage development. This is where a hybrid model combining a second-order semi-analytical potential flow formulation and a Rainey approach on slender elements could prove to be useful. It has indeed shown better accuracy than the Rainey model in the regular wave case but unfortunately was not tested in irregular waves due to time constraints. However, these simpler nonlinear hybrid methods mixing semi-analytical solutions and strip-theory approaches could prove useful and benefit from additional research.

Overall, the tank tests have demonstrated that despite the assumption made in the current approach, with the inclusion of nonlinear engineering models, DIEGO is able to simulate with relative accuracy the response of a FOWT-TLP system with a flexible tower in severe sea-states. This includes correct prediction of ringing events which informs on the use that these nonlinear models can have for ultimate design or fatigue damage models. Furthermore, this first campaign confirms that the current experimental set-up provides capacity for the EF R&D LNHE department to carry out its own tank testing for floating offshore wind turbines in unidirectional waves.

# Chapter 8

# Overall conclusion and future work

## 8.1 Conclusion

The floating offshore wind market is today a booming innovative industry due to the urgent need for a transition to de-carbonised societies. Thanks to their floating foundation these systems can harness wind power in areas which were inaccessible to this industry just a decade ago. Among all floater concepts, the tension-leg platform, abbreviated TLP, distinguishes itself by its low floater mass and its non-compliant nature due to a stiff mooring line arrangement. As presented in the introduction, these TLP systems are prone to high-frequency resonant responses. This requires taking into account non-linear hydrodynamic models in numerical simulation in order to predict the load cycle in the mooring lines and the tower-floater connection for ultimate (ULS) and fatigue limit state (FLS) design. Recommended practice by certification agencies as well as literature on the subject have suggested that these effects are dominated by high-frequency inertial (inviscid) wave loads. For that purpose, various hydrodynamic methods have been proposed by engineers and academics to take these into account in industrial aero-hydro-servo-elastic time domain solvers. Whilst the recent research on this topic has typically focused on fixed offshore wind structures, few of these methods have been compared and analysed in the framework of floating offshore wind and to date, no experimental validation of these approaches has been undertaken for a FOWT-TLP system. The project aim was therefore to provide a thorough comparative analysis of these various low to medium-fidelity approaches at the disposal of industry engineers and validate them against high-fidelity numerical tools and a new experimental data-set. These engineering numerical approaches were applied in EDF's aero-hydro-servo-elastic time-domain solvers, DIEGO. The case study used for this project was the academic EDF-TLP floater designed at EDF R&D LNHE department by Duchet (2019). Following this academic and industrial aim, the research was built along two main axes with a progression from simpler analytical cases to semi-realistic industrial conditions.

### 8.1.1 Part I - Background and Theory

Whilst Part I of this document is mostly a dive into the literature and theoretical context of this project, it is worth repeating some key points from the literature review. Based on the non-exhaustive list of papers that involve numerical simulation of FOWT-TLPs with aero-hydro-elastic time domain solvers, it was found that a minority of publications considered the effect of sum-frequency hydrodynamic forces on these systems. This is despite the significant impact that these effects are expected to have on the system response. This was seen as proof that the industry is still at the early stages of development of FOWT-TLP technologies and that the study of high-frequency resonance on such structures remains a niche research subject. This knowledge gap is also visible in existing published experimental research which has not currently attempted to validate the numerical simulation of springing and ringing responses for a FOWT-TLP.

### 8.1.2 Part II - Validation and application of low-fidelity wave-structure interaction models on fixed offshore structures

Part II of this thesis consists of the first axis of this project which aimed at comparing the various engineering approaches that exist in the industry against results from a Navier Stokes' CFD NWT built in neptune_fd, EDF's multi-phase CFD solver. High-frequency loads on fixed structures were analysed in monochromatic waves so as to isolate the high-frequency harmonics and compare the high-order force transfer functions predicted numerically. The approaches which were considered are listed below:

- Potential flow approaches (inertial):
  - BEM solver: First and second-order diffraction-radiation
  - Semi-analytical method on vertical cylinders: First, second and third-order diffraction solution (Huang & Eatock Taylor, 1996; Malenica & Molin, 1995)
- Strip theory (inertial):
  - Rainey approach on cylinders (Manners & Rainey, 1992; Rainey, 1989, 1995)
  - FNV approach on vertical cylinders (Faltinsen et al., 1995; Kristiansen & Faltinsen, 2017; Newman, 1996a)
- Strip-theory (viscous):
  - Morison drag term (Morison et al., 1950)

This analysis started with cases that were closest to the initial assumptions made in the derivation of these approaches, that is vertical cylinders. The first structure analysed consisted of a bottom-fixed vertical cylinder case, from a paper by Kristiansen and Faltinsen (2017), akin to an offshore wind monopile. The aim was to compare the numerical tools used in this thesis against existing experimental and analytical results. The results showed that the tools reproduced with a good satisfaction the published experimental data-set. This exercise also informed the implementation of the FNV approach in EDF R&D's hydrodynamic module of

DIEGO. After this validation exercise, the study edged closer to floating offshore conditions by studying the same high-frequency forces on a truncated cylinder in transitional to deep-water condition. The geometry of that cylinder was based on the central mast, or transition piece (TP), of the EDF-TLP. In this situation, semi-analytical potential flow diffraction solutions were shown to be reliable at predicting both the amplitudes and phases of the high-order force transfer functions resulting from the high-fidelity CFD NWT. Strip-theory models also appeared to provide decent estimates for the high-frequency wave load amplitudes although the phase of that load was found to be the main limit to their accuracy. Analysis of the third-order components showed that the dominant effects were due to dynamic pressure forces and the third-order diffraction effect due to the first and second-order wave scattering. Furthermore, the addition of the transverse drag force was also found to have a non-negligible impact on the total third-order force amplitude and phase.

The study then moved to a more realistic case by looking at the high-frequency force transfer functions on the full EDF-TLP floater. The comparison with the CFD NWT showed that the central mast, or TP, could still be represented relatively accurately as a truncated cylinder despite the surrounding structure. Notably, the semi-analytical solution of Malenica and Molin (1995) appeared to provide a very good estimate of the third-order force on that element both in terms of amplitude and phase whilst the strip theory approaches also gave a decent approximation of the amplitudes with phase remaining the limiting factor as mentioned above. An analysis of the distribution of the high-frequency forces on the various elements of the floater, that is, the TP, the side buoys and the bracings, showed that the third-order horizontal force was indeed dominated by the central mast. However, in the case of the vertical pitch moment which is likely to generate some of the resonant response in dynamic condition, the vertical force on the side buoys were found to be the dominating third-order contribution by a small margin. Whilst missing accurate engineering methods to assess the inertial component of the third-order vertical contribution on the side buoys, viscous effects in the form of axial drag were considered the most likely culprit. This was an interesting finding since it contradicted the assumption made at the start of this project that inertial loads dominated the third-order forces and that existing third-order wave-loading approaches applied to the central mast were sufficient to capture them. This study was the first published analysis of the high-frequency forces distribution on a FOWT-TLP floater and as such these results were presented in a journal article (Rongé, Peyrard, Venugopal, Xiao, et al., 2023).

### 8.1.3 Part III - Model application to a floating offshore wind TLP in dynamic condition

The third part of this thesis presented the results of a comparative analysis between the application of the high-frequency numerical approaches applied to the EDF-TLP in dynamic condition against results from a new experimental campaign. The experimental set-up was presented and the numerical and physical prototypes were shown to be mostly representative of the same structure. However, some issues with the set-up were identified including the presence of instrument cables and probable discrepancies with the mooring lines' initial laying angle affecting the heave natural frequency. A strong coupling between the floater pitch and the tower bending mode was observed physically and successfully reproduced numerically using a simple mass-damper system to represent the turbine tower.

Tank tests of the physical model under monochromatic waves were undertaken in two steepness conditions, $kA = 0.10, H/\lambda \approx 3\%$ and $kA = 0.20, H/\lambda \approx 6\%$. Tests were carried out in regular waves so that harmonics of the response in terms of motion and line tension could be analysed to qualify the accuracy of the springing response predicted numerically with various approaches. The first comparison included three potential models of increasing order of non-linearity. The results of this first comparison highlighted that while the inclusion of QTFs was necessary to capture the second-order springing response in the pitch-tower bending mode, the inclusion of the third-order model had a limited impact on the third-order response. Even the linear model was found to provide a decent estimate of the third-order springing peak leading to the conclusion that viscous drag was the dominant hydrodynamic factor at that order. This result had already been suggested by the CFD analysis in the case of a fixed system, presented in Part II. It was thus confirmed and extended by experimental testing on a moving foundation. These findings were presented at the 33rd International Ocean and Polar Engineering Conference ISOPE2023 conference and published in its proceedings (Rongé, Peyrard, Venugopal, Johanning, & Xiao, 2023). Further comparisons were carried out afterwards using a range of hybrid strip-theory (Rainey, FNV) and semi-analytical potential flow models which led to similar conclusions. Overall, the models including QTFs calculated from BEM were considered the most reliable whereas the third-order FNV approach seemed to lead to a slightly better estimate than the semi-analytical potential flow. However, the springing peaks were found to be strongly sensitive to the axial drag coefficient and the structural damping ratio of both the mooring lines and turbine tower. As a result, it was not possible to make a definite conclusion on the most appropriate inertial third-order model.

Finally, tests were carried out in irregular waves, considering environmental storm conditions that could be similar to a ULS design under DLC 1.6 or 6.1 in the north Atlantic. Numerical simulations were carried out using four engineering approaches:

- DIEGO-LIN + Drag: Model based on first-order potential flow theory on the entire hull and including Morison drag with constant coefficient
- DIEGO-QTFs+INST+Drag: Model based on first-order and second-order potential flow theory on the entire hull, including Morison drag with constant coefficient and application of forces on the instantaneous position of the platform
- DIEGO-QTFs+MAL+INST+Drag: Model based on first-order, second-order potential flow theory on the entire hull, third-order semi-analytical solution on the central mast, including viscous drag with constant coefficient and the application of forces on the instantaneous position of the platform
- DIEGO-QTFs+FNV+INST+Drag: Model based on first-order, second-order potential flow theory on the entire hull, third-order strip-theory FNV approach on the central mast, including viscous drag with constant coefficient and the application of forces on the instantaneous position of the platform

Numerical simulations were carried out using both the experimental free surface elevation and random sea-states generated by DIEGO using the target spectra. The results of the response power spectra and the probability of exceedance of extreme responses were relatively similar in both cases and led to the same general conclusions. Overall, the linear response was captured with very good accuracy and the probability of exceedance plots show that the lower 90% quantile of motion and line tension events are correctly predicted by all the numerical models including when using a linear hydrodynamic model. The differences were thus observed in the higher 10% quantile which includes extreme events. Whilst the second-order QTFs were found to be a significant factor for capturing the high-frequency resonant response in the pitch-tower bending mode measured experimentally, the inclusion of third-order inertial models appeared to have a negligible impact. An analysis of the dominant high-frequency forces at play in the dynamic numerical simulation confirmed that the second-order sum-frequency force and viscous drag were the dominant contributions. To accurately capture the extreme motion and extreme line tensions, the model including solely the second-order QTFs appeared sufficient. Another important factor appeared to be applying the loads on the instantaneous position of the platform. This DIEGO option was used relatively successfully to account for high-frequency effects due to the platform motion despite not including the effect of motion in the diffraction solution at second-order. The inclusion of steady wind leads to a higher level of discrepancy between the numerical and physical model due to the difference in the steady surge excursion and pitch trim. Finally, an analysis of the springing and ringing response was carried out via time-frequency analysis. The results showed that the ringing response could be identified in both experimental and numerical simulation as an event of strong resonant response in both the pitch-tower bending mode and the heave mode.

Furthermore, in agreement with previous findings, the addition of third-order models had a negligible effect on the numerical prediction of that response. The addition of QTFs and viscous drag appeared to be sufficient to capture ringing events albeit with a lower amplitude than measured experimentally. These results confirmed for the first time with an experimental data-set that existing engineering numerical approaches can predict the occurrence of ringing on a FOWT-TLP.

Overall, Part III is a confirmation in a dynamic situation of the main observation made in Part II; that the axial drag on large submerged elements has a strong impact on third-order overturning moments and hence on the numerical prediction of the springing and ringing responses. Although this is certainly due to the geometrical particularity of the EDF-TLP floater, it is suggested based on the results of this thesis to highlight the potential effect of viscous effects on the high-frequency forces and response of FOWT-TLP in recommended practice and guidance from certification bodies. However, it must be remembered that the physical model is scaled to the Froude number and hence all effects related to viscosity are not scaled properly. There are around three orders of magnitude between the full scale and the experimental Reynold's numbers. Although empirical drag coefficients used by the industry are typically based on tank test scale experimental data-sets, the question remains on the applicability of those on full-scale designs. Furthermore, the currently published data-sets of empirical drag coefficient for fully submerged vertical cylinders remain limited. Furthermore, this thesis has assumed a constant drag coefficient across time and space which is most likely an invalid assumption despite being a common method used in the industry.

## 8.2 Recommendation for future work

The findings of the thesis pave the way for further examination of the hydrodynamic causes and consequences of high-frequency loadings on FOWT-TLP. A summary of the proposed future axis of research is summarised below:

- **High-frequency viscous drag forces**: Further investigation of the high-frequency viscous effects on FOWT-TLP hulls at physical and realistic industry scale is considered important to quantify the effects of drag on high-frequency resonance such as ringing. This would aim at providing sufficient data to adapt recommended practices accordingly. The aim would be to validate the use of the Morison equation for a range of cases and validate or propose new empirical drag coefficient data-sets. This could take the form of:
  - A numerical and experimental campaign to calibrate transverse and axial drag coefficients on standard shapes such as square and circular vertical and horizontal surface-piercing and fully submerged cylinders

  - An experimental campaign focused on measuring the 3DoF high-frequency hydrodynamic forces on a fixed FOWT-TLP hull and then on a moving hull driven by a hexapod. The aim would be to collect data on the high-frequency forces in various wave conditions including regular waves, focused waves and random irregular sea-states. Comparing fixed and moving conditions could help in assessing the significance of high-frequency effects due to the body's motion and reassess the validity of the relative velocity expression of Morison's Equation
  - A numerical campaign could replicate the experimental setting but using a Navier Stokes' CFD NWT analysis with the purpose of assessing the effect of scaling up from physical model to full-scale prototype on the viscous forces
  - Following such studies, potentially revisit the Morison drag model used in the aero-hydro-elastic model including the modelling of wave kinematics with non-linear theories and stretching models which could be compared to those derived using HOS and/or other fully nonlinear models
  - Additional work could look at assessing the impact of bio-fouling on the viscous drag model and if considered significant, the impact on the high-frequency response and consequences for design and maintenance
- **Mooring and structure flexibility** A second proposed axis of research would look at the impact of the structural numerical models on the prediction of resonant response and slacking events and comparison with existing models.
  - Analysis of ringing and slacking response within a Navier Stokes' CFD NWT fully coupled to a dynamic mooring module and a simple FEM module for the tower bending and comparison with current and potential future experimental data-sets and lighter engineering numerical approaches. Such analysis could be extended by including a fully flexible hull in the numerical models
  - A review of linear and non-linear stiffness and damping models existing in the industry and the impact of these on the numerical and experimental simulations of ringing response and slacking events. Specific studies could be conducted on stiffness and damping models of mooring lines during impact load such as a slacking-snapping event. This could involve building experimental data-sets of the stress-strain history of cable sections subjected to high-frequency and snap loads.
- **Hydrodynamic cause of ringing**: Further investigation on the transient response of FOWT-TLP prototypes in ringing conditions is required combining experimental and high-fidelity numerical modelling. The aim would be to identify the various hydrodynamic regimes which trigger the ringing condition:

  - Further experimental work is likely required with a various range of platform geometry going from single column ones to more complex geometry with large submerged elements such as the EDF-TLP. Investigation in various ranges of focused waves from weakly non-linear to highly non-linear and breaking conditions could be investigated.
  - High-fidelity numerical simulations of these tests could be carried out using fully non-linear potential flow solvers and Navier Stokes' CFD NWT. Analysing the high-frequency loads causing ringing responses with both fully non-linear potential flow and Navier Stokes' solvers would enable to distinguish between effects solely due to inertial loads and effects resulting from the addition of viscosity.
  - Following those tests, further improvement on the engineering approaches, including slamming models, applied to aero-hydro-elastic time domain solver could be recommended, tested and validated
- **Consequence of resonant response**: A final axis could focus on improving the numerical models used to predict the practical consequences of the springing and ringing response and slacking events on the structural integrity of the platform, especially in the framework of the fatigue limit state. For example, an element that tends to be ignored from most dynamic simulations of FOWT is the foundation-soil interaction which for TLP can be expected to be an important consideration. The aim would be to reduce uncertainties regarding fatigue damages in the entire system by also considering effects such as soil damping and fatigue undergone at the anchor-soil interface including due to resonant responses and slacking. Understanding better the consequences of the high-frequency dynamic responses should inform designers on the level of fidelity they are to aim for their simulation at various design stages:
  - Numerical simulation including a dynamic export cable could be undertaken to understand the impact of high-frequency forces, mostly second-order ones, on the fatigue of that element and the required design/cost implication
  - Experimental and numerical work will likely have to be carried out to assess the current numerical capabilities of soil mechanics solvers to simulate the behaviour of soil under high-frequency and impact loads.
  - Structural numerical simulation and experiments will likely have to be carried out on sections of cables, elements of the floater-tower connection or even using flexible hull models and considering stress concentration factors to assess better the ultimate design failure path and significant elements subject to fatigue damages

# Appendix A

# Details on semi-analytical potential flow

## A.1 Second-order diffraction on a vertical cylinder

### A.1.1 Second-order free surface forcing

As seen in Equation 3.8b, the in-homogeneous surface forcing is known based on the first-order free surface pressure. It is subtracted by the free surface forcing term due to the quadratic product of the incident potential, $q_{II}$, since the second-order incident potential satisfies the far-field free surface boundary condition.

$$Q_D^{(2)} = \left[ -\frac{i\omega}{2g}\phi^{(1)} \left( -\omega^2 \frac{\partial \phi^{(1)}}{\partial z} + g\frac{\partial^2 \phi^{(1)}}{\partial z^2} \right) + i\omega(\nabla\phi^{(1)})^2 \right]_{z=0} - q_{II} \tag{A.1}$$

As seen in Section 3.2.1, the partial differential in Equation 3.8b can be split in a homogeneous and particular solution, therefore splitting the diffracted potential into a homogeneous and particular part as proposed by Molin (1979). These represent respectively the free-waves and locked-wave components tied to the first-order waves. These two potentials fulfil jointly the body boundary (Eq. 3.16 and 3.17).

$$\phi_D^{(2)} = \phi_{DI}^{(2)} + \phi_{DD}^{(2)} \tag{A.2}$$

And satisfy the free surface boundary condition as follows.

$$(-4\omega^2 + g\frac{\partial}{\partial z})\phi_{DI}^{(2)} = 0 \qquad \text{on } z = 0 \tag{A.3}$$

$$(-4\omega^2 + g\frac{\partial}{\partial z})\phi_{DD}^{(2)} = Q_D^{(2)} \qquad \text{on } z = 0 \tag{A.4}$$

Equation A.1 can be further developed by replacing the first-order potential with its incident and diffracted constituent.

$$
\begin{aligned}
Q_D^{(2)} = \Bigg[ & -\frac{i\omega}{2g}(\phi_I^{(1)} + \phi_D^{(1)}) \left( -\omega^2 \frac{\partial(\phi_I^{(1)} + \phi_D^{(1)})}{\partial z} + g \frac{\partial^2(\phi_I^{(1)} + \phi_D^{(1)})}{\partial z^2} \right) \\
& + i\omega \left( \frac{\partial(\phi_I^{(1)} + \phi_D^{(1)})}{\partial z} \right)^2 + i\omega \left( \frac{\partial(\phi_I^{(1)} + \phi_D^{(1)})}{\partial r} \right)^2 \\
& + i\omega \left( \frac{1}{r} \frac{\partial(\phi_I^{(1)} + \phi_D^{(1)})}{\partial \theta} \right)^2 \Bigg]_{z=0} - Q_{II}^{(2)}
\end{aligned}
\tag{A.5}
$$

Furthermore, removing terms consisting of quadratic product of the first-order incident potential and knowing that at $z = 0$, we can write that $\partial\phi/\partial z = k\tanh(kh)\phi$ and $\partial^2\phi/\partial z^2 = k^2\phi$ as well as expressing $\omega^2$ as per the wave dispersion equation, we get the following expression.

$$
\begin{aligned}
Q_D^{(2)}(r,\theta,z) = \Bigg[ & \frac{i\omega k^2 \tanh^2 kh}{2} (\phi_D^{(1)}\phi_D^{(1)} + 2\phi_I^{(1)}\phi_D^{(1)}) \\
& - \frac{i\omega k^2}{2} (\phi_D^{(1)}\phi_D^{(1)} + 2\phi_I^{(1)}\phi_D^{(1)}) \\
& + i\omega k^2 \tanh^2 kh (\phi_D^{(1)}\phi_D^{(1)} + 2\phi_I^{(1)}\phi_D^{(1)}) \\
& + i\omega \left( \frac{\partial\phi_D^{(1)}}{\partial\partial r} \frac{\partial\phi_D^{(1)}}{\partial\partial r} + 2\frac{\partial\phi_D^{(1)}}{\partial r} \frac{\partial\phi_I^{(1)}}{\partial r} \right) \\
& + i\omega \frac{1}{r^2} \left( \frac{\partial\phi_D^{(1)}}{\partial\theta} \frac{\phi_D^{(1)}}{\partial\theta} + 2\frac{\partial\phi_D^{(1)}}{\partial\theta} \frac{\partial\phi_I^{(1)}}{\partial\theta} \right) \Bigg]_{z=0}
\end{aligned}
\tag{A.6}
$$

.

$$
\begin{aligned}
Q_D^{(2)}(r,\theta,z) = \Bigg[ & \frac{i\omega k^2}{2} (3\tanh^2 kh - 1)(\phi_D^{(1)}\phi_D^{(1)} + 2\phi_I^{(1)}\phi_D^{(1)}) \\
& + i\omega \left( \frac{\partial\phi_D^{(1)}}{\partial\partial r} \frac{\partial\phi_D^{(1)}}{\partial\partial r} + 2\frac{\partial\phi_D^{(1)}}{\partial r} \frac{\partial\phi_I^{(1)}}{\partial r} \right) \\
& + i\omega \frac{1}{r^2} \left( \frac{\partial\phi_D^{(1)}}{\partial\theta} \frac{\phi_D^{(1)}}{\partial\theta} + 2\frac{\partial\phi_D^{(1)}}{\partial\theta} \frac{\partial\phi_I^{(1)}}{\partial\theta} \right) \Bigg]_{z=0}
\end{aligned}
\tag{A.7}
$$

.

The first-order incident and diffracted potentials around a vertical cylinder expressed in polar form as the sum of their Fourier terms are as follows.

$$\phi_I^{(1)}(r,\theta,z) = -\frac{igA}{\omega}\frac{\cosh(k(z+h))}{\cosh(kz)}\sum_{n=0}^{\infty}\varepsilon_n i^n J_n(kr)\cos(n\theta) \tag{A.8}$$

$$\phi_D^{(1)}(r,\theta,z) = \frac{igA}{\omega}\frac{\cosh(k(z+h))}{\cosh(kz)}\sum_{n=0}^{\infty}\varepsilon_n i^n \frac{J_n'(ka)}{H_n'(ka)}H_n(kr)\cos(n\theta) \tag{A.9}$$

The same can be done for the free surface forcing term.

$$Q_D^{(2)}(r,\theta,z) = \sum_{n=0}^{\infty}\varepsilon_n q_n(r,\theta,z) \tag{A.10}$$

Where $\varepsilon_n = 1$ for $n = 0$ and $\varepsilon = 2$ for $n\,0$. Therefore quadratic product of the potentials can be expressed as products of infinite sums by using the relation $e^{ip} + e^{-ip} = 2\cos(p\theta)$ as written in Chau & Eatock Taylor Chau and Eatock Taylor (1992). Since $\varepsilon_n = 1$ when p = 0, this allows the use of the following expression

$$\sum_{n=0}^{\infty} f(x)\varepsilon_n\cos(n\theta) = \sum_{n=-\infty}^{\infty} f(x)e^{in\theta} \tag{A.11}$$

$$\phi_I^{(1)}(r,\theta,z) = \sum_{n=-\infty}^{\infty} T_n e^{in\theta} \tag{A.12}$$

$$\phi_D^{(1)}(r,\theta,z) = \sum_{n=-\infty}^{\infty} S_n e^{in\theta} \tag{A.13}$$

$$\sum_{n=0}^{\infty} q_n(r,z)\varepsilon_n\cos(n\theta) = \sum_{n=-\infty}^{\infty} q_n(r,z)e^{in\theta} \tag{A.14}$$

Where,

$$T_n = -\frac{igA}{\omega}\frac{\cosh(k(z+h))}{\cosh(kz)}i^n J_n(kr) \tag{A.15}$$

$$S_n = \frac{igA}{\omega}\frac{\cosh(k(z+h))}{\cosh(kz)}i^n \frac{J_n'(ka)}{H_n'(ka)}H_n(kr) \tag{A.16}$$

And, the quadratic products of the infinite sum can be simplified in the following form.

$$\sum_{n=-\infty}^{\infty} T_n e^{in\theta}\sum_{q=-\infty}^{\infty} S_n e^{iq\theta} = \sum_{n=-\infty}^{\infty}\left\{\sum_{q=-\infty}^{\infty} T_{n-q}S_q\right\}e^{i\theta n} \tag{A.17}$$

This way we can change Equation A.7 by making use of the simplification of the double infinite sum into the following expression.

$$
\begin{aligned}
q(r,z) &= \sum_{n=0}^{\infty} \varepsilon_n q_n \\
&= \sum_{n=0}^{\infty} \varepsilon_n \cos(n\theta) \sum_{q=-\infty}^{\infty} \left[ \frac{i\omega k^2}{2} (3\tanh^2 kh - 1)(S_{n-q}S_q + 2T_{n-q}S_q) \right. \\
&\quad + i\omega \left( \frac{\partial S_{n-q}}{\partial \partial r} \frac{\partial S_q}{\partial \partial r} + 2 \frac{\partial T_{n-q}}{\partial r} \frac{\partial S_q}{\partial r} \right) \\
&\quad \left. + i\omega \frac{q(n-q)}{r^2} (S_{n-q}S_q + 2T_{n-q}S_q) \right]_{z=0}
\end{aligned}
\tag{A.18}
$$

### A.1.2 Expression of the second-order potentials

This section provides the equation published in Huang and Eatock Taylor (1996) with some correction made to the original formulas.

$$
\phi^{(2)} = \phi_I^{(2)} + \phi_{DI}^{(2)} + \phi_{DD}^{(2)} \tag{A.19}
$$

$$
\phi_I^{(2)}(r,z,\theta) = \frac{3iA^2\omega}{8} \frac{\cosh(2k(z+h))}{\sinh kh^4} \sum_{n=0}^{\infty} \varepsilon_n i^n J_n(2kr)\cos(n\theta) \tag{A.20}
$$

$$
\phi_{DI,n}^{(2)}(r,z,\theta) = \sum_{n=0}^{\infty} \varepsilon_n i^n \cos(n\theta) \sum_{m=0}^{\infty} \frac{1}{k_m} \frac{3iA^2\omega}{8} \frac{2kJ_n'(2ka)}{\sinh kh^4} \alpha_m \frac{U_n(k_m r)}{U_n(k_m a)} Z_m(k_m,z) Z_m(k_m,0) \tag{A.21}
$$

$$
\phi_{DD,n}^{(2)}(r,\theta,z) = \sum_{n=0}^{\infty} \varepsilon_n \cos(n\theta) \sum_{m=0}^{\infty} Z_m^{\pm}(0) Z_m^{\pm}(z) \int_a^{\infty} \xi q_n^{\pm}(\xi) G_{nm}^{\pm}(r,\xi) d\xi \tag{A.22}
$$

where $Z_m$ are the vertical eigenfunctions for the free and evanescent mode, $m$ such as:

$$
Z_0 = \frac{1}{[h/2(1+\sinh(2k_2)/(2k_2h)]^{0.5}} \cosh(k_2(z+h)) \tag{A.23}
$$

$$
Z_m = \frac{1}{[h/2(1+\sin(2k_m)/(2k_mh)]^{0.5}} \cos(k_m(z+h)) \tag{A.24}
$$

with the wave number of the free mode being the solution of the propagation equation at double pulsation:

$$
4\omega^2 = k_2^2 \tanh k_2 h \tag{A.25}
$$

and the series of evanescent modes being the solutions of the following equation:

$$
-4\omega^2 = k_m \omega^2 \tan kh \tag{A.26}
$$

The potential coefficients for the homogeneous potential, $\phi_D I^{(2)}$ are as follows.

$$\alpha_0 = \frac{2k\sinh 2kh + 4\omega^2/g\cosh 2kh}{k^2 - k_2} \tag{A.27}$$

$$\alpha_m = \frac{2k\sinh 2kh + 4\omega^2/g\cosh 2kh}{k^2 - k_m} \tag{A.28}$$

$$U_n(k_m, r) = \begin{cases} H_n(k_2 r) & m = 0 \\ K_n(k_m r) & -m > 0 \end{cases} \tag{A.29}$$

The Green's function for the in-homogeneous potential, $\phi_D D^{(2)}$, is constructed as follows.

$$G_{n0}(r,\xi) = \begin{cases} i\pi H_n(k_2\xi)[J_n(k_2 r) - \frac{J_n'(k_2 a)}{H_n'(k_2 a)} H_n(k_2 r)]/2 & r < \xi \\ i\pi H_n(k_2 r)[J_n(k_2\xi) - \frac{J_n'(k_2 a)}{H_n'(k_2 a)} H_n(k_2\xi)]/2 & r > \xi \end{cases} \tag{A.30}$$

$$G_{nm}(r,\xi) = \begin{cases} K_n(k_m\xi)[I_n(k_m r) - \frac{I_n'(k_m a)}{K_n'(k_m a)} K_n(k_m r)]/2 & r < \xi \\ K_n(k_m r)[I_n(k_m\xi) - \frac{I_n'(k_m a)}{K_n'(k_m a)} K_n(k_m\xi)]/2 & r > \xi \end{cases} \tag{A.31}$$

### A.1.3 Separation of domain for truncated cylinder case

As seen in Chapter 3, the fluid domain for a truncated cylinder can be decomposed into two parts, one exterior and one interior domain. The following expressions are recalled. The total potential in the exterior region,$\Omega_1$, is then written as the sum of the following terms.

$$\phi_1^{(p)} = \phi_I^{(p)} + \phi_{D,1}^{(p)} + \phi_{D,2}^{(p)} \tag{A.32}$$

$$\phi_1^{(p)} = \phi_0^{(p)} + \phi_{D,2}^{(p)} \tag{A.33}$$

where $\phi_0^{(p)}$ corresponds to the case of a bottom-seated vertical cylinder, and $\phi_{D,2}^{(p)}$ is the correction due to the presence of the interior domain potential, $\phi_2^{(p)}$. The approach then assumes that the relation defined in Equation A.38b between the two potentials at $r = a$ can be expressed as follows.

$$\phi_2^{(p)}(a,z) = \phi_0^{(p)}(a,z) + \phi_{D,2}^{(p)}(a,z) \tag{A.34a}$$

$$\sum_{n=0}^{\infty} \varepsilon_n \phi_{2,n}^{(p)}(a,z)\cos n\theta = \sum_{n=0}^{\infty} \varepsilon_n \left[\phi_{0,n}^{(p)}(a,z) + \phi_{D,2,n}^{(p)}(a,z)\cos n\theta\right] \tag{A.34b}$$

which for each Fourier mode $n$ gives the following relation

$$\sum_{m=0}^{\infty} A_{mn}^{(p)} V_n(\lambda_m a)\cos(\lambda_m(z+h)) = \phi_{0,n}^{(p)}(a,z) + \sum_{j=0}^{\infty} B_{jn} \frac{U_n(k_j a)}{U_n'(k_j a)} Z_j(k_j, z) \tag{A.35}$$

where:

$$V_n({}_m r) = \begin{cases} 0.5(r/a)^n & m = 0 \\ I_n(\lambda_m r)/I_n(\lambda_n a) & m > 0 \end{cases} \tag{A.36}$$

$$\lambda_m = m\pi/(h-b) \tag{A.37}$$

and where $\phi_0^{(p)}$ is the approximated solution of the diffraction potential when considering only the exterior potential and $A_{mn}$ and $B_{jn}$ are the potential coefficients which are found by solving the boundary condition of the domain decomposition which are as follows:

$$\frac{\partial \phi_1^{(n)}}{\partial r} = \begin{cases} 0 & r = a, -b \leq z \leq 0 \\ \frac{\partial \phi_2^{(n)}}{\partial r} & r = a, -h \leq z \leq -b \end{cases} \tag{A.38a}$$

$$\phi_1^{(n)} = \phi_2^{(n)} \; r = a, -h \leq z \leq -b \tag{A.38b}$$

It is worth remembering that, $\partial \phi_0^{(p)}/\partial r = 0$ on $r = a$ for the entire water column since it is the solution for a bottom-seated vertical cylinder. Hence between, $-h \leq z \leq -b$, the integral over that portion of the water column leads to a linear system to resolve such as:

$$\{B_n^{(p)}\} = [C_n^{(p)}]\{A_n^{(p)}\} \tag{A.39}$$

$$\{A_n^{(p)}\} = [D_n^{(p)}]\{B_n^{(p)}\} + \{E_n^{(p)}\} \tag{A.40}$$

where the eigenfunction series of the unknown potential coefficient $B_n$ and $A_n$ for each Fourier term of order $n$, are represented by column vectors linked by square matrices of shape $m, j$.

$$C_n^{(p)}(j,m) = \frac{V_n'(\lambda_m)}{k_j h} \int_{z=-h}^{-b} \cos\left(\lambda_m(z+h)\right) Z_j(k_j z) \; \mathrm{d}z \tag{A.41}$$

$$D_n^{(p)}(m,j) = \frac{2}{d} \frac{U_n(k_j a)}{U_n'(k_j a)} \int_{z=-h}^{-b} \cos\left(\lambda_m(z+h)\right) Z_j(k_j z) \; \mathrm{d}z \tag{A.42}$$

$$\tag{A.43}$$

The expression for the coefficient can be found in the original publication of Huang and Eatock Taylor (1996). $E_n$ represents the integral over $-h \leq z \leq -b$ of $\phi_{0,n}^{(p)}$. This way the solution at each Fourier order $n$ can be found through the following identity.

$$\{A_n\} = ([I] - [D][C])^{-1}\{E_n\} \tag{A.44}$$

The other possibility to give an approximate solution is to assume that the draft of the cylinder is deep enough so that the contribution of the interior potential is negligible on the exterior potential such as $B_n = 0$. This is suggested by Huang and Eatock Taylor (1996) as a relatively suitable assumption for the second-order potential in which case the system is much simpler

to solve with:

$$\{A_n^{(2)}\} = \{E_n^{(2)}\} \tag{A.45}$$

# Appendix B

# Further results on ringing events

## B.1 Detail on slacking due to a wave slamming event

A detail is provided in Figure B.1 of an extreme wave event that occurred in sea-state EC3a. At $t = 1225$ s, a large wave of undetermined height, and zero-crossing period of around $T = 12$ s, is observed breaking on the EDF-TLP with the reading of the probe showing a spike likely caused by the breaking water splash (see Figure B.1b). However, this wave is estimated to be around 15-16 m from front through to crest which, in a sea-state of $Hs = 10.6$m, is considered close to the normal Rayleigh distribution for wave maxima which it is typically around $H_{Max} \approx 1.6 - 2.0\ H_s$. The time series record of Line No1 tension, on the bottom right of Figure B.1b, shows that this event is shortly followed by a slacking event followed by extreme high tension and a visible ringing response. Unfortunately, the experimental signal is truncated. However, based on the width of the experimental peak, it seems like the nonlinear numerical model provides a decent depiction of the event. Whereas the linear model comes short of predicting the slacking event, all three nonlinear models do. Furthermore, the addition of the FNV leads to a slightly higher extreme tension value than using the DIEGO1-QTF model. As for the DIEGO1-QTF+MAL model, it displays a phase shift from the experimental measurement at the extreme value and as observed previously, generally does not perform well in irregular sea-sates. Therefore, it is interesting to note that despite being outside of the assumption of the potential flow and strip-theory, the nonlinear numerical models appear to perform relatively well in this situation. It is evident that simulations could be made more realistic by including slamming models. However, these are outside of the scope of this research.

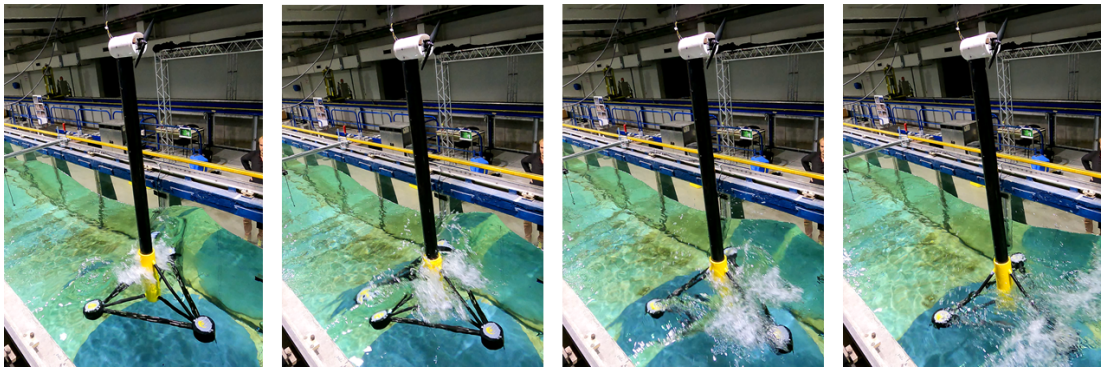

**(a)**

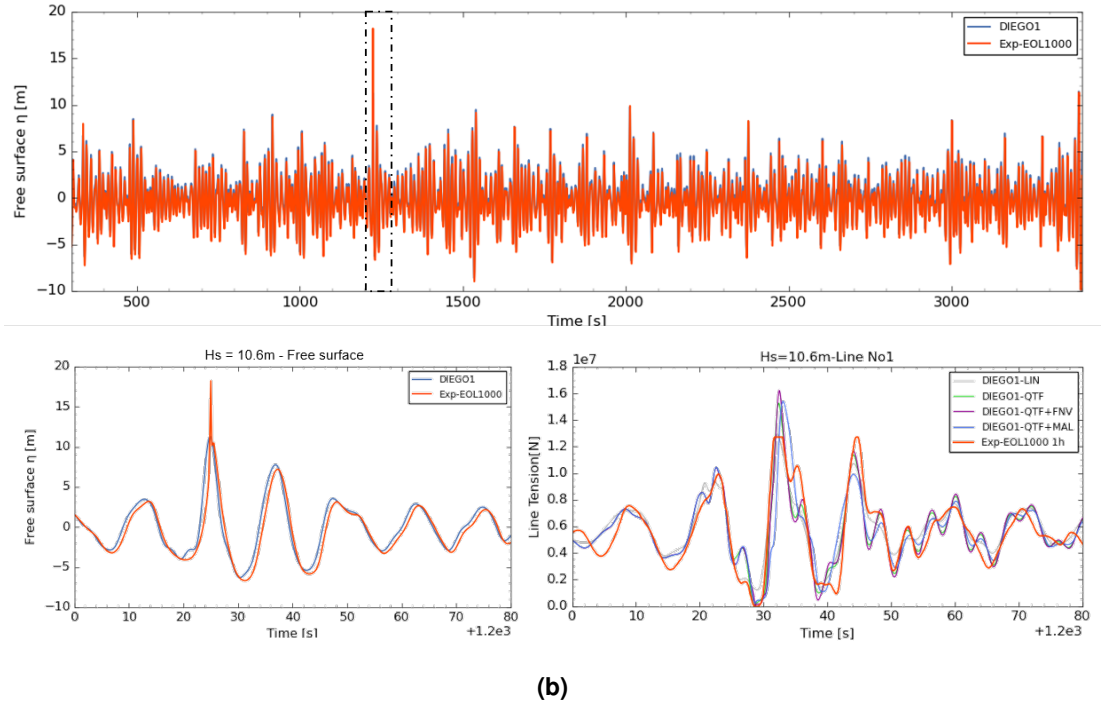


**(b)**

**Figure B.1:** Detail on wave slamming event: (a) GoPro Time-lapse of slamming event; (b) detail on time series of free surface and Line No1 vertical tension

## B.2 Additional results of time-frequency analysis of resonant response

Additional results are provided as complementary material to Section 7.3.5. These concern ringing cases in sea-state EC1a, EC2a and EC3a. A comparison between the experimental and three numerical models scalograms gives an indication of the effect of adding sum-frequency forces on capturing the springing and ringing responses.

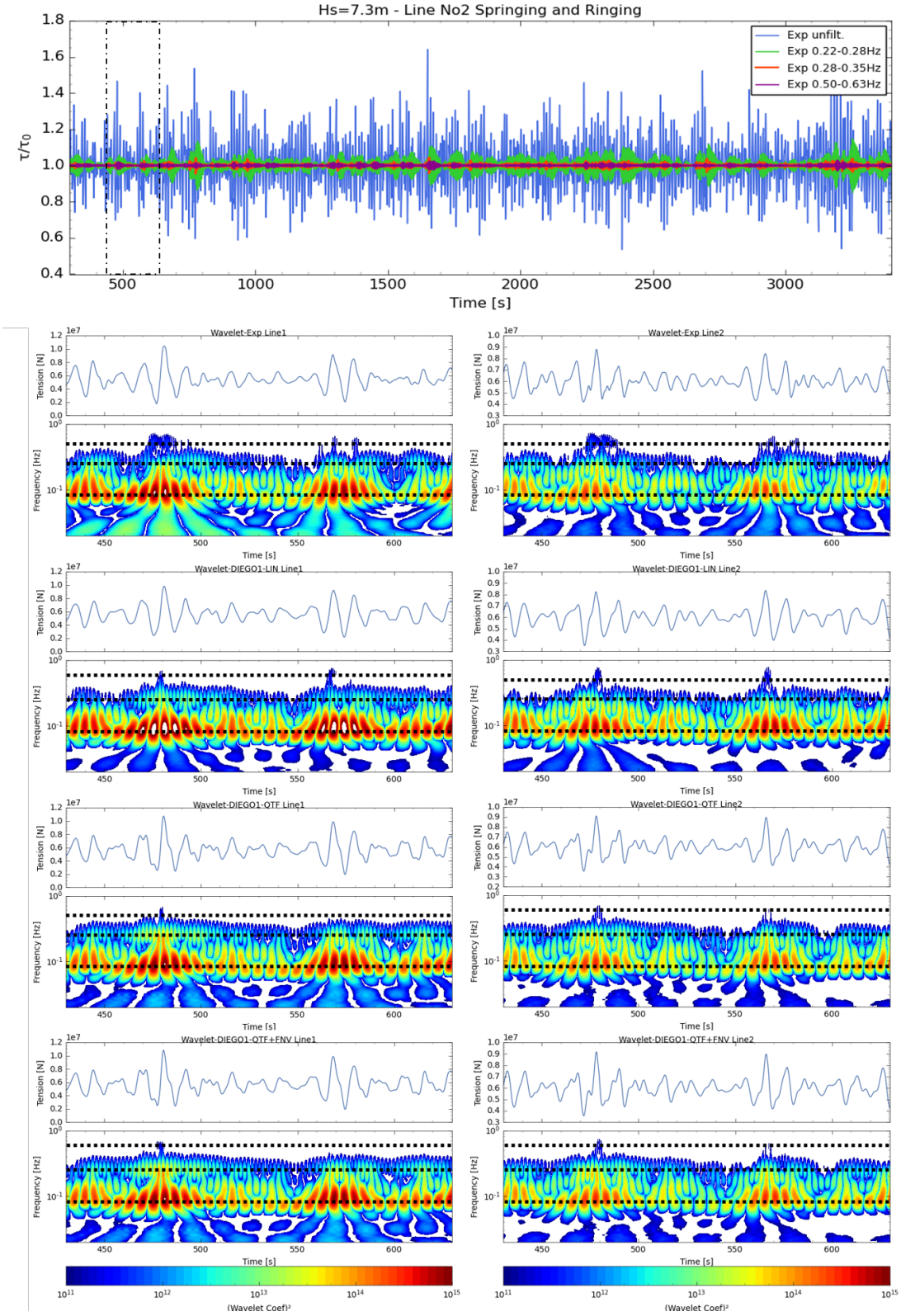


**Figure B.2**

**Figure B.3:** Springing and ringing response in case EC1a: Comparison of line-tension scalograms for Line No1 and No2 between experimental measurements and three numerical models with increasing order of nonlinearity: DIEGO1-LIN, DIEGO1-QTF, DIEGO1-QTF+FNV

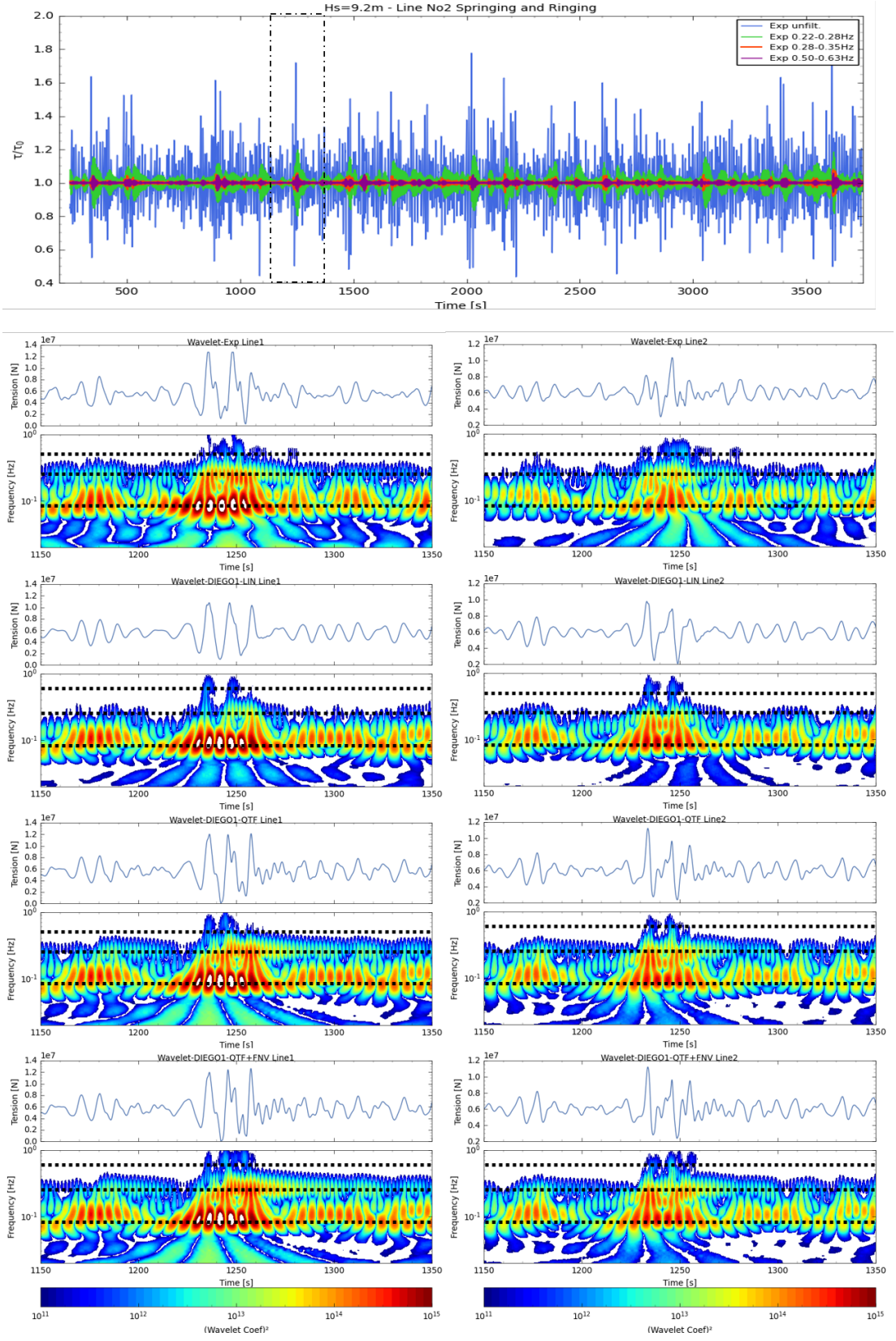


**Figure B.4**

**Figure B.5:** Springing and ringing response in case EC2a: Comparison of line-tension scalograms for Line No1 and No2 between experimental measurements and three numerical models with increasing order of nonlinearity: DIEGO1-LIN, DIEGO1-QTF, DIEGO1-QTF+FNV

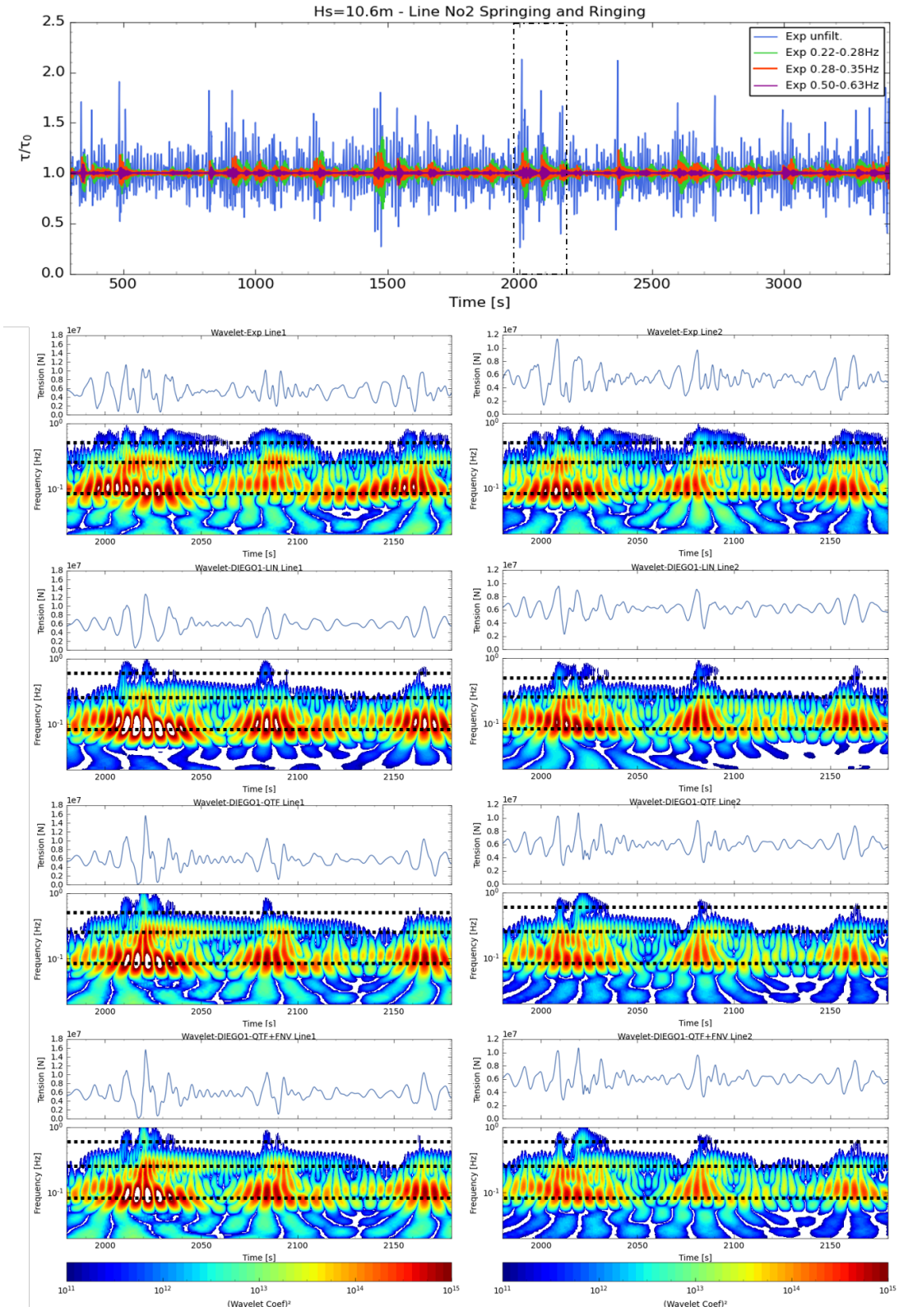


**Figure B.6**

**Figure B.7:** Springing and ringing response in case EC3a: Comparison of line-tension scalograms for Line No1 and No2 between experimental measurements and three numerical models with increasing order of nonlinearity: DIEGO1-LIN, DIEGO1-QTF, DIEGO1-QTF+FNV

# Bibliography


Abul-Azm, A. G., & Williams, A. N. (1988). Second-order diffraction loads on truncated cylinders. *Journal of waterway, port, coastal, and ocean engineering*, *114*(4), 436-454. doi: https://doi.org/10.1061/(ASCE)0733-950X(1988)114:4(436)

Adam, F., Myland, T., Dahlhaus, F., & Großmann, J. (2014, 06). Scale Tests of the GICON®-TLP for Wind Turbines. In (Vol. Volume 9A: Ocean Renewable Energy). Retrieved from https://doi.org/10.1115/OMAE2014-23216 (V09AT09A011) doi: 10.1115/OMAE2014-23216

Alves, M. (2016). Chapter 2 - frequency-domain models. In M. Folley (Ed.), *Numerical modelling of wave energy converters* (p. 11 - 30). Academic Press. Retrieved from http://www.sciencedirect.com/science/article/pii/B9780128032107000025 doi: https://doi.org/10.1016/B978-0-12-803210-7.00002-5

ANSYS Inc. (2016). *AQWA Theory Manual* (Tech. Rep.). Canonsburg, PA, USA.

Armenio, E. (2014). *Physcial Model Experiments on Floating Off-Shore WindTurbines* (PhD Thesis). Università del Salento.

Azcona, J., Bouchotrouch, F., & Vittori, F. (2019). Low-frequency dynamics of a floating wind turbine in wave tank–scaled experiments with sil hybrid method. *Wind Energy*, *22*(10), 1402-1413. Retrieved from https://onlinelibrary.wiley.com/doi/abs/10.1002/we.2377 doi: 10.1002/we.2377

Babarit, A., & Delhommeau, G. (2015, September). Theoretical and numerical aspects of the open source BEM solver NEMOH. In *11th European Wave and Tidal Energy Conference (EWTEC2015).* Nantes, France. Retrieved from https://hal.archives-ouvertes.fr/hal-01198800

Bachynski, E. E. (2014). *Design and Dynamic Analysis of Tension Leg Platform Wind Turbines* (PhD Thesis). NTNU, Trondheim,Norway.

Bachynski, E. E., Chabaud, V., & Sauder, T. (2015, jan). Real-time hybrid model testing of floating wind turbines: Sensitivity to limited actuation. In *Energy procedia* (Vol. 80, pp. 2–12). Elsevier Ltd. doi: 10.1016/j.egypro.2015.11.400

Bachynski, E. E., Pákozdi, C., Östman, A., & Stansberg, C. T. (2018, 07). Computational Fluid Dynamics Reproduction of Nonlinear Loads on a Vertical Column During Extreme Irregular Wave Events. *Journal of Offshore Mechanics and Arctic Engineering*, *140*(6), 061804. Retrieved from https://doi.org/10.1115/1.4040442 doi: 10.1115/1.4040442

Bak, C., Bitsche, R., Yde, A., Kim, T., Hansen, M., Zahle, F., ... Behrens, T. (2012). Light rotor: The 10-mw reference wind turbine. In *Proceedings of ewea 2012 - european wind energy conference exhibition.* European Wind Energy Association (EWEA). Retrieved from http://events.ewea.org/annual2012/ (EWEC 2012 - European Wind Energy Conference amp; Exhibition, EWEC 2012 ; Conference date: 16-04-2012 Through 19-04-2012)

Bak, C., Zahle, F., Bitsche, R., Kim, T., Yde, A., Henriksen, L., ... Natarajan, A. (2013). *The dtu 10-mw reference wind turbine.* (Danish Wind Power Research 2013 ; Conference date: 27-05-2013 Through 28-05-2013)

Baldock, T., & Swan, C. (1994). Numerical calculations of large transient water waves. *Applied Ocean Research*, *16*(2), 101-112. Retrieved from https://www.sciencedirect.com/science/article/pii/014111879490006X doi: https://doi.org/10.1016/0141-1187(94)90006-X

Benguigui, W., Doradoux, A., Lavieville, J., Mimouni, S., & Longatte, E. (2018). A discrete forcing method dedicated to moving bodies in two-phase flow. *International Journal for Numerical Methods in Fluids*, *88*(7), 315-333. Retrieved from https://onlinelibrary.wiley.com/doi/abs/10.1002/fld.4670 doi: https://doi.org/10.1002/fld.4670

Benguigui, W., Laviéville, J., & Merigoux, N. (2019). Fluid-structure interaction in two-phase flow using a discrete forcing method. *International Journal for Numerical Methods in Fluids*, *91*(5), 247-261. Retrieved from https://onlinelibrary.wiley.com/doi/abs/10.1002/fld.4753 doi: https://doi.org/10.1002/fld.4753

Benjamin, T. B., & Feir, J. E. (1967). The disintegration of wave trains on deep water part 1. theory. *Journal of Fluid Mechanics*, *27*(3), 417–430. doi: 10.1017/S002211206700045X

Benoit, M., Benguigui, W., Teles, M., Robaux, F., & Peyrard, C. (2022, 06). Two-Phase CFD Simulation of Breaking Waves Impacting a Coastal Vertical Wall with a Recurved Parapet. In (Vol. All Days). (ISOPE-I-22-248)

Benoit, M., Benguigui, W., Teles, M., Robaux, F., & Peyrard, C. (2023, 06). Two-phase CFD Simulation of Breaking Waves Impacting a Coastal Vertical Wall with a Recurved Parapet. *International Journal of Offshore and Polar Engineering*, *33*(02), 123-131. Retrieved from https://doi.org/10.17736/ijope.2023.sv03 doi: 10.17736/ijope.2023.sv03

Burton, T., Jenkins, N., Sharpe, D., & Bossanyi, E. (2011). *The wind resource*. John Wiley Sons, Ltd. doi: https://doi.org/10.1002/9781119992714.ch2

Caillé, F., Bozonnet, P., Perdrizet, T., Poirette, Y., & Melis, C. (2017, sep). Model test and simulation comparison for an inclined-leg TLP dedicated to floating wind. In *Proceedings of the asme 2017 36th international conference on offshore mechanics and arctic engineering* (Vol. 10). American Society of Mechanical Engineers (ASME). Retrieved from http://asmedigitalcollection.asme.org/OMAE/proceedings-pdf/OMAE2017/57786/V010T09A070/2534888/v010t09a070-omae2017-61652.pdf doi: 10.1115/OMAE2017-61652

Canard, M., Ducrozet, G., & Bouscasse, B. (2022). Varying ocean wave statistics emerging from a single energy spectrum in an experimental wave tank. *Ocean Engineering*, *246*, 110375. Retrieved from https://www.sciencedirect.com/science/article/pii/S0029801821016668 doi: https://doi.org/10.1016/j.oceaneng.2021.110375

CEREMA & Minsitere de la Transition Energetique. (n.d.). *Eoliennes en mer en France.* Webpage. Retrieved from https://www.eoliennesenmer.fr/ (Accessed on 2023-09-01)

Chabaud, V., Steen, S., & Skjetne, R. (2013, 06). Real-Time Hybrid Testing for Marine Structures: Challenges and Strategies. , *Volume 5: Ocean Engineering*. (V005T06A021) doi: 10.1115/OMAE2013-10277

Chakrabarti, S. (1987). *Hydrodynamics of offshore structures.* Computational Mechanics.

Chaplin, J. R., Rainey, R. C. T., & Yemm, R. W. (1997, nov). Ringing of a vertical cylinder in waves. *Journal of Fluid Mechanics*, *350*, 119–147. Retrieved from https://doi.org/10.1017%2Fs002211209700699x doi: 10.1017/s002211209700699x

Chatjigeorgiou, I., & Mavrakos, S. (2006, 01). Semi-analytical formulation of the second-order wave diffraction by a truncated-compound surface-piercing cylinder. *Journal of Ship Technology Research, Schiffstechnik*, *53*, 26-38. doi: 10.1179/str.2006.53.1.005

Chatjigeorgiou, I., & Mavrakos, S. (2007, November). Second-order sum-frequency wave diffraction by a truncated surface-piercing cylinder in bichromatic waves. *Journal of Marine Science and Technology*, *12*(4), 218–231. Retrieved from https://doi.org/10.1007/s00773-007-0252-y doi: 10.1007/s00773-007-0252-y

Chau, F. P., & Eatock Taylor, R. (1992). Second-order wave diffraction by a vertical cylinder. *Journal of Fluid Mechanics*, *240*, 571–599. doi: 10.1017/S0022112092000211

Chen, X.-B. (2007). Middle-field formulation for the computation of wave-drift loads. *Journal of Engineering Mathematics*, *59*, 61–82. doi: 10.1007/s10665-006-9074-x

Choisnet, T., Favré, M., Lyubimova, M., & Rogier, E. (2014, July). A robust concrete floating wind turbine foundation for worldwide applications. In *Grand renewable energy.* Tokyo, Japan.

Crown Estate Scotland. (2022). *ScotWind offshore wind leasing delivers major boost to Scotland's net zero aspirations.* Press Release. Retrieved from https://www.crownestatescotland.com/news/scotwind-offshore-wind-leasing-delivers-major-boost-to-scotlands-net-zero-aspirations (17 Jan 2022)

Cummins, W. (1962). *The impulse response function and ship motions* (Tech. Rep.).

Dadmarzi, H. F., Thys, M., & Bachynski, E. E. (2019, 06). Validation of Hydrodynamic Loads on a Large-Diameter Monopile in Regular Waves. In *Proceedings of the asme 2019 38th international conference on offshore mechanics and arctic engineering* (Vol. Volume 7A: Ocean Engineering). Retrieved from https://doi.org/10.1115/OMAE2019-95929 (V07AT06A060) doi: 10.1115/OMAE2019-95929

Dean, R. G. (1965). Stream function representation of nonlinear ocean waves. *Journal of Geophysical Research (1896-1977)*, *70*(18), 4561-4572. Retrieved from https://agupubs.onlinelibrary.wiley.com/doi/abs/10.1029/JZ070i018p04561 doi: https://doi.org/10.1029/JZ070i018p04561

Delefortrie, G.; Geerts, S.; Peeters, P.; Mostaert, F. (2017). *Ship Calibration: Determination of a Ship Model 's Moment of Inertia. Version 2.0* (Tech. Rep.).

Department for Business, Energy & Industrial Strategy. (2021). *Plans unveiled to decarbonise uk power system by 2035.* Press Release. Retrieved from https://www.gov.uk/government/news/plans-unveiled-to-decarbonise-uk-power-system-by-2035 (07 Oct 2021)

DNV-GL. (2010). *Environmental conditions and environmental loads. DNV-RP-C205* (Offshore Recommended Practice No. DNV-RP-C205).

DNV-GL. (2016, November). *Loads and site conditions for wind turbines. DNVGL-ST-0437* [Offshore Standard].

DNV-GL. (2019a, May). *Coupled analysis of floating wind turbines. DNVGL-RP-0286* [Recommended Practice].

DNV-GL. (2019b, July). *Floating wind turbine structures. DNVGL-ST-0119* [Offshore Standard].

DNV-GL. (2019c, September). *Global performance analysis of deepwater floating structures. DNV-RP-F205* [Recommended Practice].

Duan, W. Y., Chen, J. K., & Zhao, B. B. (2015, aug). Second-order Taylor expansion boundary element method for the second-order wave radiation problem. *Applied Ocean Research*, *52*, 12–26. doi: 10.1016/j.apor.2015.04.011

Duarte, T., Gueydon, S., Jonkman, J., & Sarmento, A. (2014, 06). Computation of Wave Loads Under Multidirectional Sea States for Floating Offshore Wind Turbines. In (Vol. Volume 9B: Ocean Renewable Energy). Retrieved from https://doi.org/10.1115/OMAE2014-24148 (V09BT09A023) doi: 10.1115/OMAE2014-24148

Duchet, M. (2019). *Simulate, design and manufacture a floating offshore wind turbine model dedicated to wave tank tests* (Master's thesis). ENSTA, Saclay, France.

Ducrozet, G., Bonnefoy, F., Le Touzé, D., & Ferrant, P. (2016). Hos-ocean: Open-source solver for nonlinear waves in open ocean based on high-order spectral method. *Computer Physics Communications*, *203*, 245-254. Retrieved from https://www.sciencedirect.com/science/article/pii/S0010465516300327 doi: https://doi.org/10.1016/j.cpc.2016.02.017

Edwards, E. C., Holcombe, A., Brown, S., Ransley, E., Hann, M., & Greaves, D. (2023). Evolution of floating offshore wind platforms: A review of at-sea devices. *Renewable and Sustainable Energy Reviews*, *183*, 113416. Retrieved from https://www.sciencedirect.com/science/article/pii/S1364032123002733 doi: https://doi.org/10.1016/j.rser.2023.113416

European Commission. (2022). *REPowerEU: Affordable, secure and sustainable energy for Europe.* Press Release. Retrieved from https://commission.europa.eu/strategy-and-policy/priorities-2019-2024/european-green-deal/repowereu-affordable-secure-and-sustainable-energy-europe_en (18 May 2022)

Faltinsen, O. M., Newman, J. N., & Vinje, T. (1995). Nonlinear wave loads on a slender vertical cylinder. *Journal of Fluid Mechanics*, *289*, 179–198. doi: 10.1017/S0022112095001297

Fenton, J. D. (1990). Nonlinear wave theories. In (Vol. 9 Oceaan Engineering Science, chap. Nonlinear wave theories). Wiley New York.

Ferrant, P. (1997). Simulation of strongly nonlinear wave generation and wave-body interactions using a 3-D MEL model. In *Twenty-first symposium on naval hydrodynamics.* Washington , DC, USA: The National Academies Press. doi: 10.17226/5870

Ferrant, P. (1999, January). Fully non-linear interactions of long-crested wave packets with a three -dimensional body. In *Twenty-second symposium on naval hydrodynamics.* Washington , DC, USA: The National Academies Press. doi: 10.17226/9771

Fontanet, P. (1961). Theory of the generation of a cylindrical wave by a straight-fronted wave generator (second order of approximation). *La Houille Blanche*, *47*(1), 3-31. doi: 10.1051/lhb/1961020

Geuzaine, C., & Remacle, J.-F. (2009). Gmsh: A 3-d finite element mesh generator with built-in pre- and post-processing facilities. *International Journal for Numerical Methods in Engineering*, *79*(11), 1309-1331. Retrieved from https://onlinelibrary.wiley.com/doi/abs/10.1002/nme.2579 doi: https://doi.org/10.1002/nme.2579

Goda, Y. (2010). *Random seas and design of maritime structures* (3rd ed.). World Scientific. Retrieved from https://www.worldscientific.com/doi/abs/10.1142/7425 doi: 10.1142/7425

Goda, Y., & Suzuki, Y. (1976). Estimation of Incident and Reflected Waves in Random Wave Experiments. *Coastal Engineering 1976*, 828-845. Retrieved from https://ascelibrary.org/doi/abs/10.1061/9780872620834.048 doi: 10.1061/9780872620834.048

Grue, J., Bjørshol, G., Strand, Ø., & Ohkusu, M. (1994, April). Nonlinear wave loads which may generate 'ringing'responses of offshore structures. In *Ninth international workshop on water waves and floating bodies* (p. 77-81). Kuju, Fukuoka, Japan.

Grue, J., Clamond, D., Huseby, M., & Jensen, A. (2003). Kinematics of extreme waves in deep water. *Applied Ocean Research*, *25*(6), 355-366. Retrieved from https://www.sciencedirect.com/science/article/pii/S0141118704000264 doi: https://doi.org/10.1016/j.apor.2004.03.001

Gueydon, S., Bayati, I., & de Ridder, E. J. (2020, aug). Discussion of solutions for basin model tests of FOWTs in combined waves and wind. *Ocean Engineering*, *209*, 107288. doi: 10.1016/j.oceaneng.2020.107288

Gueydon, S., Lindeboom, R., van Kampen, W., & de Ridder, E.-J. (2018, 11). Comparison of Two Wind Turbine Loading Emulation Techniques Based on Tests of a TLP-FOWT in Combined Wind, Waves and Current. In (Vol. ASME 2018 1st International Offshore Wind Technical Conference). Retrieved from https://doi.org/10.1115/IOWTC2018-1068 (V001T01A012) doi: 10.1115/IOWTC2018-1068

Gurley, K. R., & Kareem, A. (1998). Simulation of ringing in offshore systems under viscous loads. *Journal of Engineering Mechanics*, *124*(5), 582-586. Retrieved from https://ascelibrary.org/doi/abs/10.1061/%28ASCE%290733-9399%281998%29124%3A5%28582%29 doi: 10.1061/(ASCE)0733-9399(1998)124:5(582)

GWEC. (2022, June). *Global Offshore Wind Report 2022* (techreport). Global Wind Energy Council.

Hasselmann, K., Barnett, T., Bouws, E., Carlson, H., Cartwright, D., Enke, K., ... Walden, H. (1973, 01). Measurements of wind-wave growth and swell decay during the joint north sea wave project (jonswap). *Ergnzungsheft zur Deutschen Hydrographischen Zeitschrift Reihe*, *8*, 1-95.

Hinrichsen, P. F. (2014). Bifilar suspension measurement of boat inertia parameters. *Journal of Sailboat Technology*(2014-01), 1–37.

Huang, J., & Eatock Taylor, R. (1996). Semi-analytical solution for second-order wave diffraction by a truncated circular cylinder in monochromatic waves. *Journal of Fluid Mechanics*, *319*, 171–196. doi: 10.1017/S0022112096007306

Huseby, M., & Grue, J. (2000). An experimental investigation of higher-harmonic wave forces on a vertical cylinder. *Journal of Fluid Mechanics*, *414*, 75–103. doi: 10.1017/S0022112000008533

IEC. (2019). *Pd iec ts 61400-3-2:2019: Wind energy generation systems: Design requirements for floating offshore wind turbines.* British Standards Institute.

IEC. (2020). *Bs en iec 61400-3-:2019+a11:2020: Wind energy generation systems: Design requirements for fixed offshore wind turbines.* British Standards Institute.

ITTC. (2017). *Floating Offshore Platform Experiments* (Recommended Practice and Guidelines No. 7.5-02-07-03.1).

Iwanowski, B., Astrup, S., Lefranc, M., & Hansson, R. (2011, 06). Identification of Ringing Events for a Slender Tubular Marine Structure. In (Vol. Volume 6: Ocean Engineering, p. 419-432). Retrieved from https://doi.org/10.1115/OMAE2011-49511 doi: 10.1115/OMAE2011-49511

Jagdale, S., Ma, Q. W., & Yan, S. (2021, 06). Springing Response of a Tension-leg-platform Wind Turbine Excited by Third-harmonic Force in Nonlinear Regular Waves. In (Vol. All Days). (ISOPE-I-21-3105)

Johannessen, T. B. (2011, October). Nonlinear superposition methods applied to continuous ocean wave spectra. *Journal of Offshore Mechanics and Arctic Engineering*, *134*(1), 011302. doi: 10.1115/1.4003518

Jonkman, J. (2007). *Dynamics modeling and loads analysis of an offshore floating wind turbine, national renewable energy laboratory* (Tech. Rep.).

Jonkman, J., Larsen, T., Hansen, A., Nygaard, T., Maus, K., Karimirad, M., ... Fylling, I. (2010). *Offshore code comparison collaboration within iea wind task 23: Phase iv results regarding floating wind turbine modeling* (Tech. Rep.).

Journée, J., & Massie, W. (2001). *Offshore hydromechanics* (Tech. Rep. ed.). Delft University of Technology.

Keulegan, G. H., & Carpenter, L. H. (1958, 5). Forces on cylinders and plates in an oscillating fluid. *Journal of Research of the National Bureau of Standard*, *60*(5), 423-439. doi: 10.6028/JRES.060.043

Kim, M. H. (1991, December). Second-order sum-frequency wave loads on large-volume structures. *Applied Ocean Research*, *13*(6), 287–296. doi: 10.1016/S0141-1187(05)80052-5

Kim, M.-H., & Yue, D. K. (1989). The complete second-order diffraction solution for an axisymmetric body part 1. monochromatic incident waves. *Journal of Fluid Mechanics*, *200*, 235–264. doi: 10.1017/S0022112089000649

Kim, M.-H., & Yue, D. K. (1990). The complete second-order diffraction solution for an axisymmetric body part 2. bichromatic incident waves and body motions. *Journal of Fluid Mechanics*, *211*, 557–593. doi: 10.1017/S0022112090001690

Kinoshita, T., & Bao, W. (2000). Third-order wave diffraction by a truncated circular cylinder. *Proceedings of the Institution of Mechanical Engineers, Part C: Journal of Mechanical Engineering Science*, *214*(6), 789-800. Retrieved from https://doi.org/10.1243/0954406001523786 doi: 10.1243/0954406001523786

Koo, B., Goupee, A. J., Lambrakos, K., & Lim, H. J. (2013, nov). Model test correlation study for a floating wind turbine on a tension leg platform. In *Proceedings of the asme 2013 32nd international conference on offshore mechanics and arctic engineering - omae* (Vol. 8). American Society of Mechanical Engineers Digital Collection. doi: 10.1115/OMAE2013-11590

Kristiansen, T., & Faltinsen, O. M. (2017, December). Higher harmonic wave loads on a vertical cylinder in finite water depth, experimental. *Journal of Fluid Mechanics*, *833*, 773–805. Retrieved from https://doi.org/10.1017/jfm.2017.702 doi: 10.1017/jfm.2017.702

Krokstad, J. R., Stansberg, C. T., Nestegard, A., & Marthinsen, T. (1998, 02). A New Nonslender Ringing Load Approach Verified Against Experiments. *Journal of Offshore Mechanics and Arctic Engineering*, *120*(1), 20-29. Retrieved from https://doi.org/10.1115/1.2829515 doi: 10.1115/1.2829515

Kwon, S., Lee, H., Park, J., Ha, M., & Kim, Y. (2001). Analysis of ringing by continuous wavelet transform. In Y.-S. Wu, W.-C. Cui, & G.-J. Zhou (Eds.), *Practical design of ships and other floating structures* (p. 587-592). Oxford: Elsevier Science Ltd. Retrieved from https://www.sciencedirect.com/science/article/pii/B9780080439501500740 doi: https://doi.org/10.1016/B978-008043950-1/50074-0

Lamei, A., & Hayatdavoodi, M. (2020, February). On motion analysis and elastic response of floating offshore wind turbines. *Journal of Ocean Engineering and Marine Energy*, *6*(1), 71–90. Retrieved from https://doi.org/10.1007/s40722-019-00159-2 doi: 10.1007/s40722-019-00159-2

Laugesen, R., & Hansen, A. M. (2015). *Experimental Study of the Dynamic Response of the DTU 10 MW Wind turbine on a Tension Leg Platform* (Master Thesis). DTU, Roskilde, Denmark.

Lawson, C. L., & Hanson, R. J. (1995). *Solving least squares problems*. Society for Industrial and Applied Mathematics. Retrieved from https://epubs.siam.org/doi/abs/10.1137/1.9781611971217 doi: 10.1137/1.9781611971217

Lee, C. (1995). *Wamit theory manual* (Tech. Rep.). Cambridge, MA, US: Massachusettes Institute of Technology, Department of Ocean Engineering. (Report No 95-2. Joint industry project on wave effects on offshore structures)

Leroy, V., Delacroix, S., Merrien, A., Bachynski-Polić, E., & Gilloteaux, J.-C. (2022). Experimental investigation of the hydro-elastic response of a spar-type floating offshore wind turbine. *Ocean Engineering*, *255*, 111430. Retrieved from https://www.sciencedirect.com/science/article/pii/S0029801822008113 doi: https://doi.org/10.1016/j.oceaneng.2022.111430

Li, A.-J., & Liu, Y. (2019). New analytical solutions to water wave diffraction by vertical truncated cylinders. *International Journal of Naval Architecture and Ocean Engineering*, *11*(2), 952-969. Retrieved from https://www.sciencedirect.com/science/article/pii/S2092678218302747 doi: https://doi.org/10.1016/j.ijnaoe.2019.04.006

Lighthill, J. (1979). Waves and hydrodynamic loading. In (Vol. 1, pp. 1–40). Cranfield: BHRA Fluid Enginee.

Liu, Y., Kim, C., & Lu, X. (1990, 08). Comparison Of Higher-Order Boundary Element And Constant Panel Methods For Hydrodynamic Loadings. In (Vol. All Days). (ISOPE-E-90-008)

Liu, Y., Xue, M., & Yue, D. K. P. (2001). Computations of fully nonlinear three-dimensional wave–wave and wave–body interactions. part 2. nonlinear waves and forces on a body. *Journal of Fluid Mechanics*, *438*, 41–66. doi: 10.1017/S0022112001004384

MacCamy, R., & Fuchs, R. (1954). Wave forces on piles. *BEB Technical Memoir*(69).

Madgwick, S. O. H., Harrison, A. J. L., & Vaidyanathan, R. (2011). Estimation of imu and marg orientation using a gradient descent algorithm. In *2011 ieee international conference on rehabilitation robotics* (p. 1-7). doi: 10.1109/ICORR.2011.5975346

Madsen, F., Nielsen, T., Kim, T., Bredmose, H., Pegalajar-Jurado, A., Mikkelsen, R., ... Shin, P. (2020). Experimental analysis of the scaled dtu10mw tlp floating wind turbine with different control strategies. *Renewable Energy*, *155*, 330-346. Retrieved from https://www.sciencedirect.com/science/article/pii/S096014812030478X doi: https://doi.org/10.1016/j.renene.2020.03.145

Malenica, Š. (1994). *Diffraction de troisième ordre et intéraction houle-courant pour un cylindre vertical en profondeur finie* (Unpublished doctoral dissertation). Paris VI, Paris, France.

Malenica, Š., Eatock Taylor, R., & Huang, J. B. (1999). Second-order water wave diffraction by an array of vertical cylinders. *Journal of Fluid Mechanics*, *390*, 349–373. doi: 10.1017/S0022112099005273

Malenica, Š., & Molin, B. (1995). Third-Harmonic Wave Diffraction by a Vertical Cylinder. *Journal of Fluid Mechanics*, *302*, 203–229. doi: 10.1017/S0022112095004071

Manners, W., & Rainey, R. C. T. (1992, January). Hydrodynamic forces on fixed submerged cylinders. *Proceedings of the Royal Society of London. Series A: Mathematical and Physical Sciences*, *436*(1896), 13–32. Retrieved from https://doi.org/10.1098/rspa.1992.0002 doi: 10.1098/rspa.1992.0002

Mansard, E., & Funke, E. (1980). The measurement of incident and reflected spectra using a least squares method. In *Coastal engineering 1980* (p. 154-172). doi: 10.1061/9780872622647.008

Mavrakos, S., Chatjigeorgiou, I., & Lentziou, D. (2005, 06). Wave run-up and second-order wave forces on a truncated circular cylinder due to monochromatic waves. In *Proceedings of the asme 2005 24th international conference on offshore mechanics and arctic engineering - omae* (Vol. 1). doi: 10.1115/OMAE2005-67104

Mazarakos, T. P., & Mavrakos, S. A. (2017). Experimental investigation on mooring loads and motions of a tlp floating wind turbine. In *2017 twelfth international conference on ecological vehicles and renewable energies (ever)* (p. 1-6). doi: 10.1109/EVER.2017.7935945

Milano, D. (2021). *A Numerical Prototype for Floating Offshore Wind Turbines* (EngD Thesis). The University of Edinburgh, IDCORE, Edinburgh, UK.

Milano, D., Peyrard, C., & Capaldo, M. (2018). The Effect of Tendon Inclination on the Hydro-Aerodynamic Response of a 10 Mw Tension-Leg Platform Wind Turbine. In *16e journée de l'hydrodynamique.*

Milano, D., Peyrard, C., Capaldo, M., Ingram, D., Xiao, Q., & Johanning, L. (2019). Impact of High Order Wave Loads on a 10 MM Tension-Leg Platform Floating Wind Turbine at Different Tendon Inclination Angles. In *Proceedings of the asme 2019 38th international conference on ocean, offshore and arctic engineering - omae2019* (pp. 1–10). Glasgow: ASME. doi: 10.1115/OMAE2019-96243

Mohseni, M., & Guedes Soares, C. (2022). Numerical investigation of inline wave force on a truncated vertical cylinder with different cross-sections in regular head waves. *Ocean Engineering*, *251*, 111063. Retrieved from https://www.sciencedirect.com/science/article/pii/S0029801822004784 doi: https://doi.org/10.1016/j.oceaneng.2022.111063

Molin, B. (1979). Second-order diffraction loads upon three-dimensional bodies. *Applied Ocean Research*, *1*(4), 197-202. doi: https://doi.org/10.1016/0141-1187(79)90027-0

Molin, B. (2023). *Offshore structure hydrodynamics*. Cambridge University Press. doi: 10.1017/9781009198059

Molin, B., Remy, F., & Facon, G. (2004). Etude expérimentale du comportement hydro-aéro-elastique d'une eolienne offshore sur ancrages tendus. In *Ocean energy conference, brest, france.*

Molin, B., Remy, F., & Falcon, G. (2004, 10). Etude expérimentale du comportement hydro-aéroelastique d'une eolienne offshore sur ancrages tendus. In *SeaTechWeek Colloque Ifremer-ADEME: Energies Renouvelables en Mer* (Vols. Eolien offshore: Technologie, installation, maintenance). Brest, France.

Morison, J., Johnson, J., & Schaaf, S. (1950, May). The Force Exerted by Surface Waves on Piles. *Journal of Petroleum Technology*, *2*(05), 149-154. Retrieved from https://doi.org/10.2118/950149-G doi: 10.2118/950149-G

National Instruments. (n.d.). *Compactrio modules.* Web. Retrieved from https://www.ni.com/en/shop/compactrio/compactrio-modules.html

Newman, J. N. (1996a). Nonlinear scattering of long waves by a vertical cylinder. In J. Grue, B. Gjevik, & J. E. Weber (Eds.), *Waves and nonlinear processes in hydrodynamics* (pp. 91–102). Dordrecht: Springer Netherlands. Retrieved from https://doi.org/10.1007/978-94-009-0253-4_8 doi: 10.1007/978-94-009-0253-4_8

Newman, J. N. (1996b). The second-order wave force on a vertical cylinder. *Journal of Fluid Mechanics*, *320*, 417–443. doi: 10.1017/S0022112096007598

O'Brien, M. P., & Morison, J. R. (1952). The forces exerted by waves on objects. *Eos, Transactions American Geophysical Union*, *33*(1), 32-38. Retrieved from https://agupubs.onlinelibrary.wiley.com/doi/abs/10.1029/TR033i001p00032 doi: https://doi.org/10.1029/TR033i001p00032

Ocean Engineering Committee of the 28th ITTC. (2017). *ITTC Recommended Procedures and Guidelines - Floating Offshore Platform Experiments* (Tech. Rep.).

Oguz, E., Clelland, D., Day, A. H., Incecik, A., López, J. A., Sánchez, G., & Almeria, G. G. (2018, jan). Experimental and numerical analysis of a TLP floating offshore wind turbine. *Ocean Engineering*, *147*, 591–605. doi: 10.1016/j.oceaneng.2017.10.052

Orcina. (2023). *Orcaflex online manual.* Retrieved from `https://www.orcina.com/webhelp/OrcaFlex/Default.htm` (Accessed: 2023-05-12)

Otter, A., Murphy, J., Pakrashi, V., Robertson, A., & Desmond, C. (2022). A review of modelling techniques for floating offshore wind turbines. *Wind Energy*, *25*(5), 831-857. Retrieved from `https://onlinelibrary.wiley.com/doi/abs/10.1002/we.2701` doi: https://doi.org/10.1002/we.2701

Paulsen, B. T., Bredmose, H., Bingham, H., & Jacobsen, N. (2014). Forcing of a bottom-mounted circular cylinder by steep regular water waves at finite depth. *Journal of Fluid Mechanics*, *755*, 1–34. doi: 10.1017/jfm.2014.386

Pegalajar-Jurado, A., Borg, M., Robertson, A., Jonkman, J., & Bredmose, H. (2017, 06). Effect of Second-Order and Fully Nonlinear Wave Kinematics on a Tension-Leg-Platform Wind Turbine in Extreme Wave Conditions. In *Proceedings of the asme 2017 36th international conference on offshore mechanics and arctic engineering* (Vol. Volume 10: Ocean Renewable Energy). Retrieved from `https://doi.org/10.1115/OMAE2017-61798` (V010T09A077) doi: 10.1115/OMAE2017-61798

Pegalajar-Jurado, A., Hansen, A. M., Laugesen, R., Mikkelsen, R. F., Borg, M., Kim, T., ... Bredmose, H. (2016, sep). Experimental and numerical study of a 10mw tlp wind turbine in waves and wind. *Journal of Physics: Conference Series*, *753*(9), 092007. Retrieved from `https://dx.doi.org/10.1088/1742-6596/753/9/092007` doi: 10.1088/1742-6596/753/9/092007

Peyrard, C. (2018). *A note about third order wave loads on offshore wind turbine foundations. EDF R&D Report 6125-3312-2018-03541-EN.*

Peyrard, C., Benguigui, W., Barcet, M., Robaux, F., Benoit, M., & Teles, M. (2023, 06). Modeling FOWT hydrodynamic behavior with comparison to basin test experiments. In *Proceedings of the 33rd international ocean and polar engineering conference* (Vol. All days, p. ISOPE-I-23-039). (ISOPE-I-23-237)

Pinkster, J. A. (1980). *Low frequency second order wave exciting forces on floating structures* (PhD Thesis). TUDelft, Delft, Netherlands.

Rainey, R. C. T. (1989). A new equation for calculating wave loads on offshore structures. *Journal of Fluid Mechanics*, *204*, 295–324. doi: 10.1017/S002211208900176X

Rainey, R. C. T. (1995). Slender-body expressions for the wave load on offshore structures. *Proceedings: Mathematical and Physical Sciences*, *450*(1939), 391–416. Retrieved 2022-07-29, from http://www.jstor.org/stable/52715 doi: 10.1098/rspa.1995.0091

Ransley, E., Brown, S., Edwards, E., Tosdevin, T., Monk, K., Reynolds, A., ... Hann, M. (2022). Hydrodynamic response of a floating offshore wind turbine (1st FOWT Comparative Study Dataset). *PEARL Research Repository*. doi: 10.24382/71J2-3385

Ren, N., Ma, Z., Shan, B., Ning, D., & Ou, J. (2020). Experimental and numerical study of dynamic responses of a new combined tlp type floating wind turbine and a wave energy converter under operational conditions. *Renewable Energy*, *151*, 966-974. Retrieved from https://www.sciencedirect.com/science/article/pii/S0960148119317884 doi: https://doi.org/10.1016/j.renene.2019.11.095

Robaux, F. (2022). *Studies and convergences neptune cfd* (Tech. Rep.). EDF R&D - LNHE.

Robaux, F., Nadal, A. B., Peyrard, C., Benoit, M., Benguigui, W., & Guiton, M. (2022, November). Uncertainty analysis of hydrodynamic coefficients for floating wind turbine using CFD solvers. In *18eme journée de l'hydrodynamique* (Vol. All days). Poitier. doi: https://jh2022.sciencesconf.org/420869

Robertson, A., Jonkman, J., Vorpahl, F., Popko, W., Qvist, J., Frøyd, L., ... Guérinel, M. (2014, 06). Offshore Code Comparison Collaboration Continuation Within IEA Wind Task 30: Phase II Results Regarding a Floating Semisubmersible Wind System. In (Vol. Volume 9B: Ocean Renewable Energy). Retrieved from https://doi.org/10.1115/OMAE2014-24040 (V09BT09A012) doi: 10.1115/OMAE2014-24040

Robertson, A. N., Gueydon, S., Bachynski, E., Wang, L., Jonkman, J., Alarcón, D., ... Wohlfahrt-Laymann, S. (2020, September). OC6 phase i: Investigating the underprediction of low-frequency hydrodynamic loads and responses of a floating wind turbine. *Journal of Physics: Conference Series*, *1618*(3), 032033. Retrieved from https://doi.org/10.1088/1742-6596/1618/3/032033 doi: 10.1088/1742-6596/1618/3/032033

Robertson, A. N., Wendt, F., Jonkman, J. M., Popko, W., Dagher, H., Gueydon, S., ... Debruyne, Y. (2017). Oc5 project phase ii: Validation of global loads of the deepcwind floating semisubmersible wind turbine. *Energy Procedia*, *137*, 38-57. Retrieved from https://www.sciencedirect.com/science/article/pii/S1876610217352931 (14th Deep Sea Offshore Wind RD Conference, EERA DeepWind'2017) doi: https://doi.org/10.1016/j.egypro.2017.10.333

Rodriguez, S. (2019). *Applied computational fluid dynamics and turbulence modeling: Practical tools, tips and techniques*. Springer Nature.

Rongé, E., Peyrard, C., Benoit, M., Robaux, F., & Venugopal, V. (2022, November). A comparison of engineering third-order wave load models for bottom seated and truncated vertical cylinders. In *18eme journée de l'hydrodynamique* (Vol. All days). Poitier. doi: https://jh2022.sciencesconf.org/420817

Rongé, E., Peyrard, C., Venugopal, V., Johanning, L., & Xiao, Q. (2023, 06). On the Evaluation of Nonlinear Response of Floating Wind TLPs Hydrodynamics: Numerical and Experimental Modelling. In *Proceedings of the 33rd international ocean and polar engineering conference* (Vol. All Days, p. ISOPE-I-23-054).

Rongé, E., Peyrard, C., Venugopal, V., Xiao, Q., & Johanning, L. (2022, June). The application of semi-analytical diffraction formulas to predict the second-order dynamic response of a tlp floating wind turbine in monochromatic waves. In *Proceedings of the asme 2022 41st international conference on offshore mechanics and arctic engineering - omae* (Vol. Ocean Renewable Energy). Hamburg: ASME. doi: 10.1115/OMAE2022-78673

Rongé, E., Peyrard, C., Venugopal, V., Xiao, Q., Johanning, L., & Benoit, M. (2023). Evaluation of second and third-order numerical wave-loading models for floating offshore wind TLPs. *Ocean Engineering*, *288*, 116064. Retrieved from https://www.sciencedirect.com/science/article/pii/S0029801823024484 doi: https://doi.org/10.1016/j.oceaneng.2023.116064

Sarpkaya, T. (1986). Force on a circular cylinder in viscous oscillatory flow at low keulegan—carpenter numbers. *Journal of Fluid Mechanics*, *165*, 61–71. doi: 10.1017/S0022112086002999

Schäffer, H. A. (1996). Second-order wavemaker theory for irregular waves. *Ocean Engineering*, *23*(1), 47-88. Retrieved from https://www.sciencedirect.com/science/article/pii/002980189500013B doi: https://doi.org/10.1016/0029-8018(95)00013-B

Shao, Y. (2010). *Numerical potential-flow studies on weakly-nonlinear wave body interactions with/without forward speed* (PhD Thesis). NTNU, Trondheim, Norway.

Sharma, J. N., & Dean, R. G. (1981, feb). Second-order directional seas and associated wave forces. *Society of Petroleum Engineers Journal*, *21*(1), 129–140. doi: 10.2118/8584-PA

Shen, M., Hu, Z., & Liu, G. (2016). Dynamic response and viscous effect analysis of a tlp-type floating wind turbine using a coupled aero-hydro-mooring dynamic code. *Renewable Energy*, *99*, 800-812. Retrieved from https://www.sciencedirect.com/science/article/pii/S0960148116306735 doi: https://doi.org/10.1016/j.renene.2016.07.058

Stansberg, C. T. (1997, July). Comparing ringing loads from experiments with cylinders of different diameters - an empirical study. In *Boss 97: International conference on the behaviour of offshore structures.* Delft.

Stansberg, C. T., Gudmestad, O. T., & Haver, S. K. (2008, 06). Kinematics Under Extreme Waves. *Journal of Offshore Mechanics and Arctic Engineering*, *130*(2), 021010. Retrieved from https://doi.org/10.1115/1.2904585 doi: 10.1115/1.2904585

Suja-Thauvin, L., Bachynski, E. E., Pierella, F., Borg, M., Krokstad, J. R., & Bredmose, H. (2020). Critical assessment of hydrodynamic load models for a monopile structure in finite water depth. *Marine Structures*, *72*, 102743. Retrieved from https://www.sciencedirect.com/science/article/pii/S095183392030037X doi: https://doi.org/10.1016/j.marstruc.2020.102743

Teng, B., & Kato, S. (2002). Third order wave force on axisymmetric bodies. *Ocean Engineering*, *29*(7), 815–843. doi: 10.1016/S0029-8018(01)00047-6

Thilleul, O. (2014). *Projet MONACOREV: tache 1.3 Modèles et coefficients pour la prise en compte des phénomènes de dissipation visqueuse.* (Technical report No1110-1). Hydrocean. Retrieved from https://website.ec-nantes.fr/lheea/web/lib/exe/fetch.php?media=monacorev:1110_rapport_coefficients_amortissement_vc.pdf

Tromans, P., Swan, C., & Masterton, S. (2006). *Nonlinear potential flow forcing: the ringing of concrete gravity based structures - a summary report* (HSE Research Report No 468). United Kingdom: Health & Safety Executive.

Vardaroglu, M., Gao, Z., Avossa, A. M., & Ricciardelli, F. (2022). Validation of a tlp wind turbine numerical model against model-scale tests under regular and irregular waves. *Ocean Engineering*, *256*, 111491. Retrieved from https://www.sciencedirect.com/science/article/pii/S0029801822008629 doi: https://doi.org/10.1016/j.oceaneng.2022.111491

Venugopal, V., Varyani, K. S., & Westlake, P. C. (2009). Drag and inertia coefficients for horizontally submerged rectangular cylinders in waves and currents. *Proceedings of the Institution of Mechanical Engineers, Part M: Journal of Engineering for the Maritime Environment*, *223*(1), 121-136. Retrieved from https://doi.org/10.1243/14750902JEME124 doi: 10.1243/14750902JEME124

Villefer, A. (2022). *Study of wave overtopping processes ofcoastal protections in complex sea-states* (phdthesis). Ecole des Ponts ParisTech, Chatou, France.

Vita, L., Ramachandran, G. K., Krieger, A., Kvittem, M. I., Merino, D., Cross-Whiter, J., & Ackers, B. B. (2015, oct). Comparison of numerical models and verification against experimental data, using Pelastar TLP concept. In *Proceedings of the asme 2015 34th international conference on offshore mechanics and arctic engineering* (Vol. 9). American Society of Mechanical Engineers (ASME). doi: 10.1115/OMAE2015-41874

Vittori, F., Bouchotrouch, F., Lemmer, F., & Azcona, J. (2018, 06). Hybrid Scaled Testing of a 5MW Floating Wind Turbine Using the SiL Method Compared With Numerical Models. , *Volume 10: Ocean Renewable Energy*. (V010T09A082) doi: 10.1115/OMAE2018-77853

Vittori, F., Pires, O., Azcona, J., Uzunoglu, E., Soares, C. G., Rodríguez, R. Z., & Souto-Iglesias, A. (2020, October). Hybrid scaled testing of a 10mw TLP floating wind turbine using the SiL method to integrate the rotor thrust and moments. In *Developments in renewable energies offshore* (pp. 417–423). CRC Press. Retrieved from https://doi.org/10.1201/9781003134572-48 doi: 10.1201/9781003134572-48

Wehmeyer, C., Ferri, F., Frigaard, P. B., & Skourup, J. (2013, jun). Experimental Study of an Offshore Wind Turbine TLP in ULS Conditions. In *The twenty-third international offshore and polar engineering conference.* Anchorage, Alaska: International Society of Offshore and Polar Engineers.

Xiong, H., Yang, J., & Tian, X. (2020). An experimental study on the inline wave force on a truncated vertical cylinder. *Ships and Offshore Structures*, *15*(1), 39-52. Retrieved from https://doi.org/10.1080/17445302.2015.1114292 doi: 10.1080/17445302.2015.1114292

Xue, M., Xü, H., Liu, Y., & Yue, D. K. P. (2001). Computations of fully nonlinear three-dimensional wave–wave and wave–body interactions. part 1. dynamics of steep three-dimensional waves. *Journal of Fluid Mechanics*, *438*, 11–39. doi: 10.1017/S0022112001004396